

G8934

SPRAY PYROLYSED $\text{CuInS}_2/\text{In}_2\text{S}_3$ SOLAR CELL: MATERIAL
CHARACTERIZATION AND DEVICE FABRICATION

*Thesis submitted to Cochin University of Science and Technology
For the award of the degree of*

DOCTOR OF PHILOSOPHY

By

Teny Theresa John



Thin Film Photovoltaic Division
Department of Physics
Cochin University of Science and Technology
Kochi- 22, India

December 2004

Dr.K.P.Vijayakumar
Professor

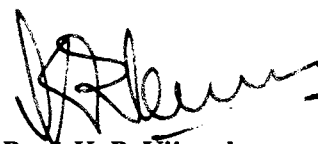
Department of Physics
**Cochin University of Science
and Technology**
COCHIN-682 022
INDIA

Ph:(off):0484-2577404
(res):0484-2577103
Fax:0484-2577595
Email : kpv@cusat.ac.in

CERTIFICATE

Certified that the work presented in this thesis entitled "*Spray Pyrolysed CuInS₂/In₂S₃ Solar Cell: Material Characterization and Device Fabrication*" is based on the bonafied research work done by Ms. Teny Theresa John under my guidance in the Department of Physics, Cochin University of Science and Technology, Kochi - 682022, and has not been included in any other thesis submitted previously for the award of any degree.

Kochi-22
30-12-2004



Prof. K. P. Vijayakumar
(Supervising Guide)

DECLARATION

Certified that the work presented in this thesis entitled "*Spray Pyrolysed CuInS₂/In₂S₃ Solar Cell: Material Characterization and Device Fabrication*" is based on the original research work done by me under the guidance of **Prof. K. P. Vijayakumar**, Department of Physics, Cochin University of Science and Technology, Kochi - 682022, and has never been included in any other thesis submitted previously for the award of any degree.

Kochi-22

30-12-2004


Teny Theresa John

Acknowledgement

I am writing this with a heart full of gratitude to all those who were instrumental in helping me realize this doctoral thesis.

First and foremost let me place on record my deep sense of gratitude to my mentor and guide, Prof. K. P. Vijayakumar. It was his sincere and devoted guidance that made this thesis possible. He was the guiding spirit behind all my endeavours throughout my stay in the University. My gratitude to him knows no bounds.

I am deeply indebted to Dr. C. Sudha Kartha for all the assistance that she extended to me during my research work. She was always a source of encouragement and showed keen interest in my progress.

I am extremely thankful to Dr. V. C. Kuriakose, Professor & Head of the Department of Physics for all the facilities extended to me in the department.

Prof. Y. Kashiwaba, Department of Electrical and Electronic Engineering, Iwate University, Japan helped me with XPS measurements and he went out of the way to extend all possible assistance to me. He and his family are fondly and gratefully remembered here for all the help extended to me during my stay in Japan. I can never forget the warmth of their love.

Dr. T. Abe showed extreme patience in taking XPS measurements and his help is gratefully acknowledged.

I would like to express my sincere thanks to all the teachers of the faculty of Physics and the members of the non-teaching staff for their timely help and co-operation.

I have been singularly lucky to have eminent teachers all through my student life and they are respectfully and fondly remembered.

Ms. Ampili and Ms. Manju shared a strong bond of friendship and cordiality with me. I am indeed thankful to them for their whole-hearted support and encouragement.

The expertise and experience of my seniors – Mr. Ramkumar, Ms. Syamala, Ms. Bindu, Ms. Lakshmi, Ms. Bini, Mr. Paulraj, Ms. Rupa, Mr. Harish and Mr. Renu came in quite handy to me during my work and I am thankful to them.

Mr. Wilson, Mr. Ratheesh, Ms. Beena, Mr. Kishore, Mr. Sreekumar A, Ms. Deepa, Mr. Jayakrishnan, Mr. Sreekumar R, Ms. Tina and Ms. Meril have always been very helpful in many ways. I am immensely pleased to reciprocate their assistance. Mr. Ratheesh deserves special mention for the innumerable ways in which he helped me right from the time I began my work on the thesis. My thanks are also due to my colleagues in the department.

My friends in the hostel Ms. Rinku (my room – mate), Ms. Radhika, Ms. Rehana, Ms. Nisha, Ms. Maya Ms. Ambili and Ms. Kochurani were a great source of encouragement. I have great pleasure in thanking them most sincerely.

My family means everything to me. Whatever I write here will be insufficient to express my sense of indebtedness to them. My efforts bore fruit to a great extent owing to the solid support that the members of my family lent me during the last few years.

Let me conclude this by raising my heart in profound gratitude to God Almighty.

Teny Theresa John

....to my Appachan, Amma, Vallyammachi, Tom
& Tony

Contents

Preface

Publications

Chapter 1 An Introduction to Photovoltaics

1.1	Introduction	1
1.2	Solar Energy	
1.2.1	The Sun	2
1.2.2	Solar Spectrum	3
1.2.3	Availability of Solar Radiation	4
1.2.4	Direct and Diffuse Radiation	5
1.2.5	Air Mass Ratio	6
1.2.6	Advantages of Solar Energy	7
1.2.7	Applications	8
1.3	Solar Cells	
1.3.1	Historical Survey	9
1.3.2	The pn Junction	10
1.3.3	The pn Junction Under Load	14
1.3.4	Junction Under Irradiation	17
1.3.5	Symbolic Representation of Solar Cell	22
1.3.6	Solar Cell Output Parameters	23
1.3.7	Spectral Response	26
1.3.8	Efficiency of an Ideal pn Junction Cell	26
1.3.9	Factors Affecting Efficiency of a Solar Cell	31
1.3.9.1	Optical Losses (Short Circuit Current Losses)	31
1.3.9.2	Recombination Losses (Open circuit Voltage Losses)	32
1.3.9.3	Series and Shunt Resistance (Fill Factor Losses)	34
1.3.9.4	Effect of Temperature	34
1.4	Why Thin Film Materials?	36

1.5	Thin Film Solar Cells	37
1.6	Structure of Thin Film Solar Cells	
1.6.1	Substrate and Superstrate Configurations	39
1.6.2	Absorber Layer	40
1.6.3	Buffer Layer	43
1.6.4	Transparent Conducting Oxide, TCO	44
1.6.5	Back Contact	46
1.6.6	Substrate	46
1.6.7	Antireflection Coating	46
1.6.8	Top Grid	46
1.7	Materials for Thin Film Solar Cells	
1.7.1	Absorber Layer	47
1.7.1.1	Copper Indium Selenide (CuInSe ₂)	47
1.7.1.2	Cadmium Telluride (CdTe)	48
1.7.1.3	Amorphous Si (a-Si)	49
1.7.1.4	Polycrystalline Si	50
1.7.1.5	Organic Semiconductors	51
1.7.2	Buffer Layer	52
1.7.2.1	Cadmium Sulfide (CdS)	52
1.7.2.2	Zn _x Cd _{1-x} S	53
1.7.2.3	Indium Sulfide (In ₂ S ₃)	53
1.7.2.4	Indium Selenide (In ₂ Se ₃)	54
1.7.2.5	Zinc Oxide (ZnO)	55
1.7.2.6	Indium Hydroxy Sulfide (In _x (OH,S) _y)	55
Chapter 2 Review on In₂S₃ and CuInS₂ Thin Films		
2.1	Introduction	64
2.2	In ₂ S ₃ Thin Films	64
2.2.1	Preparation Techniques	65
2.2.1.1	In ₂ S ₃ Using Chemical Spray Pyrolysis (CSP)	78
2.2.2	Optical and Electrical Properties	80

2.2.3 Doping in In_2S_3	87
2.2.4 Different Studies on In_2S_3	91
2.3 CuInS_2 Thin Films	92
2.3.1 Preparation Techniques	93
2.3.1.1 CuInS_2 Using Chemical Spray Pyrolysis Technique	101
2.3.2 Electrical and Optical Properties	105
2.3.3 Effect of Na Incorporation	108
2.3.4 Effect of KCN Etching	110
2.3.5 Different Studies on CuInS_2	111
2.3.6 Defects in CuInS_2	116
2.4 CuInS_2 as Absorber Layer	120
2.5 Review on CuInS_2 Based Solar Cells	121
Chapter 3 Studies on Indium Sulfide Thin Films Prepared Using Chloride Based Precursor Solution	
3.1 Introduction	148
3.2 Experimental Details	150
3.3 Results and Discussion	152
3.3.1 Effect of Variation of Substrate Temperature	152
3.3.1.1 Structural Analysis	152
3.3.1.2 Scanning Electron Micrograph (SEM)	157
3.3.1.3 Atomic Force Microscopy (AFM)	158
3.3.1.4 XPS Analysis	159
3.3.1.5 Optical Studies	162
3.3.1.6 Photosensitivity Measurements	167
3.3.2 Effect of Variation of Sulfur Concentration	168
3.3.2.1 Structural Analysis	169
3.3.2.2 Energy Dispersive X-Ray Analysis (EDAX)	170
3.3.2.3 XPS Analysis	171
3.3.2.4 Optical Studies	173
3.3.2.5 Photosensitivity Measurements	177

Contents

3.3.2.6 Electrical Conductivity	178
3.3.3 Effect of Variation of Indium Concentration	178
3.3.3.1 Structural Analysis	179
3.3.3.2 XPS Analysis	179
3.3.3.3 Optical Studies	182
3.3.3.4 Photosensitivity Measurements	184
3.3.4 Thermally Stimulated Conductivity (TSC) Measurements	185
3.3.5 Variation of Thickness	187
3.3.5.1 Structural Analysis	187
3.3.5.2 Measurement of Thickness	188
3.3.5.3 Optical Studies	189
3.3.5.4 Electrical Resistivity	192
3.3.6 Effect of Annealing	193
3.3.6.1 Structural Analysis	193
3.3.6.2 Surface Morphology	194
3.3.6.3 XPS Analysis	195
3.3.6.4 Optical Studies	196
3.3.6.5 Variation of Sheet Resistance	199
3.4 Conclusion	200
Chapter 4 Properties of Indium Sulfide Thin Films Prepared Using Nitrate Based Precursor Solution	
4.1 Introduction	204
4.2 Experimental Details	205
4.3 Results and Discussion	
4.3.1 Effect of Variation of Sulfur Concentration	205
4.3.1.1 Structural Analysis	205
4.3.1.2 Surface Morphology	207
4.3.1.3 AFM	209
4.3.1.4 EDAX Measurements	210
4.3.1.5 XPS Analysis	212

4.3.1.6	Optical Studies	215
4.3.1.7	Resistivity and Photosensitivity	219
4.3.2	Effect of Variation of Indium Concentration	221
4.3.2.1	Structural Analysis	221
4.3.2.2	Optical Studies	222
4.3.2.3	Photosensitivity Measurements	223
4.4	Conclusion	224
Chapter 5 Studies on CuInS₂ Thin Films Prepared Using Chloride and Nitrate Based Precursor Solutions		
5.1	Introduction	228
5.2	Experimental Details	230
5.3	CuInS ₂ from Chloride Based Precursor Solution	
5.3.1	Structural Analysis	230
5.3.2	Surface Morphology	232
5.3.3	EDAX Measurements	234
5.3.4	XPS Analysis	235
5.3.5	Optical Studies	237
5.3.6	Photosensitivity Measurements	239
5.4	CuInS ₂ from Nitrate Based Precursor Solution	
5.4.1	Structural Analysis	239
5.4.2	Surface Morphology	240
5.4.3	EDAX Measurements	242
5.4.4	XPS Analysis	244
5.4.5	Optical Studies	245
5.4.6	Photosensitivity Measurements	246
5.5	Temperature Dependent Conductivity of Chloride and Nitrate Based CuInS ₂ Films	247
5.6	Conclusion	253

Chapter 6 Properties of CuInS₂ Films Prepared Using Repeated Spray Pyrolysis Technique	
6.1 Introduction	257
6.2 Experimental Details	258
6.3 Results and Discussion	259
6.3.1 Structural Analysis	259
6.3.2 Surface Morphology	260
6.3.3 EDAX Measurements	263
6.3.4 XPS Analysis	264
6.3.5 Optical Studies	265
6.3.6 Resistivity and Photosensitivity	267
6.3.7 Temperature Dependent Conductivity Measurements	268
6.4 Conclusion	271
Chapter 7 Fabrication and Characterization of All-Sprayed CuInS₂/In₂S₃ Solar Cell	
7.1 Introduction	275
7.2 Device Fabrication	277
7.2.1 Back Contact (ITO)	277
7.2.2 CuInS ₂ Absorber Layer	279
7.2.3 In ₂ S ₃ Buffer Layer	279
7.2.4 Electrode Deposition	280
7.3 J-V Characteristics of the Cell	281
7.4 Results and Discussion	
7.4.1 Effect of Having Superstrate Structure	282
7.4.2 Effect of Layer Thickness Variation	283
7.4.3 Effect of Variation of Atomic Concentration	288
7.4.4 Effect of Post Deposition Annealing	291
7.5 Conclusion	295

Chapter 8 CuInS₂/In₂S₃ Solar Cell Prepared Using CSP Technique: Design Modifications for Improved Performance	
8.1 Introduction	299
8.2 Device Fabrication	300
8.3 Results and Discussion	
8.3.1 Cell-A	301
8.3.2 Cell-B	302
8.3.3 Cell-C	308
8.4 Conclusion	313
Chapter 9 Summary and Conclusions	316

Preface

Photovoltaic conversion of solar energy appears to be one of the most promising ways of meeting the increasing energy demands of the future in a time when conventional energy sources are being depleted. The present growing interest in photovoltaic conversion is a consequence of the concern to identify future sources of energy that will be inexpensive as well as ecofriendly.

Semiconductors have emerged as the most promising class of materials that can convert sunlight directly into electrical energy. Currently, a wide range of semiconductors is explored for their potential use in photovoltaic applications. The general criteria determining the choice of a particular semiconductor are efficiency and cost considerations, the environmental conditions (eg. terrestrial or space applications and duration of sunshine) and the availability and toxicity of the raw materials. Each material requires a particular solar cell device structure for optimum performance, and the choice is primarily determined by the available processing techniques and the photovoltaic properties that can be achieved under these conditions.

Lowering the cost of solar cell production is one of the most important intentions in photovoltaic research. To achieve this, thin film technology need to be developed with thin film materials having good photovoltaic properties and appropriate band gap that can be deposited uniformly over large areas. Recent developments in solar cell research proved that CuInSe_2 and its alloys and CuInS_2 are promising absorber layers for high efficiency solar cells. Recently efficiency upto 19.2% has been achieved with $\text{ZnO/CdS/CuInGaSe}_2$ (CIGS) cell structure.

CuInS_2 is particularly important because of band gap of 1.5 eV, which is close to the optimum value for photovoltaic conversion and controllable conversion type. Moreover, the constituents of this compound are non-toxic. Efficiency of the order of 13% was obtained for $\text{TCO/CdS/CuInS}_2/\text{CuGaS}_2$ cell structure. Nowadays lot of

research is going on for the replacement of the buffer layer CdS by a Cd-free, wider band gap materials like $\text{In}_x(\text{OH,S})_y$, ZnO, ZnSe, In_2Se_3 or In_2S_3 . In_2S_3 films deposited using Atomic Layer Chemical Vapour Deposition (ALCVD) yielded an efficiency of 16.4% in CIGS based cells.

In the present work, we have prepared and characterized CuInS_2 and In_2S_3 thin films using the simple and low cost Chemical Spray Pyrolysis (CSP) technique. The technique is also suitable for large area film deposition. The films were optimized for different substrate temperatures and atomic concentrations. Making use of the optimized conditions for films with good photovoltaic activity, we could fabricate all sprayed $\text{CuInS}_2/\text{In}_2\text{S}_3$ having 9.5% efficiency, which is the first one of its kind to the best of our knowledge. The thesis is divided into nine chapters and a brief description of the contents of each chapter is described below.

CHAPTER 1 is a general introduction to photovoltaics. It begins with the description of the origin and use of solar energy along with detailed theory of *pn* junction. The factors affecting the efficiency of solar cell and the importance of thin film materials are also explained here. In the next section structure of the thin film solar cell with description of the requirements of different layers is given. This chapter is concluded with a discussion on different materials presently used for thin film solar cells.

CHAPTER 2 presents an exhaustive review on copper indium sulfide, indium sulfide and CuInS_2 based solar cells.

Preparation and characterization of indium sulfide thin films, using Chemical Spray Pyrolysis technique (CSP), is described in **CHAPTER 3**. Chloride based precursor solutions were used for sample preparation. CSP technique is essentially suitable for solar cell production, because of the possibility of large-area deposition of thin films in any required shape, easiness of doping and/or variation of atomic ratio and low cost/low tech nature of the technique. We prepared indium sulfide thin films systematically, at different substrate temperatures and by varying the In/S ratio in the

spray solution. Structural, compositional, optical and electrical characterizations of the films were carried out using X-Ray Diffraction (XRD), X-ray Photoelectron Spectroscopy (XPS), EDAX, resistivity, photosensitivity, optical absorption and transmission. Surface analysis was done using Scanning Electron Microscopy (SEM) and Atomic Force Microscopy (AFM). We could optimize the composition of the spray solution to get good values of resistivity and photosensitivity. When this material is used as buffer layer in solar cells, these two parameters are important. In terms of crystallinity, photosensitivity and band gap the sample having In/S ratio 1.2/8 was selected for fabricating solar cells in this work.

CHAPTER 4 deals with the studies on indium sulfide thin films prepared using nitrate based precursor solutions. The motivation behind the replacement of the precursor solution was to remove chlorine, which caused the enhancement of electrical resistivity of In_2S_3 films. Another advantage was that indium nitrate could be pyrolysed at relatively low temperature. Interestingly the In/S ratio 2/3 only showed crystallinity. We could get better control over stoichiometry of the films by varying In/S ratio taken in the solution, using nitrate based precursor. But there was considerable decrease in the photosensitivity of the samples. Maximum photosensitivity was obtained for the sample having In/S ratio 2/4. Nitrate based samples were found to be more conducting compared to chloride based ones.

We used chloride and nitrate based precursor solutions for preparing CuInS_2 samples also. The details of preparation and characterization are given in **CHAPTER 5**. Films were prepared with different Cu/In ratio in the initial spray solution. The maximum thickness that could be achieved with single spray was 0.6 μm and 375 ml of the solution was sprayed for this. Structural, compositional, electrical and optical characterizations of the films obtained were carried out. It was found that chemical composition of the solution controlled film resistivity and photoresponse.

Conductivity of the films was found to increase with increase in Cu/In ratio. Defect levels were identified using temperature dependent conductivity measurements.

We tried multiple spray pyrolysis technique to increase the thickness of CuInS₂ film. A systematic study on the samples prepared with different Cu/In ratio is presented in **CHAPTER 6**. Thickness of the samples could be increased to 1.17 μm by spraying 225 ml of the solution four times (total volume 900 ml). Thicker absorber layer was found to improve the performance of the cell (explained in chapter 8). Enhanced conductivity was obtained for samples having greater Cu/In ratio. Oxygen was absent in the bulk of the sample even after multiple spraying as revealed by XPS studies. EDAX measurements pointed out that Cu/In ratio was slightly less than that taken in the solution. Structural, optical and electrical characterizations of the films were also done.

CHAPTER 7 describes the fabrication of all sprayed CuInS₂/In₂S₃ solar cell. The effect of variation of the thickness and atomic concentration of the absorber (CuInS₂) and buffer layer (In₂S₃) are explained in this chapter. Performance of the cell improved by annealing in air or keeping it at the preparation temperature itself for 1 hour after spray. The effect of annealing on the characteristics of the cell depends on the thickness and atomic concentration of the layers.

Modifications made to improve the performance of the cell are described in **CHAPTER 8**. The thickness of the buffer layer was increased to compensate for copper diffusion from CuInS₂ to In₂S₃. Silver, used as the top electrode, was found to improve the crystallinity of the In₂S₃ layer and this is resulted in enhancement of efficiency to 9.5% for all sprayed CuInS₂/In₂S₃ solar cell.

CHAPTER 9 is a summary of the entire work. All the important points are highlighted. The chapter ends with future scope of the present work.

Publications

Journals

1. Characterisation of spray pyrolysed indium sulfide thin films
Teny Theresa John, S. Bini, Y. Kashiwaba, T. Abe, Y. Yasuhiro, C. Sudha Kartha and K. P. Vijayakumar
Semiconductor Science and Technology **18** (2003) 491-500
2. CuInS₂ films using repeated chemical spray pyrolysis
Teny Theresa John, K. C. Wilson, P. M. Ratheesh Kumar, C. Sudha Kartha, K. P. Vijayakumar, Y. Kashiwaba, T. Abe and Y. Yasuhiro
Physics Status Solidi (a) **202 (1)** (2005) 79-84
3. CuInS₂/In₂S₃ thin film solar cell using spray pyrolysis technique having 9.5% efficiency
Teny Theresa John, Meril Mathew, C. Sudha Kartha, K. P. Vijayakumar, T. Abe and Y. Kashiwaba
Solar Energy Materials and Solar Cells (in press)
4. Characterization of CuInS₂ based Cd-free thin film solar cell prepared using chemical spray pyrolysis technique
Teny Theresa John, C. Sudha Kartha, K. P. Vijayakumar, T. Abe and Y. Kashiwaba
Journal of Physics D: Applied Physics (under revision)
5. Preparation of indium sulfide thin films by spray pyrolysis using a new precursor indium nitrate

Teny Theresa John, C. Sudha Kartha, K. P. Vijayakumar, T. Abe and Y. Kashiwaba

Applied Surface Science (under revision)

6. Observation of phase transitions in chemical bath deposited copper selenide thin films through conductivity studies

Rupa R Pai, **Teny Theresa John**, M. Lakshmi, K. P. Vijayakumar and C. Sudha Kartha

Thin Solid Films **473** (2) (2004) 208-212

7. Defect characterization of spray pyrolysed β - In_2S_3 thin film using Thermally Stimulated Current Measurements

Rupa R Pai, **Teny Theresa John**, Y. Kashiwaba, T. Abe, K. P. Vijayakumar and C. Sudha Kartha

Journal of Material Science **39** (2004) 1-6

Papers Communicated

1. Modification in cell structure necessary for better performance of all sprayed $\text{CuInS}_2/\text{In}_2\text{S}_3$ thin film solar cell

Teny Theresa John, C. Sudha Kartha, K. P. Vijayakumar, T. Abe and Y. Kashiwaba

Communicated to Applied Physics A

2. Structural, optical and stoichiometric studies of CuInS_2 thin films prepared from chloride and nitrate based precursor solutions

Teny Theresa John, C. Sudha Kartha, K. P. Vijayakumar, Y. Kashiwaba and T. Abe

Communicated to Thin Solid Films

3. Effect of variation in stoichiometry and precursor solutions on electrical properties of CuInS_2 films prepared using CSP technique

Teny Theresa John, C. Sudha Kartha and K. P. Vijayakumar

Communicated to Materials Research Bulletin

4. PL studies on $\beta\text{-In}_2\text{S}_3$ thin films prepared using CSP technique

R. Jayakrishnan, **Teny Theresa John**, C. Sudha Kartha, K. P. Vijayakumar, T. Abe and Y. Kashiwaba

Communicated to J. Luminescence

5. Effects of post deposition annealing on structural, electrical and optical properties of evaporated $\beta\text{-In}_2\text{S}_3$ thin films

P. M. Ratheesh Kumar, **Teny Theresa John**, C. Sudha Kartha and K. P. Vijayakumar

Communicated to J. Vacuum Science and Technology A

Conference Papers:

International

1. Characterisation of spray pyrolysed $\beta\text{-In}_2\text{S}_3$ thin films with different In/S ratio

Teny Theresa John, S. Bini, C. Sudha Kartha, K. P. Vijayakumar, T. Abe and Y. Kashiwaba

Proc. International Symposium on Recent Advances in Inorganic Materials

(RAIM- 2002) IIT Bombay Mumbai (2002) 106 (**presented**)

2. Effect of variation of indium on structural and optical properties of indium sulfide thin films

Teny Theresa John, K. P. Vijayakumar, C. Sudha Kartha, T. Abe and Y. Kashiwaba

Proc. World Conference on Photovoltaic Energy Conversion (WCPEC-3) Osaka, Japan 1P-C3-24 (2003) **(presented)**

3. XPS investigations on CuInS₂ solar cell having In₂S₃ buffer layer

Teny Theresa John, C. Sudha Kartha, K. P. Vijayakumar, T. Abe and Y. Kashiwaba

Proc. The 12th International Conference on Solid Films and Surfaces (ICSFS-12), Hamamatsu, Japan (2004) 101 **(presented)**

4. A novel cadmium free buffer layer for CIS based sprayed solar cells-An attempt

K. P. Vijayakumar, **Teny Theresa John** and C. Sudha Kartha

19th European Photovoltaic Solar Energy Conference and Exhibition, Paris, France (2004)

5. CuInS₂/In₂S₃ thin film solar cell prepared entirely using CSP technique

Teny Theresa John, C. Sudha Kartha, K. P. Vijayakumar, Y. Kashiwaba and T. Abe

International Conference on the Physics, Chemistry and Engineering of Solar Cells (SCCELL- 2004), Badajoz, Spain

6. Indium sulfide thin films prepared using CSP technique

Teny Theresa John, C. Sudha Kartha and K. P. Vijayakumar

The 2nd International Conference on Technological Advances of Thin Films and

Surface Coatings (Thin Films 2004), Singapore

National

1. Preparation of CuInS₂ thin films using multiple spray pyrolysis technique
Teny Theresa John, C. Sudha Kartha, K. P. Vijayakumar, T. Abe and Y. Kashiwaba
MRSI Theme Symposium, Banarus Hindu University, Varanasi (2004)
2. CuInS₂ based solar cell with In₂S₃ buffer layer having 9.5% efficiency
Teny Theresa John, C. Sudha Kartha, K. P. Vijayakumar, T. Abe and Y. Kashiwaba
DAE Solid State Symposium, GNDU University, Amritsar (2004)
3. Deposition and characterization of β -In₂S₃ prepared using Successive Ionic Layer Adsorption and Reaction
R. Ranjith, **Teny Theresa John**, C. Sudha Kartha and K. P. Vijayakumar
MRSI Theme Symposium: Novel Polymeric Materials BARC, Mumbai (2003)
4. β - Indium sulfide thin films prepared using SILAR and CSP: A Comparison
R. Ranjith, **Teny Theresa John**, C. Sudha Kartha and K. P. Vijayakumar
DAE Solid State Symposium, Jiwaji University, Gwalior (2003)
5. Thermally stimulated current measurements on β -In₂S₃ thin films
Rupa R Pai, **Teny Theresa John**, P. M. Ratheesh Kumar, K. P. Vijayakumar and C. Sudha Kartha
MRSI Theme Symposium, Banarus Hindu University, Varanasi (2004)

6. Temperature dependent dark conductivity measurements on In_2S_3 thin films
K. C. Wilson, **Teny Theresa John**, C. Sudha Kartha and K. P. Vijayakumar
MRSI Theme Symposium, Banarus Hindu University, Varanasi (2004)

7. An observation on the effect on traps in $\beta\text{-In}_2\text{S}_3$ thin films by varying the thermally stimulated current measurement parameters
Rupa R Pai, **Teny Theresa John**, P. M. Ratheesh Kumar, K. P. Vijayakumar and C. Sudha Kartha
MRSI Theme Symposium, Banarus Hindu University, Varanasi (2004)

8. Effect of 120 keV nitrogen ion implantation on In_2S_3 thin films
K. C. Wilson, **Teny Theresa John**, P. Magudapathi, K. G. M. Nair, C. Sudha Kartha and K. P. Vijayakumar
DAE Solid State Symposium, GNDU University, Amritsar (2004)

9. Low temperature PL studies on sprayed $\beta\text{-In}_2\text{S}_3$ thin films
R. Jayakrishnan, **Teny Theresa John**, C. Sudha Kartha and K. P. Vijayakumar
DAE Solid State Symposium, GNDU University, Amritsar (2004)

10. SHI induced modifications in spray pyrolysed $\beta\text{-In}_2\text{S}_3$ thin films
P. M. Ratheesh Kumar, **Teny Theresa John**, C. Sudha Kartha, K. P. Vijayakumar and D. K. Avasthi
Indo- German Workshop on Synthesis and Modification of Nano Structured Materials by Energetic Ion Beams (NANO- 2005) NSC. New Delhi (2005)

11. **Structural and electrical characterisation of copper selenide thin films prepared using chemical bath deposition**
Rupa R Pai, Teny Theresa John, M. Lakshmi, S. Bini, K. Bindu, K. P. Vijayakumar and C. Sudha Kartha
Workshop on Complete Cycle Characterization of Materials (CCM-2001)
IGCAR, Kalpakkam (2001)

12. **Effect of stoichiometric variation on band gap of copper selenide thin films**
Teny Theresa John, M. Lakshmi, C. Sudha Kartha and K. P. Vijayakumar
National Conference on Thin Film Techniques and Applications (NACTTA-2002) P S G College of Arts and Science, Coimbatore (2002)

13. **Studies on spray pyrolysed indium sulfide thin films at different substrate temperatures**
Teny Theresa John, C. Sudha Kartha, K. P. Vijayakumar, T. Abe and Y.Kashiwaba
National Conference on Recent Advances in Material Science (NCMS-2002)
Nehru Memorial College, Thiruchirappalli (2002)

14. **Characterisation of In_2S_3 and ZnO thin films for photovoltaic application using photothermal deflection technique**
M. Paulraj, S. Ramkumar, Teny Theresa John, P. M. Ratheesh Kumar, C. Sudha Kartha, K.P. Vijayakumar and K. G. M. Nair
Regional Conference on Photoacoustics in Condensed Matter Physics and NDT, Madurai (2004)

Chapter 1**AN INTRODUCTION TO PHOTOVOLTAICS****1.1 Introduction**

There was a dramatic increase in the usage of Renewable energy during the past decade, mainly due to two reasons. First one is the environmental damage due to large-scale usage of fossil and nuclear fuels while the second reason is the depletion of fossil fuels itself. The term renewable energy can be defined in several ways: Twidel and Weir (1986) defined renewable energy as “energy obtained from continuous or repetitive currents of energy recurring in the natural environment”. Sorensen (1979) defined renewable energy as “energy flows which are replenished at the same rate as they are used”. The term ‘renewable energy’ may be taken to include, more broadly, ‘the usage of any energy storage reservoir which is being “refilled” at rates comparable to that of extraction’ [1]. Recently, the UK Renewable Energy Advisory Group (REAG) defined renewable energy as “the term used to cover those energy flows that occur naturally and repeatedly in the environment and can be harnessed for human benefit”. The ultimate sources of this energy are the sun, gravity and the earth’s rotation.

Most of the so-called renewable energy sources (renewables) are manifestation of solar energy. This includes direct radiation from the sun (which is used for heating or electricity generation) and indirect forms of solar energy such as energy from the wind, waves and ocean thermal energy, waterfalls and biomass (wood, straw, dung and other plant/animal wastes). Renewables allow a major reduction in the usage of fossil and nuclear fuel - or better still, if they can replace them entirely in the long run.

1.2 Solar Energy

1.2.1 The Sun

Sun is an enormous fusion reactor at a distance of 150×10^6 km from earth, which turns hydrogen into helium at the rate of 4 million tones per second. It radiates energy towards the earth by virtue of its high surface temperature, approximately 6000°C . The quantity of solar energy flowing to and from the earth and its atmosphere is very large. Amount of solar energy incident on the earth every year is

- ❖ Equivalent to 160 times the energy stored in the world's proven reserves of fossil fuels.
- ❖ Equivalent to more than 15000 times the world's annual use of fossil and nuclear fuels and hydropower [2].

Spectrum of solar radiation extends from 200 to 3000 nm in wavelength. It is almost identical with the 6000 K black body radiation spectrum. The radiation is distinguished as:

- (a) ultra-violet radiation (200 to 380) producing photochemical effects, bleaching, sunburn etc.
- (b) visible light (380 (violet) to 700 nm (red)).
- (c) infra-red radiation (700 to 3000 nm) or radiant heat, with some photochemical effects.

As the solar radiation passes through the earth's atmosphere [Fig. 1.1], it is absorbed or scattered or reflected according to the following processes.

- (a) A portion of the solar radiation is scattered when striking on molecules of air, water vapor and dust particles. The portion scattered downward through the atmosphere arrived at the earth surface in the form of diffuse radiation (30%).
- (b) Another portion of solar radiation is absorbed (19%), and

- (c) The remaining portion of the solar radiation traverses through the atmosphere and reaches the earth's surface in the form of direct radiation (51%).

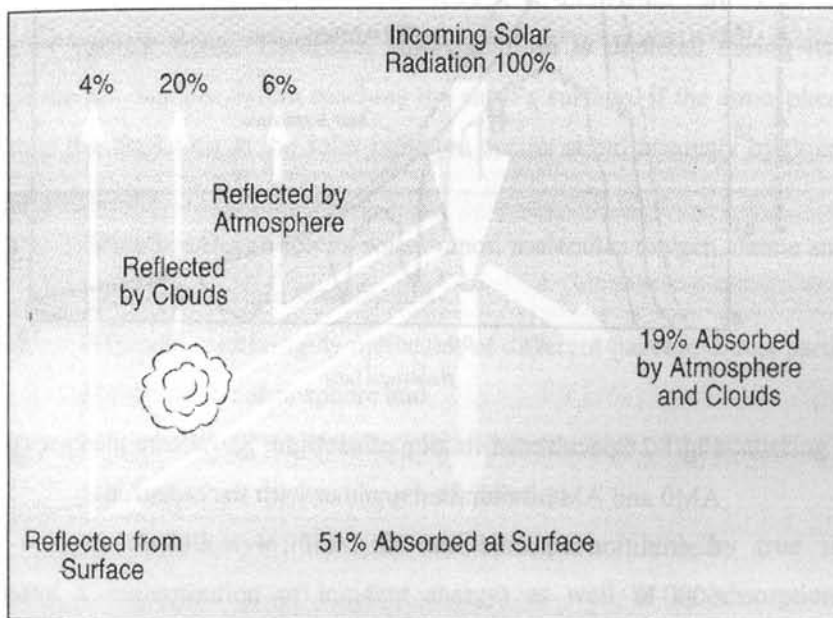


Fig.1.1 Global modification of incoming solar radiation by atmospheric and surface process

1.2.2 Solar Spectrum

We perceive solar radiation as white light. In fact, it spreads over a wider spectrum of wavelength, from infrared (longer than red light) to ultraviolet (shorter than violet). Pattern of wavelength distribution is critically determined by the temperature of the surface of the sun [2]. Spectral distribution of sunlight is given in Fig.1.2.

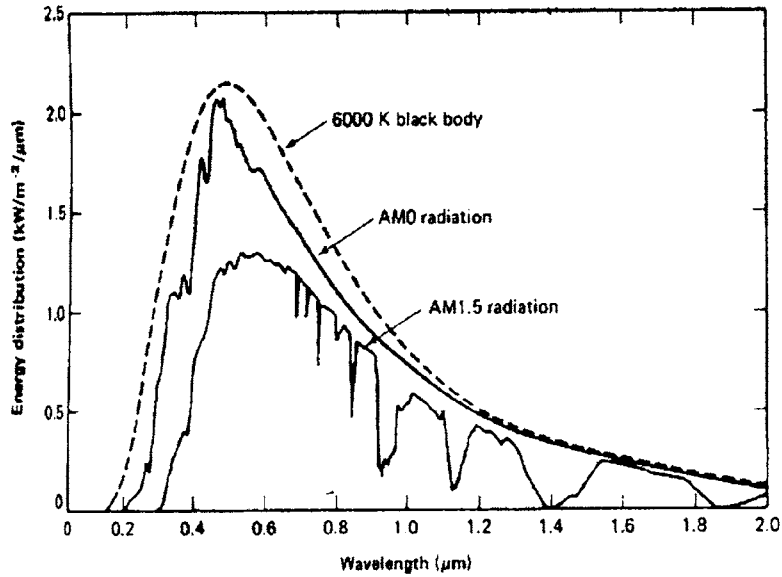


Fig.1.2 Spectral distribution of sunlight. Shown are the cases of AM0 and AM1.5 radiation together with the radiation distribution expected from the sun if it were a black body at 6000 K

1.2.3 Availability of Solar Radiation

Despite the absorption and scattering of the solar radiation in the earth's atmosphere, amount of energy received on earth's surface in one hour would still be enough to cover the energy requirements of the whole world for 1 year. Hence the issue is not one of availability of solar energy, but of the feasibility of converting it into forms suitable for human use. As indicated earlier, 30% of solar radiation is reflected immediately back to the space. The remaining 70% is mainly used to warm the earth's surface, atmosphere and oceans (47%) or is absorbed for the evaporation of water (23%). Relatively very small proportions are used to drive the winds, waves and

for plants (in photosynthesis). Ultimately, all the energy used on earth is radiated back to space, in the form of infrared radiation.

1.2.4 Direct and Diffuse Radiation

The earth is surrounded by atmosphere, which contains various gaseous constituents, suspended dust and other minute solid and liquid particulate matter and clouds of various types. Therefore, solar radiation is depleted during its passage through the atmosphere before reaching the earth's surface. If the atmosphere is very clear then the depletion in the solar radiation occurs simultaneously by three distinct physical processes:

- (i) Selective absorption by water vapor, molecular oxygen, ozone and carbon dioxide in certain wavelengths
- (ii) Rayleigh scattering by molecules of different gases and dust particles that constitute the atmosphere and
- (iii) Mie scattering, which takes place where the size of the scattering particles is greater than the wavelength of radiation.

Hence depletion in the solar radiation occurs both by true scattering (involving a redistribution of incident energy) as well as by absorption by the particles, where part of the radiant energy is transformed into heat [3]. The radiation received after its direction has been changed by scattering and reflection is known as "diffuse radiation". During clear days, magnitude of diffuse radiation is about 10 to 14% of the total solar radiation received at the earth's surface. Only diffuse radiation may reach the earth's surface during extremely cloudy days. Radiation received without any change in direction or scattering is known as "direct radiation" (beam radiation). On a clear day, direct radiation falling on earth's surface can have the maximum power density of 1 kW/m^2 and is known as '1 sun' for solar collector testing purposes [2]. Direct and diffuse radiations are useful for most solar thermal applications. But only direct radiation can be focused to generate very high

temperatures. On the other hand, it is the diffuse radiation that provides most of our “day light”. Sum of these two is called “total radiation” or “global radiation”.

1.2.5 Air Mass Ratio

Radiation available on the surface of earth is less than the radiation available outside the earth’s atmosphere and this reduction in intensity depends on atmospheric conditions (amount of dust particles, water vapor, ozone content, atmospheric pressure, cloudness etc) and solar altitude. The latter factor determines the length of atmosphere through which solar beam has to travel before reaching the earth’s surface. If the altitude of the sun is small, the length traversed by the beam is long. On the other hand if the sun is at the zenith (overhead), solar beam traverses a vertical path, which is the shortest path through the atmosphere. Path length of solar beam through atmosphere is accounted through the term ‘air mass’ (solar constant) which is a numerical comparison between the path length (which the solar beam actually traverses) and the vertical path through the atmosphere [3] Thus at the sea level air mass (m), is unity when the sun is at the zenith. In general,

$$\text{Air mass} = \frac{\text{path length traversed}}{\text{Vertical depth of atmosphere}} \dots\dots\dots (1.1)$$

There is a widespread international agreement that performance of PV cells and modules should be measured under a set of standard test conditions. Essentially, these specify that temperature of a cell or module should be 25°C and that solar radiation incident on the cell should have a total power density of 1000 W/m² with a spectral power distribution known as *Air Mass 1.5 (AM1.5)*. Spectral power distribution is a graph describing the way in which power contained in the solar radiation varies across the spectrum of wavelengths. Or the concept of Air Mass relates to the way in which the spectral power distribution of radiation from the sun is affected by the distance the sun’s rays have to travel through the atmosphere before reaching PV module or array.

In space, solar radiation is obviously unaffected by the earth's atmosphere and has a power density of approximately 1365 W/m^2 . The characteristic spectral power distribution of solar radiation, as measured in space is described as *Air Mass 0 (AM0)* distribution. When the sun is at its zenith (ie, directly overhead) the path length of solar beam is minimum, the characteristic spectral power distribution of solar radiation is known as the *Air Mass 1 (AM1)* distribution.

When the sun is at a given angle q to the zenith (as perceived by an observer at sea level) the air mass is defined as the ratio of the path length of the sun's rays under these conditions to the path length when the sun is at its zenith [2]. This leads to the second definition of Air Mass ratio as:

$$\text{Air Mass} \sim 1/\text{Cos}q \quad \dots\dots\dots(1.2)$$

An air mass distribution of 1.5, as specified by the standard test conditions, therefore corresponds to the spectral power distribution observed when the sun's radiation is coming from an angle to overhead of about 48 degrees, since $\text{Cos}(48) = 0.67$ and the reciprocal of this is 1.5.

Knowledge of exact distribution of energy content in sunlight is important in solar cell characterization because cells respond differently to different wavelength of light. Distribution of energy over wavelength [4] is given in Fig.1.2. Photovoltaic (PV) devices or solar cells as they are often referred to, are semiconductor devices that convert sunlight into direct current (DC) electricity without any physical movement. Group of PV cells are electrically configured into modules and arrays, which can be used to charge batteries, operate motors and to power any number of electrical loads. Interesting aspect of this device is that it can be used for producing milliwatt and megawatt at the same efficiency. Moreover this is modular in nature, one can add more units to the existing unit as per the power requirements.

1.2.6 Advantages of Solar Energy

Solar energy has the following advantages over conventional energy: -

- Energy from the sun is virtually free after the initial cost has been recovered
- Depending on utilization of energy, pay backs can be very short, when compared to cost of other common energy sources used
- Solar and other renewable energy systems can be stand alone, thereby not requiring connection to a power or natural gas grid
- The sun provides a virtually unlimited supply of solar energy
- Use of solar energy displaces conventional energy, which usually results in a proportional decrease in green house gas emissions
- Use of solar energy is an untapped market

1.2.7 Applications

Solar energy can be used to heat building air or water (low temperature use) and for industrial application in concentrated form (high temperature use) in many different ways [5]. Next direct application is production of electricity using PV conversion. An average home has more than enough roof area, to produce enough solar electricity to supply for all the power requirements. Other current terrestrial applications of solar energy are:

- Salt production by evaporation of sea water or inland brines
- Solar distillation on a small community scale
- Solar drying for agricultural products
- Solar cookers
- Solar engines for water pumping
- Food refrigeration
- Solar furnaces
- Solar thermal electrical power generation
- Industrial process heat

1.3 Solar Cells

1.3.1 Historical Survey

The term “photovoltaic” is derived by combining the Greek word for light, *photos*, with *volt*, the name of the unit of electromotive force (the force which causes motion of electrons). The ‘volt’ was named after the Italian Physicist Count Alessandro Volta, the inventor of the ‘Volta cell’. The term photovoltaic therefore signifies the generation of electricity from light. Discovery of photovoltaic effect is attributed to French Physicist, Edmond Becquerel (1839). He found that photo voltage resulted from the action of light on an electrode in an electrolyte solution [6]. The first report of PV effect in a solid substance was made in 1877 when two Cambridge scientists Adams and Day observed variations in electrical properties of selenium when exposed to light [7]. In 1883, Charles Edgar Fritts, a New York electrician, constructed a selenium solar cell, having low efficiency. Nevertheless, selenium cells eventually came into widespread use in photographic exposure meters. By 1914, solar conversion efficiency of about 1% was achieved with the selenium cell after it was realized that an energy barrier was involved both in this cell and in the copper/copper oxide cell.

But it was only in 1950’s that the breakthrough occurred which resulted in the development of modern high efficiency solar cells. It took place at Bell Telephone Laboratories (Bell Labs) in USA where a number of scientists were studying the effect of irradiation of semiconductors. In 1954, Chapin et al reported conversion efficiency of 6% for Si single crystal cell [8]. Eventhough PV effect was discovered in 1839, it remained a laboratory curiosity until the mid 1950’s when US space programme was started. In 1958, solar cells were used to power a small radio transmitter in the second US space satellite, Vanguard I. Although PV cells were used since 1950’s in spacecraft, the interest in their terrestrial use enhanced very much due to the oil embargoes of early 1970’s.

The $\text{Cu}_2\text{S}/\text{CdS}$ heterojunction [9] was the first - all - thin - film - photovoltaic system to receive significant attention. Since then, the science and technology of PV devices and systems underwent revolutionary developments. Today, the best single crystal Si solar cells reached an efficiency of 24.7%, compared to the theoretical maximum value of 30% [10]. The industrial production of PV modules is growing at approximately 25 percent annually, and major programs in the US, Japan and Europe are rapidly accelerating the implementation of PV systems on buildings and interconnection to utility networks.

1.3.2 The *pn* Junction

Photovoltaic energy conversion requires separation of electrons and holes by an internal electric field. For solar cells, the most common device structure is *pn* junction, although there are other concepts.

In thermodynamic equilibrium, the two differently doped parts of the crystal are separated by a potential step. At the interface between n-type and p-type, both carrier concentrations have a strong gradient. Electrons flow from n-type portion to the p-type portion where they recombine with the holes. At the same time, holes flow from the p-type to n-type section and there they recombine with electrons. This has the consequence that the charge of the ionized, immobile impurities near the interface have to remain uncompensated, resulting in a negative space charge in p-type part and a positive one in n-type part. These space charges produce an electric field and hence a potential difference (the diffusion voltage V_d) at the *pn* junction. In thermodynamic equilibrium, the diffusion currents due to the concentration gradients are compensated, just as the field induced currents of the two types of carriers.

Formation of a potential step means that the band schemes of p-type and n-type semiconductors (assumed to be initially separated) are shifted with respect to one another until their Fermi energies have reached the same value ζ [Fig.1.3].

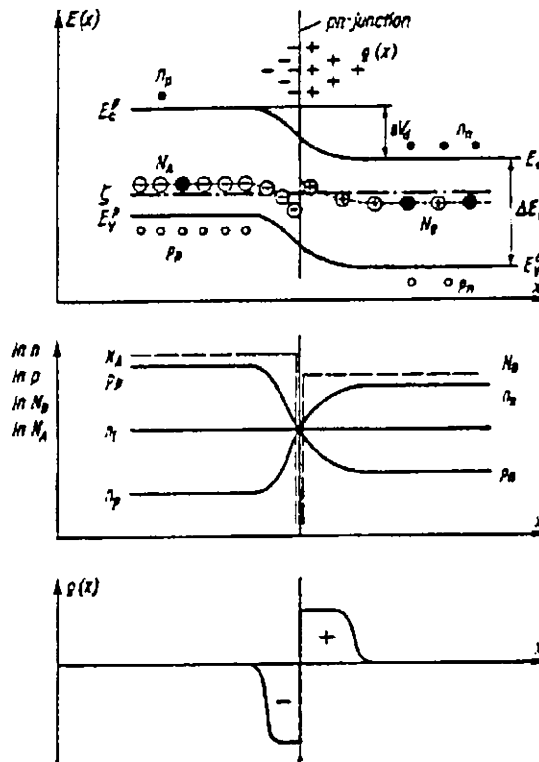


Fig. 1.3 Band scheme, Carrier concentration, impurity concentration and charge density for a pn junction

Owing to the transition of electrons from the n-type to the p-type semiconductor the energy of the former decreases and the energy of the latter increases. The barrier created at the junction is equivalent to an imaginary battery connected at the junction with positive on n-side and negative on p-side.

Height (eV_d) of the potential energy step is equal to difference of initial Fermi energies and is related to carrier concentrations of n-type and p-type sections outside the space charge regions; n_n , p_n and n_p , p_p where n_n is the majority carrier concentration (electrons) in the n-type, p_n is the minority carrier concentration (holes)

in the n-type, n_p is the minority carrier concentration (electrons) in the p-type and p_p is the majority carrier concentration (holes) in the p-type.

In the case of non-degenerate semiconductors under thermodynamic equilibrium we have,

$$n_n = n_0 \exp\left(\frac{\zeta - E_c^n}{kT}\right) \dots\dots\dots(1.3)$$

$$p_n = p_0 \exp\left(\frac{E_v^n - \zeta}{kT}\right) \dots\dots\dots(1.4)$$

$$n_p = n_0 \exp\left(\frac{\zeta - E_c^p}{kT}\right) \dots\dots\dots(1.5)$$

$$p_p = p_0 \exp\left(\frac{E_v^p - \zeta}{kT}\right) \dots\dots\dots(1.6)$$

where E_c^n , E_c^p , E_v^n , E_v^p are the band edge energies in n-type and p-type sections outside the space charge regions. Also we obtain intrinsic density n_i from

$$n_i^2 = n_n p_n = n_p p_p = n_0 p_0 \exp\left(-\frac{E_g}{kT}\right) \dots\dots\dots(1.7)$$

where $E_g = E_c^n - E_v^n = E_c^p - E_v^p \dots\dots\dots(1.8)$

Dividing eqn (1.3) by eqn (1.5) and eqn (1.4) by eqn (1.6)

$$\frac{n_n}{n_p} = \exp\left(\frac{E_c^p - E_c^n}{kT}\right) = \exp\left(\frac{eV_d}{kT}\right) \dots\dots\dots(1.9)$$

$$eV_d = kT \ln\left(\frac{n_n}{n_p}\right) = kT \ln\left(\frac{p_p}{p_n}\right) = kT \ln\left(\frac{n_n p_p}{n_i^2}\right) \dots\dots\dots(1.10)$$

where $eV_d = E_c^p - E_c^n = E_v^n - E_v^p \dots\dots\dots(1.11)$

Eqn (1.10) shows that step height is directly linked with majority and minority carrier

densities.

It is easy to show that in the case of strong doping, ie, if $n_n \gg n_i$ and $p_p \gg n_i$,

$$n_0 \exp\left(\frac{\zeta - E_c^n}{kT}\right) \gg (n_0 p_0)^{1/2} \exp\left(-\frac{E_g}{2kT}\right) \dots\dots\dots(1.12)$$

$$p_0 \exp\left(\frac{E_v^p - \zeta}{kT}\right) \gg (n_0 p_0)^{1/2} \exp\left(-\frac{E_g}{2kT}\right) \dots\dots\dots(1.13)$$

Effective state densities n_0 and p_0 are different only because of the different effective masses of electrons and holes and in many cases they are of the same order of magnitude, ie,

$$n_0 \approx p_0 \approx (n_0 p_0)^{1/2} \dots\dots\dots(1.14)$$

and from equations (1.12) and (1.13) we obtain

$$E_c^n - \zeta \ll 1/2 E_g \dots\dots\dots(1.15)$$

and

$$\zeta - E_v^p \ll 1/2 E_g \dots\dots\dots(1.16)$$

Addition of these two relations yield

$$E_c^n - E_v^p \ll E_g \dots\dots\dots(1.17)$$

and a combination of equations (1.8) and (1.11) yields

$$eV_d = E_c^n - E_v^p - (E_c^n - E_v^p) = E_g - (E_c^n - E_v^p) \dots\dots\dots(1.18)$$

With the assumptions $n_n \gg n_i$ and $p_p \gg n_i$, ie, using eqn (1.17) we obtain,

$$eV_d \approx E_g \dots\dots\dots(1.19)$$

But this is an extreme case. While the height V_d of the potential step depends only on the carrier concentrations of the n-type and p-type substances, the potential curve $V(x)$ at the pn junction depends on the local distribution of the space charges,

ie, on the distribution of impurities $N_A(x)$ and $N_D(x)$ near the boundary surface. These distributions are called “impurity profiles”. Electrical properties of pn junctions adapt themselves to the impurity profiles and thus to the potential curve.

Both in metal-semiconductor contacts and pn junctions, carrier transport depends on the width d of space charge layer as compared with an “average mean free path” of the charge carriers. In pn junctions, this mean free path is the so called diffusion length (L) of the minority carriers. It is determined by the mean free path traversed by a minority carrier before it recombines with a majority carrier [11]. The most important electrical property of a pn junction, namely its rectifying action, can be understood without exact knowledge of the impurity profiles and the potential curve.

1.3.3 The pn Junction Under Load

Application of a voltage U at the pn junction changes height of potential step (ie, the step height V_d). If the p-type part is positive with respect to the n-type part, the barrier voltage is reduced to $eV_d - eU$. In the case of inverse polarity, it is raised to $eV_d + eU$. The unilateral thermal current of minority carriers, $j(n_p)$ and $j(p_n)$, flowing towards the interface, are independent of the voltage applied, as these are diffusion currents. These are proportional to the equilibrium concentrations n_p and p_n :

$$j(n_p) = C_1 n_p \dots\dots\dots(1.20)$$

$$j(p_n) = C_3 p_n \dots\dots\dots(1.21)$$

C_1 and C_3 are constants.

The unilateral thermal currents of majority carriers, $j(n_n)$ and $j(p_p)$ are proportional to the fraction of carriers able to surmount the potential step of height $eV_d \pm eU$, ie,

$$j(n_n) = C_2 n_n \exp\left(-\frac{eV_d \pm eU}{kT}\right) \dots\dots\dots(1.22)$$

$$j(p_p) = C_4 p_p \exp\left(-\frac{eV_d \pm eU}{kT}\right) \dots\dots\dots(1.23)$$

where C_2 and C_4 are constants.

From the condition of thermodynamic equilibrium ($U = 0$)

$$j_0(n_n) = j_0(n_p) = j(n_p) \dots\dots\dots(1.24)$$

and

$$j_0(p_p) = j_0(p_n) = j(p_n) \dots\dots\dots(1.25)$$

The net current through the pn junction is then obtained as the sum of the electron current and the hole current:

$$j = j(n_n) - j(n_p) + j(p_p) - j(p_n) \dots\dots\dots(1.26)$$

Substituting equations (1.20) and (1.21) as well as (1.22) and (1.23) the current-voltage characteristic of the pn junction

$$j = [j(n_p) + j(p_n)] \left[\exp\left(\pm \frac{eU}{kT}\right) - 1 \right] \dots\dots\dots(1.27)$$

Reduction of the barrier height, ie, application of a negative potential to the n -type section, corresponds to the forward biasing. Magnitude of the saturation current densities $j(n_p)$ and $j(p_n)$ depends on the potential curve at the pn junction and on the recombination mechanism.

Measurements of the current-voltage characteristics of pn junctions are essentially in agreement with the theoretical relation (eqn 1.27). If very high voltages are applied in the reverse direction of the rectifier (n-type section positive, negative sign of the exponent), eqn (1.27) loses its validity. Above the so called 'breakdown voltage' the saturation current grows rapidly, ie, the number of carriers passing through the junction increases very much. There are two mechanisms, which are responsible for this effect:

i. Production of secondary electrons by impact ionization (carrier multiplication)

When (reverse bias) blocking voltage is increased the electric field strength at the junction will reach very high values (-37.5 V, Si diode). The carriers are then strongly accelerated in this high field so that their energy is sufficient for excitation of additional electron from the valence band. The holes and electrons supplied in this way result in sudden increase of the reverse current [Fig. 1.4].

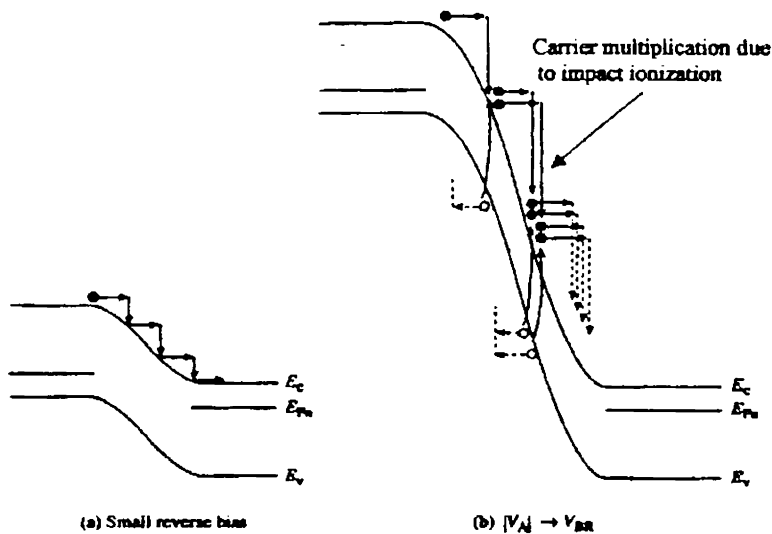


Fig. 1.4 Carrier activity within a reverse biased junction

ii. Internal field emission (Zener effect)

When reverse voltage is sufficiently high, electric field strength at junction region becomes so high that the energy bands in this region became strongly inclined there making E_v^p and E_c^n in this region almost equal [Fig.1.5]. If the spacial separation between valence and conduction bands is sufficiently small, tunneling between valence and conduction bands becomes probable. Zener was the first to calculate the corresponding tunneling probability. At sufficiently high reverse voltage, condition for tunneling is satisfied in the case of narrow pn junctions (pn junctions with steep impurity profiles) so that electrons from the valence band of the p-type section may tunnel to the n-type conduction band. This will also cause a steep increase of the reverse current with increasing voltage.

1.3.4 Junction Under Irradiation

Semiconductor pn junction, which can convert radiative energy into electrical energy, is called *Solar Cell*. Structure of a typical solar cell is depicted in Fig. 1.6. If a homogeneous semiconductor is exposed to light or some other radiation, electrons are excited from the valence band to the conduction band (generation of electron-hole pairs), the carrier concentrations and thus the conductivity of the semiconductor will increase (photoconduction). However growth of carrier concentration is counteracted by increased recombination and ambipolar diffusion, ie, by diffusion of electron-hole pairs without charge transport [11].

If, however, electron-hole pairs are produced in the region of a pn junction, they are separated from one another by the electric field of the space charge region. This gives rise to a charge transport (an electric current) through the junction.

Let us assume the excess concentrations due to light absorption to be denoted by Δn and Δp for electrons and holes respectively. If the wavelength of light corresponds to the energy gap of the semiconductor,

$$\Delta n = \Delta p \dots\dots\dots(1.28)$$

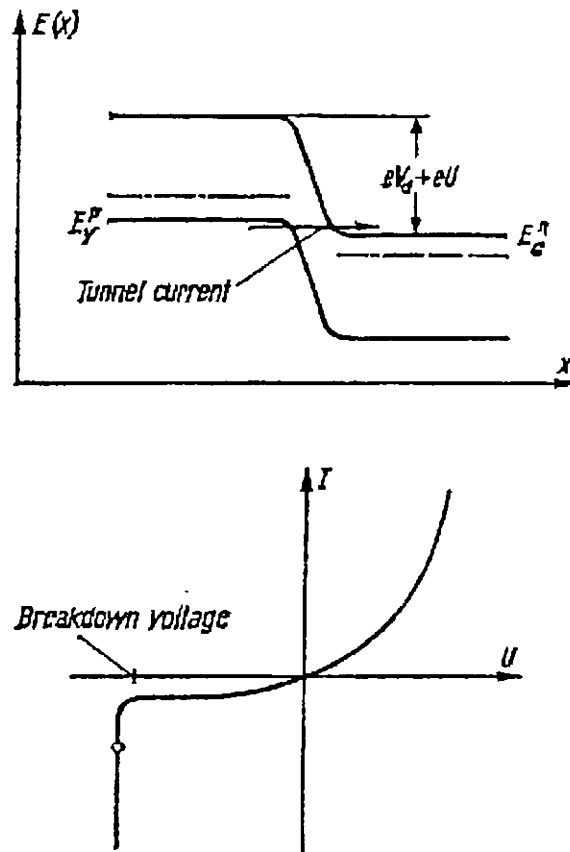


Fig 1.5 Band scheme of a pn junction in the Zener effect and schematic current-voltage characteristic for a Zener diode. The band scheme is represented for a blocking voltage belonging to the working point indicated on the characteristic

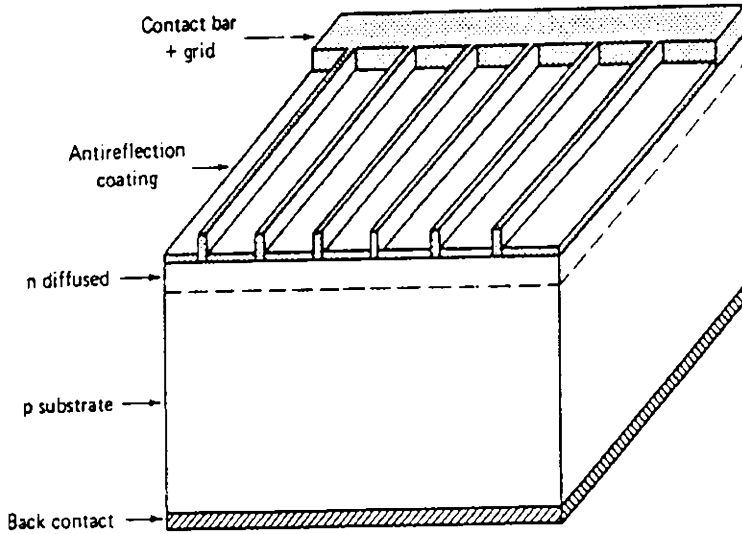


Fig.1.6 Structure of solar cell

In extrinsic semiconductors, excess concentrations of minority carriers are usually much lower than concentrations of the majority carriers. For the two sections of a *pn* junction, we can therefore write in a good approximation

$$\Delta n \ll n_n \dots\dots\dots(1.29)$$

$$\Delta p \ll p_p \dots\dots\dots(1.30)$$

Thus concentrations of the majority carriers are virtually unchanged due to irradiation of light. Minority carrier concentrations, however, reach the values $(n_p + \Delta n)$ and $(p_n + \Delta p)$. Hence minority carrier currents are increased by irradiation as;

$$j_{hv}(n_p) = j(n_p) + j(\Delta n) = C_1(n_p + \Delta n) \dots\dots\dots(1.31)$$

and

$$j_{hv}(p_n) = j(p_n) + j(\Delta p) = C_3(p_n + \Delta p) \dots\dots\dots(1.32)$$

Because of equations (1.29) and (1.30) the majority carrier currents remain unchanged, ie,

$$j_{hv}(n_n) \approx j(n_n) \dots\dots\dots(1.33)$$

and

$$j_{hv}(p_p) \approx j(p_p) \dots\dots\dots(1.34)$$

In the case of thermodynamic equilibrium, ie. If $U = 0$ and $h\nu = 0$, eqns (1.24) and (1.25) are again valid. Instead of eqn (1.26) we obtain for the total net current from (1.33) and (1.34)

$$j = j(n_n) - j_{hv}(n_p) + j(p_p) - j_{hv}(p_n) \dots\dots\dots(1.35)$$

or, using eqns (1.31) and (1.32),

$$j = j(n_n) - j(n_p) + j(p_p) - j(p_n) - j_{hv} \dots\dots\dots(1.36)$$

where

$$j_{hv} = j(\Delta n) + j(\Delta p) \dots\dots\dots(1.37)$$

Hence it follows by analogy with eqn (1.27) that

$$j = j_s \left(\exp\left(\pm \frac{eU}{kT}\right) - 1 \right) - j_{hv} \dots\dots\dots(1.38)$$

with the saturation current for $h\nu = 0$:

$$j_s = j(n_p) + j(p_n) \dots\dots\dots(1.39)$$

In closed circuit with condition $U = 0$, the photocurrent flows as short-circuit current in the reverse direction of the pn junction. From eqn (1.38) we have

$$j = -j_{hv} \dots\dots\dots(1.40)$$

When the pn junction in an open circuit condition is irradiated, an external photoelectric voltage arises as open circuit voltage. The photodiode acts as a photocell. For $j = 0$ from eqn (1.38)

$$j_{hv} = j_s \left(\exp\left(\pm \frac{eU}{kT}\right) - 1 \right) \dots\dots\dots(1.41)$$

or
$$j_{hv} + j_s = j_s \exp\left(\pm \frac{eU}{kT}\right)$$

$$1 + \frac{j_{hv}}{j_s} = \exp\left(\pm \frac{eU}{kT}\right)$$

$$U = \frac{kT}{e} \ln\left(1 + \frac{j_{hv}}{j_s}\right) \dots\dots\dots(1.42)$$

But we know that $j_{hv} = j(\Delta n) + j(\Delta p) \cong 2j(\Delta n) \propto \Delta n$

$$j_s = j(n_p) + j(p_n) \cong 2j(n_p) \propto n_p$$

Therefore
$$U = \frac{kT}{e} \ln\left(1 + \frac{\Delta n}{n_p}\right) \dots\dots\dots(1.43)$$

The voltage U in equations (1.42) and (1.43) is developed because of accumulation of separated minority carriers in p and n regions. This voltage is always forward biasing leading to the decrease of the built in field at the junction.

Open circuit voltage causes a reduction of the potential step between the p -type and n -type sections. In the case of irradiation of the pn junction in open circuit, the height of the potential step drops to $eV_d - eU$. From the band scheme, it is easy to see that the maximum of photoelectric voltage will be $U_{\max} = V_d$. The potential step and thus the electric field at the pn junction become smaller as the radiation intensity is raised. As soon as the field vanishes, minority carriers are no longer separated and net charge flow through the pn junction becomes equal to zero.

According to eqn (1.19) the barrier height at the doped *pn* junction, and thus also the maximum photoelectric voltage, is given by the value E_g of the energy gap. The maximum photoelectric voltage is then of the order of 0.1 - 1V.

1.3.5 Symbolic Representation of Solar Cell

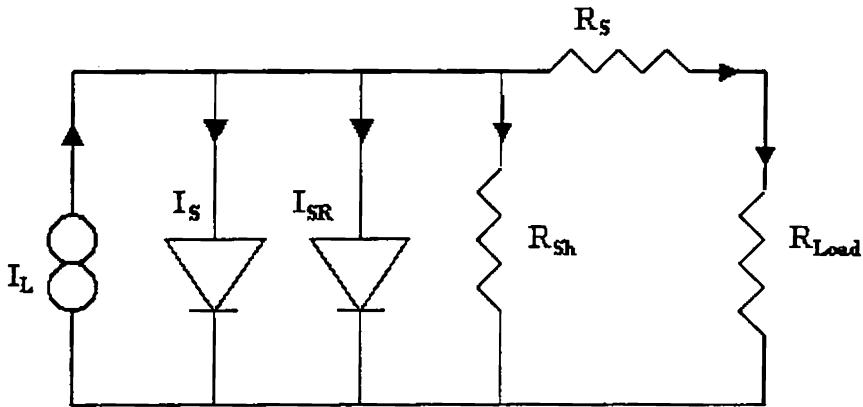


Fig.1.7 Equivalent circuit of a *pn* junction for the two diode model with diffusion I_s , recombination current I_{SR} , series resistance R_s , shunt resistance R_{sh} and light generated current I_L

Current-voltage characteristics of a *pn* junction are further modified because of a parasitic series (R_s) and shunt resistance (R_{sh}) associated with the solar cell. Bulk resistance of the semiconductor and the resistance of the contacts and interconnections are the origin of the series resistance. Shunt resistance can be caused by lattice defects in the depleted region, such as grain boundaries and large precipitates. Another reason may be the leakage currents around the edges of the cell. To evaluate the effects of these parameters, one can theoretically obtain the current-voltage behavior of the *pn* junction in the equivalent circuit as shown in Fig.1.7 using the following equation,

$$I = C_1 I_s \left(\exp\left(\frac{e(U - IR_s)}{kT}\right) - 1 \right) + C_2 I_{SR} \left(\exp\left(\frac{e(U - IR_s)}{2kT}\right) - 1 \right) + \left(\frac{U - IR_s}{R_{sh}} \right) - I_{hv} \dots\dots\dots(1.44)$$

In many practical cases, this *two diode model* gives a good description of the current-voltage behavior of real pn junction solar cells [12]. Parameters C_1 and C_2 are then obtained by curve fitting technique.

1.3.6 Solar Cell Output Parameters

Performance of a solar cell under illumination can be completely described by the current-voltage characteristics [Fig.1.8]. For practical purposes, it is sufficient in many cases, to characterize the current-voltage characteristics with a few parameters only. If we consider a typical current-voltage curve of a *pn* junction diode in dark and under illumination as depicted in Fig. 1.8, we can define three parameters that give rather complete description of the electrical behavior.

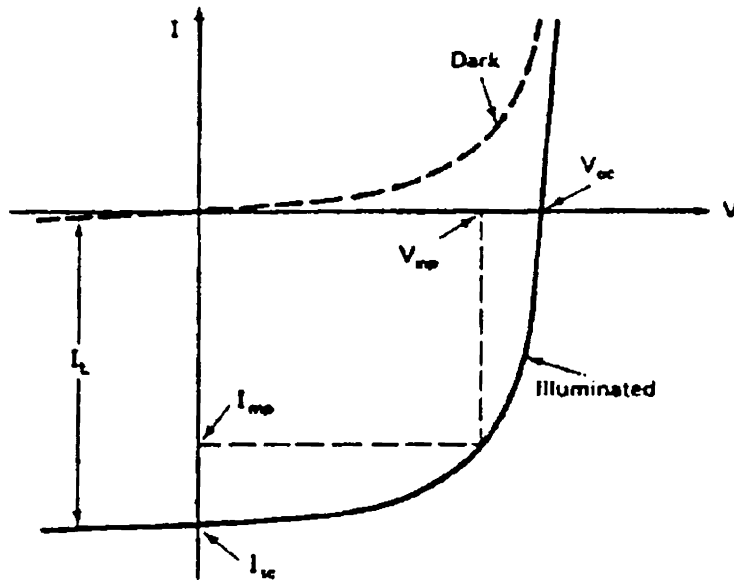


Fig. 1.8 I-V characteristics of a *pn* junction diode in dark and when illuminated

First one is the *short-circuit current* (I_{sc}) which is obtained for $U = 0$. This is the maximum current that can be extracted from the device by connecting upper and

lower electrodes of the cell to an ammeter with negligible internal resistance. Considering the analytical expression (1.44) for the current-voltage curve, it is evident that I_{sc} is equal to the light generated current I_{hv} , if the series resistance R_s is zero. A finite series resistance R_s reduces short-circuit current. Low energy band gap and high diffusion length of minority carriers are favorable for high short-circuit current.

$$I_{sc} = I_s \left(\exp\left(\pm \frac{eV_{oc}}{kT}\right) - 1 \right) \dots\dots\dots(1.45)$$

Second parameter is *open-circuit voltage* (V_{oc}), which is obtained for $I = 0$. In general, two-diode model (eqn (1.44)) leads to a transcendental equation, which can only be solved numerically. Only in the ideal case where $I_{sR} = R_s = 0$ and $R_{sh} = \infty$ an analytical expression can be derived:

$$V_{oc} = \frac{kT}{e} \ln\left(1 + \frac{I_{hv}}{I_s}\right) \dots\dots\dots(1.46)$$

V_{oc} is determined by the ratio I_{hv}/I_s . In order to get high open circuit voltage, saturation current of the diode must be as small as possible and for this, high band gap is essential. But this is contrary to the requirements for high photocurrent. Maximum conversion efficiency is obtained for semiconductors with an energy band gap between 1.2 and 1.5 eV.

Performance of solar cell is eventually determined by the fraction of the total power of incident light that can be converted into electrical power. Under illumination, the junction is forward biased and the external load resistance determines an operating point on the current-voltage curve. Electrical power output $P = IV$ is equal to area of the rectangle that is defined by the corresponding values V_p and I_p . In the I-V characteristic, for simplicity, the ideal diode behavior eqn (1.38) shall be considered again, which yields for P

$$P = I_p \frac{kT}{e} \ln \left(1 + \frac{I_p + I_{hv}}{I_s} \right) \dots\dots\dots(1.47)$$

In general, solar cell will be operated under conditions that give the maximum power output. One particular operating point (V_{mp} , I_{mp}) will maximize this power output [4]. The maximum possible area $P_{max} = V_{mp} I_{mp}$ for a given current-voltage curve determines the *Fill Factor FF*, which is determined by

$$FF = \frac{V_{mp} I_{mp}}{V_{oc} I_{sc}} \dots\dots\dots(1.48)$$

Evidently FF is larger, the more “square-like” the current-voltage curve is. Typically it has a value of 0.7 to 0.9 for cells with a reasonable efficiency [11]. P_{max} can be calculated from eqn (1.44) by taking the derivative with respect to U . In the ideal case, with $I_{sr} = R_s = 0$ and $R_{sh} = \infty$, the equation yields a relationship for FF which is only dependent on the open circuit voltage and can be approximated by

$$FF = \frac{eV_{oc}/kT - \ln(0.72 + eV_{oc}/kT)}{1 + eV_{oc}/kT} \dots\dots\dots(1.49)$$

In general, numerical methods have to be applied to determine the fill factor FF. The three parameters V_{oc} , I_{sc} and FF are sufficient to calculate the *energy-conversion efficiency* η of the solar cell, which is defined by

$$\eta = \frac{V_{mp} I_{mp}}{P_{in}} = \frac{FF V_{oc} I_{sc}}{P_{in}} \dots\dots\dots(1.50)$$

where P_{in} is the total power of the incident light. Considering the general expressions for V_{oc} and I_{sc} , essential material parameters that determine the efficiency of a solar cell are lifetime and mobility of the minority charge carriers and surface recombination velocities. Since technical design of a solar cell device is closely linked to material parameters, practical solar cells will have efficiencies lower than the ideal

values. A discussion of the major limiting factors will be given in the following section.

1.3.7 Spectral Response

Spectral response measurement can provide information about nature of junction and contribution of various cell components to the output of the device. Photocurrent collected at each wavelength relative to the number of photons incident on the surface at that wavelength determines the spectral response of the device. The “internal spectral response” ($SR(\lambda)$) is the number of electron-hole pairs collected under short circuit conditions relative to the number of photons entering the material and is given by

$$SR(\lambda) = \frac{J_p(\lambda)}{qF(\lambda)[1-R(\lambda)]} + \frac{J_n(\lambda)}{qF(\lambda)[1-R(\lambda)]} + \frac{J_{dr}(\lambda)}{qF(\lambda)[1-R(\lambda)]} \dots\dots\dots(1.51)$$

while the external response ($SR(\lambda)_{ext}$) is the internal response modified by reflection losses of the surface of the device and is represented as

$$SR(\lambda)_{ext} = SR(\lambda)[1-R(\lambda)] \dots\dots\dots(1.52)$$

where $J_p(\lambda)$, $J_n(\lambda)$, $J_{dr}(\lambda)$ are the hole diffusion, electron diffusion and depletion region contribution respectively, to the total photocurrent density J_L . $F(\lambda)$ is the number of photons per square centimeter per second per unit band width incident on the device at wavelength λ , and $R(\lambda)$ is the fraction of these photons reflected from the surface.

1.3.8 Efficiency of an Ideal pn Junction Cell

On analyzing the performance of ideal *pn* junction solar cell, upper limit of efficiency can be obtained for a particular semiconductor. Three parameters describing the performance of a cell are open circuit voltage (V_{oc}), short circuit

current (I_{sc}) and fill factor (FF). Since FF can be expressed in terms of V_{oc} and I_{sc} , only ideal limits of these two parameters be examined.

It is relatively easy to calculate upper limit of short-circuit current $I_{sc} = I_{hv}$ for any semiconductor from the light generated current I_{hv} given in equation (40). For simplicity, we assume a crystal of infinite thickness $W_p = \infty$ having no current from the depletion region ($W = 0$), no surface recombination ($S_n = S_p = 0$), and a uniform diffusion length $L_n = L_p = L$. Total current density $j_{hv}(j(\Delta n) + j(\Delta p))$ is then given by

$$j_{hv} = \frac{e\beta S_0(1-R)}{\cosh(x_n/L)} \frac{\alpha L}{(\alpha L)^2 - 1} \left(\alpha L - \exp\left(-\frac{(\alpha L - 1)x_n}{L}\right) \right) \dots\dots(1.53)$$

Value of j_{hv} depends on position of the junction below top surface and assumes a maximum value at x_n^{\max} , which can be determined from eqn (1.53) by taking derivative with respect to x_n . The corresponding current density is then given by

$$j_{hv}^{\max} = \frac{e\beta S_0(1-R)}{\cosh(x_n^{\max}/L)} \quad \text{with} \quad x_n^{\max} \approx L \frac{\ln(\alpha L)}{\alpha L - 1} \dots\dots\dots(1.54)$$

For a high quality material, one can assume a large diffusion length L and $\alpha L \gg 1$ over most of the wavelength range of solar radiation. One obtains $x_n^{\max} < L$ and $\cosh(x_n^{\max}/L) \approx 1$ so that the current mainly depends on the photon spectrum of the sunlight $S_0(\nu)$. Integrating from the lowest possible photon energy that can generate an electron-hole pair, one obtains the maximum current as a function of the band gap of the semiconductor.

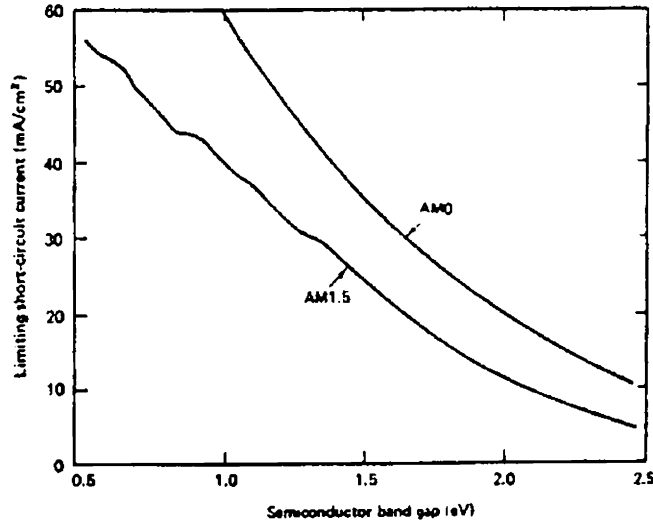


Fig. 1.9 Calculated upper limits of the short-circuit current density as a function of the energy band gap of the solar cell semiconductor for a photon flux corresponding to AM0 and AM1.5

Figure 1.9 shows results for spectral distribution AM0 and AM1.5. It is quite evident that current increases with decreasing band gap, since more photons have enough energy to generate charge carriers [4].

Limitations on open circuit voltage of pn junction solar cell are less clearly defined. For the ideal cell, expression for V_{oc} is given in eqn (1.46). Inserting the saturation current I_s ,

$$I_s = I_{s0} \exp\left(-\frac{E_g}{kT}\right) \dots\dots\dots(1.55)$$

V_{oc} can be approximated for $I_{hv} > I_s$ by

$$V_{oc} = \frac{kT}{e} \left(1 + \frac{I_{hv}}{I_s}\right) \approx \frac{1}{e} \left(E_g + kT \ln \frac{I_{hv}}{I_{s0}}\right) \dots\dots\dots(1.56)$$

This equation is valid for low injection conditions where $I_{hv}/I_{s0} < 1$ and $V_{oc} < E_g/e$. The prefactor for the saturation current I_{s0} depend on the mobilities and life times of charge carriers and can be expressed by

$$I_{s0} = eAN_cN_v \left(\frac{kT}{e} \right)^{1/2} \left(\frac{\mu_n^{1/2}}{\tau_n^{1/2} N_A} + \frac{\mu_p^{1/2}}{\tau_p^{1/2} N_D} \right) \dots\dots\dots(1.57)$$

It is evident that saturation current I_s has to be as small as possible for a maximum V_{oc} . The important parameter that determines the choice of semiconductor material is the band gap, and the expression given above shows that, with increasing E_g , the saturation current decreases and the open circuit voltage increases. However this condition is just the opposite of that required for a high I_{sc} . Hence there exists, a maximum in the efficiency of a cell. One can assign favorable values to mobility and lifetime to calculate efficiency as a function of band gap energy. For instance, the lifetime of electrons and holes are intrinsically limited by radiative recombination in semiconductor. Calculations for two different sun spectra [13] are given in Fig. 1.10 and this shows that optimum band gap occurs between 1.4 and 1.6 eV. The near optimal efficiency for AM1.5 (29%) occurs for GaAs (1.4 eV), whereas the peak efficiency for silicon (1.1 eV) is about 26% which is lower than optimum but relatively high. Corresponding open circuit voltage is about 0.7 V and FF is 0.84.

There are two fundamental reasons for the limited efficiency of a semiconductor solar cell based on an ideal *pn* junction device. First, losses occur because energy of photons above E_g is wasted in the form of heat. Second, eqn (1.56) indicates that output voltage is smaller than the maximum voltage, which corresponds to the band gap energy E_g/e . In general, it can be shown that a *pn* junction is inherently incapable of fully utilizing the maximum voltage by which electron-hole pairs are separated.

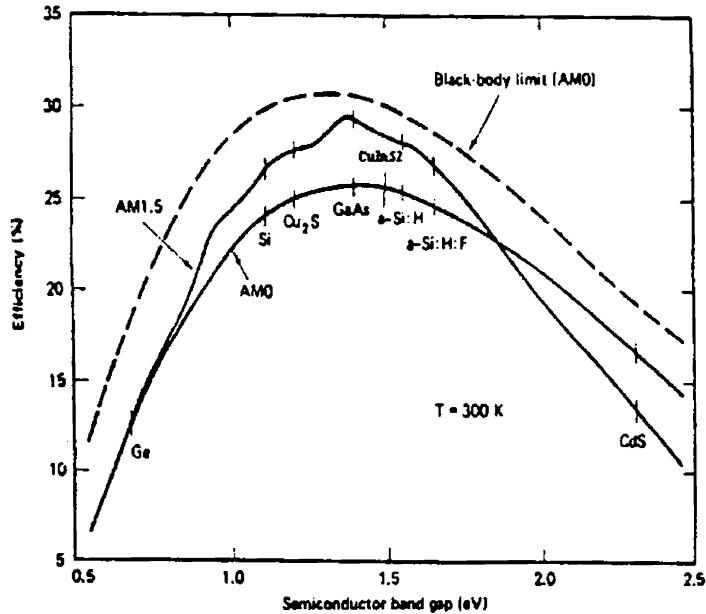


Fig. 1.10 Solar cell efficiency limits as a function of the band gap of the cell material

Equation (1.56) also suggests that open circuit voltage can be increased by enhancing intensity of the incident sunlight. Numerical calculation shows that this is most effective near the maximum. For instance, for 1000 suns (ie, 844 kW/m^2), the maximum efficiency increases to 37%. This increase is primarily caused by open circuit voltage V_{oc} , since the ratio I_{sc}/p_{in} in eqn (1.50) is essentially independent of the incident power, as can be seen from eqn (1.45). Technically this concept is realized in *concentrator solar cells*, which need, however, direct sunlight and a tracking system to follow the path of the sun in the sky.

It is also obvious that energy of the incident photons can be used more effectively if band gap of the semiconductor could be adjusted to different wavelength ranges. This idea has led to development of *multiple or tandem cells* with different band gap energies [12].

1.3.9 Factors Affecting Efficiency of a Solar Cell

Ideal limits of efficiency have been calculated assuming optimal parameters for material quality and design of solar cell. Important material parameters are lifetime and mobility of minority carriers in the bulk, and recombination velocity at front and back surfaces of the cell. Though for some semiconductors like silicon and GaAs, high quality material can be produced; it is generally difficult to retain quality of material during processing of a cell, especially under the constraint of low production costs. Since material parameters are closely linked to technical design and fabrication of solar cell, actual device characteristics of *pn* junction will be lower than its ideal values.

1.3.9.1 Optical Losses (Short Circuit Current Losses)

Losses in the light generated current directly reduce short circuit current and open circuit voltage (eqn (1.46)). Incident light cannot be fully utilized because of finite reflectivity *R*, which, in the case of bare silicon, is about 30%. Basically two approaches are employed to decrease *R*. Most commonly used one is *antireflection (AR) coating* on the top surface of the cell. Minimum of reflection is then given by

$$R_{\min} = \left(\frac{n_1^2 - n_0 n_2}{n_1^2 + n_0 n_2} \right)^{1/2} \dots\dots\dots(1.58)$$

where *n*₀, *n*₁ and *n*₂ are the refractive indices for air (or glass), coating and substrate respectively. Reflectivity is zero if *n*₁² = *n*₀*n*₂ which can only be fulfilled for a small range of wavelengths. In practical cases, the condition is adjusted to the wavelength at the maximum intensity of the solar spectrum (600 nm), which reduces total reflectivity. AR coatings have to be transparent and are usually deposited as amorphous layers to suppress light scattering at grain boundaries.

A further improvement is possible by using multilayer coatings with different refractive indices. Another possibility for changing reflectivity is by texturing top

surface. This can be achieved by using particular etchants that preferentially attack inclined crystallographic planes, so that pyramidal structures are formed. With the combination of both techniques, it is currently possible to keep total reflectivity below 3%.

Optical losses also occur because of finite thickness of solar cell. In order to collect major fraction of the sunlight inside the cell, a certain thickness is required for any material. This is particularly large for indirect band gap semiconductors having lower optical absorption coefficient. For silicon, a thickness of about 100 to 400 μm is needed to absorb most of the light. Optical thickness of a semiconductor can be reduced by *light trapping technique*. Here trapping of light inside the crystal is achieved by reflecting light several times between front and back surfaces before it is finally absorbed. This requires a mirror at the backside and textured surfaces at the top, which reflects the light at oblique angles.

The metal grid on the top further reduces incident sunlight, which is necessary to make electrical contacts on the emitter side of the junction. Even under optimum conditions, front contact blocks about 5% to 10% of the incoming light unless more sophisticated cell structures are used. Design of top contact grid is an important area in cell fabrication.

1.3.9.2 Recombination Losses (Open Circuit Voltage Losses)

A fraction of charge carriers is always generated far away from the junction, and some losses occur because minority carriers recombine before they can diffuse to device terminals. In a pure defect free monocrystalline semiconductor, radiative recombination and Auger recombination determine carrier lifetime, which depends on doping concentration. This is approximately given by the following equation for p-type side,

$$\tau_1 = \frac{1}{S_n N_a + S_{an} N_a^2} \dots\dots\dots(1.59)$$

Here S_n and S_{an} are the transition probabilities for different recombination processes and, in practice, these parameters have to be determined experimentally.

If deep trap impurities or other lattice defects are present, lifetime for this process becomes approximately (for the p-type region)

$$\tau_2 = \frac{1}{\sigma_n \nu_T N_T} \left(1 + \frac{p_1}{N_a} \right) \dots\dots\dots(1.60)$$

where $p_1 = N_V \exp\left(\frac{E_V - E_T}{kT}\right)$, N_T is the trap concentration, σ_n is the capture cross section of the defect and ν_T the thermal velocity of electrons. Corresponding expressions can be derived for an n-type region. Total lifetime τ is given by

$$\tau = \frac{\tau_1 \tau_2}{\tau_1 + \tau_2} = \frac{1}{S_n N_a + S_{an} N_a^2 + \sigma_n \nu_T N_T N_a / N_a + p_1} \dots\dots\dots(1.61)$$

Thus τ decreases with doping level N_a . Since a shorter lifetime reduces diffusion length of minority carriers (as $L = (D\tau)^{1/2}$), higher doping level also reduces the light generated current I_{hv} .

Other important recombination centers are surfaces, dislocations, grain boundaries in polycrystalline semiconductors and interfaces in heterostructure solar cells. Each of these is discussed in detail by L. L. Kazmerski [14]. Recombination at surface and in bulk are also fundamental processes that determine V_{oc} . In general, recombination processes in the entire cell should be minimized as much as possible. Bulk recombination occurs due to trap levels near the middle of the band gap. If appropriate trap levels are present, this condition is especially met in depletion region of the junction. Recombination in space charge region, which has been neglected in the calculation of the ideal current-voltage characteristics of the *pn* junction, can

actually become very important. Increase of recombination current results in an increased saturation current, which reduces open circuit voltage.

1.3.9.3 Series and Shunt Resistance (Fill Factor Losses)

Current-voltage characteristics of *pn* junction are further modified because of series R_s and a shunt resistance R_{sh} associated with solar cell. In any real cell, $R_s > 0$ and $R_{sh} < \infty$, resulting in some power losses [15]. Origin of series resistance is from bulk resistance of semiconductor and resistance of contacts and interconnections. Shunt resistance can be caused by extended lattice defects in depleted region or leakage currents around edges of the cell. Extended defects, which can easily occur in low-cost semiconductors, are dislocations, grain boundaries and large precipitates.

Plots of current-voltage characteristics for various combinations of series and shunt resistance are given in Fig.1.11. This shows that essentially shape of the current-voltage characteristics and hence FF is changed due to even a small change in these parameters. When shunt resistance as low as 100 Ω does not appreciably change the power output of the device, it can be seen that even a small series resistance of 5 Ω reduces total efficiency by 30%. For a typical n- on p-type silicon solar cell, the series resistance is about 0.7 Ω .

1.3.9.4 Effect of Temperature

A considerable fraction of the incident light (about 80% to 90%, depending on the efficiency) is transformed into heat and hence operating temperature of a solar cell can vary over a wide range, especially in the case of concentrator cells. Material parameters, which mainly change with the temperature, are band gap energy, which usually decreases. and the minority lifetime, which generally increases, with increasing temperature. This will increase light generated current (I_{sc}) slightly due to increased light absorption and increase in minority carrier diffusion length. However, open circuit voltage will more rapidly decrease because of exponential dependence of

saturation current on temperature, and correspondingly, the fill factor will degrade too.

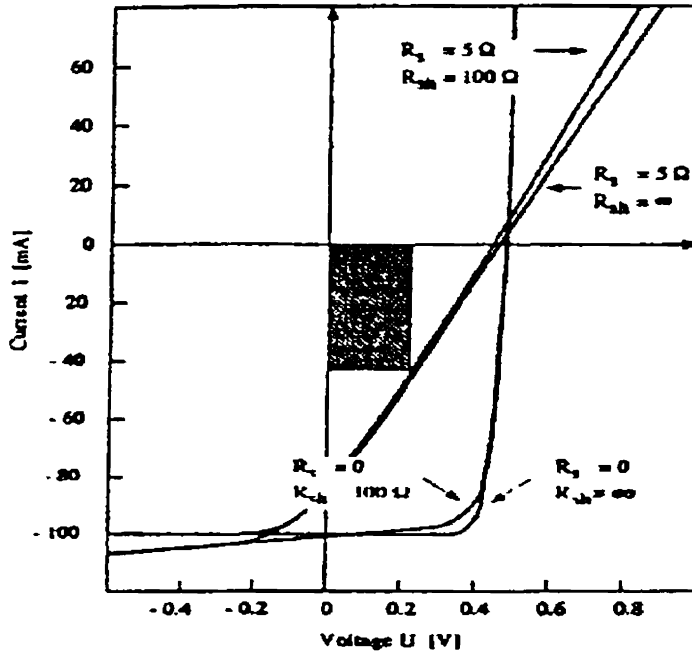


Fig. 1.11 Calculated I-V characteristics for *pn* junction solar cells under illumination with different series R_s and shunt resistance R_{sh}

Therefore, overall effect causes a reduction of cell efficiency, as temperature increases.

$$\Delta V_{oc} = \frac{eV_{oc} + \gamma kT - E_{g0}}{eT} \Delta T \dots\dots\dots(1.62)$$

where E_{g0} is the band gap at $T = 0$ K and γ is a parameter that summarizes the temperature dependence in the prefactors of I_{hv}/I_s , and varies approximately between 1 and 4. Inserting appropriate values for silicon, it can be seen that open-

circuit voltage decreases with temperature (2.3 mV/°C at room temperature) and the efficiency is reduced by about 0.5% per 1°C. This effect is reduced for larger band gap materials, such as GaAs, where the sensitivity to increasing temperature is about half as much compared to silicon.

1.4 Why Thin Film Materials?

A thin film is a material created *ab initio* by random nucleation and growth processes of individually condensing/ reacting atomic/ ionic/molecular species on a substrate. Structural, chemical, metallurgical and physical properties of such a material are strongly dependent on large number of deposition parameters and may also be thickness dependent. Thin film may encompass a considerable thickness range, varying from a few nanometers to tens of micrometers and hence can be best defined in terms of the “birth process” rather than by thickness. Being simpler, cheaper and having relatively much larger throughput or rate of deposition, thin film techniques are of considerable interest for Thin Film Solar Cell (TFSC) technologies. Atomic, random nucleation and growth processes bestow new and exotic properties to thin film materials [16]. These properties can be controlled and reproduced, provided a range of deposition parameters are monitored and controlled precisely.

Features of thin film processes that are of interest for solar cell technologies are listed below.

- A variety of physical, chemical, electrochemical, plasma based and hybrid techniques are available for depositing thin films of the same material
- Power to mass ratio will be always high in the case of thin film cells
- Microstructure of films of most materials can be varied from one extreme of amorphous/nanocrystalline to highly oriented and/or epitaxial growth, depending on the technique, deposition parameters and substrate
- A wide choice of shapes, sizes, areas and substrates are available (unlike in the case of crystalline Si cells)

- Because of relaxed solubility conditions and a relaxed phase diagram, doping and alloying with compatible, as also in many cases, incompatible materials can be obtained
- Surface and grain boundaries can be passivated with suitable materials
- Different types of electronic junctions, single and tandem junctions are feasible
- Graded band gap, graded composition, graded lattice constants etc., can be obtained to meet requirements for a designer solar cell
- In case of multicomponent materials, composition and hence band gap and other optoelectronic properties can be graded in desired manner
- Surfaces and interfaces can be modified to provide an interlayer diffusion barrier and surface electric field
- Surfaces can be modified to achieve desired optical reflectance/transmission characteristics, haze and optical trapping effect
- Integration of unit processes for manufacturing solar cells and integration of individual solar cells can be easily accomplished
- Besides conservation of energy and materials, thin film processes are in general eco-friendly and are thus 'Green' processes

But, keeping in mind the factor that all good things have a price, the ability to tailor numerous properties of thin films required for an efficient solar cell demands good understanding of the material so produced with the help of a range of monitoring and analytic facilities. High sensitivity of film properties to deposition parameters can produce a multitude of undesired results and hence thin film materials should be treated carefully.

1.5 Thin Film Solar Cells

In thin film solar cells, active semiconductor is a polycrystalline or amorphous thin film that has been deposited on a supporting substrate made from

glass, ceramic, metal, plastic or another semiconductor. Various deposition techniques such as evaporation, CVD or sputtering are available today and offer great flexibility in forming semiconducting films of various compositions. Basic requirement is that thickness of the film is larger than inverse of the absorption coefficient for the longer wavelengths of the spectrum so that most of the light can be absorbed. Next requirement is that diffusion length of minority carriers is larger than the film thickness so that most light generated carriers can be collected. Thin film solar cells are therefore mainly made from compound semiconductors with direct band gaps and high absorption coefficients.

Main advantage of thin film solar cells is the low fabrication cost (due to energy for processing), relatively lower costs and quantity of the materials required, and possibility of large scale production. Flexibility in deposition techniques also allows development and utilization of novel semiconductors, which otherwise, might be difficult to produce. Deposition of semiconductors on foreign substrates usually results in polycrystalline or amorphous films with optical and electrical properties that can be substantially different from single crystal behavior. This is mainly due to large number of grain boundaries and other lattice defects. However, one of the major problems with thin film cells is that, in many cases, higher defect density also reduces efficiency and stability of the cells compared to the single crystal cells. Great efforts have therefore been made to understand influence of lattice defects on photovoltaic and/or photoconductive properties of the semiconductor. Though remarkable improvements have been obtained in particular cases, many fundamental problems still need to be solved especially in the case of compound semiconductors suitable for thin film cells.

A variety of junctions such as Schottky barrier, homojunction and heterojunction have been studied. Junctions can be abrupt, graded, buried, heteroface etc., involving materials of different conductivity/ type of conductivity [15]. Different junction devices with appropriately graded band gap can be placed in tandem to form

a multijunction device [17]. Theoretically if all solar photons can be converted into electricity, one may approach thermodynamic Carnot cycle efficiencies [18]. Theoretical analysis shows that 53% efficiency can be achieved with four junction devices and as the number of junctions goes to infinity [19], the efficiency can reach as high as 68%. In view of difficulty and complexity of fabricating such optoelectronically matched junctions, commercial devices with only three junctions could be produced using a-Si:H [20] and GaAs [21].

1.6 Structure of Thin Film Solar Cells

Thin film solar cells consist of several layers of different materials in thin film form. In general the solar cell consists of substrate, transparent conducting oxide (TCO), buffer layer (p or n type), absorber layer (i or p type) and metal contact layer. Each of the component materials has different physical and chemical properties and each affects the overall performance of the device in some form or other. A critical understanding of behavior of these individual components is essential for designing a device. Also important are the various interfaces between different layers. Since each layer has different crystal structure, microstructure, lattice constant, electron affinity work function, thermal expansion coefficient, diffusion coefficient, chemical affinity, mobility, mechanical adhesion etc, the interfaces can cause stress, defect and interface states, surface recombination centers, interdiffusion and chemical changes with attendant electro-optical changes.

1.6.1 Substrate and Superstrate Configurations

Thin film solar cell devices are configured in either “substrate” or “superstrate” structure. For substrate configuration, the substrate is metal or metallic coating on a glass/polymer substrate, which also acts as a contact. The structure of the cell in substrate configuration is glass/metal/metallic/TCO coating/absorber layer/buffer layer/metal contact and the cell is illuminated from the front side. The term superstrate refers to a solar cell configuration where the glass substrate is not

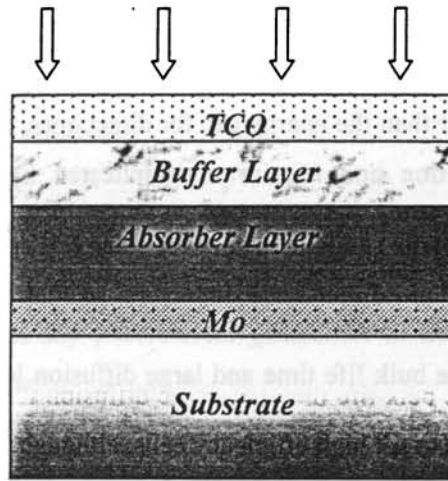
only used as supporting structure but also as window for the illumination and as part of the encapsulation. The solar cell is grown on a glass substrate, but in operation the glass is “above” the solar cell structure, thus the name “Super”strate. For superstrate configuration, the substrate is transparent and a conducting oxide coating on the substrate makes the contact. The structure here is glass/TCO/buffer layer/absorber layer/metal contact and illumination is given through the substrate side.

Both superstrate and substrate device structures are currently being pursued for CIGS device fabrication. The film growth and interdiffusion and hence the device properties are dependent on the device structure. The CIGS solar cells based on superstrate structure is inferior to substrate structure because of the interdiffusion of CdS during high temperature CIGS film growth. The best device efficiency of 10.2% was reported on superstrate device configuration having ZnO buffer layer. On the other hand, a substrate configuration with CdS buffer layer resulted in a 19.2% efficiency device. CdTe devices are fabricated preferably in superstrate configuration because the CdTe surface is exposed for contacting. In addition the benign feature of CdS diffusion during the processing reduces the lattice mismatch between CdTe and CdS. The importances of the different layers are discussed in the following section. The substrate and superstrate configurations are given in Fig. 1.12 (a) and (b).

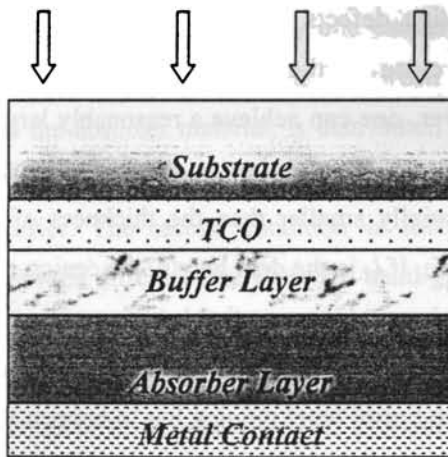
1.6.2 Absorber Layer

This is the layer, which absorb light to convert its electromagnetic energy into the energy of electron-hole pairs. The material requirements are the following:

- (i) The energy gap of the material should match the spectral region where the cell is expected to operate. Energy gap can be measured by optical absorption, photoreflectance and photoluminescence measurements.



(a)



(b)

Fig. 1.12 (a) substrate and (b) superstrate configurations of the cell

- (ii) Optical absorption coefficient of the absorber material has to be high in order to absorb most of the illumination energy within the thin layer. Indirect semiconductors, where the energy gap for indirect transitions is smaller than the energy gap for direct ones, usually show too small optical absorption and require a complicated light-trapping scheme. Typical chalcopyrite semiconductors for solar cell applications, like CuInSe_2 and CuInS_2 , are direct semiconductors, so that large absorption coefficients can be achieved.
- (iii) A large bulk life time and large diffusion length are desired for minority carriers to get high efficiency cells, although these requirements are not so stringent for thin film solar cells compared to the bulk ones, due to a much smaller distance the carriers have to diffuse through, in the cell. In order to achieve a large carrier diffusion length, one has to avoid crystalline defects and impurities, which could produce recombination levels close to the middle of the band gap decreasing the mobility. However, one can achieve a reasonably large short circuit current from a cell, in which absorber is made of a material with diffusion length substantially smaller than the thickness of the cell, if one uses a p-i-n structure. If l_d is the drift length, the design criterion to choose thickness d of the absorber layer so that $l_d > d$.
- (iv) n- and p- type dopability. Although the absorber layer of i-type may be used, no Fermi level pinning has to happen throughout the band gap. As it follows from the work of Klein and Jaegermann [22], Fermi level pinning and the absence of the dopability of a certain type may be related to a Fermi level-dependent formation of compensating defects. Also, Fermi level pinning may result in tunneling-enhanced interface recombination current across the junction.

- (v) No degeneration should be possible in the material, independently of the defects. Otherwise random impurities will make the semiconductor degenerate and tunneling through the narrow space charge region will short-circuit the structure.

1.6.3 Buffer Layer

Primary function of a buffer layer in a heterojunction is to form a junction with absorber layer while admitting a maximum amount of light to the junction region and absorber layer; without any photocurrent generation in the buffer layer. The requirements are listed below.

- (i) Large energy band gap for high optical transmission in the visible region. Novel p-type material like CuI with a band gap of 2.9 eV may even outperform traditional CdS material ($E_g = 2.4$ eV) from this point of view.
- (ii) Optimal band discontinuities. Ideal solar cell junction will separate electrons and holes, letting through only one carrier type. This may be achieved if the energy band discontinuity, between the wide band gap buffer layer and the absorber material, is distributed in such a way, that there is no band offset for the minority carriers, but there is a large barrier for majority carrier. The second condition is fulfilled if the first is fulfilled, provided the difference between the band gaps is significant. If there is a band offset for the minority carriers in the buffer layer, then it may lead to the formation of 'spike' or a 'cliff', depending on sign of the offset. If the band offset produces a cliff, probability of the interface cross-recombination is increased, and flat band condition is achieved at bias smaller than E_g/q of the absorber [23]. One consequence is that output voltage of the cell is limited in this case, because of the lack of barrier height. Band alignment with a moderate spike is rather optimal, although the presence of a spike means the band offset for the minority carrier decreases and the interface becomes less selective. In a more

general case even a moderate spike may be dangerous as far as efficiency is concerned. Band discontinuities are usually studied using photoemission spectroscopy. Recent measurement using X-ray photoemission spectroscopy of the valence band discontinuity at CuInS₂/CuI interface resulted in virtually no band offset [24], making this material combination attractive for solar cell applications.

- (iii) Lattice mismatch (and consequent effects) at the junction is important for consideration for epitaxial or highly oriented layers. In the case of microcrystalline layers, mismatch varies spatially and thus the complicated effect, if any, is averaged out.
- (iv) Doping density in the buffer layer has to exceed that in the absorber sufficiently, in order to confine the space charge region in the absorber, where its electric field helps to separate charge carriers [25]. Moreover larger doping density in the buffer layer is necessary to suppress the minority carrier generation in order to reduce the bucking current density, and to hold the Fermi level away from the middle of the band gap at the interface in order to suppress the interface recombination. However, strongly doped buffer layer material or buffer material with a doping limitation can induce the tunneling-enhanced interface recombination current [26] if there is a corresponding doping limitation in the absorber, or in the presence of a spike band alignment.

Interestingly the oldest and only well studied buffer layer material is CdS. Works on cells using CdS started in 1954, almost at the same time when works on silicon cells started. But currently people are trying hard to avoid this material as it contains cadmium.

1.6.4 Transparent Conducting Oxide, TCO (Window Layer)

Transparent conducting oxides in general are n-type degenerate semiconductors with good electrical conductivity and high transparency in the visible

spectrum. Thus, a low resistance contact to the device and transmission of most of the incident light to the absorber layer is ensured. Conductivity of a TCO depends on carrier concentration and mobility. An increase in carrier concentration may result in enhanced free carrier absorption, which reduces the transparency of the TCO in the higher wavelength region. Hence increasing mobility by improving crystalline properties is considered to be the pathway for a good TCO [27]. Typical materials achieve mobility of approximately $40 \text{ cm}^2/\text{Vs}$. Besides these, optoelectronic properties, mechanical, thermal, chemical and plasma-exposure stability and passivity [28] of TCO's are important considerations. Studies have shown [29] that only ZnO-based TCO's can withstand H-bearing plasma and are also stable upto 800 K. Therefore, ZnO based materials are being increasingly used in thin film solar cell technologies. Table 1.1 lists typical values of resistivity and transmission in the visible region for various TCO's of interest for photovoltaic application.

Table 1.1 Typical resistivity, transmission and band gap for various TCO materials investigated for solar cell applications (visible region)

Material	Resistivity ($\Omega\text{-cm}$)	Transparency (%)	Band Gap (eV)
SnO_2	8.0×10^{-4}	80	3.7 - 4.6
$\text{In}_2\text{O}_3:\text{Sn}$ (ITO)	2.0×10^{-4}	>80	3.5 - 4.6
$\text{In}_2\text{O}_3:\text{Ga}$ (IGO)	2.0×10^{-4}	85	3.30
$\text{In}_2\text{O}_3:\text{F}$	2.5×10^{-4}	85	3.50
Cd_2SnO_4 (CTO)	2.0×10^{-4}	85	2.7 - 3.0
Zn_2SnO_4 (ZTO)	10^{-2}	90	3.35 - 3.85
$\text{ZnO}:\text{In}$	8.0×10^{-4}	85	3.30
CdO	2.0×10^{-2}	90	2.50

1.6.5 Back Contact

In superstrate structure it should be beneficial to use a wider band gap material for the back contact in order to increase carrier type selectivity and to reduce interface recombination [30]. This back contact must transmit maximum light to the buffer layer. In the substrate configuration, in order to form an ohmic contact, it can be a metal used for the contact and should have work function higher than that of the p-type semiconductor. This aligns the metal Fermi level with the upper valence band edge.

1.6.6 Substrate

Solar cell substrate has to be stable at the cell fabrication temperature. Another important issue is good adhesion to the layers of the cell. Depending on the application, it should be cheap like a soda lime glass or a polyimide film [31]. Usually one tends to avoid diffusion of impurities from the substrate, although sometimes it may lead to better results as in the case of sodium to the cell [32]. Substrate appears to play an active role in improving the photovoltaic performance of the CIGS absorber materials. Sodium in soda-lime glass substrate has been considered as a key prerequisite for efficient CIGS device fabrication. Na diffuses from the substrate into CIGS absorber and improves the grain growth and cell performance [33]. Sodium is inherently present in soda-lime glass (SLG) and in the case of Na free substrate Na precursors (Na_2Se , Na_2S , NaF) are intentionally incorporated in the device fabrication.

1.6.7 Antireflection Coating

Antireflection coating may be used in order to avoid efficiency loss due to the light reflection during penetration of the interface to an optically denser material, which is the solar cell. It may be applied as an alternative, or in addition to the surface texturization.

1.6.8 Top Grid

For a top grid, metal films or their stacks are usually used. Bottom layer of the grid has to provide a good ohmic contact to the window layer and it has to have a

large melting point in order to avoid diffusion into the cell structure during the whole period of operation. Nickel is often used for this purpose. Top layer of the grid has to be good electrical conductor, and it has to be readily connectable. Aluminium is often used as the top layer. Metallic grids are not necessary. Screen-printed top grids used in Si technology may be applied. Monolithically interconnected modules do not use any top grid at all.

Long - term stability is vital for success of any cell. For this, stability of the materials is required. Diffusion and reaction at interfaces have to be controlled. Also, good adhesion between layers of the cell is important. Above all materials for the cell have to be cheap and abundant.

1.7 Materials for Thin Film Solar Cells

1.7.1 Absorber Layer

1.7.1.1 Copper Indium Selenide (CuInSe₂)

The I-III-VI chalcopyrite materials have very desirable properties suitable for photovoltaic application. CuInS₂, having a band gap of 1.53 eV, is considered as an ideal material for photovoltaic application. Difficulties in controlling sulfur during deposition and the relatively rapid diffusion of metals and impurity species, even at low temperatures, slow down the large-scale usage of this material [34]. However devices with efficiency 12.5% have been reported [35]. On the other hand, CuInSe₂ with band gap of 1 eV, has proved to be a leading candidate for photovoltaic application. It is one of the most absorbing semiconductor materials (absorption coefficient of 3 - 6 x 10⁵/cm) and also makes an excellent junction and a solar cell. CuInSe₂ and other chalcopyrites appear to tolerate wide range of anion-to-cation off-stoichiometry. Unlike the II-VI analogue, CuInSe₂ can be doped to make n- and p-type to a low resistivity level, merely via introduction of native defects. The most benevolent feature of polycrystalline CuInSe₂ lies in the electrically benign nature of its numerous structural defects and hence polycrystalline CuInSe₂ films are as good an electronic material as its single-crystal counterpart. This makes CuInSe₂ based solar

cells less sensitive to the impurities, grain size and crystalline defects. Devices with active area efficiency of 15.4% were fabricated from CuInSe₂ [36]. Superior device performance is achieved when the junction is matched to the solar spectrum by increasing the band gap. Resultant increase in V_{oc} is also beneficial to the manufacturing process and device properties by: (a) reducing the number of scribes for the monolithic integration the cells into module; (b) reducing the top and bottom electrode thickness; (c) lowering the temperature coefficient at maximum power point and (d) making it less sensitive to light intensity fluctuations. Alloying with Ga [37], Al [38], or S [39] increases band gap of CuInSe₂ so as to make it more suitable for high efficiency single-junction and multi junction devices. An increase in the band gap and improved process conditions resulted in the fabrication of high performance solar cells with efficiencies of 19.2% for small area [40] and 13.1% for large area (90 x 60 cm²). However increasing number of alloy components makes multiple processes extremely complex and thus intelligent processes are required for precise control of the composition during deposition. Use of expensive and rare metals such as In and Ga also adds to the cost of manufacturing.

1.7.1.2 Cadmium Telluride (CdTe)

Owing to its optoelectronic and chemical properties, CdTe is an ideal absorber material for high efficiency low cost thin film polycrystalline solar cells. CdTe is a direct band gap material with an energy gap of 1.5 eV, and an absorption coefficient $\sim 10^5$ /cm in the visible region, which means that a layer thickness of a few micrometers is sufficient to absorb $\sim 90\%$ of the incident photons. Owing to the requirement of high temperature for deposition, in most cases, films are deposited with Cd deficiency, giving rise to p-type conductivity. Because of the high ionicity (72%) of CdTe, the crystallite formed is well passivated with strong chemical bonding (5.75 eV) resulting in high chemical and thermal stability. CdTe solar cell devices have proven to be remarkably tolerant to the deposition methods and devices with efficiency $> 10\%$ have been fabricated by several deposition techniques. Some of

these techniques, (like close-spaced sublimation (CSS), PVD, electrodeposition and screen printing) have been scaled to yield large area modules. Solar cells based on CdS/CdTe junction have achieved an efficiency 16.5% in small areas compared with the theoretical maximum efficiency [41] of 29%. For the past ten years the efficiency has only changed from 15.8% [42] to 16.5% [43]. The reason for such a slow progress appears to be lack of research efforts on the issues as the requirement of activation treatment that changes the bulk, interfacial and grain boundary properties and difficulty of forming an ohmic contact without degrading the device.

1.7.1.3 Amorphous Si (a-Si)

Amorphous silicon is widely accepted as a thin film solar cell material because (a) it is abundant and non-toxic; (b) it requires low processing temperature enabling module production on flexible and low cost substrates; (c) The technological capability for large area deposition exists; and (d) material requirement is low, (only 1-2 μm) due to the inherent high absorption coefficient compared with crystalline silicon. High absorption results from the inherent high disorder, due to dangling bond of the order of $10^{19} / \text{cm}^3$, in the material so that all-optical transition are allowed. On the other hand disorder acts as recombination centers that severely reduce the carrier lifetime and pin the Fermi level so that the material cannot be doped either n-or p-type. Incorporation of 10% hydrogen in the film during deposition greatly reduces density of defects to $10^{16}/\text{cm}^3$, yielding a new and exotic material, a-Si:H which has a well defined optical threshold (mobility gap) at 1.75 eV compared with the crystalline Si indirect band gap at 1.1 eV. The reduction in the defect density makes a-Si:H material suitable for doping and alloying with a range of materials and for junction device fabrication. However, the properties of the material and the junction device are severely affected by the light induced creation of meta-stable defects, known as Staebler- Wronski effect. Light induced degradation of a-Si:H devices is partially tackled by reducing the a-Si:H layer thickness so that photogenerated carriers need to move only a short distance to reach electrode. However, thinning down also results in

lower light absorption and thus optical confinement techniques employing diffusely reflecting front and back contact are required to increase effective layer thickness in order to absorb the photons.

The a-Si alloy materials are no longer strictly classical amorphous materials with short range order (<1 nm). Under suitable deposition conditions and strong hydrogen dilution, nanocrystalline and microcrystalline materials [44] are obtained. The existence of very small Si crystallites dispersed in amorphous matrix deposited by plasma enhanced chemical vapor deposition (PECVD) under high H dilution was confirmed with infrared absorption and XRD measurements [45]. While crystallite size and volume fraction are very small, these crystallites catalyze crystallization of the remainder of the amorphous matrix upon annealing. Microcrystalline materials deposited by this method is found to have less defect density and are more stable against light degradation compared with a-Si. Recently developed improved efficiency materials consist of this heterogeneous mixture of the amorphous and an intermediate range order microcrystalline material. Laser [46], rapid thermal annealing and optically assisted metal-induced crystallization techniques [47] were also used to obtain microcrystalline film from amorphous film and to increase the grain size.

1.7.1.4 Polycrystalline Si

New high rate deposition technologies for polycrystalline Si films and innovative solar cell designs are being evolved to make reasonably efficient solar cells. Crystalline silicon on glass (CSG) technology combines low manufacturing cost of thin film technology with established strengths of silicon wafer technology [48]. Owing to high conductivity, no TCO was required for the current collection. Main advantage of polycrystalline silicon over a-Si is that mobility can be order of magnitude larger and material also shows greater stability under electric field and light induced stress. With the assistance of light trapping technique, efficient modules (as high as 7%) have been fabricated on $2\ \mu\text{m}$ thick silicon films [48]. High rate

deposition of polycrystalline silicon films can also be obtained by hot-wire CVD technique [49]. Large grain, 5-20 μm , polycrystalline silicon layers have been deposited at rates as high as 3 $\mu\text{m}/\text{min}$ using iodine vapor transport at atmospheric pressure [50]. Microcrystalline and polycrystalline silicon films have lower optical absorption in contrast to high optical absorption in a-Si.

1.7.1.5 Organic Semiconductors

There are at least three very good reasons why organic materials are promising for PV application. Two of them are based on the necessity to reduce the cost of production. Requirements on quality and purity of organic material are small and their large-scale production is relatively easy as compared to most inorganic materials. Third is connected to the infinite variability of organic compounds, which can, in principle, be tailored to all needs. Organic semiconductors can be classified into three categories, depending on their chemical properties, as insoluble, soluble and liquid crystalline. They can be further classified as monomers (such as dyes), pigments and polymers [51]. Doping of organic semiconductors can be done by introducing foreign atoms or molecules, or by electrochemical oxidation/reduction process. Some dopants for p-type materials are, Cl_2 , Br_2 , I_2 , NO_2 , organic molecules such as *o*-chloranil and 2,4,7-trinitrofluorenone, high electron affinity semiconductors such as C_{60} and perylene diamides. Some dopants for n-type material are, alkali metals, phenothiazines or semiconductors with low ionization potential. Mobile charge concentration can also be changed by trapping of stray electrons in conduction band (material becoming better hole conductor than electron conductor by shifting the Fermi level close to the volume bond due to the reduction of free electron concentration), making the material doped p-type conductor. Since there is no net increase in the charge carrier concentration, conductivity does not increase unless mobility is affected.

Organic solar cells have the advantage of using chemically tailored materials with desired properties and can potentially be manufactured by inexpensive technologies. In order to be attractive from manufacturing point of view, organic solar cell device efficiency has to be improved from the current ($< 3\%$) efficiency [52]. Also, organic solar cells have stability problem common to conjugated polymers [53]. However, these may not be very serious problems and may be overcome in the near future due to intense research going on in this field.

1.7.2 Buffer Layer

1.7.2.1 Cadmium Sulfide (CdS)

CdS cells have a history of development, dating back to 1954 [54], about the same year as the first results appeared for diffused silicon cells. Since then, there have been several attempts to produce a commercial solar cell based on this material. It is one of the most extensively investigated semiconductors in thin film form and a large variety of deposition techniques have been utilized to obtain solar cell quality layers. These preparation techniques include evaporation [55], spray pyrolysis [56], chemical bath deposition [57], MBE [58], CVD [59], anodization [60], electrophoresis [61] etc. Among them, CBD has been proven to be the most suitable method to produce CdS thin films for photovoltaic application. In general films deposited using CBD are stoichiometric, which results in high dark resistivity and high photosensitivity 10^6 - 10^9 in CdS [62, 63]. The CIGS solar cells typically using CdS window layer (which is deposited by a chemical bath deposition (CBD) technique) provide a superior device performance, with efficiencies upto 19.2% has been achieved [40]. Eventhough lattice mismatch between CdTe (111) and CdS (001) is $\sim 9.7\%$, CdS remains the best heterojunction partner for CdTe. CdS has an energy band gap of 2.42 eV. Relatively low band gap of CdS as a buffer layer reduces the blue response, but the effect is mitigated in both CdTe and CIGS devices by utilizing thinner CdS films.

1.7.2.2 $Zn_xCd_{1-x}S$

Composition of the alloy films play a dominant role in determining their structural, electronic and optical properties. In general, CdS and ZnS form a solid solution over the entire composition range and the alloy films exist in a single-phase wurtzite structure upto 60% Zn concentration irrespective of the deposition technique. Beyond 80% ZnS, the films exhibit cubic structure. Between 60 and 80% ZnS concentration the films exist in both wurtzite and sphalerite structures. Optical band gap of these films is direct at all compositions [64] and varies sublinearly with composition from that of pure CdS (2.4 eV) to that of pure ZnS (3.6 eV). Variation of E_g with the alloy composition x can be expressed as

$$E_g(x) = E_g(0) + [E_g(1) - E_g(0)]x - cx(1-x) \dots\dots\dots(1.63)$$

where $E_g(0)$ and $E_g(1)$ are the energy gaps of the two constituent compounds and c is the optical bowing [65]. Increase in band gap results in increased V_{oc} when it is used as buffer layer in solar cells.

1.7.2.3 Indium Sulfide (In_2S_3)

On the one hand research is aimed at a better understanding of the junction formation in classical devices with chemical bath deposited CdS. On the other hand works are in progress to replace cadmium sulfide by cadmium free buffer layers due to environmental reasons. Numerous studies are going on for cadmium - free buffer layers. Many are related to the growth of buffer layers (from solutions by chemical bath deposition) such as ZnS, ZnSe and indium sulfide, which are not pure and often contain oxygen impurities. Indium sulfide (In_2S_3) is a III-VI compound originating from II-VI semiconductor by replacing group II metals by group III elements [66]. A number of techniques have been used to prepare this compound such as CBD [67], organometallic chemical evaporation [68], spray pyrolysis [69-71], thermal evaporation [72], rf sputtering [73] and atomic layer epitaxy [74]. Naghavi et al proved Atomic Layer Chemical Vapour Deposition (ALCVD) as an effective method

for the deposition of indium sulfide. They reported an efficiency of 16.4% for a copper indium gallium diselenide (CIGS) solar cell with indium sulfide deposited using ALCVD [75]. Band gap of the indium sulfide layer was about 2.7 – 2.8 eV and hence wider than that of CdS (2.4 eV). They considered quantum size effect as a possible origin for this difference [76]. An increase of band gap upto 3 eV is possible for very small grain sizes between 2 and 3 nm. Presence of oxygen and sodium has been reported also to increase markedly band gap of indium sulfide prepared by PVD [77, 78]. As a buffer layer, being a wider band gap material than CdS, this material should decrease optical absorption losses at short wavelengths, leading to a gain in efficiency due to an increase in short circuit current. Indium sulfide layer (ALCVD) has also been used for CIGS solar modules (module area 30 x 30 cm²) with an efficiency of 10.8% [79]. Stability test indicated a similar behavior of standard cadmium containing modules. In our lab, we deposited indium sulfide thin films using spray pyrolysis technique, which was found to deliver an efficiency of 9.5% with CuInS₂ as the absorber layer [80] and detailed descriptions on this work are given in following chapters.

1.7.2.4 Indium Selenide (In₂Se₃)

In recent years, thin film of In₂Se₃ compound has attracted considerable attention as a new semiconducting material for photovoltaic solar cell [81]. In₂Se₃ crystallizes in a layered structure (α -phase), β -In₂Se₃ obtained by heating α -In₂Se₃, defect wurtzite structure (γ -phase) [82] and a recently discovered anisotropic structure (κ phase) [83]. In general, band gap of In₂Se₃ is 1.7 eV and depending on the preparation conditions it can vary upto 2.4 eV close to that of CdS [84]. One of the advantages of indium selenide is that it forms negligible lattice mismatch with CuInSe₂. However, the low transmittance of indium selenide is a limiting factor to get high current densities. Gordillo et al obtained an efficiency of 9.2% with the cell structure Mo/CIS/In₂Se₃/ZnO with evaporated In₂Se₃ layer [85]. They also suggest

that decreasing the thickness of In_2Se_3 leads to an increase of J_{sc} . On the other hand, the reduction of the thickness of In_2Se_3 layer leads to a decrease in open circuit voltage (V_{oc}). Most likely explanation of this behavior is reduction of the band bending in the absorber layer by decreasing buffer thickness. In our lab, we have prepared indium selenide thin films using SEL (Stack Elemental Layer) structure [86]. SEL structure was grown using chemical bath deposited a-Se film and vacuum evaporated indium thin films. Whole process of film preparation of In_2Se_3 involved two steps. First step was the preparation of Se-In stack layers while second stage involved the process of annealing the stack layers. Works are in progress for the fabrication of $\text{CuInSe}_2/\text{In}_2\text{Se}_3$ junction.

1.7.2.5 Zinc Oxide (ZnO)

Zinc oxide is a wide gap semiconductor $A^{II}B^{VI}$ with n-type conduction. Because of its structural, electrical and optical properties, ZnO is useful for many applications in different devices, including gas sensors, transparent electrodes in solar cells and acousto- and electro-optical devices. Optical band gap energy of the films is 3.3 eV. This allows maximum light to be transmitted to the cell when it is used as the window layer. Many different techniques such as chemical vapour deposition [87] spray pyrolysis [88], sputtering [89] and laser deposition [90] are used for the preparation of ZnO thin films. Today, chalcopyrite –based devices with the structure ZnO/buffer layer/CIS or CIGS/Mo/glass reach highest efficiencies. A record 19.2% efficiency was obtained for the cell structure ZnO/CdS/Cu(In,Ga)Se₂ solar cells [40]. Bi-layer structure of the window layer also was found to yield good efficiency cells. Cell having structure $\text{MgF}_2/\text{ZnO}:\text{B}/\text{i-ZnO}/\text{CdS}/\text{CIGS}/\text{Mo}$ fabricated by Hagiwara et al yielded an efficiency of 18% [91].

1.7.2.6 Indium Hydroxy Sulfide ($\text{In}_x(\text{OH},\text{S})_y$)

Indium sulfide thin films often contain oxygen impurities (O or OH groups), which contribute to widening the band gap. Band gap energy depends on the film stoichiometry (between 2.0 eV and 3.7 eV) and is between band gap energies of In_2S_3

and In_2O_3 respectively [92]. Huang et al obtained an efficiency of 7.39% for the $\text{In}_x(\text{OH},\text{S})_y/\text{CIGS}$ solar cells [93]. A still better efficiency of 15.7% was reported by Hariskos et al [94]. In both the cases the films were deposited using CBD technique. Some of the alternate buffer layers investigated for solar cell applications are listed in Table 1.2.

Table 1.2 Alternate buffer layers for solar cell

Alternate buffer layer	Deposition technique	Reference
$\text{In}_x\text{Se}_y, \text{In}_2\text{Se}_3$	Co-evaporation	95
$\text{Ga}_x\text{Se}_y, \text{Ga}_2\text{S}_3, \text{Ga}_2\text{Se}_3$	Co-evaporation	95
$\text{In}(\text{OH})_x\text{S}_y, \text{In}(\text{OH})_3$	CBD	96
ZnIn_xSe_y	ALD	97
$\text{Sn}(\text{S},\text{O})_2$	Spray	98
ZrO_2	CBD, PLD	99
$\text{ZnO}, \text{GaZnO}, \text{ZnO}:\text{B}$	RF/DC sputtering	100
ZnSe, ZnS	Sputtering, Co-evaporation	101
$(\text{ZnCd})\text{S}$	Spray, PVD, CBD	102
a-CdS:O	Sputtering	103

References

- [1] B. Sørensen *Renewable Energy*, Academic Press (1979)
- [2] Godfrey Boyle *Renewable Energy: Power for a Sustainable Future*, Oxford University Press (1996)
- [3] H. P. Garg and J. Prakash *Solar Energy: Fundamentals and Applications*, Tata McGraw Hill Publishing Company Ltd (2002)
- [4] Martin A. Green *Solar Cells:- Operating Principles, Technology and System Applications*, University of New South Wales (1992)
- [5] G. D. Rai *Solar Energy Utilization*, Khanna Publishers (1997) 4
- [6] A. E. Becquerel *C. R. Hebd. Seances Acad. Sci.* **9** (1839) 561
- [7] W. G. Adams and R. E. Day *Proc. Royal Society*, London **A25** (1877) 113
- [8] D. M. Chapin, C. S. Fuller and G. L. Pearson *J. Appl. Phys.* **25** (1954) 676
- [9] D. C. Reynolds, G. Leies, L. L. Antes and R. E. Marburger *Phys. Rev.* **96** (1954) 533
- [10] K. L. Chopra, P. D. Paulson and V. Dutta *Prog. Photovolt: Res. Appl.* **12** (2004) 69
- [11] G. Busch and H. Schade *Lectures on Solid State Physics*, Pergamon Press (1976) 337
- [12] H. J. Möller *Semiconductors for Solar Cells*, Artech House, Boston (1993)
- [13] S. M. Sze *Physics of Semiconductor Devices*, New York: Wiley and Sons (1981) 798
- [14] L. L. Kazmerski *Polycrystalline and Amorphous Thin Films and Devices*, Academic Press (1980)
- [15] A. L. Fahrenbruch and R. H. Bube *Fundamentals of Solar Cells*, Academic Press (1983) 220
- [16] K. L. Chopra *Thin Film Phenomena*, Mc Graw Hill: New York (1969)

- [17] T. J. Coutts, K. A. Emery and J. S. Ward *Prog. Photovolt: Res. Appl.* **10** (2002) 195
- [18] A. D. Vos *Endoreversible Thermodynamics of Solar Energy Conversion*, Oxford University Press, Oxford (1992)
- [19] R. W. Birkmire *Sol. Energy Mater. Sol. Cells* **65(1-4)** (2001) 17
- [20] J. Yang, A. Banerjee, T. Glatfelter, K. Hoffman, X. Xu and S. Guha *Proc. 1st World Conference on Photovoltaic Energy Conversion* (1994) 380
- [21] R. R. King, J. H. Ermer, D. D. Krut, J. E. Granata, M. S. Gillanders, B. T. Cavicchi and N. H. Karam *Proc. Space Power Workshop* (2001)
- [22] A. Klein and W. Jaegermann *Appl. Phys. Lett.* **74** (1999) 2283
- [23] A. Niemegeers, M. Burgelman and A. De Vos *Appl. Phys. Lett.* **67** (1995) 843
- [24] I. Konovalov and R. Szargan *Appl. Phys. Lett.* **82** (2003) 2088
- [25] R. Klenk *Thin Solid Films* **387** (2001) 135
- [26] U. Rau *Appl. Phys. Lett.* **74** (1999) 111
- [27] K. L. Chopra, S. Major and D. K. Pandya *Thin Solid Films* **102(1)** (1983) 1
- [28] S. Major, S. Kumar, M. Bhatnagar and K. L. Chopra *Appl. Phys. Lett.* **49** (1986) 394
- [29] S. Major and K. L. Chopra *Sol. Energy Mater.* **17(5)** (1988) 319
- [30] I. Konovalov *Thin Solid Films* **451-452** (2004) 413
- [31] B. M. Basol, V. K. Kapur, C. R. Leidholm, A. Halani and K. Gledhill *Sol. Energy Mater. Sol. Cells* **43** (1996) 93
- [32] D. Schmid, M. Ruckh and H. W. Schock *Sol. Energy Mater. Sol. Cells* **41-42** (1996) 281
- [33] M. Bodegård, L. Stolt and J. Hedström *Proc. 12th European PVSEC* (1994) 1743
- [34] L. L. Kazmerski *Proc. NBS Workshop on the Stability of Thin Film Solar Cells Materials, NBS Special Publication (U.S)* **30** (1978) 400
- [35] J. Klaer, J. Bruns, R. Henninger, K. Siemer, R. Klenk, K. Ellmer and D. Bräunig *Semicond. Sci. Technol.* **13** (1998) 1456

- [36] J. Hedström and H. Ohlsén *Proc. 23rd IEEE Photovoltaic Specialists Conference* (1993) 364
- [37] W. N. Shafarman, R. Klenk and B. E. McCandless *J. Appl. Phys.* **79** (1996) 7324
- [38] P. D. Paulson, M. W. Haimbodi, S. Marsillac, R. W. Birkmire and W. N. Shafarman *J. Appl. Phys.* **91** (2002) 10153
- [39] M. Engelmann, B. E. McCandless and R. W. Birkmire *Thin Solid Films* **387** (2001) 14
- [40] K. Ramanathan, M. A. Contreras, C. L. Perkins, S. Asher, F. S. Hasoon, J. Keane, D. Young, M. Romero, W. Metzger, R. Noufi, J. Ward and A. Duda *Prog. Photovolt: Res. Appl.* **11** (2003) 225
- [41] A. De Vos, J. E. Parrot, P. Baruch and P. T. Landsberg *Proc. 12th European Photovoltaic Solar Energy Conference* (1994) 1315
- [42] J. Britt and C. Ferekides *Appl. Phys. Lett.* **62** (1993) 2851
- [43] X. Wu, J. C. Keane, R. G. Dhere, C. DeHart, A. Duda, T. A. Gessert, S. Asher, D. H. Levi and P. Sheldon *Proc. 17th European Photovoltaic Solar Energy Conference* (2001) 995
- [44] D. V. Tsu, B. S. Chao, S. R. Ovshinsky, S. Guha and J. Yang *Appl. Phys. Lett.* **71** (1997) 1317
- [45] A. H. Mahan, J. Yang, S. Guha and D. L. Williamson *Phys. Rev. B* **61** (2000) 1677
- [46] K. Yamamoto, A. Nakashima, T. Suzuki, M. Yoshimi, H. Nishio and M. Izumina *Jpn. J. Appl. Phys.* **33** (1994) L 1751
- [47] W. Chen, B. Sopori, K. Jones, R. Reedy, N. M. Ravindra, R. Aparicio, R. W. Birkmire, S. Morrison, S. K. Coats and A. Madan *Proc. MRS Spring Meeting, Pittsburgh* **685E** (2001) D3.2.1-6
- [48] P. A. Basore *Proc. 29th IEEE Photovoltaic Specialists Conference* (2002) 49
- [49] A. H. Mahan *Sol. Energy Mater. Sol. Cells* **78(1-4)** (2003) 299

- [50] T. H. Wang, T. F. Ciszek, M. R. Page, R. E. Bauer, Q. Wang and M. D. Landry *Proc. 29th IEEE Photovoltaic Specialists Conference* (2002) 94
- [51] K. Petritsch *Ph.D Thesis*, Technisch-Naturwissenschaftliche Fakultät, der Technischen Universität Graz, Austria (2000)
- [52] S. E. Shaheen, C. J. Brabec, N. S. Sariciftci, F. Padinger, T. Fromherz and J. C. Hummelen *Appl. Phys. Lett.* **78** (2001) 841
- [53] C. J. Brabec, N. S. Sariciftci and J. C. Hummelen *Advances in Functional Materials* **11(1)** (2001) 15
- [54] F. A. Shirland *Advanced Energy conversion* **6** (1966) 201
- [55] N. Romeo, G. Shervoglieri and L. Terricone *Thin Solid Films* **55** (1978) 413
- [56] P. Domens, M. Cadene, G. W. Cohen-Solal and S. Martinuzzi *Proc. 1st EC Photovoltaic Solar Energy Conference*, Luxemburg (1977) 770
- [57] I. Kaur, D. K. Pandya and K. L. Chopra *J. Electrochem. Soc.* **127** (1981) 943
- [58] D. C. Cameron, W. Duncan and W. M. Tsang *Thin solid Films* **58** (1979) 61
- [59] M. Arienzo and J. J. Loferski *Proc. 2nd EC Photovoltaic Solar Energy Conference*, Berlin (1979) 361
- [60] J. Vedel, M. Soubeyrand and E. Castel *J. Electrochem. Soc.* **124** (1977) 177
- [61] E. W. Williams, K. Jones, A. J. Griffiths, D. J. Roughley, J. M. Bell, J. H. Steven, M. J. Huson, M. Rhodes and T. Costich *Proc. 2nd EC Photovoltaic Solar Energy Conference*, Berlin (1979) 874
- [62] O. Vigil, O. Zeleya-Angel and Y. Rodriguez *Semicond. Sci. Technol.* **15** (2000) 259
- [63] P.K. Nair, P. Parmananda and M. T. S. Nair *J. Cryst. Growth* **206** (1999) 68
- [64] S. R. Das *Ph.D Thesis*, Indian Institute of Technology, Delhi, India (1978)
- [65] C. Laroz, C. Bellabarba and C. Rincon *Appl. Phys. Lett.* **65(13)** 1996 1650
- [66] J. Herrero and J. Ortega *Sol. Energy Mater.* **17** (1988) 357
- [67] C. D. Lokhande, A. Ennaoui, P. S. Patil, M. Giersig, K. Diesner, M. Muller and H. Tributsch *Thin Solid Films* **340** (1999) 18

- [68] R. Nomura, K. Konishi and H. Matsuda *Thin Solid Films* **198** (1990) 339
- [69] W. T. Kim and C. D. Kim *J. Appl. Phys.* **60** (7) (1986) 2631
- [70] M. Amlouk, M. A. Ben Said, N. Kamoun, S. Belgacem, N. Brunet and D. Barjon *Jpn. J. Appl. Phys.* **38** (1999) 26
- [71] L. Bhira, H. Essaidi, S. Belgacem, G. Couturier, J. Salardenne, N. Barreau and J. C. Bernède *Phys. Stat. Sol. (a)* **181** (2000) 427
- [72] A. A. El Shazly, D. Abd Elhady, H. S. Metoually and M. A. M. Seyam *J. Phys.: Condens. Mater.* **10** (1998) 5943
- [73] H. Ihara, H. Abe, S. Endo and T. Irie *Solid State Commun.* **28** (1970) 563
- [74] T. Asikainen, M. Ritala and M. Leskelä *Appl. Surf. Sci.* **82/83** (1994) 122
- [75] N. Naghavi, S. Spiering, M. Powalla, B. Cavana and D. Lincot *Prog. Photovolt: Res. Appl.* **11** (2003) 437
- [76] E. B. Yousfi, B. Weinberger, F. Donsanti, P. Cowache and D. Lincot *Thin Solid Films* **387** (2001) 29
- [77] N. Barreau, J. C. Bernède, C. Deudon, L. Brohan and S. Marsillac *J. Cryst. Growth* **241** (2002) 51
- [78] N. Barreau, J. C. Bernède, S. Marsillac and A. Mokrani *J. Cryst. Growth* **235** (2002) 439
- [79] S. Spiering, D. Hariskos, M. Powalla, N. Naghavi and D. Lincot *Thin Solid Films* **431-432** (2003) 359
- [80] Teny Theresa John, Meril Mathew, C. Sudha Kartha, K. P. Vijayakumar, T. Abe and Y. Kasiwaba *Sol. Energy Mater. Sol. Cells (in press)*
- [81] J. Herrero and J. Ortega *Sol. Energy Mater.* **16** (1987) 477
- [82] T. Ohtsuka, K. Nakanishi, T. Okamoto, A. Yamada, M. Konagai and U. Jahn *Jpn. J. Appl. Phys. Part I* **40** (2001) 509
- [83] C. H. de Groot and J. Moodera *J. Appl. Phys.* **89** (2001) 4336
- [84] K. Bindu, C. Sudha Kartha, K. P. Vijayakumar, T. Abe and Y. Kashiwaba *Appl. Surf. Sci.* **191** (2002) 138

- [85] G. Gordilla and C. Calderon *Sol. Energy Mater. Sol. Cells* **77** (2003) 163
- [86] K. Bindu *PhD Thesis*, Cochin University of Science and Technology, Kochi, India (2002)
- [87] Y. Natsume, H. Sakata, T. Hirayama and H. Yanagita *Phys. Stat. Sol (a)* **148** (1995) 485
- [88] P. M. Ratheesh Kumar, C. Sudha Kartha, K. P. Vijayakumar, F. Singh, D. K. Avasthi, Y. Kashiwaba, T. Abe, G. S. Okram, M. Kumar and S. Kumar *J. Appl. Phys.* **97** (2005) 13509
- [89] V. Gupta and A. Mansingh *J. Appl. Phys.* **80** (1996) 1063
- [90] V. Srikant and D. R. Clarke *J. Appl. Phys.* **81** (1997) 6357
- [91] Y. Hagiwara, T. Nakada and A. Kunioka *Sol. Energy Mater. Sol. Cells* **67** (2001) 267
- [92] R. Bayon, C. Guillen, M. A. Martinez, M. T. Gutierrez and J. Herrero *J. Electrochem. Soc.* **145** (1998) 2775
- [93] C. H. Huang, S. S. Li, W. N. Shafarman, C. H. Chang, E. S. Lambers, L. Rieth, J. W. Johnson, S. Kim, B. J. Stanbery, T. J. Anderson and P. H. Holloway *Sol. Energy Mater. Sol. Cells* **69** (2001) 131
- [94] D. Hariskos, M. Ruckh, U. Rühle, T. Walter, H. W. Schock, J. Hedstrom and L. Stolt *Sol. Energy Mater. Sol. Cells* **41/42** (1996) 345
- [95] G. Gordillo, G. Cediél, L. M. Caicedo, I. I. Infante and J. Sandino *Proc. 28th IEEE Photovoltaic Specialists Conference* (2000) 614
- [96] C. H. Huang, S. L. Sheng, L. Rieth, A. Halani, M. L. Fisher, J. Song, T. J. Anderson and P. H. Holloway *Proc. 28th IEEE Photovoltaic Specialists Conference* (2000) 696
- [97] A. Shimizu, S. Chaisitsak, T. Sugiyama, A. Yamada and M. Konagai *Thin Solid Films* **361-362** (2000) 193
- [98] L. Amalraj, C. Sanjeeviraja and M. Jayachandran *J. Cryst. Growth* **234** (2002) 683

- [99] S. B. Qadr, H. Kim, H. R. Khan, A. Piqué, J. S. Horwitz, D. Chrisey, W. J. Kim and E. F. Skelton *Thin Solid Films* **377-378** (1) (2000) 750
- [100] K. Kushiya, S. Kuriyagawa, I. Hara, Y. Nagoya, M. Tachiyuki and Y. Fujiwara *Proc. 29th IEEE Photovoltaic Specialists Conference* (2002) 579
- [101] T. L. Chu, S. S. Chu, G. Chen, J. Britt, C. Ferekides and C. Q. Wu *J. Appl. Phys.* **71** (1992) 3865
- [102] S. Y. Yin, A. L. Fahrenbruch and R. H. Bube *J. Appl. Phys.* **49** (1978) 1294
- [103] X. Wu, R. G. Dhere, Y. Yan, M. J. Romeo, Y. Zhang, J. Zhou, C. De Hart, A. Duda and C. Perkins *Proc. 29th IEEE Photovoltaic Specialists Conference* (2002) 531

Chapter 2

REVIEW ON In_2S_3 AND CuInS_2 THIN FILMS

2.1 Introduction

In_2S_3 is one of the numerous compounds in the In-S phase system [1]. Three well defined modifications of In_2S_3 have been reported in the literature. The cubic α -form [2] is stable above 693 K and crystallizes in the defect spinel structure ($a = 10.77$ Å). The stable room temperature phase is β - In_2S_3 [3]. A third modification (γ - In_2S_3) with trigonal symmetry has been reported above 1047 K [4].

It belongs to the III-VI compounds, is a wide band gap semiconductor with high photoconductive and luminescent properties. Thus the material finds its application as buffer layer in solar cells. Eventhough CdS is very efficient in achieving promising cells, it is undesirable from the point of view of environmental safety. Moreover a wider band gap material than CdS can reduce optical absorption losses at short wavelengths.

CuInS_2 belongs to the group of I-III-VI₂ compounds, which are probably the most interesting ternary members in the tetrahedral family. These compounds usually have chalcopyrite structure [5]. It is the simplest, noncubic ternary analogue of the well-understood binary zinc blende structure, with c/a ratio approximately equal to two. CuInS_2 in particular, having an optimum band gap of 1.5 eV and high absorption coefficient, is a potential candidate as absorber layer in solar cells.

Some of the works done earlier on these materials and on solar cells based on CuInS_2 are described in this chapter.

2.2 In_2S_3 Thin Films

The physical properties and structure of indium sulfide [Fig. 1] thin films are given below. Indium atoms are in red colour and sulfur in blue colour.

Structure : Tetragonal

Colour	: Yellow
Appearance	: Crystalline solid
Melting Point	: 1050°C
Density	: 4450 kg/m ³
Lattice Parameters	: a = b = 7.619 Å and c = 32.329 Å

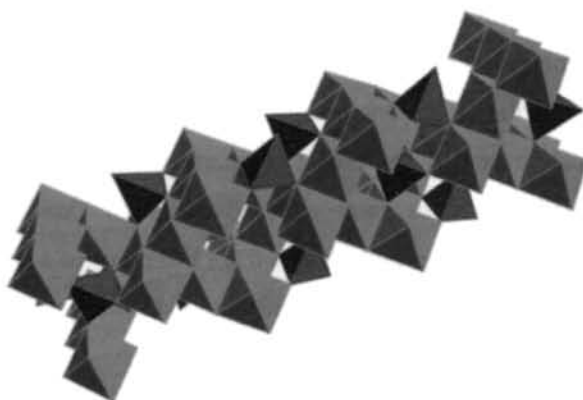


Fig. 1 Crystal structure of In_2S_3

The crystal structure of indium sulfide had been studied by Hahn et al [2] who ascribed to it the cubic structure of a disordered cation deficient spinel. C. J. X Rooymans [3] found that some “extra lines” in the X-Ray diagram were conclusive evidence indicating that In_2S_3 was in fact tetragonal. The tetragonal unit cell was formed by the superposition of three spinel blocks, a four-fold screw axis appeared as the result of indium vacancy ordering.

2.2.1 Preparation Techniques

Variety of preparation techniques were reported for this material and some of them are discussed below.

Thin films of In_2S_3 were prepared by chemical precipitation onto glass substrates by Kitaev and Dvounin [6]. These films were amorphous regardless of their thickness (150 to 400 nm) and crystallized when heated to 773 K in vacuum.

Use of single source evaporation for the deposition of compound semiconductor films often leads to highly non-stoichiometric films. This was because of the decomposition of the solid when heated in vacuum and of preferential evaporation of the components. To avoid these difficulties indium sulfide was deposited by reactive evaporation of indium in a sulfur atmosphere by George et al [7]. They used a glass crucible placed in a canonical basket of molybdenum wire to evaporate sulfur and a molybdenum boat to evaporate indium. The substrate (micro glass slides) temperature was varied between room temperature and 600 K. The source to substrate distance was 15 cm and the deposition rate was around 20 to 30 nm/min. Films showed β - In_2S_3 phase. They optimized the substrate temperature to be 425 ± 50 K ie, the films were smoother, had good transmission and the refractive index approached the bulk value at this temperature. They found that this was in good agreement with the concept of critical optimization of Vincett [8]. He concluded from many experimental results that, when the substrate temperature approached about 0.33 of the boiling point of the material, the film qualities (surface smoothness, optical transmission, carrier mobility etc) improved considerably. Also the bulk diffusion was large at these temperatures, which helped the filling of gaps created by the evaporation of amorphous or disordered materials.

In_2S_3 crystals were grown by direct melting of stoichiometric mixtures of the components [9]. Stoichiometric quantities of high purity indium and sulfur were reacted in evacuated double-wall sealed silica tubes. Temperature of the furnace was raised to 800°C in first step and then up to 1150°C. The molten mixtures were held at this temperature for three days under occasional stirring for homogenization. The samples were then let to cool to about 10 K below the melting point (1050°C) and

were kept at this temperature for a week. Two methods were used to cool the sample. In the first one, the tube was pulled out of the furnace progressively achieving a cooling rate of 0.5 K/h. Large surfaces of ordered crystals were obtained in this way. The second method of sample preparation consisted of rapid quenching of the ingot into ice water. Disordered crystals with random distribution of cation vacancies were produced by this procedure. Annealing in vacuum to avoid oxidation was performed for duration of three months at 400°C just below the transformation temperature (420°C) between α and β - In_2S_3 modifications.

N. Barreau et al compared the properties of indium sulfide thin films prepared using Chemical Bath Deposition (CBD) and Physical Vacuum Deposition (PVD) and the influence of the synthesis conditions on the physico-chemical, optical and electrical properties were discussed [10]. In CBD, the deposition took place in aqueous solution containing indium chloride (InCl_3) and thioacetamide (CH_3CSNH_2). Temperature of the bath was 345 K. The substrates were immersed vertically in the stirred solution. In PVD the deposition of the constituents was carried out by vacuum thermal evaporation at a pressure of 5×10^{-4} Pa with the purities of indium and sulfur maintained at 99.99 and 99.98% respectively. In order to obtain films this indium and sulfur layers were sequentially deposited, their thickness and evaporation rate being controlled in situ by an rf quartz monitor. The S/In ratio was ≥ 3 . Structure obtained from this process were then annealed in a tubular oven for 30 min under a constant argon flow of 0.6 dm^3/min . They studied films annealed at five different temperatures 523, 573, 623, 673 and 723 K. The threshold temperature was found to be 623 K. Above this temperature, the films were wholly crystallized. From the XPS analysis they found that, for PVD deposited films, there was partial bond formation between In and S even before annealing. Film after annealing contained oxygen and Na in the bulk while there was no such contamination before annealing. However the films were amorphous, with large amount of excess sulfur. Best β - In_2S_3 thin films were obtained

with a heat treatment at 673 K. They had the same crystallization as those annealed at 723 K and they were lightly contaminated as those obtained at 623 K. The CBD films were sulfur deficient and there was more oxygen than sulfur in the film with the oxygen compensating sulfur deficiency. The major difference between the two kinds of films was in their crystalline properties. The crystalline property of PVD film was far better than that of CBD.

Indium monosulfide (InS) thin films were prepared by thermal evaporation onto quartz and glass substrates held at 473 K during deposition process by Seyam [11]. The deposition rate was held at 10 nm/sec keeping the pressure at 10^{-6} Torr. InS granules (99.999% pure) were allowed to evaporate. The films obtained were amorphous, and stoichiometric.

Nanocrystalline In_2S_3 modified In_2O_3 electrodes were prepared with sulfidation of In_2O_3 thin film electrodes under H_2S atmosphere by Hara et al [12]. The aqueous slurry of In_2O_3 was prepared from 2 g of commercial In_2O_3 powder, 10 μl of acetylacetone, 50 μl of Triton X-100 (as a surfactant) and distilled water (4 ml). This slurry was deposited on a fluorine doped SnO_2 transparent conducting glass using a scotch tape as the spacer with doctor blade painting and calcinated at 500°C for 1 hour under air. The In_2O_3 thin films were treated under H_2S at $200\text{-}300^\circ\text{C}$ for 10-30 min, resulting in the formation of an $\text{In}_2\text{S}_3/\text{In}_2\text{O}_3$ thin film electrode.

Herrero et al prepared thin films by chalcogenisation of electroplated metallic indium films onto Ti substrates in a flowing stream of H_2S at about 350°C for 1 hour with a pretreatment of 3 hour at 130°C [13]. X-ray diffraction patterns showed that $\beta\text{-In}_2\text{S}_3$ thin films were grown with good crystallinity. This material in a photoelectrochemical cell with polysulfide solution showed low dark current, a noticeable photocurrent characteristic of n-type semiconductors. Photostability tests of the semiconductor in aqueous polysulfide showed that it was photodegraded, and from

the band scheme of In_2S_3 it was inferred that the photocorrosion was a kinetic process and that its stability in this electrolyte was, at least thermodynamically possible.

Thin films of In_2S_3 were deposited on soda lime glass and SnO_2 coated glass using indium acetyl acetonate ($\text{In}(\text{acac})_3$) and H_2S precursors by atomic layer deposition (ALD), a sequential deposition technique allowing the formation of dense and homogeneous films [14]. ALD is based on alternate saturative surface reactions. Each precursor is pulsed into the reaction chamber alternately, one at a time, and the pulses are separated by inert gas purging periods. With properly chosen growth conditions, the reactions are surface saturated and the film growth is thereby self limiting. In that case, each ALD cycle deposits maximum one monolayer of the desired material. However the amount of material deposited per cycle depends on the temperature, precursor combination and the reactive sites on the surface and therefore only rarely is a full monolayer growth per cycle obtained. The required thickness can be obtained simply by repeating these ALD cycles. The precursors must be volatile and thermally stable up to the reaction temperature. They should chemisorb on the surface and react rapidly at the adsorbed state with the other precursors. To obtain In_2S_3 , the pulsing orders were

1. indium acetyl acetonate 0.7 s
2. nitrogen (purge 1) 1 s
3. hydrogen sulfide 0.5 s
4. nitrogen (purge 2) 0.8 s

The surface chemical reactions were

Step 1 Indium pulse



Step 2 Sulfur pulse



In a temperature window between 130 and 260°C, a maximum growth rate of about 0.7 Å per cycle was obtained at 180°C.

Yousfi et al [15] also employed Atomic Layer Deposition (ALD) for depositing In_2S_3 thin films. Depositions were carried out in an ALD machine. Indium sulfide layers were prepared from indium acetylacetonate at 130°C and hydrogen sulfide. Deposition temperature was approximately $150\text{-}160^\circ\text{C}$. The purging gas was nitrogen with 300/500/300/500 ms. Composition measurements were made by RBS on film deposited on silicon substrates. The In/S ratio was found to be 0.66 indicating the film to be In_2S_3 . As the composition of the films did not change with annealing, they related the high band gap value to structural effects like quantum size effects.

R. Bayón et al used the simple and low cost CBD technique for the preparation of indium hydroxy sulfide films [16]. Thin films of $In(OH)_xS_y$ were prepared from an acidic bath ($\text{pH} = 2.2\text{-}2.5$) containing indium (III) chloride, acetic acid (AcOH) and thioacetamide (TA). Indium (III) chloride concentration was kept constant (0.025 M) [TA] was varied from 0.05 M to 0.5 M and [AcOH] from 0 M to 0.3 M being the bath temperature 70°C . The formation of In_2S_3 films was based on the slow release of In^{3+} and S^{2-} ions in an acidic medium and their subsequent condensation on the substrates when the ionic product exceeded the solubility product. Sulfide ions were provided by the hydrogen sulfide produced during the thioacetamide hydrolysis in dilute acid solutions. Finally the hydrogen sulfide was dissociated to give rise the sulfide ions needed for the In_2S_3 precipitation. Acetic acid was added to the reaction mixture either to reduce the pH, which would favour the TA hydrolysis and avoid the formation of hydrolysed species, or to complex the In^{3+} ions. The thickness of the films was 1800 Å after deposition of about 45 min. From XPS characterization they proved that the films were mainly composed by indium hydroxyl sulfide, indium oxide and indium sulfate having absorbed on the surface, some contaminant species from the solution and also CO_2 from air. Samples annealed in air were found to have greater oxygen concentration. The non-annealed samples had more than 80% indium hydroxy sulfide in their composition. The molecular formula of the as deposited film was close to $In(OH)S$.

Growth of indium sulfide by deposition of indium onto MoS_2 surface was studied [17]. Topotactical growth of indium sulfide at the initial stages of the film growth had been observed. From the electron microscopic images of the film, it was found that by the increment of In_2S_3 particle size, InS was also produced. On increasing the film thickness to more than 20 nm indium crystals predominantly grew.

Kaito et al [18] prepared single crystals of β - In_2S_3 by the reaction of indium metal and sulfur vapour. Sulfur vapour was obtained by evaporating sulfur powder from a quartz boat. Indium was evaporated from a nichrom boat. β - In_2S_3 particles grew as single crystal octahedra.

In_2S_3 crystals of α , β and γ form were synthesized by Diehl et al [19]. Ampoule was charged with elements of indium and sulfur in quantities corresponding to the stoichiometric composition. They found that growth temperature of 800°C and sulfur vapour pressure of 4 atm were required to prevent dissociation of In_2S_3 and to maintain stoichiometry. This was achieved by adding 80 mg of extra sulfur in a volume of 25 cm^3 . Iodine was used as the transport agent.

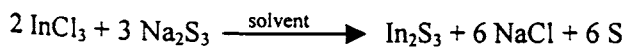
β - $\text{In}_2\text{S}_{3-3x}\text{O}_{3x}$ thin films were prepared using a dry physical process on glass substrate [20]. The temperature during the synthesis process was 473 K. Na free substrates were used to avoid diffusion of Na. They found that the films were smooth, continuous and homogeneous from SEM analysis and the grain size was 50 nm as obtained from AFM.

Temperature of the bath and the concentration of the reactants were important parameters for films deposited using CBD. In_2S_3 thin films were successfully deposited using CBD technique by Lokhande et al [21]. The chemicals used were indium sulfate ($\text{In}_2(\text{SO}_4)_3$), 80% hydrazine hydrate, thioacetamide, triethanolamine (TEA) and ammonium chloride (NH_4Cl). For the deposition of In_2S_3 thin films 10 ml of indium sulfate solution was taken in a glass vessel to which 1 ml of 7.4 M TEA and 10 ml of NH_4Cl solutions were added successively. Under continuous stirring, 0.2 ml

of hydrazine hydrate (80%) was mixed and the reactant vessel was kept in a constant temperature water bath ($\pm 0.5^\circ\text{C}$). When the appropriate temperature (25 to 70°C) was attained 10 ml of thioacetamide solution was added to the bath. The resultant solution was transparent. The solution was stirred with a magnetic stirrer for a few seconds and cleaned glass substrates were immersed vertically. The solution colour change to lemon yellow and finally to bright yellow. The presence of $\text{In}(\text{OH})_3$ in the deposition bath was unavoidable due to the aqueous nature of the bath. For In_2S_3 films the concentration of the reactants taken in the solution were 0.1 M indium sulfate, 0.5 M thioacetamide, 1.4 M NH_4Cl , 14.7 M TEA and 80% hydrazine hydrate. Temperature increase favored homogeneous precipitation, but lower film thickness. Samples deposited on FTO (F doped tin oxide) exhibited better crystallinity. Presence of oxygen in the film had been detected using RBS.

Bulk indium sulfide was prepared by passing H_2S gas through a solution of indium chloride in water [22]. The precipitate, orange in colour, was washed several times with distilled water and then dried in a desiccator. The powder thus formed was then vacuum deposited on different faces of rocksalt, on the cleavage face of mica, polycrystalline NaCl tablets and also on the glass substrates at temperatures varying from 25 to 450°C . X-ray diffraction showed that the material consisted of predominantly α phase of In_2S_3 mixed with little amount of β phase. The deposits were of β variety at high temperatures.

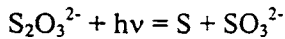
Uniform nanocrystalline $\beta\text{-In}_2\text{S}_3$ powders were prepared using organothermal synthesis by S. H. Yu et al [23]. The reaction was



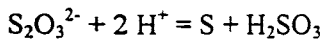
This was conducted in a glovebox filled with argon gas. Toluene and 1, 2-dimethoxy ethane (DME) were used as solvents. An appropriate amount of analytical grade InCl_3 and 0.01M of Na_2S_3 were added into a teflon-lined autoclave of 100 ml capacity, which was filled with organic solvent upto 80% of the total volume. The air dissolved

in the solution was driven off by passing argon gas through it. The autoclave was sealed and maintained at 140°C for 12 hour and cooled to room temperature naturally. The yellow precipitate was filtered and washed respectively with CS_2 , acetone, distilled water and absolute ethanol several times to remove the byproducts of S, NaCl and other impurities. The product was then dried under vacuum at 80°C for 4 hours. The broad nature of diffraction peaks indicated formation of nanocrystalline β - In_2S_3 . They found that the particle size of nanocrystalline β - In_2S_3 could be controlled by choosing different solvents. Particle size in Toluene was smaller than that in DME (8 and 16 nm respectively). They also studied the influence of water content, organothermal time and temperature on the samples. No evidence for organic impurities in the samples was obtained from IR spectrum.

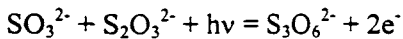
Kumaresan et al deposited indium sulfide thin films by photochemical deposition technique (PCD) [24]. The $S_2O_3^{2-}$ ions present in the solution absorb UV radiation and release S according to the following equation



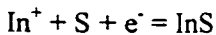
This spontaneous release of S in a more acidic medium takes place according to the equation



Also the $S_2O_3^{2-}$ ions get excited by absorbing the UV radiation and release electrons according to the equations



The sulfur atoms and electrons combine with the In^+ metal ions present in the solution of $In_2(SO_4)_3$ to form InS according to the relation



The as deposited InS films were amorphous in nature and phase transition to crystalline In_2S_3 occurred upon annealing at 500°C. Raman analysis of the as deposited

film confirmed the formation of In-S phase. The films had 3 μm thickness over a deposition period of 90 min. Thickness decreased to 1 μm upon annealing at 500°C. Presence of oxygen in the film was detected by AES analysis and the sulfur to oxygen ratio was 6:1. Even after annealing at 500°C oxygen was present in the film and there was a possibility for the formation of $\text{In}_2\text{S}_{3-3x}\text{O}_{3x}$ and the S to O ratio was about 9:1. The as deposited films did not show a clear absorption edge, possibly because of the amorphous nature of the film, while upon annealing sample show clear absorption edge. Annealed samples exhibited a direct band gap of 2.1 eV.

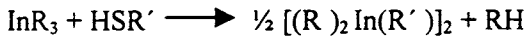
Indium sulfide thin films were deposited using CBD technique from aqueous solution containing InCl_3 and thioacetamide [25]. The pH of the fresh solution was 3.1 and it could be adjusted by adding HCl to the reaction bath. Temperature of the bath was 50-90°C and the reaction time was varied between 5 and 600 min to achieve required film thickness. The deposits consisted of nano-sized particles of $\beta\text{-In}_2\text{S}_3$ or its mixture with $\alpha\text{-In}_2\text{S}_3$ as found by crystallographic study and TEM. The EDAX and XPS analysis revealed the presence of excess sulfur in the film.

A new approach for the electrosynthesis of indium sulfide thin films (In_2S_3) was described by Tacconi et al [26]. Electrosynthesis using a sulfur modified gold electrode and alternative exposure to indium and sulfur ion containing aqueous bath consisted of four steps (a) A polycrystalline gold surface was first modified with a sulfur layer (b) indium was placed onto this layer forming indium sulfide (c) indium continues to deposit atop the indium sulfide layer (d) transfer back to a sulfide ion containing bath resulted in the sulfidization of the residual indium sites. $\text{In}_2(\text{SO}_4)_3$ was used as the indium containing electrolyte and Na_2SO_4 as sulfur containing medium. Raman active modes present at 235, 268 and 309 cm^{-1} indicated presence of the $\beta\text{-In}_2\text{S}_3$ defect spinel structure.

Asikainen et al described the growth of In_2S_3 thin films by Atomic Layer Epitaxy (ALE) [27]. InCl_3 and H_2S were employed as the reactants. Nitrogen was

used as a carrier and purging gas. The reactor pressure was about 10 mbar. $InCl_3$ was evaporated inside the reactor from a crucible held at 275°C. H_2S flow rate was 9 cm^3/min . The films were deposited on glass substrates at 300-400°C. The films were cooled to about 200°C under nitrogen flow before removing from the reactor. The highest growth rate obtained was 1.4 Å/cycle at 300°C. The resulting films were polycrystalline β - In_2S_3 . SEM analysis showed that the film consisted of densely packed particles with a diameter of about 100-150 nm. RBS analysis revealed the composition of the film grown at 300°C as $In_{0.40}S_{0.57}Cl_{0.03}$.

Indium sulfide films were prepared using MOCVD by Barron [28]. The majority of studies have employed the thiolate compounds prepared from the parent trialkyl indium:



Films grown using either $[('Bu)_2 In(S' Bu)]_2$ or $[(^nBu)_2 In(S' Bu)]_2$ as the precursor at each of the temperatures 300, 350 and 400°C were essentially independent of the precursor in terms of morphology and phase present. The microstructural features and chemical composition of the deposited films were, however, observed to have significant dependence on the deposition temperature. Films deposited from methyl substituted precursor $[(Me)_2 In(S' Bu)]_2$ showed marked difference from those grown using either $[('Bu)_2 In(S' Bu)]_2$ or $[(^nBu)_2 In(S' Bu)]_2$. Films deposited from the methyl precursor at 400°C yielded a crystalline diffraction pattern In_2S_3 .

Stoichiometric thin films of In_2S_3 were prepared by thermal evaporation technique for the first time by Shazly et al [29]. The as deposited films were amorphous and crystallinity was built in on annealing at 423 K. The crystal structure, as determined by both x-ray and electron diffraction showed that tetragonal films of β - In_2S_3 phase were obtained. The degree of crystallinity was found to increase with increasing either the film thickness or the annealing temperature.

A novel layered indium sulfide material consisting of corner and edge shared InS_4 tetrahedra was synthesized under solvothermal conditions by Cahill et al [30]. The synthesis of DPA-InS-SB₃ was synthesized by reacting elemental In and elemental S with the organic structure directing agent dipropylamine in the approximate molar ratio 1:2.3:3.5. Reactant slurries were sealed in pyrex tubes and held static at 180°C under autogenous pressures for five days. The resultant product, a white powder, was then washed with ethanol and water and allowed to dry in air. Large single crystals upto 0.2 mm on edge were obtained. Qualitative electron probe microanalysis revealed the presence of In, S and N. The In-S bond lengths range from 2.42 to 2.534 Å with an average of 2.432 Å.

β - In_2S_3 powder with particles having an average size of 13 nm and spherical shape was successfully prepared through the hydrothermal treatment of an acidic sol (pH = 3) from indium trichloride and sodium sulfide at 140°C [31]. Hydrothermal treatment of an alkaline sol gave amorphous In_2S_3 powder. The effects of temperature, time and the pH value of the sol on the formation of nanocrystalline β - In_2S_3 powders were investigated. The results showed that hydrothermal treatment of an acidic sol (pH = 3) at 140°C for 6 to 12 h was the optimum condition for crystallization of amorphous In_2S_3 .

In_2S_3 films were grown using indium (III) isopropyl xanthate, $\text{In}(\text{S}_2\text{COC}_3\text{H}_7\text{-iso})_3$, a readily available chelate, which volatilized when heated in vacuum and yielded β - In_2S_3 when thermally decomposed in an inert atmosphere [32]. The resistivity of In_2S_3 films (~ 200 nm thick) increased from 10^{-1} to $5 \times 10^2 \Omega\text{-cm}$ as the deposition temperature was raised from 230 to 450°C. It was suggested that the lower resistivity of films deposited at lower temperatures might be due to a higher degree of disordering in the structure of In_2S_3 . Analysis of film composition using AES revealed presence of In, S and O. The average ratios were $I_S/I_{\text{In}} = 3$ and $I_O/I_{\text{In}} = 0.55$. Triangular

features were seen from SEM analysis, which were indicative of film growth along (111) direction.

Chemical bath Deposition of indium sulfide thin films from aqueous mixtures containing indium chloride and thioacetamide under the two extreme reaction conditions 30 and 70°C was examined by Yamaguchi et al [33]. X-ray analysis of the films indicated the formation of amorphous indium hydroxysulfide in the early stage, followed by the formation of nanocrystalline indium sulfide in the late stage of the film growth. The films deposited at 30°C had a cauli-flower like morphology, whereas the fibrous structure was obtained at 70°C.

Indium sulfide thin films had been prepared by a novel modulated flux deposition technique [34]. Experimental parameters were adjusted to obtain high band gap and low absorption material at low deposition temperature as required for photovoltaic applications. Films were deposited in a home-made evaporation chamber containing a rotating holder that transported standard soda-lime glass substrates cyclically around three different areas: indium source beam, heating lamps and reactive sulfur region. The parameters that had been controlled in the film deposition were the evaporation source temperatures, the substrate temperature and the angular velocity of the rotating substrate holder. Substrates were rotated at 30 rev/min and maintained at 200°C. Samples showed tetragonal β - In_2S_3 phase. The layer thickness did not affect the crystalline phase, but influenced the average crystallite size.

Successive Ionic Layer Adsorption and Reaction (SILAR) technique was used by Sankapal et al to deposit indium sulfide thin films [35]. This was achieved using indium sulfate ($In_2(SO_4)_3$) and thioacetamide solutions. The temperature of deposition was 25-70°C and the deposition time was 4-5 hours. The films were 0.2 μm thick. Films deposited on glass substrates showed poor crystallinity, but on FTO samples were crystalline. TEM analysis revealed that the initial growth of film on glass

substrate was the γ phase of In_2S_3 with particle size ranging from 20 - 40 Å. Presence of oxygen was detected by RBS analysis.

A novel in situ oxidation-sulfidation growth route via a self purification process was developed to synthesize β - In_2S_3 dendrites by Xiong et al [36]. The precursor of InSb dendrites was firstly obtained by a sonochemical coreduction route. In subsequent , the mixtures of InSb dendrites (0.473 g, 2 mmol), CS_2 (0.18 mL, 3 mmol), NaOH (0.72 g, 18 mmol) and 30% H_2O_2 (0.60 mL, 6 mmol) were loaded into a 50 mL teflon-lined autoclave, which was then filled with distilled water upto 90% of the total volume. The autoclave was sealed and maintained at 180°C for 24 h and was then cooled to room temperature naturally. The precipitate was filtered off, washed with distilled water and absolute ethanol for several times, and then dried in vacuum at 60°C for 4 h. The product obtained was pure In_2S_3 .

2.2.1.1 In_2S_3 Using Chemical Spray Pyrolysis (CSP)

Chemical Spray Pyrolysis is a simple and low cost method for the fabrication of In_2S_3 thin films. Review of the earlier works done on indium sulfide films prepared using spray technique is given below.

Bhira et al prepared In_2S_3 thin films using spray pyrolysis technique. Films were deposited on pyrex glass by spraying a solution of 10^{-3} M indium chloride and 2×10^{-3} M thiourea [37]. The substrate temperature was kept at 340°C. They used nitrogen as carrier gas keeping the solution and gas flow rates at 2 cm^3/min and 4 l/min . Well crystallized films showed β - In_2S_3 phase with preferential orientation along (400) plane. Microanalysis of the films pointed out a deficit of chalcogen (46%) and from XPS analysis they confirmed that this deficit was compensated by oxygen bonded to indium in addition to that as a surface contaminant. They detected traces of chlorine also in the bulk of the sample. Photoconductivity measurements were carried out within the range of wavelengths in the visible spectrum at different modulation frequencies and bias voltages ranging from 5 to 300 Hz and from 3 to 25 V

respectively. They observed a fast increase of photocurrent signal toward 2 eV connected with a progressive decrease in the high absorption region. They attributed this to the presence of trap centers at the grain boundaries or to the presence of structural defects or secondary phases in the film. The response increased with increase in illumination time and bias voltage. They found out the mean absorption edge from the photocurrent measurements using Devore's model [38]. The band gap value (2.05 eV) was found to be in close agreement with that obtained from optical absorption measurements (2.08 eV).

Optical properties using transmittance and reflectance measurements of InS films with composition close to that of In_2S_3 , prepared using airless spray technique was studied by Kamoun et al [39]. Samples were prepared with different In/S ratio. They observed a broadening and/or shift of the short wavelength absorption edge for smaller In/S values which was ascribed to the presence of secondary phases and to a more disordered structure. They performed spectroscopic ellipsometric measurements over the 0.5 to 4 eV spectral ranges. It was found that the refractive index (n) and absorption coefficient (α) decreased with increase in In/S value. Annealing of the films at high temperature (500°C) induced a strong decrease in the value of both n and α which was explained by an improvement in sample crystallinity, while annealing at rather low temperatures (300°C) has little effect on the optical constants.

Energy band gap of In_2S_x thin films grown using spray solution composition from $x = 2.0$ to $x = 3.9$ was studied by Kim et al [40]. Films showed β - In_2S_3 phase with tetragonal structure. They found that the band gap increased from 2.15 eV to 2.43 eV on increasing the x composition.

The effect of substrate temperature on structural and morphological properties of indium sulfide films deposited on glass substrate by spray method was studied by Bouguila et al [41]. In_2S_3 was formed from the chemical reaction

$$2\text{InCl}_3 + 3 \text{CS}(\text{NH}_2)_2 + 6 \text{H}_2\text{O} \longrightarrow \text{In}_2\text{S}_3 + 3\text{CO}_2 + 6 \text{NH}_4\text{Cl}$$

X-ray diffraction had shown that In_2S_3 was the main phase present in these films and that the structure and the allotropic form of this phase were affected by substrate temperature. Analysis of the layers by SEM and AFM revealed that best crystallinity and homogeneity were obtained for the substrate temperature 613 K.

2.2.2 Optical and Electrical Properties

The first optical measurements of In_2S_3 were reported by Kauer and Rabenau [42]. Investigations by Bube and McCarroll [43] and Gilles [44] et al were mainly concerned with photoconduction in indium sulfide. Garlick et al [45] reported on the IR emission and luminescence properties. Rehwald and Harbeke [46] reported on the electrical and optical properties. All the studies were done on single crystals or polycrystalline bulk materials. For $\beta\text{-In}_2\text{S}_3$ the absorption edge was mainly due to direct transitions [47] and weak indirect transition was also reported [46].

Studies of conduction mechanism in single crystal $\beta\text{-In}_2\text{S}_3$ [46] showed that the conductivity is always n-type and p-type is observed when the samples are doped with copper or cadmium. Becker [48] obtained a p-response when single crystals were prepared with an excess of sulfur or InP, but n- response was also present.

George et al [7] calculated refractive index from the optical transmission spectra of the samples prepared using reactive evaporation of indium in sulfur atmosphere. They used the method given by Manifacier et al [49]. The value was found to be 2.56. Band gap was found to be 2.01 eV corresponding to a direct forbidden transition. They attributed the unresolved absorption peaks just before the onset of band-to-band transition from the plot of α vs $h\nu$ as due to different energy levels (sulfur vacancies) in the forbidden gap to which transition may take place. They also found that films prepared above a substrate temperature of 350 K were low resistive and indium made good ohmic contact to these films while films prepared below this temperature showed high resistivity and indium did not make ohmic

contact to these films. From the temperature dependence of resistance of these films, the activation energy for electronic conduction was obtained as 0.26 ± 0.02 eV.

Temperature dependence of band gap of β - In_2S_3 thin films was studied by Kambas et al [47]. They found that the transition was direct and the E_g dependence on T was linear, band gap increased with decrease in temperature. The value was found to be 2 eV at room temperature.

Gilles et al [44] studied the photoconduction in In_2S_3 prepared by the direct synthesis under a pressure of sulfur of the order of 5 to 10 atmospheres. They found that under an illumination of nearly 1000 lux, the conductivity of this material increased by five orders of magnitude. Traces of copper increased the photosensitivity of the compound markedly. The diffusion length was found to be of the order of few millimeters. They observed a correlation between the reciprocal of the diffusion length and the photosensitivity of copper doped samples: the maximum photocurrent was obtained in samples where the reciprocal of the diffusion length is a maximum. From the thermal analysis, they found two-phase transitions in indium sulfide. The first one was in the temperature range between 414°C and 421°C while the second one was around 738°C . Thermal activation energy was determined from the measurements of resistivity as a function of temperature and was found to be 0.56 eV below first transition point and 0.63 eV above 420°C .

The band gap of PVD β - In_2S_3 films increased with annealing temperature until 623 K, whereas for higher annealing temperature the absorption threshold was stable [10]. Band gap was found to be 2.8 eV to 2.9 eV, which was greater than that of earlier reports. They observed that when oxygen was introduced into the films, the band gap values were far higher than that of the single crystals. The wide band gap of PVD films was attributed to the presence of In-O bonds. The substitution of indium by Na was also found to increase the band gap. When heating rate was increased, the band gap was not as broad, because of the fast crystallization. They found that oxygen

contamination had a positive effect to obtain layers with properties matching well with the specification of solar cell buffer layers.

Indium monosulfide thin films prepared using thermal evaporation by Seyam [11] exhibited absorption coefficient of the order of 10^5 cm^{-1} and the band gap was 1.94 eV. He calculated the refractive index (n) and extinction coefficient (k) from the transmittance and reflectance spectra and the values were estimated to be 2.2 and 2.3 respectively. The high frequency dielectric constant was calculated from the plot of $(n^2-1)^{-1}$ vs λ^{-1} and the value was found to be 5.76. He found that the dark resistivity decreased with increasing temperature and film thickness. Thermal activation energy of the charge carriers, from the electrical resistivity measurements, was found to be 0.84 eV. Density of charge carriers was found to be 10^{21} m^{-3} from the space charge limited current analysis.

Hara et al prepared nano crystalline In_2S_3 modified In_2O_3 electrodes with sulfidation of In_2O_3 thin film electrodes under H_2S atmosphere [12]. Band gap of In_2S_3 estimated from the onset of absorption spectra was 2 eV. This photoelectrochemical cell could convert visible light of 400-700 nm to electrical energy. A highly efficient incident photon to electron conversion efficiency of 33% was obtained at 410 nm. The solar conversion efficiency η , under AM 1.5 was 0.31% with $J_{\text{sc}} = 3.1 \text{ mA/cm}^2$, $V_{\text{oc}} = 0.26 \text{ V}$ and $\text{FF} = 38\%$.

Optical and electrical properties of $\beta\text{-In}_2\text{S}_3$ thin films containing Na ($[\text{In}_{16}\text{O}_h][\text{In}_{5.33-x}\text{Na}_{3x}\text{S}_{2.66-2x}]_{\text{Td}}\text{S}_{32}$) were studied by Barreau et al [50]. Both transmission and reflectivity curves showed interference fringes, which put in evidence for the homogeneity of the morphology of the films. They found that the band gap linearly increased from 2.1 eV (when the films were pure) to 2.95 eV (when their Na content was 8.4 at%). The electronegativity of Na is 0.9 while that of In is 1.7. Therefore when it was substituted for indium, the sodium increased the ionicity of the tetrahedral cationic-sulfur bonds, which could be an explanation of the increase of the optical

band gap. They also suggested that incorporation of Na in the tetrahedral vacant sites, attracted electrons of sulfur inducing an increase of In-S bond length which in turn produced perturbation of the electronic structure of the material resulting in the increase of band gap. All the films had n-type conductivity. Incorporation of Na was found to increase the conductivity of In_2S_3 films. But when the Na content was increased from 0.2 at% to 5 at% the conductivity decreased, while on further increasing (above 6 at%) conductivity drastically increased.

Optical band gap varied from 2.1 eV for pure In_2S_3 to 2.9 eV for samples, which contained 8.5 at% oxygen as reported by Barreau et al [20]. They found that the electronic structure of indium sulfide was very much disturbed due to the presence of even a few oxygen atoms substituted to sulfur in the crystalline matrix, which induced the high increase of optical band gap. The electrical conductivity of the oxygen containing samples was found to be greater by approximately 2 orders than that of pure In_2S_3 films. They attribute this effect to the modification of the properties of the grains or their grain boundaries when oxygen was introduced in the films. The films showed n-type conductivity indicating that the introduction of oxygen did not change the type of majority carriers.

The optical band gap of indium sulfide thin films prepared using CBD technique by Lokhande et al [21] was found to be 2.75 eV. The as prepared samples were photoactive as observed from Time Resolved Microwave Conductivity (TMRC) studies. The same value of band gap was obtained for SILAR samples [35]. Band gap value could be tuned between 2.3 and 2.7 eV by changing the reaction temperature or pH of the aqueous chemical bath as shown by Yoshida et al [25]. Variation of E_g values were discussed in terms of the change of chemical composition, crystal modification and crystal size.

Refractive indices of the films prepared using Atomic Layer Epitaxy were found to be of the order of 2.5-2.7 and the band gap was 2.3 eV [27]. Samples were

highly resistive and they showed photoresponse when exposed to daylight. The photoresponse was reversible and fast.

Both dark electrical resistivity and thermoelectric power (Seebeck coefficient S) were measured for films prepared by thermal evaporation technique, before and after annealing [29]. Dark electrical resistivity decreased exponentially with increasing film thickness. Resistivity decreased after annealing also. Thermoelectric power of all films decreased with increasing the sample temperature. The In_2S_3 films showed n-type conduction. Existence of two distinct activation energies ΔE_1 and ΔE_2 belongs to two types of level: a shallow level of $\Delta E_1 = 0.319$ eV before annealing and $\Delta E_1 = 0.166$ eV after annealing and deep level of $\Delta E_2 = 0.61$ eV for as deposited films and $\Delta E_2 = 0.515$ eV for annealed films. The deep level was also detected by the space charge limited current technique and the trap density was found to be $3.92 \times 10^{22} \text{ m}^{-3}$. The decrease in ΔE_1 for the shallow levels as a result of annealing indicated that these levels were structure defect levels.

The electrical properties of single crystal indium sulfide was studied by Rehwald et al [46]. They showed that the range of electrical resistivity and Hall coefficient at room temperature covered more than six decades. When these parameters were low, it was found that they changed only little with temperature or even remain constant down to liquid nitrogen temperature, where as the very high values had strong dependence on temperature. By heat and sulfur vapour treatment, it was demonstrated that this large variation had its origin in the deviations from stoichiometric composition of the material. The nearly exponential dependence of the measured Hall mobility on temperature, observed in specimens of high resistivity, was explained by different scattering mechanisms for electrons and hole in the same temperature region. All crystals were found to be n-type, regardless of doping during growth. Impurities, which otherwise produce p-type conductivity in similar materials, did not have the effect of changing the sign of charge carriers in In_2S_3 . The main effect on concentration and sign of charge carriers come from the deficiency in sulfur,

which could not be completely avoided during growth. The cation vacancies, forming a constituent of the lattice due to the chemical formula, were assumed to be mainly ordered in indium sulfide. The small fractions of disordered cations and cation vacancies acted as donors and acceptors nearly compensating each other. Their difference in concentration was determined by the lack of sulfur. They also suggested that high resistivity material might be useful as a photoconductor.

Barreau et al studied the optical properties of In_2S_3 thin films grown using PVD [51]. Optical properties of indium sulfide thin film depended on their synthesis process and composition. High homogeneity and excellent surface state of the films were confirmed by the presence of interference fringes on transmission and reflectivity spectra. Band gap was found to be independent of the annealing temperature and the value was about 2.8 eV, higher than that of $\beta\text{-In}_2\text{S}_3$ single crystal, due to the presence of oxygen in the film. The refractive index (n) and the extinction coefficient (k) were also found to be independent of annealing temperature. The values were in the range 2.1- 2.8 and 0.01 – 0.3 for wavelengths in the range 250 nm to 2500 nm.

Absorption onset indicated a band gap value above 2.5 eV for indium sulfide thin films, prepared using a novel modulated flux deposition technique [34]. Energy band gap increased for reduced indium sulfide layer thickness, which was related to a reduction of the average crystallite size of the films.

Thermally stimulated current measurements were carried out on as grown n-InS single crystals having orthorhombic structure in the temperature range 10-125 K by Gasanly et al [52]. They identified four trap levels located at 20, 35, 60 and 130 meV and suggested that these levels in undoped layered crystals might be associated with presence of structural defects and/or unintentional impurities. Trap parameters were determined by curve fitting method, peak shape method and initial rise method and found that they agreed well with each other. The retrapping process was

negligible for these levels, as confirmed by the good agreement between the experimental results and the theoretical predictions of the model that assumed slow retrapping.

Photoluminescence spectra (PL) of InS single crystals were investigated in the wavelength region 477.5-860 nm and in the temperature range 8.5-293 K [53]. They observed three PL bands centered at 605 nm, 626 nm and 820 nm. The first two bands were due to radiative transitions from the donor level at 0.01 eV below the bottom of the conduction band to the valence band and from the donor level at 0.06 eV below the bottom of the conduction band to the acceptor level at 0.12 eV above the top of the valence band respectively.

ALD In_2S_3 thin films, deposited by Yousfi et al [15] were amorphous and the band gap was approximately 3.3 eV which was much greater than that of the bulk value. Band gap reduced to 2.25 eV after annealing while that deposited by Naghavi et al [14] were crystallized in a tetragonal form with band gap values of about 2.7 eV. Quantum size effect was considered as a possible origin for wide band gap. A shift of 0.7 eV was expected for grain size of about 3 nm. Electrical properties had been addressed by using impedance measurements on semiconductor electrolyte junctions. The films were n-type with a doping level around 10^{16} - 10^{17} cm^{-3} and possessed a good blocking behaviour under reverse bias. The doping level increased with increasing the deposition temperature. Their flat band potential was close to -1.1 V versus MSE.

Mane et al deposited indium sulfide thin films by SILAR technique using indium chloride and sodium sulfide as cation and anion source in an aqueous medium [54]. The films were amorphous. The optical band gap was 2.3 eV and the films were highly resistive possessed resistivity of the order of 10^5 Ω -cm.

Fifteen normal modes of vibrations were observed for β - In_2S_3 dendrites from Raman spectra, which correspond exactly to those given by a sample of β - In_2S_3 with unpolarised light [36]. The sample showed strong quantum confinement of excitonic

transition, which was expected for In_2S_3 dendrites. Under PL excitation at 330 nm, the In_2S_3 dendrites emitted blue light at 358 nm, which clearly indicated the existence of electronic transition at particular wavelength (358 nm), and was stronger than in the bulk In_2S_3 .

Some authors attribute the widening of band gap of indium sulfide films to quantum size effect [55] while some authors explained this due to excess sulfur [40]. Recently presence of oxygen and sodium was also reported to increase the band gap markedly [10].

2.2.3 Doping in In_2S_3

$\beta\text{-In}_2\text{S}_3$ and $\beta\text{-In}_2\text{S}_3\text{:Co}^{2+}$ single crystals were produced using chemical transport reaction method employing ZnCl_2+I_2 as a transport agent by Choe et al [56]. For In_2S_3 single crystal, In_2S_3 powder (purity 99.999%), 15 mol% of excess sulfur (purity 99.9999%) and 5 mol% of ZnS (purity 99.9999%) were used as starting materials. For $\beta\text{-In}_2\text{S}_3\text{:Co}^{2+}$ single crystal, 2 mol% of Co (purity 99.99%) was added to the starting materials. Temperatures of the growth and source-zones were maintained at 670°C and 830°C respectively for 7 days. Dimension of the single crystals were approximately 6 x 5 x 3 mm and they crystallized into tetragonal structure. Optical absorption spectra were measured in the temperature range 5 K to 300 K. At 290 K, they obtained an indirect optical energy band gap of 2.24 eV for $\beta\text{-In}_2\text{S}_3$ and 1.814 eV for $\beta\text{-In}_2\text{S}_3\text{:Co}^{2+}$ while the direct energy band gap was 2.639 eV for $\beta\text{-In}_2\text{S}_3$ and 2.175 eV for $\beta\text{-In}_2\text{S}_3\text{:Co}^{2+}$. Three groups of impurity optical absorption peaks for $\beta\text{-In}_2\text{S}_3\text{:Co}^{2+}$ single crystal were observed in the wavelength ranges of 675-830 nm, 1300- 1900 nm and 2800- 3200 nm. These peaks could be attributed to the electron transition between the energy levels of Co^{2+} ions sited in the Td symmetry point.

$\text{CoIn}_2\text{S}_{3+x}$ thin films were grown [57] on thoroughly cleaned glass slides by spraying a solution prepared by dissolving CoCl_2 , InCl_3 and thiourea in solvent solutions composed of methanol and distilled water (ratio of 1:1) to give 0.2 molar

solutions of each solute, and then by mixing these solutions in appropriate volume ratio to give the desired x composition. An additional 20% in volume of thiourea solution compensated for the loss of sulfur caused by vapourisation. Rate of spray was 6 ml/min and the substrate was maintained at 270°C. They found that, β - In_2S_3 thin films were grown over the range $x = 0$ to 0.4 and amorphous thin films over the range 0.6 to 1. Band gap was found to be decreasing with increasing x composition. The samples showed impurity absorption corresponding to wavelengths 695 nm, 750 nm and 802 nm. Intensities of these peaks increased with increasing x composition and they found that the Cobalt atoms in $Co_xIn_2S_{3+x}$ existed as Co^{2+} ions.

Kim et al found that as Cobalt was introduced into In_2S_3 single crystals, the structural defects were decreased [58]. The Cobalt atoms were located at the Td symmetry site of the β - In_2S_3 host lattice as Co^{2+} ion. Three peaks at 752 nm, 802 nm and 825 nm in the absorption spectrum of Co doped crystals were ascribed to Cobalt impurities. The photoacoustic spectrum of β - $In_2S_3:Co^{2+}$ crystal when compared with that of β - In_2S_3 single crystal in the wavelength region 500 to 2500 nm, possessed four peaks at 650, 760, 1700 and 2130 nm. The first peak was ascribed to crystal defect and the rest to Cobalt impurities. Photoconductivity spectra of β - In_2S_3 single crystal at 286 K showed a broad peak centered at 663 nm and a tail in the long wavelength region. As ambient temperature decreased to 28 K, the broad peak also appeared at 626 nm and the tailing phenomenon in the long wavelength region was not reduced. The photoconductivity spectrum of β - $In_2S_3:Co^{2+}$ single crystal at 284 K had two peaks centered at 620 and 705 nm. The long wavelength tail in the spectrum was reduced when compared to that of β - In_2S_3 single crystals. When the temperature was reduced to 21 K, the spectrum showed two peaks at 585 and 655 nm and the tail in the long wavelength region was rapidly reduced.

β - In_2S_3 and β - $In_{2-x}Al_xS_3$ thin films were deposited on different substrates (pyrex glass, SnO_2 /pyrex and steel) using spray pyrolysis technique at 320°C [59]. In

the case of the growth on a steel substrate, the crystallography of the film was good and the introduction of Al did not noticeably change the spectrum. In the case of deposition on pyrex, the structure of $\beta\text{-In}_2\text{S}_3$ was of poor quality. Al improved the crystallinity. On $\text{SnO}_2/\text{pyrex}$ substrate, presence of Al resulted in broader and smaller diffraction peaks. The surface structure was studied using AFM and SEM. Crystallite size increased on going from steel to SnO_2 . For steel substrates, characterized by a poor structural quality and a lattice disorder the impinging atoms strongly interacted with the surface but with little surface migration. The layers were having good stability; Work function and surface photovoltage did not change with time. They used Auger studies to get information on the surface layer composition. They also studied effect of heat treatment and substitution of a few indium atoms by aluminium atoms to this composition. In all the cases the work function topographies were flat and variation of $\Delta\phi$ along the surface were small indicating uniformity of the surface layer of the films.

$\text{In}_{2-2x}\text{Al}_{2x}\text{S}_{3-3y}\text{O}_{3y}$ alloys were prepared on pyrex glass substrates by spray pyrolysis technique and their photoelectrical properties were studied by Bhira et al [60]. The spraying solution contained InCl_3 , AlCl_3 and $\text{CS}(\text{NH}_2)_2$ as starting materials. The Al/In ratio (x) was varied from 0 to 1. Solution and gas flow rates were kept at $2 \text{ cm}^3/\text{min}$ and $4 \text{ l}/\text{min}$ respectively. Nitrogen was used as the carrier gas and the substrate temperature was 340°C . The shape of the photoconductivity spectra $I_{\text{ph}}(h\nu)$ and the variations $I_{\text{ph}}(f)$ and $I_{\text{ph}}(V)$ helped them to understand the conduction mechanism and the photocarrier's recombination. For low compositions ($x \leq 0.2$), $I_{\text{ph}}(V)$ parabolic variation showed that this conduction was limited by the space charge zone in accordance with Child's law ($I_{\text{ph}} \propto V^2$). This showed that the density of trap centers increased with the composition. With increased Al doping, the photoconductivity measurements depended on the photo carrier recombination mechanism due to the presence of trap centers at grain boundaries. For $x \geq 0.4$, the

electrical conduction followed Ohm's law. Band gap showed a parabolic profile with x , varied in the range from 2.05 to 2.42 eV. For low compositions ($x = 0, 0.05, 0.1, 0.2$) the conductivity study as a function of temperature presented a deviation to Arrhenius law in the temperature domain 80 to 330 K. At very high temperatures, ranging from 330 to 575 K, a quasi-linear variation of σ as a function of temperature according to Arrhenius law was observed. They found that for higher Al compositions, films were amorphous having poor electrical and photoelectrical properties.

A variety of differently doped samples of In_2S_3 were prepared by chemical vapor phase transport (CVT) and gradient freeze techniques by Becker et al [48]. For CVT, I_2 was used as the transport agent. X-ray diffraction of pure, tin doped, samples with excess sulfur and those with P and InP doping were shown to be single-phase β - In_2S_3 . They found that if a sample with excess sulfur having n- and p-type responses was heated at 750°C for 0.5 hour, the resistivity dropped by ~ 5 orders of magnitude and the n- and p-type responses were replaced by solely an n-type response. The result was explained by the removal of S giving excess interstitial In donors. Doping of phosphorous and indium phosphide resulted in a weak p- response but n-response was also present. In the case of Sn doping, low resistance n-type material resulted. Whether this was due to true Sn^{4+} substitution for In^{3+} or whether Sn disrupted the lattice order such that the concentration of interstitial In was greater than In vacancies was not known.

Kulińska et al prepared $\text{Li}_x\text{In}_2\text{S}_3$ electrochemically with different amounts of Lithium ($0 \leq x \leq 0.13$) [61]. They applied Perturbed Angular Correlation (PAC) to understand the mechanisms that occur during Li insertion. PAC experiments could measure the hyperfine interaction between a radioactive probe and the Electric Field Gradient (EFG) generated by direct neighborhood at the site of the probe atom. At lower temperatures undoped material showed a strong damping of the PAC spectra

while after doping (with electron donor Li) the higher concentration of mobile charge carriers repaired this damping. PAC spectra showed a new dynamic behavior, which increased with increasing Li content. They proposed that for higher temperatures ($T \geq 500$ K) migration of indium atoms from the tetrahedral site started and this was favored by the presence of empty sites in the direct neighborhood of a tetrahedral site, in contrast to the octahedral sites. They also proposed that the Li insertion lowered the threshold which confined the indium ions to the tetrahedral sites. The dynamic behavior between room temperature and 500 K was caused by the mobile Li ions, because the dynamic fraction was proportional to the Li content.

2.2.4 Different Studies on In_2S_3

IR reflectivity of In_2S_3 crystals were studied and higher reflectivity was observed for quenched sample at low frequencies [9]. The peaks for the annealed samples were sharper and well resolved. They obtained 12 reflectivity bands for polarized light having $E \perp c$ case and eight bands for $E \parallel c$ case.

Amlouk et al [62] showed that acoustic techniques, more specifically acoustic signature $V(z)$, are very powerful non destructive methods to characterize $\beta\text{-In}_2\text{S}_3$ thin films prepared using CSP technique. Young's modulus of the order of 443 GPa, was consistent with the assumption of the $\beta\text{-In}_2\text{S}_3$ material to be in ceramics group. Acoustic microscopy study revealed the possibility of presence of surface and bulk defects in this thin film.

Temperature dependence of Raman-active mode frequencies in indium sulfide was measured in the range from 10 to 300 K [63]. InS polycrystals were synthesized from particular high purity elements taken in stoichiometric proportions. Single crystals of InS were grown by the modified Bridgman method. Analysis of temperature dependence of Ag symmetrical optical modes in InS crystal showed that Raman frequency shift was well described by considering the thermal expansion and pure temperature (phonon-phonon coupling) contributions.

Crystal structure of In_2S_3 thin films obtained by the chemical vapor deposition from the volatile complex compounds indium (III) isopropyl xanthate and indium (III) diethyl dithiocarbonate was studied by synchrotron radiation diffraction [64]. High photon beam intensity (3×10^{10} photons/ mm^2s) and high angular resolution (0.02°) of the reflexes made it possible to study weak reflexes to analyze the phase composition of samples in more detail, to determine the size of the particles and to evaluate stress at the microscopic level. They showed that the films obtained at $T = 230^\circ\text{C}$ crystallized as cubic $\alpha\text{-In}_2\text{S}_3$. At the deposition temperature $T > 250^\circ\text{C}$, the films crystallized in the tetragonal β phase. Annealing of the films synthesized at 230°C , lead to $\beta\text{-In}_2\text{S}_3$ phase formation as well. Size of the particles increased as the deposition temperature increased. Values of the interplanar spacing d , for close packed planes, were almost the same for all samples deposited at temperatures $T = 230 - 370^\circ\text{C}$ and practically did not depend on crystal modification, deposition temperature and thickness of the samples. They also showed that microstress decreased after annealing or for higher deposition temperatures. For the sample deposited at 430°C , splitting of the reflex (5,0,15) was observed, which could be explained as a monoclinic or hexagonal distortion of $\beta\text{-In}_2\text{S}_3$.

Band alignment at the interface of the heterostructure $\beta\text{-In}_2\text{S}_3/\text{SnO}_2$ was studied using XPS by Bernède et al [65]. They had shown that the conduction band discontinuity (ΔE_c) between $\beta\text{-In}_2\text{S}_3$ and SnO_2 was -0.45 eV. From this value and using SnO_2 work function and the Cu(In,Ga)Se_2 electronic affinity values reported in the literature, they estimated the conduction band discontinuity at the interface $\text{Cu(In,Ga)Se}_2/\beta\text{-In}_2\text{S}_3$ to be about 0 eV.

2.3 CuInS_2 Thin Films

The structure [Fig.2] and physical properties of copper indium sulfide thin films are given below.

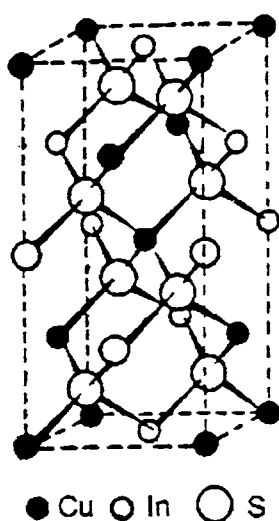


Fig.2 The tetragonal chalcopyrite structure of $CuInS_2$

Structure	: Tetragonal chalcopyrite
Melting Temperature	: 1000 - 1050°C
Density	: 4739 kg/m ³
Lattice Parameters	: a = b = 5.52 Å and c = 11.13 Å

2.3.1 Preparation Techniques

During mid 1970's, the chalcopyrite ternary compounds received considerable attention and attempts were made to prepare these compounds in thin film form. If a material is to attain any large scale and economical device utilization, its production in thin film form is a necessity. In 1975, two deposition schemes for producing $CuInS_2$ thin films (viz., single and double source methods), were reported for the first time by Kazmerski et al [66]. For the single-source method, single-phase $CuInS_2$ was used as the starting material. The second, and more controllable and reproducible scheme involved a two-source arrangement. First, the single-phase $CuInS_2$ powder was evaporated from a resistive-heated alumina crucible, and a second sulfur source was

utilized to vary the amount of sulfur in the system [66]. Since then a number of methods were used to prepare CuInS_2 thin films, which will be discussed in the following part of this section.

n-type CuInS_2 thin films were deposited on glass substrate from bulk CuInS_2 crystal by single source thermal evaporation technique by Akaki et al [67]. The bulk CuInS_2 crystal was grown by the hot-press method at 700°C for 1 hr under high pressure (22.5 Mpa) from stoichiometric Cu_2S and In_2S_3 powders. Pressure during evaporation was maintained at 10^{-5} Torr. After evaporation, the films were annealed at 100 to 500°C for 5-30 min in air. Polycrystalline CuInS_2 films started to grow at annealing 200°C in air. However, binary or ternary phases like In_6S_7 , CuIn_3S_8 and $\text{CuIn}_{11}\text{S}_{17}$ were included by annealing at 200, 300 and 400°C respectively. The samples were highly resistive as observed from four probe method.

Copper indium sulfide thin films were grown by close-spaced vapor transport in a vertical closed reactor under vacuum [68]. Solid iodine was used to provide the reagent. The source temperature was kept in the range 360 - 680°C . The high p-type conductivity layers generally showed sphalerite structure and the low p-type conductivity ones showed chalcopyrite structure. Well crystallized grains with sizes of the order of $2\ \mu\text{m}$ were observed using SEM micrograph.

Since CuInS_2 dissociated incongruently, it was found very difficult to deposit single phase CuInS_2 thin films by the flash evaporation method. Single phase CuInS_2 thin films prepared using flash evaporation technique on NaCl and glass substrates by Agarwal et al [69]. The films were found to be n-type. Source and substrate were kept at a distance of 12 cm. A molybdenum boat, maintained at a sufficiently high temperature of about 1873 K, was found to lead to monophase film formation. Substrate temperature was varied in the range 300-650 K. When the substrate temperature was raised to 423 K films became polycrystalline and the crystallinity

increased upto 523 K, with temperature. A further rise in temperature led to sulfur deficient films.

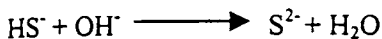
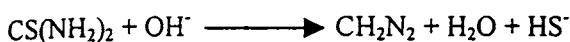
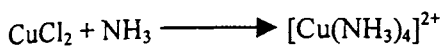
Direct homoepitaxial growth of stoichiometric CuInS_2 thin films on sapphire (0001) substrates was achieved by rf sputtering [70]. The sputtered layers grew in (112) orientation with a chalcopyrite structure. Compared with MBE, sputtering had the advantage of simple and flexible control of stoichiometry over a large scale at relatively low cost. A Cu-In alloy disk (Cu/In = 9/11) with diameter 4.00 in. and thickness 0.25 in. was used as sputter target, and H_2S (purity 98%) was introduced as both reactive and working gas during sputtering. H_2S flow was varied in the range 30-35 sccm, while the rf power was fixed at 200 W and the substrate temperature was kept fixed at 500°C. AFM demonstrated a smooth surface of the resultant films and suggested a three dimensional island like growth mechanism.

Hahn et al demonstrated direct heteroepitaxial growth of direct semiconductor CuInS_2 on silicon (001) substrates using three source molecular beam epitaxy [71]. The pretreatment of silicon wafers included a high temperature exposure to the sulfur beam, which lead to ideal (1 x 1) sulfur terminated surface, defining the starting condition for successful epitaxy. The sulfur termination as well as the film deposition leads to ordered surfaces as indicated by LEED. Combining results of x-ray, electron diffraction and TEM, they found that the films grew predominantly in a tetragonal structure which was close to zinc blende but showed a nonchalcopyrite ordering in the cation sublattice.

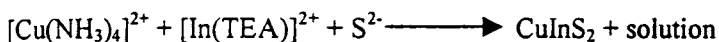
Effect of deposition temperature on structural and optical properties of CuInS_2 thin films grown by thermal evaporation was studied by Kanzari et al [72]. CuInS_2 powder was evaporated from resistively heated tungsten boats. Thickness of the samples was found to be in the range 0.24-0.33 μm . Surface roughness of the films were in the range 4-26 nm. They found that the optimal substrate temperature for

depositing good quality thin films were $T_s \approx 140^\circ\text{C}$ and $T_s \approx 240^\circ\text{C}$ for good crystallinity, low roughness and high grain size.

Structural, optical and electrical properties of chemically and thermally prepared $CuInS_2$ thin films were studied by Mahmoud et al [73]. The chemical bath deposition was based on the slow reaction between the slowly released Cu^+ , In^+ and S^{2-} ions from their complexes according to the following steps:

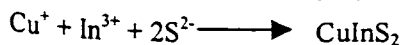


The overall reaction was:



Temperature of the growth solution was maintained at 338 K during deposition. For the evaporation method, starting ingot was prepared by mixing stoichiometrically, elements of copper, indium and sulfur in a sealed silica tube which was then evacuated to a pressure of about 10^{-2} Pa. The mixture was then heated at 873 K for 55 hours. The films were thermally deposited by evaporation from a tungsten boat, under a vacuum of 10^{-4} Pa. Deposition was carried out on glass substrates at room temperature.

Pathan et al used the simple SILAR technique for the preparation of copper indium disulfide thin films [74]. Copper (II) sulfate ($CuSO_4 \cdot 5H_2O$), indium (III) sulfate ($In_2(SO_4)_3$), triethanolamine (TEA) and hydrazine hydrate (HH) served as the cationic precursor and Na_2S as anionic precursor. The pH of the cationic solution was maintained at 5 by adding TEA and HH while that of anionic precursor was 12. Adsorption of Cu and In ions and their reaction with sulfur to form CIS can be represented in the following equation



Thickness of the film obtained from 110 SILAR cycles was $0.48 \mu\text{m}$. Immersion time was 30 seconds while the rinsing time was 50 seconds at room temperature. XRD studies indicated formation of Cu_2S with $CuInS_2$. Along with HRTEM it revealed nanocrystallinity of CIS thin films. Electrical resistivity of the films was of the order of $10 \Omega\text{-cm}$. Presence of oxygen in the film had been detected using RBS.

Cu-In-S films on Ti substrates were prepared by electrodeposition from aqueous solutions of $CuCl$, $InCl_3$, thiourea, triethanolamine and ammonia [75]. Plating on the titanium substrate was carried out using a calomel reference and a platinum auxiliary electrode. The plating voltage (vs. SCE) was -1.5 to 2 V. The plating current was between 6 and 8 mA/cm^2 and plating duration was between 10 and 15 min. All electrodepositions were carried out in stirred baths at room temperature. The as deposited layers were annealed in Ar at $550\text{-}600^\circ\text{C}$ for $30\text{-}60$ min. After annealing, the electrodes were dipped in 1M KCN (room temperature) for 15 min, to dissolve any excess sulfur or Cu. A subsequent heat treatment in H_2S further improved photoresponse of the layers. X-ray powder diffraction showed the annealed layers to be mainly $CuInS_2$ with chalcopyrite structure, with some $CuIn_5S_8$ mixed in.

Dzionk et al explained the reactive annealing of Cu-In precursors in H_2S atmosphere as a favourable method for large scale and low-cost production of $CuInS_2$ [76]. Thin films of indium were prepared by evaporation of indium metal (99.9999%) from an open tungsten boat onto glass substrates. Afterwards, copper films (99.9999%) of different thickness, according the desired Cu-In composition, were evaporated from an open tantalum boat onto the indium films. The samples were annealed in the UHV chamber at 150°C for several hours. Then the samples were removed from the chamber and the reactive annealing was carried out in a quartz-tube hot-wall reactor at temperatures between 300°C and 600°C . Single phase $CuInS_2$ films having chalcopyrite structure can be obtained at 400°C and 500°C . At higher temperatures a significant loss of indium via volatile In_2S compound occurred. With increasing

reaction time, the binary sulfides disappeared giving single phase CuInS_2 . The composition range, where single phase CuInS_2 was obtained, was determined to be a copper- and sulfur- rich region of the phase diagram. Based on these results, they suggested a three-step model for the phase formation during the reactive annealing process. This included the intermediate formation of sulfur rich binary sulfides CuS and In_2S_3 , which then react to form CuInS_2 .

CuInS_2 films were deposited by atmospheric pressure spray chemical vapor deposition (CVD). Films were deposited at 390°C using $[(\text{PPh}_3)_2\text{CuIn}(\text{SEt})_4]$ as a single source precursor in an argon atmosphere [77]. Spray CVD combines the benefits of traditional metal-organic chemical vapor deposition (MOCVD) with those of spray pyrolysis, while avoiding the disadvantages of each. The technique not only offered film growth in inert atmospheres, large area deposition and laminar flow over the substrate (which are features usually associated with MOCVD), but also the low temperature solution reservoir of spray pyrolysis. As evident from the SEM images, grain growth appeared dense and columnar, despite the small grain size. X-ray diffraction of the films revealed that there was a preferred orientation gradient along the substrate, with only two third of the film (from the back) having desired (112) crystal orientation. The films also range in thickness, with the leading edge being thinner than the trailing edge. Schottky diodes prepared by thermal evaporation of aluminium contacts onto the CuInS_2 yielded diodes for films that were annealed at 600°C . Solar cells prepared using annealed films having structure $\text{Al/ZnO/CdS/CuInS}_2/\text{Mo/glass}$ yielded a low efficiency of 0.68%.

CuInS_2 films were prepared by rf sputtering in argon atmosphere (3×10^{-2} Torr) with a frequency of 13.56 MHz supplied from a crystal-controlled generator via a matching unit [78]. The loose powder sputter target was prepared from a p-type polycrystalline material. The target to substrate separation was 3 cm and the normal working pressures were in the 5×10^{-6} to 5×10^{-7} Torr range in the chamber before

68934
539-316: 601-884-61
2011

sputtering. Annealing at 410°C in an Argon atmosphere for 30 min was found to improve the crystallinity of the samples. Composition analysis by RBS and XRF revealed the deficiency of sulfur and the presence of Argon impurities trapped during sputter deposition process. Ohmic contacts were achieved by sputtering gold for the electrical measurements. As grown films were highly resistive and the resistivity reduced upon annealing. Although effect of the grain boundaries could not be ignored, small increase in mobility with temperature could be explained by the scattering of the charge carriers mainly by acoustic phonons and ionized and neutral impurities.

Matsushita et al investigated formation of the CuInS_2 phase from both $\text{Cu} + \text{In} + 2\text{S}$ and $\text{CuIn} + 2\text{S}$ mixtures using differential thermal analysis and powder x-ray diffraction measurements [79]. In the chemical reaction process of the former mixture, an explosive exothermic reaction occurred at 640°C, which was ascribed to the formation of In-S materials. In the latter case, an explosive sulfurization reaction occurred at about 700°C, leading to the complete formation of the CuInS_2 phase. They found that the sulfurization of a CuIn alloy at a temperature higher than 750°C could suppress the formation of heterogeneous products also, bulk single crystals with good crystalline quality could be grown by sulfurization method with S vapor pressure around 200 Torr.

A two-step process that involved the deposition of alternate layers of Cu and In onto Mo coated glass substrates using magnetron sputtering followed by annealing in an environment containing elemental sulfur around 350°C was used to prepare CuInS_2 thin films for the first time by Miles et al [80]. The Cu/In ratio was adjusted by adjusting the In deposition power. The grain sizes were greater than 0.75 μm for 1 μm thick layers. They found that the sputtered multilayer process resulted in good mixing of the Cu and In to produce a single phase alloy without heating.

Copper-indium alloys were prepared by electroplating from citric acid ($\text{C}_6\text{H}_8\text{O}_7 \cdot \text{H}_2\text{O}$) solution [81]. These baths were shown to be suitable for co

deposition or sequential electroplating of the alloy. Presence of Cu_7In_4 in direct deposit as well as in sequentially electrodeposited material was observed during alloy formation. As deposited layers were heated in H_2S . X-ray diffraction showed that the annealed layer was $CuInS_2$ with chalcopyrite structure, where the $CuIn_5S_8$ phase was included during the annealing process. They attributed the reason for poor or no photoresponse of the Cu rich samples to the progressive formation of a $Cu_{2-x}S$ degenerated semiconductor.

$CuInS_2$ films prepared by coevaporation of elements onto heated glass substrates ($500^\circ C$) from a three source configuration showed that the composition of In-rich and Cu-rich films obey the relations $In_2S_3-CuInS_2$ and $CuS-CuInS_2$ in the ternary phase diagram [82]. Indium rich films exhibited a platelet-like grain structure where Cu-rich films showed a textured morphology with grain sizes in the range 1-4 μm . Compositional relations in the ternary phase diagram of Cu-In-S can be expressed by the parameters “molecularity deviation (Δm)” and “stoichiometric deviation (Δs)”.

$$\Delta m = \frac{[Cu]}{[In]} - 1, \text{ and } \Delta s = \frac{2[S]}{[Cu] + 3[In]} - 1$$

Polycrystalline thin film of single-phase $CuInS_2$ was made from copper/indium/sulfur stacked layer at various heat treatment in nitrogen atmosphere [83]. Optimum heat treatment temperature was found to be $500^\circ C$. Resistivity, Hall mobility and carrier concentration of the fabricated $CuInS_2$ at optimum heat treatment were $3 \times 10^{-2} \Omega\text{-cm}$, $0.1 \text{ cm}^2/Vs$ and $2 \times 10^{20} \text{ cm}^{-3}$ respectively.

One-step electrodeposition using sodium thiosulfate ($Na_2S_2O_3$) as a sulfur source was studied for the preparation of Cu-In-S thin films [84]. The deposited film was found to have a sufficiently high sulfur content compared with films deposited using thiourea as a sulfur source and was also found to have excellent morphology. HCl content added to the solution was found to be one of the predominant factors to

control the $S/(Cu+In)$ and In/Cu ratios in the film. Sulfur content in the bath was also one of the important factors to control the In/Cu ratio in the film.

$CuInS_2$ films were prepared using RF sputtering from binary compounds Cu_2S and In_2S_3 [85]. X-ray diffraction studies showed that the film sputtered from the target with the mixing ratio $[Cu_2S]/[In_2S_3] = 1.5$ had a single phase with chalcopyrite structure. Films showed higher absorption coefficients and the band gap was found to be 1.52 eV.

An original technology for producing Cu-In chalcogenide solar cells on a Cu tape had been recently developed. This approach called "CIS on Cu tape" (CISCuT) is promising for the fabrication of low cost solar cells [86]. An indium precursor on a Cu tape, sulfurized under special transient conditions, showed an internal structure with at least four different semiconducting layers. This structure had a rectifying I-V characteristic also without any buffer layer [87]. An EBIC investigation and an original thermopower measurement revealed a pnp-structure with n-type layer being In-rich one.

Formation of Cu chalcogenide secondary phases in samples prepared using coevaporation, sulfurization of stacked elemental layers and spray pyrolysis had been studied by Scheer et al [88]. It was found that the films grown by coevaporation and sulfurization established a CuS overlayer at the front surface of the films. The CuS segregation was missing for films grown by spray pyrolysis. It was shown that the sulfur acted as scavenger for excess Cu atoms in the $CuInS_2$ matrix. They proved that the induced CuS segregation promoted the recrystallization of the films.

2.3.1.1 CuInS₂ Using Chemical Spray Pyrolysis Technique

$CuInS_2$ films as absorbers for solar cells were deposited using spray pyrolysis method on commercially available ITO and TCO glasses and two different types of TiO_2 and ZnO electrodes- flat and porous [89]. The solution composition of $Cu:In:S = 1:1:3$ resulted in nearly stoichiometric films. $CuInS_2$ crystallite sizes of 6-10 nm on flat electrodes and 20-30 nm on randomly oriented porous underlayers had been

calculated. Doped large band gap oxides were found to be appropriate conductive electrodes for $CuInS_2$ deposited with the spray process. Size of crystallites in dense films was inversely proportional to the orientation rate of the underlayer. The cell having structure $ZnO:In/ZnO/CdS/CuInS_2$ showed output characteristics of $V_{oc} = 430$ mV and $J_{sc} = 8.1$ mA/cm² respectively.

$CuInS_2$ and $CuIn_{(1-x)}Al_xS_2$ thin films were prepared on various substrates using CSP technique by Kamoun et al [90]. They showed that nature of the substrate and presence of Al atoms in the material noticeably contributed to growth and structure of deposited films. The best crystallinity was obtained for films grown on SnO_2 /pyrex substrate and annealed under vacuum at 593 K. Using Kelvin method it was found that, putting Al atoms in the film increased the work function by about 50 meV and induced the formation of a negative surface barrier. Concentration of S and C elements increased when the samples were annealed in vacuum, whereas the concentration of Cu, In and O decreased as observed from Auger studies.

Chemical spray pyrolysis technique had been used by several authors to prepare $CuInS_2$ thin films. Pamplin et al studied variations in the lattice constants and band gaps of spray pyrolysed I-III-VI chalcopyrite films [91]. Gorska et al used spraying solution containing Cu_2Cl_2 , $InCl_3$ and thiourea for preparing $CuInS_2$ thin films [92]. A few drops of HCl were added to the solution to increase the stability of Cu_2Cl_2 . Some films were produced from a solution in which cuprous acetate was used in place of cuprous chloride, but films made from this solution were extremely deficient in copper. Nitrogen was used as carrier gas and the solution temperature was maintained at 100°C during spraying. Substrate temperature was varied from 180 to 300°C and the spraying rate from 1 to 20 ml/min. Films were found to be p-type and the resistivity could be adjusted over the range 0.1 Ω-cm to very high values by controlling the temperature of the substrate.

Spray pyrolysis conditions required to prepare single phase $CuInS_2$ films were optimized by Tiwari et al [93]. They used aqueous solutions of copper (II) acetate, indium chloride and thiourea as the precursor solutions. Sphalerite structure of as deposited films transformed to chalcopyrite on annealing. They found that properties of the films could be determined by controlling Cu/In ratio in the solution. Single phase films had band gap of 1.38 eV. Mixed films had an additional band gap at about 1.2 eV corresponding to a Cu_xS impurity phase. This impurity phase reduced resistivity of the films from about $10^3 \Omega m$ to about $10^4 \Omega m$.

Totally sprayed $CuInS_2/Cd(Zn)S$ cells were fabricated by Raja Ram et al [94] which yielded an efficiency of 2.6%. They explained the low fill factor (27.8%) as due to the low shunt resistance and high series resistance. The Cu:In:S ratio was maintained at 1.2:2:4.

Widely used precursor solutions for preparing the film of $CuInS_2$ were $CuCl_2$, $InCl_3$ and thiourea. Bihri et al [95] deposited single phase $CuInS_2$ with chalcopyrite structure, when the films were sprayed at 1:1:3 ratio and the films sprayed with excess sulfur were nearly stoichiometric. They obtained carrier concentration of $2.7 \times 10^{17} cm^{-3}$ and hole mobility was $11.6 cm^2/Vs$.

López et al showed the possibility of having $CuInS_2$ thin films with a wide range of resistivities ranging from $10^4 \Omega\text{-cm}$ to $10^{-2} \Omega\text{-cm}$ by changing the Cu/In and S/Cu ratios in the film [96]. Films with copper excess had low resistivity and better crystallinity than those, which were stoichiometric or having indium excess.

Surface study of the In- rich films revealed, flat surface with multiphase while Cu-rich initial solution led to single phase $CuInS_2$ [97]. Crystal growth in Cu-rich films was accelerated by the presence of molten phases, which segregated on the surface of the film.

A physico-chemical characterization of $CuInS_2$ films deposited using CSP technique showed that good quality films could be obtained on $SnO_2(F)$ coated glass

substrates [98]. XPS study revealed the presence of oxygen, bound to cations. Band gap was found to be closer to the single crystal values as the substrate temperature increases.

Etching in KCN solution and thermal treatments in vacuum and hydrogen were applied to as deposited films by Krunk et al [99]. KCN etching removed conducting copper sulfide from the surface of Cu-rich films, but had no effect on matrix composition. Vacuum annealing at 500°C and hydrogen treatment at 400-500°C purified the films prepared from the solution with Cu/In=1, from secondary phases, reduced chlorine content and improved crystallinity. Vacuum annealing resulted in n-type films due to the formation of In_2O_3 phase. Treatment in hydrogen reduced oxygen-containing residues and resulted in p-type $CuInS_2$ films.

It had been found that concentration of residues, originated from the precursors, was mainly controlled by the growth temperature [100]. The content of impurities was less depending on the Cu/In ratio in spray solution as the use of Cu-rich solutions lead to larger crystallites and lower impurity concentrations. Inversely to the residues originated from the precursors, concentration of oxygen increased with the higher growth temperatures. Post deposition treatment in flowing hydrogen was found to improve the crystalline quality of the samples.

Improvement of $CuInS_2$ films stoichiometry was found by increasing the sulfur content in the spray solution ($S = 6$). Single phase films with preferential orientation along (112) plane having chalcopyrite characteristic peak (103) was obtained by increasing the sulfur content [101].

$CuInS_2$ thin films were deposited using CSP technique at 650 K and heat treated under a sulfur atmosphere for 1 hour at the same temperature. Effect of this treatment on properties of the films was studied by Marsillac et al [102]. Films showed better crystallinity after heat treatment. They obtained stoichiometric films and chlorine present in the as deposited films disappeared after sulfurization. Sodium

concentration was slightly increased. The band gap of the samples was 1.46 eV. A heat treatment for 1 hour led to lower conductivity and higher activation energy. From the Arrhenius plot, they found that observed slopes were increasing with temperature, which was compatible with grain boundary scattering mechanisms. Changes in the properties, mainly electrical, were attributed to the replacement of oxygen present at the grain boundaries and linked to indium by sulfur. In_2O_3 was also removed from the grain boundaries. The treated films were therefore more suitable for solar cell applications where transversal parasitic effects along grain boundaries were an important issue.

2.3.2 Electrical and Optical Properties

Interest in I-III-VI₂ group ternary semiconductors arose first in 1971 when researchers of the Bell Laboratory put in evidence for the existence of visible direct band gap for these compounds.

Hole mobility of CuInS_2 , prepared from close-spaced vapour transport, was very high for samples grown at low temperatures, which was explained by the presence of iodine and more probably CuI [68]. Band gap was found to vary from 1.34 eV (for samples grown at low temperature) to 1.43 eV (for samples grown at high temperature). Carrier densities were of the order of 10^{16} - 10^{18} cm^{-3} and Hall mobilities from 0.5 to 6.5 cm^2/Vs and even more.

Agarwal et al obtained highly resistive samples at room temperature using flash evaporation, and the resistivity decreased with increase in substrate temperature [69]. The activation energy values indicated presence of localized gap states below the conduction band edge in n-type CuInS_2 . For films deposited at 473 K the electron mobility and concentration were 5 cm^2/Vs and 2×10^{18} cm^{-3} respectively. Band gap was found to be increasing with increase in substrate temperature (1.16 eV to 1.31 eV). The low band gap at low substrate temperature was explained to be due to the presence of localized states.

Films deposited above 200°C, using thermal evaporation, were found to have relatively high absorption coefficient (10^4 - 10^5 cm^{-1}) in the visible and near IR spectral range [72].

Mahmoud et al studied optical and electrical properties of chemically and thermally prepared CuInS_2 thin films [73]. The chemically prepared samples, both as prepared and annealed showed a band gap of 1.5 eV. On the other hand, the thermally prepared films (in as deposited condition) demonstrated two optical direct transitions of 1.5 eV and 1.72 eV. They explained the band gap at 1.75 eV, due to the optical transition from Copper d-states in the valence band to the lowest conduction band minimum, which disappeared by heating. Resistivity of the chemically prepared samples decreased on annealing in vacuum. But on annealing in sulfur, the value was further reduced due to addition of carriers by sulfur interstitials. Activation energy of 0.12 eV was calculated in the low temperature region, for both as prepared and annealed samples, which was attributed to some shallow acceptor levels, introduced by copper vacancies. On annealing in excess of sulfur, the activation energy in the low temperature region increased upto 0.33 eV, which was associated with a deep acceptor level created by the interstitial sulfur atoms.

Temperature dependence of the energy gaps for sulfur-annealed copper indium disulfide was studied using Photoreflectance (PR) in the temperature range of 10-300 K by Hsu et al [103]. Single crystals of CuInS_2 were grown by traveling heater method. The as grown crystals were n-type with resistivity near 1 $\Omega\text{-cm}$, a carrier concentration of 10^{16} - 10^{17} cm^{-3} , and the mobility near 40 cm^2/Vs at room temperature. The p-type CuInS_2 was obtained due to thermal treatment in the sulfur vapor. The as-grown crystal had been annealed under maximum sulfur pressure at 750°C. Resistivity of the p-type samples was near 10 $\Omega\text{-cm}$, with carrier concentration near $3 \times 10^{17} \text{ cm}^{-3}$ and mobility of 10 cm^2/Vs . The sulfur annealed samples were found to have larger transition energies, smaller positive temperature coefficients of energy gaps and larger

spin-orbit splitting energies compared with those of as grown samples. They explained the experimental results by a decrease of d orbital contributions to the upper valence band for the sulfur annealed sample which was probably caused by the variation of lattice distance due to native defects.

Alt et al investigated the influence of cooling rate in a deposition process on the electrical conductivity of $CuInS_2$ thin films for solar cells [104]. The films were grown by simultaneous evaporation of Cu, In and S, at growth temperature of 730 K, and growth rate of 10 Å/s. The final film thickness was 2-4 μm. It was found that the room temperature electrical conductivity depended significantly on the cooling rate of the film after deposition. The value reached 1×10^{-3} S/cm for a cooling rate (R_c) of 2.0 ± 0.2 K/min whereas for abrupt cooling and higher cooling rates it reduced to 10^{-6} and 10^{-5} S/cm respectively. The possible explanations could be related to thermal stress in the films or to the defect chemistry. Difference in the thermal expansion between a thin film and the substrate could induce structural defects in the film. In the other case, S atoms could adsorb at the grain boundaries during the cool down period thereby passivating the grain boundaries. A further decrease in R_c , reduced conductivity by more than one order of magnitude with respect to the maximum value.

The photoelectrochemical characterization of Cu-In-S films, prepared using electrodeposition was done in polysulfide electrolyte under AM1 equivalent tungsten-halogen illumination [75]. From the spectral response they found the existence of an indirect band gap at 1.3 eV, which was attributed to the presence of $CuIn_5S_8$.

Wu et al prepared both p-type and n-type $CuInS_2$ films by three source evaporation [105]. They found that the resistivities were between 0.01 and 10 Ω-cm. The best electron mobility obtained was 21.84 cm²/Vs and the best hole mobility was 1.42 cm²/Vs. They noted a spread of WMRS (Wavelength Modulated Reflectance Spectroscopy) spectra, which they suggested to be due to the inferior crystalline quality.

Minority carrier lifetime and surface recombination velocity were measured in both n-type and p-type CuInS_2 chalcopyrite compounds, combining the photoelectromagnetic effect (PEM) and stationary photoconductivity (PC) effect [106]. CuInS_2 single crystals were grown by the method of vapor phase transport. The values were calculated to be 1.2×10^{-10} sec and 1.2×10^5 cm/sec for p- CuInS_2 and 6.5×10^{-7} sec and 1.3×10^3 cm/sec for n- CuInS_2 . Using these values they calculated the theoretical maximum conversion efficiency between 24 and 26%.

Two distinct absorption regions were observed for vacuum deposited CuInS_2 thin films by Sun et al [107]. The absorption edge at 1.54 ± 0.02 eV corresponds to the direct band gap transition. Another one was observed at low energies 1.41 to 1.42 eV, which was due to the transitions from a copper vacancy band to the conduction band. The improvement in the absorption characteristics due to annealing was attributed to the grain growth as well as the reduction of copper vacancies.

Studies of optical properties of CuInS_2 thin films prepared by flash evaporation revealed an indirect transition at 1.565 ± 0.005 eV along with a direct transition at 1.524 ± 0.005 eV [108]. This was ascribed to an optical transition from the valence band maxima at the boundary of the Brillouin zone to the lowest conduction band minimum at the zone center. Three further optical transitions which were probably due to the copper d states in the valence band were observed at energies well above the fundamental edge.

2.3.3 Effect of Na Incorporation

Doping of Cu-poor CuInS_2 thin films by sodium and oxygen species, such as O_2 and O, was investigated using SIMS and conductivity measurements. Samples were prepared by co-evaporation of the elements Cu, In and S. Na increased grain size of the polycrystalline films, thereby reducing volume density of grain boundaries and hence increasing carrier concentration within the grains. For low Na content, conductivity increased with Na content while for very high Na concentration,

conductivity decreased. Increased oxygen concentration was observed for Na-doping. The SIMS signals of CuO and CuOS were also detected. They coincided with O-doped films but differed for Na and O_2 doped films. This was interpreted as due to grain boundary effects. Oxygen was found to play a major role in Na doping. It was proposed that the active role of O on the electrical properties was mediated via grain boundaries in $CuInS_2$ materials [109].

Changes in the electronic structure of $CuInS_2$ thin films due to Na incorporation were studied by Fukuzaki et al [110]. XPS spectra were recorded for Na free Cu deficient $CuInS_2$ and Na incorporated films. Peaks corresponding to Cu 2p, In 4d and S 2p of $CuInS_2$ films were shifted by -0.5 eV, due to Na incorporation, without changes in both line width and shape. They suggested the formation of a new $(Na,Cu)InS_2$ phase on the film surface. Electron density of states increased by Na incorporation and the increments were larger for films with larger Cu deficiency. Explanation was that the electrons were delivered from Na_{Cu} into the valence band of the Cu-deficient p- $CuInS_2$.

Yamamoto et al. investigated electronic structures of Na-incorporated and In-rich $CuInS_2$, based on *ab initio* electronic band structure calculations. They found that formation of ionic Na_{Cu} -S bond decreased Madelung energy, resulting in a shift in energy levels of S 3p orbitals, in the vicinity of Na atoms, towards lower energy regions [111]. Mobile Na acted as a passivator of donor states such as In_{Cu} and interstitial In. They also studied the effect of codoping using Na and O into p-type Cu-deficient $CuInS_2$ [112]. Codoping of Na and O led to the formation of a complex, containing Na_{Cu} and O_S , where they occupied nearest neighbour sites, causing the annihilation of the deep level in the band gap due to n-type Cu-S divacancy.

Sodium incorporation into $CuInS_2$ was of great interest because controlled incorporation of Na into this material improved cell performance remarkably. In 1997, Watanabe et al investigated the characteristics of the Na-incorporated $CuInS_2$ films by

intentional addition and diffusion from a soda-lime glass [113]. They observed a striking difference in the film morphology between the Na-containing and Na-free $CuInS_2$ films in size and shape of the grains. SEM micrographs revealed that Na-free $CuInS_2$ films had needle like grains on the surface. However, with sodium, the grains changed significantly to large and coarse. Also full width at half maximum (FWHM) of the (112) peak for sodium-containing $CuInS_2$ films was much narrower than that of sodium free films. Enhancements in conductivity, crystallite quality and device performance were also reported in controlled Na- incorporated $CuInS_2$.

2.3.4 Effect of KCN Etching

Dissolution of metal chalcogenides in cyanide solutions was established since long before and was applied in the surface treatment of solar cells. KCN was known to dissolve copper selenides and copper sulfides and was used successfully to prepare $CuGaSe_2$ based solar cells from very Cu-rich material. [114]. Post deposition stoichiometric adjustment could be done through chemical etching, using KCN. Complexing of copper by cyanide resulted in removal of a variety of electronically deleterious copper chalcogenides as this became soluble [88].

In order to remove quasi-metallic CuS layer, which predominantly precipitated at the front surface of the Cu-rich films, Scheer et al. chemically treated the samples in a XCN solution with $X = Na, K$ [115].

Ogawa et al. had also applied KCN treatment on the $CuInS_2$ film [116]. For this, the grown $CuInS_2$ film was dipped in an aqueous solution of 10% KCN for 3 minutes at room temperature and rinsed with deionized water. They found that after KCN treatment, Cu/In ratio was lowered to ~ 1 and is almost independent of the ratio existing before treatment. Resistivity increased by a factor of ~ 100 , mainly due to a reduction of excess carrier concentration.

Hashimoto et al. found that KCN treatment adjusted the conduction band offsets from -0.7 eV to -0.05 eV. It also changed the interface Cu/In ratio. KCN

treatment removed the Cu_xS phase or corrected structurally poor interface and made the band offsets close to the theoretical estimation [117].

Thin films of KCN-etched CuInS_2 surfaces during an annealing procedure were investigated using photoelectron spectroscopy and scanning electron microscopy combined with energy dispersive X-ray analysis by Müller et al [118]. Films were prepared using sputter deposition of Cu and In followed by sulfurization in S_2 vapour at 500°C . Surface of the films was cleaned in situ by soft argon sputtering to remove residual contents of oxygen or carbon impurities. SEM micrograph indicated an average grain size of approximately $2\ \mu\text{m}$. SEM pictures directly after etching and without sputtering and annealing indicated no significant difference in roughness, homogeneity or grain size. In contrast, surface composition of the etched samples showed significant deviation from stoichiometry. Heat treatment of the samples after etching with KCN, led to CuInS_2 with almost ideal elemental composition.

Removal of a deleterious CuS phase in CuInS_2 through KCN etching is considered to be problematic. Aggour et al. developed a novel electrochemical treatment for CuInS_2 films, to remove the segregated CuS phase [119]. Electrochemical treatments were carried out in a glass cell having three electrode potentiostatic arrangement with a Pt counter and a saturated calomel electrode as the reference. They were able to remove CuS phase and the photoeffect observed using this method was as good as that obtained after the KCN etch.

2.3.5 Different Studies on CuInS_2

Electron beam annealing of phosphorous-implanted CuInS_2 single crystals had been shown for the first time to be an effective way for p-type conductivity control by extrinsic impurities by Lin et al [120]. CuInS_2 single crystals were grown by chemical vapor transport (CVT). Phosphorous implantation in CuInS_2 followed by thermal treatment, resulted in the formation of P_4S_3 precipitates, which made it difficult to control p-type conductivity. Effect of doping by Zn and vacuum annealing

were also discussed. When Zn was introduced into CuInS_2 , the crystals became n-type and resistivity was reduced, which was the evidence of it being a shallow donor in CuInS_2 . The electrical resistivities of both undoped and Zn-doped crystals were found to increase with the annealing temperature, and a large increase in resistivity was found when heated beyond 300°C .

Chemical shifts of the K absorption discontinuity of copper had been studied in ternary chalcopyrite compounds by Deshpande et al [121]. It was observed that there existed a linear relationship between the chemical shift (ΔE) and the band gap (E_g) in the system.

Changes in the electronic structure of Na doped CuInS_2 thin films with Ga incorporation increased the energy conversion efficiency of $\text{CdS}/\text{CuInS}_2$ solar cells from 10.6 to 11.2% as reported by Abe et al [122]. Optical absorption energy of the CuInS_2 : Na film increased from 1.40 to 1.43 with the Ga incorporation. They ascribed the enhancement of open circuit voltage from 0.76 to 0.80 V by Ga incorporation to the observed widening of band gap. Films were prepared by sulfurisation of the precursor films at 550°C for 1 hour in the 5% $\text{H}_2\text{S}/\text{Ar}$ atmosphere.

Bridenbaugh et al were the first to observe homojunction electroluminescence in CuInS_2 [123]. This homojunction was made by two different annealing procedures, which converted a surface layer of p-type crystals. Diodes made by low temperature (200°C) In-Ga diffusion showed a rectification ratio of 17000:1 at 2V and a zero bias resistance of $1 \times 10^7 \Omega$. For diodes made by high temperature (600°C) annealing in InCl_3 the values were 15000:1 and $3 \times 10^7 \Omega$ respectively. Electroluminescence had been observed in diodes made by In-Ga diffusion. Two peaks at 1.48 and 1.40 eV were present in the spectrum at 300 K and 1.42 eV peak dominated for that at 77 K. The internal quantum efficiency was 10^{-5} at 300 K and 10^{-3} at 77 K.

One of the best-suited techniques for structurally assessing the films is Raman Scattering. Micro Raman scattering along with Auger electron spectroscopy

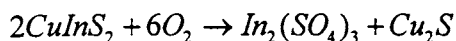
measurements were used to identify the main secondary phases in the Cu poor samples as CuIn_5S_8 and CuS for Cu-rich ones [124]. The presence of secondary phases was strongly related to the temperature of processing. Secondary phases were inhibited when the growth temperature decreased to 420°C . Raman spectra of these samples were characterized by the presence of an additional mode at about 305 cm^{-1} . The analysis of the layers by TEM and XRD suggested that the sphalerite structure was not directly related to this additional mode, but to either CuAu ordering or to local arrangements of cations vibrating around S anions. Hwang et al [125] identified eight vibration modes at frequencies 61, 84, 240, 268, 289, 304, 321 and 342 cm^{-1} by Raman scattering for single crystal CuInS_2 prepared using iodine vapor transport.

Guha et al studied the Raman and PL spectra of CuInS_2 powder produced by chemical route [126]. Films of CuInS_2 were prepared by Doctor's blade technique. Crystalline quality of CuInS_2 improved with the pH value of the precursor solution and the best crystalline quality was obtained at $\text{pH} > 11$. There were four prominent peaks in the Raman spectra, at 292, 305, 340 and 472 cm^{-1} in addition to the peak at 265 cm^{-1} . They attributed the strong peak 292 cm^{-1} to the characteristic A_1 mode while the peak at 340 cm^{-1} to B_2 mode. Formation of $\beta\text{-In}_2\text{S}_3$ binary phase created a peak at 305 cm^{-1} and the peak at 472 cm^{-1} was ascribed to the internal stretching mode of SO_4^{2-} ion which disappeared above $\text{pH} = 11$. The peak at 265 cm^{-1} was obtained only for $\text{pH} = 9$ and was attributed to B_2 mode. PL studies revealed the formation of sulfur vacancy during H_2 annealing.

The Au/p- CuInS_2 /Cu structure was found to exhibit electronic switching characteristics [127]. Amorphous CuInS_2 films were deposited using single source thermal evaporation technique. The switching was explained to be associated with electronic processes than the thermal ones.

Grzanna et al. studied chemical stability of CuInS_2 in oxygen at 298 K [128]. They performed a thermochemical analysis in the quaternary system Cu-In-S-O. They

found twelve quaternary two-phase equilibria for Cu-In-S-O system. From the predominance area diagram of Cu-In-S-O for different partial pressures of oxygen, they found that the area of existence of $CuInS_2$ became smaller and those of In_2O_3 and $In_2(SO_4)_3$ became larger with increasing oxygen pressure. The field of $CuInS_2$ just vanished when the oxygen pressure became -51.5 Pascal. This pressure corresponds to the equilibrium,



Thus for oxygen pressures larger than this value, $CuInS_2$ was unstable and was transformed into Cu_2S and $In_2(SO_4)_3$.

Electric and magnetic properties of Mn and Fe doped $CuInS_2$ compounds were studied by Tsujii et al [129]. Electrical conductivity changed drastically with increasing Mn concentration, indicating an increase of carrier density. It was found that susceptibility was reduced due to increase in Mn concentration, which indicated enhancement of anti ferromagnetic interaction. However, magnetic ordering was not observed in these systems. In the case of samples doped with Fe, the magnetization increased monotonically without any step as the anti ferromagnetic interaction of Fe ions was weak since the Fe-Fe distance was much larger than that of Mn-Mn.

Hydrogen diffusion in $CuInS_2$ thin films was studied by measuring the spreading of implantation profiles upon annealing [130]. Hydrogen diffusion observed was too slow to be attributed to the intrinsic diffusion. It was found that in polycrystalline $CuInS_2$ films, hydrogen left the samples through the pores between grains.

Interaction of atomic hydrogen with the surface of Cu-III-VI₂ chalcopyrite semiconductors was studied by Lippold et al [131]. The technique of low energy broad beam ion implantation into heated targets was used to introduce atomic hydrogen. They found that for temperatures above 150°C, surface layer became rich in indium. Based on the results of micro Raman analysis and EDAX, they proposed a

model for this effect: copper in-diffusion, caused by the filling of Cu vacancies and possible substitution of Cu by hydrogen. They also suggested that incorporation of atomic hydrogen at elevated temperatures could be a tool for controlled post growth stoichiometry variation of Cu chalcopyrite surfaces.

Otte et al. implanted H^{3+} at 300 eV into Cu-chalcopyrite semiconductors at temperatures between 50°C and 300°C [132]. They found an increase of radiative recombination, which was attributed to defect passivation due to hydrogen incorporation.

Electron-phonon contribution to the energy gap in $CuInS_2$ was studied using the photocurrents of a Schottky barrier diode in the temperature from 10 to 300 K [133]. The Schottky barrier diode was constructed by evaporating a layer of about 100 Å gold film on the front surface of the sample. It was showed that the electron-phonon interaction for the band transition was dominated by the highest-energy phonons, and the results confirmed the positive temperature coefficient of the energy gap for the thermal expansion in $CuInS_2$.

In solar cells made of amorphous silicon or Indium phosphide, hydrogen is either an essential part of the system or is used to improve the performance of the cells. Effect of hydrogen in the chalcopyrite materials is now beginning to receive attention. Gil et al. performed muon spin rotation (μ SR) experiments on $CuInS_2$ to study the effect and behavior of hydrogen in the material [134]. Muon spin rotation could provide information on the local structure and electronic configuration of isolated hydrogen because, muon can be regarded as a proton analogue or 'light isotope' of hydrogen.

Influence of post deposition annealing of coevaporated $CuInS_2$ films in hydrogen and oxygen atmosphere was studied using photoluminescence (PL) and nuclear reaction analysis (NRA) techniques [135]. Intensity of the PL peak at 1.445 eV could be drastically influenced by post-deposition treatments. This transition was ascribed to the donor-acceptor pair recombination between a sulfur vacancy and a



copper vacancy. They found that the sulfur vacancy could be activated by hydrogen annealing and passivated by oxygen annealing.

Vijaya Lakshmi et al prepared $CuInS_2$ thin films doped with Mn using spray pyrolysis technique. The band gap was found to increase with Mn content in the range 1.38 to 1.56 eV [136]. The decrease of hole concentration with doping indicated the creation of donor levels by Mn.

The piezoelectric photoacoustic spectra had been investigated using a tunable laser for $CuInS_2$ crystals grown by the traveling heater method [137]. The spectrum observed at 9 K showed two dips in the band edge region corresponding to free excitons located at 1.536 and 1.556 eV respectively. The dip suggested that the probability of non-radiative recombination of excited electrons and holes decreased at the free exciton energies.

2.3.6 Defects in $CuInS_2$

Understanding of the defect chemistry of a material is very important in view of the practical applications. The efficiency of $CuInS_2$ solar cells is determined by the presence of native (extrinsic) lattice defects. These defects introduce energy levels in the band gap, which determine the conductivity type and the minority carrier life time. Defect Physics and chemistry of $CuInS_2$ films were studied by Nanu et al [138]. The films were obtained by sulfurization of a Cu-In (Cu/In = 1.8) metallic alloy. Nature of the sulfur precursors was found to play an important role in the defect chemistry of $CuInS_2$ films. From Raman spectra it was concluded that with H_2S , the concentration of Cu-Au ordering was much higher than that when Sn was used. If O_2 was added Cu-Au order diminished substantially. Since the use of H_2S yielded a higher concentration of sulfur vacancies, and since O_2 was known as a passivator for V_s , it was postulated that the presence of Cu-Au ordering and V_s were correlated. This model was supported by PL spectroscopy. PL emission taken from H_2S -treated samples was much stronger than PL emissions from Sn treated samples. The PL bands could be assigned to donor-to-valence band and donor-acceptor recombination and gave

support to the idea that a high concentration of V_s was connected to a high concentration of anti-site defects, Cu_{In} and In_{Cu} . These anti site defects form an ordered arrangement being the Cu-Au order. Thus, they were able to establish a link between the presence of Cu-Au ordering and PL spectra.

It was established that electrical and optical properties of ternary chalcopyrite semiconductors were dominated by the presence of intrinsic defects (vacancies, interstitial and anti-site defects). The influence of intrinsic defects, cation vacancies (V_{Cu} , V_{In}) and anti-site defects (In_{Cu} , Cu_{In}) on the band structure of nonstoichiometric $CuInS_2$ based upon the *ab-initio* electronic band structure calculations using augmented spherical wave (ASW) method was done by Yamamoto et al [139]. They found that an energy shift of the center of gravity of S 3p band was a key parameter for controlling change in the type of conductivity and resistivities of $CuInS_2$ crystals with intrinsic cation defects. In p-type crystals (V_{Cu} , Cu_{In} and V_{In}) the physical characteristics were determined by the change in the interaction between Cu and S atoms.

Photoluminescence (PL) is a very sensitive method that investigates defect and impurity states. So, far a number of PL studies on $CuInS_2$ were performed. But not much is known about the native defects associated with bound excitons because of the difficulty of high quality crystal growth. Wakita et al investigated the effects of annealing on PL spectra in $CuInS_2$ crystals grown by traveling heater method [140]. They found that after vacuum annealing at 400°C the emission of bound exciton at 1.525 eV (E_{x2}) was completely eliminated while another bound exciton peak appeared at 1.520 eV (E_{x3}). On the other hand, when the crystals were annealed in contact with In_2S_3 powder, bound exciton emissions almost did not change compared with the spectra of the as-grown crystals. They proposed that the defects associated with E_{x2} and E_{x3} bound excitons were attributed to interstitial S-atoms and In-vacancies or substitutional Cu-atoms at In-site respectively. The radiative life times of the E_{x2} and

E_{x3} with single exponential decay had been estimated as 2.1 and 3.5 ns respectively [78]. Similar analysis of slow component of E_{x1} emission showing double exponential decay gave a radiative life time value of 500 ps. Charge state of the defect centers associated with the bound excitons was argued to be neutral.

Binsma et al used PL as an effective tool to identify defect levels in CuInS_2 [141]. They found that in In-rich material, the acceptor level was located at 0.10 eV above the valence band, which was ascribed to V_{Cu} . In Cu-rich samples, the acceptor level was located at 0.15 eV above the valence band, due to either V_{In} or Cu_{In} . Two donor levels having ionization energies 35 and 72 meV were also identified in both Cu-rich and In-rich samples, which originated from either intrinsic defects or impurities.

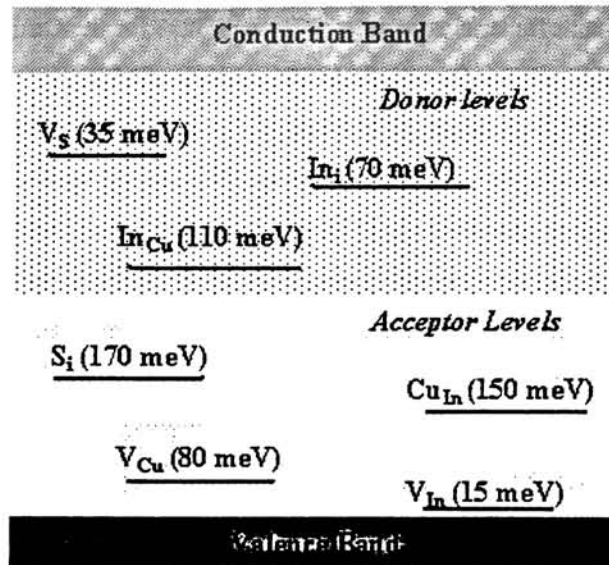
Combining the studies of electrical, photoluminescence and stoichiometry analyses, the defect structure of CuInS_2 single crystals was revealed [142]. Ionization energies were determined to be 0.038, 0.068 and 0.145 eV for the sulfur vacancy, indium interstitial and indium occupying copper vacancy respectively. They also found that for CuInS_2 , a high hole concentration could only be obtained by phosphorous implantation and pulse electron beam annealing and a high electron concentration could be obtained by zinc diffusion [143]. They obtained ionization energy of 0.018 eV for phosphorous occupying sulfur vacancy and the ionization energy of zinc occupying copper site was 0.18 eV.

Deep PL emission bands at $h\nu = 0.954$ eV and 0.864 eV were observed in CuInS_2 single crystals [144]. They were resulted from a donor-acceptor pair (DAP) recombination, such that the donor atom of the DAP occupied an interstitial position within the chalcopyrite lattice and the acceptor atom was at a cation site next to it. The probable donor defect was identified as an interstitial Cu atom and the associated acceptor defect as a cation vacancy V_{In} .

Massé et al studied the cathodoluminescence of single crystals of CuInS_2 obtained by iodine chemical transport [145]. As grown crystals and crystals annealed in In, S, (In + S) or in vacuum were used. Two types of spectra were observed. One for n- type crystals due to S vacancies and the other for p-type or compensated crystals, which was interpreted as donor-acceptor pair transitions between S-vacancy (donor ~ 90 meV) and the Cu vacancy (acceptor ~ 45 meV) and by the corresponding free-to-bound transitions.

Töpper et al investigated the PL spectra of both CuInS_2 films and solar cells prepared by coevaporation as a function of post deposition treatments for different temperatures and excitation intensities [146]. No significant difference was found between thin films and solar cells. Annealing in hydrogen atmosphere caused an increase of PL intensity at 1.445 eV by more than a factor of 100, while subsequent annealing in oxygen or air ambient passivated this transition, which was ascribed to a donor-acceptor pair recombination between a sulfur vacancy and a copper vacancy. They suggested a defect mechanism that assumed the passivation of sulfur vacancies by oxygen in grain surfaces, which could be activated by hydrogen annealing.

Electrical and PL measurements had been carried out on chemical vapor transport grown CuInS_2 single crystals in order to determine intrinsic defect levels in this material [147]. Post-growth treatments, like annealing in vacuum, air, Cu, In and S atmosphere were used to identify the observed electronic defect levels. Combining these results with those given by Lewerenz et al [148], a band diagram for CuInS_2 could be proposed [Fig. 3].

Fig. 3 Band Diagram of CuInS_2

2.4 CuInS_2 as Absorber Layer

The main function of this component is to absorb light and to convert its electromagnetic energy into the energy of electron-hole pairs, which is of a chemical nature [149]. CuInS_2 possesses several exceptional material properties, which make it potentially suited for photovoltaic applications. Energy gap of the absorbing material should match the spectral region where the cell is expected to operate. CuInS_2 is having a direct band gap of 1.5 eV, which is the optimum value for solar energy conversion. Optical absorption coefficient of the absorber material has to be high in order to absorb most of the illumination energy within the thin layer. Indirect semiconductors, where the energy gap for indirect transitions is smaller than the energy gap for the direct ones, usually show too small optical absorption and require a complicated light-trapping scheme. Typical chalcopyrite semiconductors for solar cell applications like CuInSe_2 and CuInS_2 (CIS) are direct band gap semiconductors, so that large absorption coefficients can be achieved here. This material can be prepared both in p-type and n-type form so that homojunction is also possible. Meese et al

predicted theoretical efficiencies between 27% and 32% for the CuInS_2 homojunction and this is the highest figure for any photovoltaic device [150].

Some of the requirements for forming a good quality heterojunction are: (i) the lattice constants of the two materials should be nearly equal, (ii) the electron affinities should be compatible and (iii) the thermal expansion coefficients should be close. Mismatch of lattice constants and thermal expansion coefficients leads to interfacial dislocations at the heterojunction interface, giving rise to interface states, which act as trapping centers. Difference in electron affinity between the two materials can result in energy discontinuities in the form of a notch or a spike, in one or both of the energy bands in an abrupt heterojunction [151]. Current emphasis in photovoltaic technology is directed toward the development of high performance inexpensive solar cells.

2.5 Review on CuInS_2 Based Solar Cells

Thin film solar cell is a promising approach for terrestrial and space photovoltaic and offer a wide variety of choices in terms of device design and fabrication. Since the discovery of *pn* junction Si photovoltaic (PV) devices [151] reported in 1954, the science and technology of PV devices (solar cells) and systems have undergone revolutionary developments. The problem of high cost of Si was recognized right from the beginning. Silicon being an indirect band gap material with band gap ~ 1.1 eV is by no means an ideal material. For effective solar absorption, Si wafers have to be at least $50 \mu\text{m}$ thick unless optical enhancement techniques are used to improve the effective absorption. It has also been recognized that cheaper solar cells can be produced only if cheaper materials and lower cost technologies are utilized. The I-III-VI chalcopyrite materials have some of these desirable properties for photovoltaic application. CuInS_2 , having a direct band gap of 1.5 eV is considered as an ideal material for photovoltaic application.

Fabrication and characterization of several vacuum deposited photovoltaic heterojunction involving CuInS_2 , were reported by Kazmerski et al in 1972 [152] with CdS as the buffer layer. The CuInS_2 films having 2-4 μm thicknesses were grown by a dual source deposition technique and CdS was evaporated from a Ta- baffled source. The substrates were polished alumina with a Zn-Au metalisation for back contact. The devices were fabricated completely in-situ and the $\text{CuInS}_2/\text{CdS}$ had a measured efficiency of 2.55%.

They also reported formation of a n-p CuInS_2 homojunction solar cell in the same year [153]. The CuInS_2 films for the device investigation were grown by a dual source deposition technique, employing a resistive heated quartz or beryllium oxide crucible for the single phase ternary powder and Ta boat for the sulfur. The purpose of this second, chalcogen source was to alter the S content in the film during growth, and hence to control carrier type. The measured efficiency of the device was 3.33%.

An attempt to prepare solar cells using spray pyrolysis was made by Gorska et al in 1979 [92]. They prepared heterojunction by spraying CuInS_2 onto heated CdS single crystals. They also prepared an all-thin-film heterojunction device, by spraying CdS over CuInS_2 layer. But weak photo activity was observed in both cases. In 1985, totally sprayed $\text{CuInS}_2/\text{Cd}(\text{Zn})\text{S}$ cell having efficiency 2.66% was reported by Ram et al [94].

Heterojunctions of hydrogenated a-Si films prepared by rf sputtering with spray pyrolysed CuInS_2 films were studied by Kumar et al in 1986 [154]. Capacitance-Voltage measurements established the formation of an abrupt heterojunction which exhibited photovoltaic behavior with $V_{oc} = 220$ meV and $J_{sc} = 0.20$ mA/cm².

In 1992, Walter et al investigated heterojunction formed with co evaporated CuInS_2 and $\text{CuIn}(\text{S},\text{Se})_2$ [114]. Heterojunctions of single and bilayer CuInS_2 thin films were completed by evaporation of Ga doped n-type $(\text{Zn}_{0.1}\text{Cd}_{0.9})\text{S}$ window or a highly

conductive ZnO layer with a chemical bath deposited thin CdS buffer layer (50 nm) and Al contact. During spectral response measurements, they observed a negative response (reversal on photocurrent) under forward bias and at equilibrium condition for the red end of the absorption spectrum resulted in the cross over of the dark and illuminated J-V curve. This could be correlated to the existence of a quasi-metallic CuS phase, because the effect was not observed when using a bilayer or a KCN etched single layer. Thus it was possible to overcome the phase inhomogeneities by applying bilayer recipe and therefore avoiding CuS. They could get an efficiency of 6.1% for a (Zn,Cd)S/CuInS₂ heterostructure and an active area efficiency of 10% for a ZnO/CdS/CuIn(Se_{0.58}S_{0.42})₂ solar cell. Using a graded band gap in order to overcome interface problems, the efficiency improved to 11.7%.

In 1993, Scheer et al reported the cell structure glass/Mo/p-CuInS₂/n-CdS/n⁺-ZnO/Al, which delivered 10.2% efficiency at stimulated AM1.5 conditions [115]. The Cu-rich p-type absorber having 3 μm thickness was prepared by thermal coevaporation. Deposition of a thin CdS layer was performed in a chemical bath and sputtered ZnO:Al layer served as the transparent conductive window layer. An evaporated Al grid completed the cell structure. They also attempted to leave out the bath deposited CdS layer using a configuration of CuInS₂/ZnO. These cells exhibited much lower photovoltage.

Thin film photovoltaic cells were fabricated using the heterostructure consisting of an atom beam sputtered ZnO films, a chemical bath deposited CdS layer and a CuInS₂ film obtained by sulfurization of a metallic precursor in 1994 by Uenishi et al [155]. They prepared two types of cells using CdS buffer layer prepared from aqueous solution containing iodides and chlorides. The cell prepared with Cu/In ratio 1.21 for CuInS₂ and CdS from iodide solution showed 2.2% efficiency while that with CdS from chloride solution yielded only 1% efficiency. 3.1% efficiency was achieved

for the cell where the heterojunction consisting a CdS layer (iodide solution) and CuInS_2 thin film (Cu/In ratio 1.21) was annealed in vacuum at 150°C for 30 minutes.

An efficient (9.7%) thin film photovoltaic cell was fabricated by Ogawa et al [116] in the same year, using the heterostructure consisting of a CuInS_2 film obtained by sulfurization of a metallic precursor, a chemical bath deposited CdS layer and an atom- beam sputtered In_2O_3 film. CdS was deposited from an aqueous solution containing CdI_2 , NH_4I and thiourea. A preceding KCN treatment of the Cu-rich CuInS_2 film removed the possible Cu_xS layer and/or excess Cu phase in the compound until the CuInS_2 film became stoichiometric.

Subbaramaiah et al reported an all-sprayed p- $\text{CuIn}(\text{S}_{0.5}\text{Se}_{0.5})_2$ /n- $\text{CdZnS}:\text{In}$ heterojunction in back wall configuration having conversion efficiency 1.1% [156].

In 1995, Hashimoto et al studied band offsets at CdS/ CuInS_2 heterojunction using X-ray Photoemission spectroscopy [117]. In order to accurately determine the band offsets, they measured the Cd_{4d} and In_{4d} core levels as well as the valence band maximum (VBM). Then, the band offsets are given by

$$\Delta E_v = E_{v-\text{In}4d} - E_{v-\text{Cd}4d} - \Delta E_{\text{CL}}$$

$$\Delta E_c = -\Delta E_v - E_g(\text{CuInS}_2) + E_g(\text{CdS})$$

where ΔE_v is the valence band offset and ΔE_{CL} is the energy difference between the Cd_{4d} and In_{4d} levels of a CdS/ CuInS_2 heterojunction. They determined the band offsets for untreated CdS/ CuInS_2 junction as $\Delta E_v = 1.8 \pm 0.3$ eV and $\Delta E_c = -0.7 \pm 0.4$ eV. The values obtained for the KCN treated one were $\Delta E_v = 1.18 \pm 0.1$ and $\Delta E_c = -0.05 \pm 0.15$ eV. The result revealed that the KCN treatment not only reduced the carrier concentration of the CuInS_2 film but also adjusted the conduction band offsets from -0.7 eV to -0.05 eV, improving the interface to establish the alignment of the conduction band minima. The reduction in the conduction band offset at the CdS/cyanide treated CuInS_2 junction suggested that the cyanide treatment improved the interface to give rise to the alignment of the conduction band minima, which was suitable to the solar cell applications.

CdS had been successfully used as buffer layer for I-III-VI₂ thin film absorber for a long time. Recently lot of research was going on for an alternate to CdS buffer layer in order to eliminate toxic cadmium for an environmentally friendly photovoltaic technology. Moreover improvement of transmission in the blue wavelength region by using a material with a wider band gap compared to CdS was one of the aims to obtain an improved device performance.

In 1996, $CuInS_2$ solar cell with 6.3% efficiency had been achieved without KCN treatment by Watanabe et al [157]. They prepared $CuInS_2$ films using a two stage process in which Cu-In-S precursor were sputtered in H_2S/Ar with metal targets (Cu and In) and then annealed in H_2S atmosphere. They also found that control of S content in the precursor was essential for fabricating high- efficiency solar cells. This efficiency was obtained when $S/(Cu+In)$ ratio of the precursor was 0.3. They suggested that a reduction of In-rich phase (In_2S_3 , $CuIn_3S_8$ etc) was also important in order to achieve a high efficiency in $CuInS_2$ solar cells without using poisonous KCN.

Fabrication of a 11.4% efficient thin film solar cell based on $CuInS_2$ with an $In_x(OH,S)_y$ buffer layer (Cd- free) was reported by Braunger et al [158]. $CuInS_2$ thin films were deposited in a single layer process by thermal coevaporation of the three elements onto a heated Mo-coated soda lime glass substrate. Absorption layer thickness was adjusted to approximately 3 μm and the films were grown with 10% excess of copper and fifteen fold surplus sulfur in the vapor. The secondary CuS phase was removed by KCN etching. The cadmium free buffer layer was deposited from an aqueous solution of thioacetamide $(CH_3CSNH_2)_2$ and $InCl_3$ at temperature upto 70°C.

Another such material was n-Si. Crystalline Si (c-Si) probably represented the most attractive substrate material, as lattice mismatch between CIS and Si was only 2%. In 1997, Metzner et al presented the first epitaxial Si/ $CuInS_2$ heterojunction device [159]. By means of Molecular Beam Epitaxy (MBE), slightly Cu- rich $CuInS_2$ epilayers were deposited on sulfur- terminated Si-(111) surfaces of n-type wafers. In



the first step, an ITO film of about 100 nm thickness was deposited onto the CIS layer by means of electron beam evaporation. In the second step, a structured Cr/Ag grid was deposited on top of the ITO layer, by means of lift off process. Finally, the Ga metallic back contact was formed on the unpolished side of the substrate by means of mechanical alloying. However the photo activity of the device was very low. Illumination with an AM1.5 spectrum yielded a photocurrent of typically 1-2 mA.

Negami et al [160] showed that sulfurization of Cu-In-O films could suppress the formation of binary phases in $CuInS_2$. $CuInS_2$ solar cells with a structure of ITO/ZnO/CdS/ $CuInS_2$ /Mo/Glass were fabricated after KCN treatment of the $CuInS_2$ films, since the obtained films had a Cu-rich composition with Cu/In ratios of above 1.2. CdS buffer layers of 50-100 nm thick were deposited using chemical bath deposition (CBD). After that, ZnO and ITO layers were deposited by RF-magnetron sputtering with thickness of 0.2 and 0.3 μm respectively. They studied the dependence of the performance of the cell on the H_2 gas pressure during the sulfurization process. Open circuit voltage (V_{oc}), short circuit current (J_{sc}) and fill factor (FF) increased with increasing H_2 gas pressure. They suggested that small amount of oxygen remained in the $CuInS_2$ films could affect the cell performance. ie, A sufficient reduction of Cu-In-O system during sulfurization process was necessary to achieve higher cell efficiencies. The $CuInS_2$ solar cell fabricated showed a conversion efficiency of 7.5 %.

An active area efficiency of 10.4% had been achieved for the cell structure $CuInS_2$ /CdS/ZnO by Klenk et al [161]. $CuInS_2$ films were prepared by sulfurization of sequentially deposited Cu/In stacks with elemental sulfur. Films were etched in a 10% aqueous solution of KCN for 5 minutes at room temperature prior to window layer deposition. Window layer consisted of a solution grown CdS and rf-sputtered i-ZnO and ZnO:Al. Substrate were float glass 1" x 1", bare or coated with e- beam evaporated Mo. The cell structure was completed with e-beam evaporated Ni/Al grid.

Controlled incorporation of Na onto the absorber layer of $CuInS_2$ solar cells improved cell performance remarkably. Without toxic KCN treatment, conversion efficiency of over 6% was achieved by sulfurization of sodium containing precursor by Watanabe et al [162], while the cell having Na free absorber layer showed poor cell performance of only 1%. They also investigated the characteristics of sodium incorporated $CuInS_2$ films by intentional addition and diffusion from soda lime glass. The striking difference in the film morphology between sodium-containing and sodium-free $CuInS_2$ films was the size and shape of grains. Na free $CuInS_2$ films had needle like grains on the surface. With Na the grains changed significantly to large and coarse. The enhancement of V_{oc} (235 mV to 665 mV) and FF (27% to 52.6%) was striking compared with J_{sc} . However, higher concentration of Na reduced cell efficiency. They related this effect to the formation of a highly resistive $NaInS_2$ phase on the surface of $CuInS_2$ films.

Park et al reported an efficiency of 5.66% for a $CuInS_2/CdS$ solar cell fabricated by depositing CdS thin film with dopant In of 1% on ternary compound $CuInS_2$ thin film [163]. A still better efficiency of 8.25% was obtained for a four layer structure low ρ - $CuInS_2$ /high ρ - $CuInS_2$ /high ρ -CdS/low ρ -CdS, which had back surface field and internal electric field by graded band gap. Mo coated glass slides were used as the substrate.

Nature of the substrate had very much influence on the properties of film deposited over it. The solar cell, which consisted of a $CuInS_2$ thin film prepared by sulfurization of a metallic precursor, deposited either on a Pt sheet or a Mo-coated soda lime glass substrate exhibited an efficiency of 10.5% at AM1.5 without antireflection coating [164]. Initially more Cu-rich film was often torn off from the substrate when Mo coated soda lime glass was used as substrate. Thin Ga layer with different thicknesses were initially deposited on Mo-coated glass substrate to improve the film adhesion. They obtained a relatively good efficiency when Ga layer

sandwiched between the precursor and Mo-coated substrate was 27 nm thick when compared to Ga free cell. Comparable efficiency was obtained for cells prepared on Pt substrate. It was revealed by XPS depth profiling that, after KCN treatment, the chalcopyrite absorber consisted of a stoichiometric portion in the bulk of the film and also an interface portion, which might be formed by the reaction of In with a Pt substrate. A comparable device performance was obtained when Mo-coated glass was used as a substrate.

Scheer et al investigated the electrical properties of polycrystalline CuInS_2 thin film grown by coevaporation by lateral electrical conductivity measurements [165]. They showed that annealing of Cu-poor films in S atmosphere, during an extended cool-down period, enhanced the lateral conductivity at room temperature, clearly showed the influence of the cool down step on the electronic film properties of $\text{CuInS}_2/\text{CdS}/\text{ZnO}$ devices. This influence was explained by the saturation of S vacancies during the cool-down period. By reducing the cooling rate from 10 K/min to 2 K/min, the efficiency increased from 3% to 8.3%, under AM1.5 illumination. They suggested that further improvements were expected, provided the room temperature conductivity in these films could be further increased.

In 1998 Gal et al electrodeposited films of size quantised CdS as a buffer layer on CuInS_2 [166]. The resulting $\text{CuInS}_2/\text{CdS}$ thin film solar cells gave increased photocurrents and higher light conversion efficiencies (>11%) than those made with conventional non-quantised CdS films. This was mainly due to the increased band gap of the quantised CdS, allowing more light to reach the active CuInS_2 layer. CIS films were deposited on Mo-coated glass by co evaporation of the elements. The films were etched in aqueous KCN for 30 seconds. ZnO was deposited onto the $\text{CuInS}_2/\text{CdS}$ structure by rf sputtering from a ceramic ZnO target doped with 2% by weight of Al_2O_3 . A Ni/Al grid was electron beam evaporated onto the ZnO as top contact.

Ennaoui et al [167] used ZnO, grown using SILAR technique, as buffer layer for CuInS_2 based solar cells. The motivation of searching for this alternative was to

eliminate the toxic cadmium and to improve the light transmission in the blue wavelength region since ZnO had a wider band gap (3.3 eV) compared to CdS (2.42 eV). Due to the higher band gap of the Cd free buffer layer, an enhanced response in the short wavelength of the spectrum was observed. However the cells still had lower efficiency (around 4%) compared to the standard devices with CdS buffer layer prepared under the same conditions (efficiency around 9%). Nevertheless they found comparable values of fill factor and photocurrent.

In the same year Penndorf et al developed a new technique “CIS CuT” for the preparation of polycrystalline single-phase CuInS_2 thin films for solar applications [86]. In a continuous roll-to-roll process, a copper tape was at first electrochemically plated with an In layer. In the second step, this tape underwent a rapid sulfurization process at about 600°C at atmospheric pressure. The Cu_{2-x}S layer formed at the top of CIS was removed by KCN etch. For CuInS_2 based solar devices, attempts to prepare the common $\text{CuInS}_2/\text{CdS}$ heterostructure had failed all the time. Surprisingly only a substrate of CuInS_2/p -type semiconductors lead to a diode characteristic. ZnTe, Cu_2O , Cu_{2-x}S and $\text{Cu}(\text{S},\text{O})$ had successfully been used to form such devices. For a $\text{CuInS}_2/\text{Cu}(\text{S},\text{O})$ device, the efficiency was determined to be 6.1%.

For CuInS_2 based thin film solar cells, total area efficiency of 11.1% and active area efficiency of 12.5% was reported by Klaer et al [168]. The sequential process for CuInS_2 preparation used in this study was based on dc magnetron sputtering for metal deposition, followed by sulfurization in elemental sulfur vapor. The CuInS_2 layer thickness was about 3 μm . Heterojunctions were then prepared by chemical bath deposition of 50 nm CdS and a sputtered transparent conducting ZnO window layer. Finally, an aluminium grid for contacting and an MgF_2 antireflection coating completed the cell. The best conversion efficiency was obtained with strongly copper-rich precursors with a Cu/In ratio of 1.8.

As Na incorporation resulted in a remarkable increase in the lateral conducting of Cu-poor CuInS_2 films, Watanabe et al investigated the effect of Na doping in CuInS_2 -based solar cells [169]. They explained the increase in the conductivity by Na incorporation by the annihilation of donor states, most likely In. They obtained drastic enhancement of efficiency to over 8% by incorporation of Na. CuInS_2 films were fabricated through sulfurization of In-S/Cu/Na₂S/In precursors. The cell structure was ITO/CdS/ CuInS_2 /Mo/SiO₂/SLG.

Two methods were commonly used to prepare CuInS_2 thin films for high efficiency solar cells. One was a Cu-rich process in which Cu-excess CuInS_2 thin films are grown by simultaneous evaporation or sulfurization with sulfur vapor or H₂S and then the CuS phase that segregated on the film surface was removed by treatment with potassium cyanide (KCN) solution. Using this method, it was possible to fabricate high-quality CuInS_2 films because CuS promoted the formation of large grains. Another method was the sodium-incorporation process. In this process, Cu-poor CuInS_2 films were grown by sulfurization of sodium containing precursor. It was well known that it was difficult to realize high efficiency Cu-poor CuInS_2 films compared with Cu-rich CuInS_2 ones because the films had poor crystallinity and extremely low hole concentration that were inadequate for solar cell applications. Sodium incorporation into CuInS_2 enhanced films conductivity and the conversion efficiency of the solar cells. Currently, this was the only means of fabricating high-efficiency solar cells based on Cu-poor CuInS_2 . In CuInSe_2 and CuInS_2 absorber films, gallium was commonly used as an isovalent substrate for In in order to enlarge the band gap.

In 1999, Watanabe et al obtained a high open circuit voltage exceeding 0.8 V by adding Ga to Na incorporated CuInS_2 thin films [170]. Cu(In,Ga)S_2 films were fabricated by sulfurization of Cu-In-Ga precursors containing Na in H₂S atmosphere. The cell structure was ITO/ZnO/CdS/ Cu(In,Ga)S_2 /Mo/Ti/SiO₂/SLG. They achieved

an efficiency of 11.2% with $V_{oc} = 802$ mV, $J_{sc} = 20.9$ mA/cm² and FF = 66.7% without any KCN treatment.

In 2000, Kneisel et al used thermal admittance spectroscopy, to study the defect properties of high efficiency $\text{CuInS}_2/\text{CdS}/\text{ZnO}$ thin film solar cells [171]. They found that defect spectra did not depend on the buffer layer. Two pronounced trap levels were found at 0.3 and 0.5 eV. Both were identified as majority carrier traps in the bulk of the p-CIS space charge region. The trap at 0.5 eV was correlated with a decrease in the open circuit voltage of the cells.

Performance of CuInS_2 solar cell, consisting of a transparent conductive oxide/ $\text{CdS}/\text{CuInS}_2$ heterostructure, had been analyzed by Ito et al [172]. A theoretical mode, in which a very thin n-type layer was assumed to exist at the interface between the p-type CuInS_2 and the n-type CdS buffer layer, had been developed to explain their characteristics. In this case an n-n heterojunction was formed between n-type CdS buffer layer and n-type CuInS_2 layer. The substrate material was found to have substantial influence on the device characteristics. When the absorber layer was prepared on a Mo-coated soda lime glass substrate by sulfurization, the heterostructure was an abrupt junction (in which the acceptor concentration was uniform throughout the p-type region). When prepared on a Pt foil substrate, the heterostructure was a linearly graded junction (in which the acceptor concentration increased linearly with the distance from the junction). These two types of junctions were theoretically discussed.

Hengel et al used Ga incorporated highly efficient CuInS_2 thin film solar cells for fundamental investigations on the recombination mechanism [173]. They demonstrated that the incorporation of small amount of Ga did not change the recombination mechanism as such. They also postulated a change from tunneling into interface states in the dark to a thermally activated process under illumination for $T > 150$ K.

In 2001, Siemer et al employed a rapid thermal process (RTP) for CuInS_2 absorbers to get an efficiency of 11.4% for the cell structure glass/Mo/ CuInS_2 /ZnO [174]. They used a sequential process with metallic layers of Cu and In rapidly heated in elemental sulfur vapor. All samples were prepared under Cu excess with atomic ratio $[\text{Cu}]/[\text{In}] = 1.8$. Segregation of CuS due to Cu excess had been removed by KCN etch. Admittance spectra showed a maximum in defect distribution about 140 meV which was attributed to interface states. The vapor pressure of sulfur and its constancy during the process had an important influence on device quality as the efficiency of solar cell was significantly improved by the use of a smaller reaction volume.

For CIS CuT cells, p-type Cu(O,S) buffer layer was commonly used which was having a band gap of 2.6 eV. This had been replaced by copper iodide (CuI), another p-type semiconductor with a higher band gap of 3.1 eV, to improve the cell performance [175]. They investigated two different configurations of the cell (i) the window layer concept, with a ZnO:Al window layer on the top of the buffer layer and (ii) the grid concept with direct contacting of CuI by the application of a metal grid. They formed Cu/CuInS₂/CuI/ZnO in the most promising concept. The efficiency had been improved from 3.89% to 5.38% on replacing Cu(O,S) by CuI.

Recently Klaer et al fabricated a CuInS_2 based mini-module on a $5 \times 5 \text{ cm}^2$ glass substrate consisting of seven integrated series connected cells with 9.2% efficiency [176]. The absorber layer was grown by a sequential process consisting of sputtering the metals with subsequent sulfurization in elemental sulfur vapor. The secondary CuS phase which formed due to copper excess ($\text{Cu}/\text{In} = 1.8$) was subsequently removed by KCN etching, leaving behind 2-3 μm stoichiometric CuInS_2 . CdS layer was deposited in a chemical bath and ZnO by sputtering. Thus layer structure of the complete module was Mo/ CuInS_2 /CdS/ZnO.

The composition and solar cell behavior of CuInS_2 /ZnSe junctions had been studied with XPS and electroreflectance (ER) techniques [177]. CuInS_2 films ($\text{Cu}/\text{In} =$

1.8) having thickness $\sim 2 \mu\text{m}$ were prepared by dc-sputtering deposition of a copper film and indium film onto a dc-sputtered Mo film on glass followed by sulfurization at 600°C . The secondary CuS phase was removed by KCN etching. ZnSe films were deposited by chemical bath deposition and ZnO window layer by sputtering. This configuration has given efficiencies above 9%.

For polycrystalline cells grain size must be large compared with the absorber layer thickness, if an appreciable fraction of short circuit current potentially available was to be realized in practice. Onuma et al developed a process to fabricate high efficiency solar cells using CuInS_2 films with very large grain [178]. They successfully prepared CuInS_2 film with a maximum precursor atomic Cu/In ratio of 3 without peeling from the substrate by heating during Cu/In evaporation and/or depositing Pt or Pd interlayer between Mo and CuInS_2 . They characterized CuInS_2 films, varying thickness from 2-9 μm and found that devices using thick films (which were over 4 μm) gradually showed low efficiency and low stability in spite of the high quality of the film without chemical etching. Therefore film thickness was controlled to be within 3-4 μm by chemical etching (Cu-rich), and the respective cells delivered an efficiency of 12%. The cell structure was SLG/Mo/(Pt or Pd)/ CuInS_2 /(CdS or $\text{In}(\text{OH},\text{S})$)/(ZnO:Al or In_2O_3)/(Ag paste or Ni/Al).

Luck et al investigated the influence of different Na concentrations on Cu rich CuInS_2 absorbers and devices [179]. Using different glass substrate types, the Na content in sequentially (and Cu-rich) prepared CuInS_2 films and corresponding CuInS_2 /CdS/ZnO thin film solar cells was varied. Even though the defect chemistry of Cu-rich sequentially processed CuInS_2 films changed as a consequence of Na presence, these changes were not relevant for the performance of the corresponding solar cells. Na did not seem to be critical for the Cu-rich preparation of high efficiency CuInS_2 /CdS/ZnO thin film solar cells using a sequential process.

Thin film solar cells of $\text{CuInS}_2/\text{Zn}(\text{Se},\text{O})/\text{ZnO}$ configuration had been studied from the point of view of their dependence on the $\text{Zn}(\text{Se},\text{O})$ chemical bath deposition (CBD) conditions by Chaparro et al [180]. The CBD growth was carried out under variable conditions in the bath (temperature and composition), to allow for buffer layers with identical thickness but under different kinetic regimes ie, electroless and chemical, and the effect on solar cell performance was studied. They characterized solar cells current-voltage curves (I-V) and quantum efficiency (QE) measurements. $\text{CuInS}_2/\text{Zn}(\text{Se},\text{O})$ heterojunctions were studied with Electron Beam Induced Current (EBIC) and cathodoluminescence (CL), which allowed for a closer view of the $\text{CuInS}_2/\text{Zn}(\text{Se},\text{O})$ interface and defects generated close to the CuInS_2 surface as a consequence of the CBD buffer growth.

In 2003, the superstrate configuration $\text{ZnO}/\text{CdS}/\text{CuInS}_2$ solar cells were prepared by cost-effective spray pyrolysis technique for all layers using Cu/In ratios of 0.9, 1 and 1.1 in spray solution by Mere et al [181]. But the conversion efficiency was low. They suggested that the columnar microstructure and small size of crystallites in sprayed films might be responsible for low output characteristics of sprayed cells.

The influence of sodium on the growth path and properties of Cu-poor prepared CuInS_2 thin films was investigated in situ using experiments of X-ray diffraction and Raman spectroscopy by Rudigier et al [182]. On Mo coated soda lime glass, sodium doping had been provided by exploration of NaF. Solar cell devices showed efficiencies of 1% without Na doping while with sodium, efficiencies as high as 5% could be achieved. The achieved improvements in conductivity and electronic properties opened the possibility to use Cu-poor prepared CIS thin films as absorber material in thin film solar cells.

Solar cells with structure $\text{glass}/\text{Mo}/\text{CIGS}/\text{buffer}/\text{i-ZnO}/\text{ITO}/\text{Ni-Al}$ grids had been realized and studied by Barreau et al [183]. They showed that $\beta\text{-In}_2\text{S}_3$ containing

Na thin films (BINS), having wider band gap could be used as good candidate to substitute CBD-CdS as buffer layer in CIGS-based solar cells. The best cell, reaching a conversion efficiency of 8.2%, has been achieved with a 100 nm thick BINS thin film.

Nakamura et al prepared $CuInS_2$ films by sulfurization of electrodeposited Cu-In precursors [184]. To remove Cu-S phases, the films were etched by KCN solution. Then n-CdS and ZnO:Al as a transparent electrode were deposited by chemical bath deposition and sputtering respectively. Thus the cell structure was Ag/ZnO:Al/CdS/ $CuInS_2$ /Ti. They obtained an efficiency of 1.3% for the first time with $CuInS_2$ -based solar cells prepared from electrodeposited Cu-In precursor.

Very recently in 2004, copper indium disulfide films were grown on Ti substrates by sulfurization of Cu-In precursors prepared by sequentially electrodeposited Cu and In layers [185]. Thin films of ZnSe were electrodeposited on $CuInS_2$ film in order to fabricate solar cell. The solar cell structure Ti/ $CuInS_2$ /ZnSe/metal produced an open circuit voltage, V_{oc} of 325 mV and short circuit current J_{sc} of 2 mA/cm² under AM 1.5 illumination.

Efficiency above 9% with V_{oc} exceeding 650 mV and fill factors well above 65% was achieved with copper indium disulfide cells fabricated on a continuous copper tape at IST(D) [186] by Verschraegen et al. They carried out capacitance and inductance vs voltage and vs frequency measurements, at temperatures varying between 80 and 300 K. Maxima were observed in the curves at high forward bias voltage. C-F and G-F measurements were interpreted in terms of deep states.

Introduction of a very thin $CuGaS_2$ base layer prepared on a Mo coated SLG in the heterostructure consisting of a $CuInS_2$ absorber was found to have beneficial effect on the cell performance [187]. A 13% efficiency cell was obtained using TCO/CdS/ $CuInS_2$ / $CuGaS_2$ structure. For this a Cu-Ga stacked precursor layer was vacuum evaporated onto the substrate followed by sulfurization in Ar/H₂S mixture gas. It was then treated with KCN solution. In the next step, an In-Cu-In-Cu stacked

precursor layer was deposited on the surface, again sulfurized and etched using KCN. They suggested the improvement in efficiency due to high crystallinity and electron barrier of the heterostructure. This was the best efficiency reported so far $CuInS_2$ based solar cell.

References

- [1] H. G. Ansell and R. S. Boorman *J. Electrochem. Soc.* **118** (1971) 133
- [2] H. Hahn and W. Klinger *Z. Inorg. Chem.* **260** (1949) 97
- [3] C. J. X. Rooymans *J. Inorg. Nucl. Chem.* **260** (1959) 78
- [4] J. V. Landuyt, H. Hatwell and S. Amelinckx *Mater. Res. Bull.* **3** (1968) 59
- [5] J. L. Shay and J. H. Wernick *Ternary Chalcopyrite Semiconductors: Growth, Electronic Properties and Applications*, Pergamon Press, Oxford (1975) 4
- [6] G. A. Kitaev and U. T. Dvounin *Inorg. Mater.* **12** (1976) 1448
- [7] J. George, K. S. Joseph. B. Pradeep and T. I. Palson *Phys. Stat. Sol. (a)* **106** (1988) 123
- [8] P. S. Vincett *Thin Solid Films* **100** (1983) 371
- [9] M. Kambas, J. Spyridelis and M. Balkanski *Phys. Stat. Sol. (a)* **105** (1981) 291
- [10] N. Barreau, J. C. Bernède, H. E. Maliki, S. Marsillac, X. Castel and J. Pinel *Solid State Commun.* **110** (1999) 231
- [11] M. A. M. Seyam *Vacuum* **63** (2001) 445
- [12] K. Hara, K. Sayama and H. Arakawa *Sol. Energy Mater. Sol. Cells* **62** (2000) 441
- [13] J. Herrero and J. Ortega *Sol. Energy Mater.* **17** (1988) 357
- [14] N. Naghavi, R. Henriquez, V. Latev and D. Lincot *Appl. Surf. Sci.* **222** (2004) 65
- [15] E. B. Yousfi, B. Weinberger, F. Donsanti, P. Cowache and D. Lincot *Thin Solid Films* **387** (2001) 29
- [16] R. Bayón, C. Maffiotte and J. Herrero *Thin Solid Films* **353** (1999) 100
- [17] C. Kaito, A. Ito, S. Kimura, Y. Kimura, Y. Saito and T. Nakada *J. Cryst. Growth* **218** (2000) 259
- [18] C. Kaito, Y. Saito and K. Fujita *J. Cryst. Growth* **94** (1989) 967
- [19] R. Diehl and R. Nische *J. Cryst. Growth* **28** (1975) 306
- [20] N. Barreau, S. Marsillac, D. Albertini and J. C. Bernède *Thin Solid Films* **403-404** (2002) 331



- [21] C. D. Lokhande, A. Ennaoui, D. S. Patil, M. Giersig, K. Diesner, M. Muller and H. Tributsch *Thin Solid Films* **340** (1999) 18
- [22] A. Goswami, G. D. Talele and S. B. Badachhape *Indian J. Pure Appl. Phys.* **14** (1976) 716
- [23] S. H. Yu, L. Shu, Y. S. Wu, J. Yang, Y. Xie and Y. T. Qian *J. Am. Ceram. Soc* **82** (2) (1999) 457
- [24] R. Kumaresan, M. Ichimura, N. Sato and P. Ramasamy *Mat. Sci. Eng.* **B96** (2002) 37
- [25] T. Yoshida, K. Yamaguchi, H. Toyoda, K. Akao, T. Sugiura, H. Minoura and Y. Nosaka *Proc. Electrochem. Soc.* **PV 97-20** (1997) 37
- [26] N. R. de Tacconi and K. Rajeshwar *J. Electro. Anal. Chem.* **444** (1998) 7
- [27] T. Asikainen, M. Ritala and M. Leskelä *Appl. Surf. Sci.* **82/83** (1994) 122
- [28] A. R. Barron *Adv. Mat. Opt. Elec.* **5** (1995) 245
- [29] A. A. El Shazly, D. Abd Elhady, H. S. Metwally and M. A. M. Seyam *J. Phys.:Condens. Mater.* **10** (1998) 5943
- [30] C. L. Cahill, B. Guliotta and J. B. Parise *Chem. Commun.* (1998) 1715
- [31] S. Yu, L. Shu, Y. Qian, Y. Xie, J. Yang and L. Yang *Mat. Res. Bull.* **33** (5) (1998) 717
- [32] V. G. Bassergenev, E. N. Ivanova, Y. A. Kovalevskaya, S. A. Gromilov, V. N. Kirichenko and S. V. Larionov *J. Inorg. Mat.* **32** (6) (1996) 592
- [33] K. Yamaguchi, T. Yoshida and A. Minoura *Thin Solid Films* **431-432** (2003) 354
- [34] C. Guillén, T. García, J. Herrero, M. T. Gutiérrez and F. Briones *Thin Solid Films* **451-452** (2004) 112
- [35] B. R. Sankapal, S. D. Sartale, C. D. Lokhande and A. Ennaoui *Sol. Energy Mater. Sol. Cells* **83** (2004) 447
- [36] Y. Xiong, Y. Xie, G. Du, X. Tian and Y. Qian *J. Solid state Chem.* **166** (2002) 336
- [37] L. Bhira, H. Essaidi, S. Belgacem, G. Couturier, J. Salardenne, N. Barreaux and J. C. Bernède *Phys. Stat. Sol (a)* **181** (2000) 427

- [38] H. B. Devore *Phys Rev.* **102** (1956) 1
- [39] N. Kamoun, R. Bennaceur, M. Amlouk, S. Belgacem, N. Milki, J. M. Frigerio and M. L. Theye *Phys. Stat. Sol (a)* **169** (1998) 97
- [40] W. T. Kim and C.D. Kim *J. Appl. Phys.* **60(7)** (1986) 2631
- [41] N. Bouguila, H. Bouzouita, E. Lecaze, A. B. Amara, H. Bouchriha and A. Dhoubi *J. Phys. III* **7** (1997) 1647
- [42] E. Kauer and A. Rabenau *Z. Naturef* **13a** (1958) 531
- [43] R. H. Bube and W. Mc Carroll *J. Phys. Chem. Solids* **10** (1959) 333
- [44] J. M. Gilles, H. Hatwell, G. Offergeld and J. Van Cakenberghe *Phys. Stat. Sol.* **2** (1962) K73
- [45] G. F. Garlick, M. Springford and H. Checinska *Proc. Phys. Soc.* **82** (1963) 16
- [46] M. Rehwald and G. Harbeke *J. Phys. Chem. Solids* **26** (1965) 1309
- [47] M. Kambas, A. Anagnostopoulos, S. Ves, B. Ploss and J. Spyridelis *Phys. Stat. Sol. (a)* **127** (1985) 201
- [48] R.S. Becker, T. Zhang, J. Elton and M. Saeki *Sol. Energy Mater.* **13** (1986) 97
- [49] J. C. Manificier, J. Gasiot and J. P. Fillard *J. Phys. E* **9** (1976) 1002
- [50] N. Barreau, J. C. Bernède and S. Marsillac *J. Cryst. Growth* **241** (2002) 51
- [51] N. Barreau, S. Marsillac, J. C. Bernède, T. B. Nasrallah and S. Belgacem *Phys. Stat. Sol (a)* **184 (1)** (2001) 179
- [52] N. M. Gasanly, A. Aydinli, N. S. Yaksek *Mat. Res. Bull.* **38** (2003) 699
- [53] N. M. Gasanly and A. Aydinli *Solid State Commun.* **101 (11)** (1997) 797
- [54] R. S. Mane and C. D. Lokhande *Mat. Chem. Phys.* **78** (2002) 15
- [55] S. Chaisitsak, T. Sugiyama, A. Shimizu, A. Yamada and M. Konagi *Proc. 11th PVSEC* (1999) 34
- [56] S. H. Choe, T. H. Bang, N. O. Kim, H. G. Kim, C. I. Lee, M. S. Jim, S. K. Oh and W. T. Kim *Semicond. Sci. Technol.* **16** (2001) 98
- [57] W. T. Kim, C. S. Yun, H. M. Jong and C. D. Kim *J. Appl. Phys.* **60(7)** (1986) 2357

- [58] W. T. Kim, W. S. Lee, C. S. Chung and C. D. Kim *J. Appl. Phys.* **63** (11) (1988) 5472
- [59] N. Kamoun, S. Belgacem, M. Amlouk, R. Bennaceur, J. Bonnet, F. Touhari, M. Nouaoura and L. Lassabatere *J. Appl. Phys.* **89**(5) (2001) 2766
- [60] L. Bhira, S. Belgacem and J. C. Bernède *J. Appl. Phys* **92**(19) (2002) 5327
- [61] A. Kulińska, M. Uhrmacher, R. Dedryvère, A. Lohstroh, H. Hofsäss, K. P. Lieb, A. P. Garcia and J. C. Jumas *J. Solid State Chem.* **177** (2004) 109
- [62] M. Amlouk, M. A. Ben Said, N. Kamoun, S. Belgacem, N. Brunet and D. Barjon *Jpn. J. Appl. Phys.* **38** (1999) 26
- [63] N. M. Gasanly, H. Özkan, A. Aydinli and I. Yilmaz *Solid State Commun.* **110** (1999) 231
- [64] V. G. Bessergenev, A. V. Bessergenev, E. N. Ivanova and Y. A. Kovaevskaya *J. Solid State Chem.* **137** (1998) 6
- [65] J. C. Bernède, N. Barreau, S. Marsillac and L. Assmann *Appl. Surf. Sci.* **195** (2002) 222
- [66] L. L. Kazmerski, M. S. Ayyagari and G. A. Sanborn *J. Appl. Phys* **46**(11) 1975 4865
- [67] Y. Akaki, H. Komaki, K. Yoshino and T. Iakari *J. Vac. Sci. Technol. A* **20**(4) (2002) 1486
- [68] K. Djessas, G. Massé and M. Ibannaim *J. Electro Chem. Soc.* **147**(4) (2000) 1235
- [69] M. K. Agarwal, P. D. Patil, S. H. Chaki and D. Lekshminarayana *Bull. Mater. Sci.* **21**(4) (1998) 291
- [70] Y. B. He, W. Kriegseis, B. K. Meyer, A. Polity and M. Serafin *Appl. Phys. Lett.* **83**(9) (2003) 1743
- [71] H. Hahn, H. Metzner, B. Plikat and M. Seibt *Appl. Phys. Lett.* **72**(21) (1998) 2733
- [72] M. Kanzari and B. Rezig *Semicond. Sci. Technol.* **15** (2000) 335
- [73] S. Mahmoud and A. Hamid Eid *FIZIKA A* **6** (1997) 171
- [74] H. M. Pathan and C. D. Lokhande *Appl. Surf. Sci.* **239** (2004) 11

- [75] R. N. Battacharya, D. Cahen and G. Hodes *Sol. Energy Mater.* **10** (1984) 41
- [76] C. Dzionk, H. Metzner, S. Hessler and H. E. Mahnke *Thin Solid Films* **299** (1997) 38
- [77] J. D. Harris, K. K. Banger, D. A. Scheiman, M. A. Smith, M. H. C. Jin and A. F. Hepp *Mat. Sci. Engg. B* **98** (2003) 150
- [78] K. Wakita, K. Nishi, Y. Ohta and T. Onishi *Appl. Phys. Lett.* **85(15)** (2004) 3083
- [79] H. Matsushita, T. Mihira and T. Takizawa *J. Cryst. Growth* **197** (1999) 169
- [80] R. W. Miles, K. T. R. Reddy and I. Forbes *J. Cryst. Growth* **198/199** (1999) 169
- [81] J. Herrero and J. Ortega *Sol. Energy Mater.* **20** (1990) 53
- [82] R. Scheer, K. Diesner and H. J. Lewerenz *Thin Solid Films* **268** (1995) 130
- [83] S. K. Kim, W. J. Jeong, G. C. Park, Y. G. Back, Y. G. Jeong and Y. T. Yoo *Synthetic Metals* **71** (1995) 1747
- [84] S. Nakamura and A. Yamamoto *Sol. Energy Mater. Sol. Cells* **49** (1997) 415
- [85] Y. Yamamoto, T. Yamaguchi, T. Tanaka, N. Tanahashi and A. Yoshida *Sol. Energy Mater. Sol. Cells* **49** (1997) 399
- [86] J. Penndorf, M. Winkler, O. Tober, D. Röser and K. Jacobs *Sol. Energy Mater. Sol. Cells* **53** (1998) 285
- [87] I. Konovalov, O. Tober, M. Winkler and K. Otte *Sol. Energy Mater. Sol. Cells* **67** (2001) 49
- [88] R. Scheer, I. Luck, H. Sehnert and H. J. Lewerenz *Sol. Energy Mater. Sol. Cells* **41/42** (1996) 261
- [89] O. Kijatkina, M. Krunk, A. Mere, B. Mahrov and L. Dlozik *Thin Solid Films* **431-432** (2003) 105
- [90] N. Kamoun, N. Jebbari, S. Belgacem, R. Bennaceur, J. Bonnet, F. Touhari and L. Lassabatere *J. Appl. Phys.* **91 (4)** (2002) 1952
- [91] B. Pamplin and R. S. Feigelson *Thin Solid Films* **60** (1979) 141
- [92] M. Gorska, R. Beaulieu, J. J. Loferski and B. Rossler *Sol. Energy Mater.* **1** (1979) 313

- [93] A. N. Tiwari, D. K. Pandya and K. L. Chopra *Thin Solid Films* **130** (1985) 217
- [94] P. Raja Ram, R. Thangaraj, A. K. Sharma and O. P. Agnihotri *Solar Cells* **14** (1985) 123
- [95] H. Bihri, C. Messaoudi, D. Sayah, A. Boyer, A. Mzerd and M. Abd-Lefdil *Phys. Stat. Sol. (a)* **129** (1992) 193
- [96] M. Ortega López and A. M. Acevedo *Thin Solid Films* **330** (1998) 96
- [97] M. Krunks, V. Mikli, O. Bijakina and E. Mellikov *Appl. Surf. Sci.* **142** (1999) 356
- [98] M. C. Zouaghi, T. B. Nasrallah, S. Marsillac, J. C. Bernède and S. Belgacem *Thin Solid films* **382** (2001) 39
- [99] M. Krunks, O. Bijakina, V. Mikli, H. Rebane, T. Varema, M. Altosaar and E. Mellikov *Sol. Energy Mater. Sol. Cells* **69** (2001) 93
- [100] M. Krunks, O. Kijatkina, H. Rebane, I. Oja, V. Mikli and A. Mere *Thin Solid Films* **403-404** (2002) 71
- [101] H. Bihri and M. Abd-Lefdil *Thin Solid Films* **354** (1999) 5
- [102] S. Marsillac, M. C. Zouaghi, J. C. Bernede, T. B. Nasrallah and S. Belgacem *Sol. Energy Mater Sol. Cells* **76** (2003) 125
- [103] T. H. Hsu, J. S. Lee and H. L. Hwang *J. Appl. Phys.* **68(1)** (1990) 283
- [104] M. Alt, H. J. Lewerenz and R. Scheer *J. Appl. Phys* **81(8)** (1997) 3667
- [105] Y. L. Wu, H. Y. Lin, C. Y. Sun, M. H. Yang and H. L. Hwang *Thin Solid Films* **168** (1989) 113
- [106] S. Mora, N. Romeo and L. Tarricone *Solid State Commun.* **29** (1979) 155
- [107] L. Y. Sun, L. L. Kazmerski, A. H. Clark, P. J. Ireland and D. W. Morton *J. Vac. Sci. Technol.* **15(2)** (1978) 265
- [108] H. Neumann, W. Hörig, V. Savelev, J. Lagzdonis, B. Schumann and G. Kühn *Thin Solid Films* **79** (1981) 167
- [109] R. Scheer, I. Luck, M. Kaniso, R. Kurps and D. Krüger *Thin Solid Films* **361-362** (2000) 468

- [110] K. Fukuzaki, S. Kohiki, H. Yoshikawa, S. Fukushima, T. Watanabe and I. Kojima *Appl. Phys. Lett.* **73** (10) (1998) 1385
- [111] T. Yamamoto *Jpn. J. Appl. Phys.* **37** (1998) L1478
- [112] T. Yamamoto, T. Watanabe and Y. Hamashoji *Physica B* **308-310** (2001) 1007
- [113] T. Watanabe, H. Nakazawa, M. Matsui, H. Ohbo and T. Nakada *Sol. Energy Mater. Sol. Cells* **49** (1997) 357
- [114] T. Walter, A. Content, K. O. Velthaus, and H. W. Schock *Sol. Energy Mater. Sol. Cells* **26** (1992) 357
- [115] R. Scheer, T. Walter, H. W. Schock, M. L. Fearheiley, and H. J. Lewerenz *Appl. Phys. Lett.* **63** (1993) 3294
- [116] Y. Ogawa, A. J. Waldau, Y. Hashimoto and K. Ito *Jpn. J. Appl. Phys.* **33** (12B) (1994) L1775
- [117] Y. Hashimoto, K. Takeuchi, and K. Ito *Appl. Phys. Lett.* **67**(7) (1995) 980
- [118] K. Müller, R. Scheer, Y. Burleov and D. Schmeißer *Thin Solid Films* **451-452** (2004) 120
- [119] M. Aggour, U. Störkel, C. Murrell, S. A. Campbell, H. Jungblut, P. Hoffmann, R. Mikalo, D. Schmeißer and H. J. Lewerenz *Thin Solid Films* **403-404** (2002) 57
- [120] J. L. Lin, L. M. Lue, J. T. Lue, M. H. Yang and H. L. Hwang *J. Appl. Phys.* **59**(2) (1986) 378
- [121] A. P. Deshpande, V. B. Sapre and C. Mande *J. Phys. C: Solid State Phys.* **16** (1983) L 433
- [122] T. Abe, S. Kohiki, K. Fukuzaki, M. Oku and T. Watanabe *Appl. Surf. Sci.* **174** (2001) 40
- [123] P. M. Bridenbaugh and P. Migliorato *Appl. Phys. Lett.* **26**(8) (1975) 459
- [124] J. A. Garcia, A. P. Rodriguez, A. R. Rodriguez, J. R. Morante, L. C. Barrio, R. Scheer and R. Klenk *J. Vac. Sci. Technol. A* **19**(1) (2001) 232
- [125] H. L. Hwang, C. Y. Sun, C. Y. Leu, C. L. Cheng and C. C. Tu *Revue De Physique* **13** (1978) 745

- [126] P. Guha, D. Das, A. B. Maity, D. Ganguli and S. Chaudhuri *Sol. Energy Mater. Sol. Cells* **80** (2003) 15
- [127] M. Kanzari and B. Rezig *J. Mater. Sci: Mater. Electronics* **10** (1999) 151
- [128] J. Grzanna and H. Migge *J. Mater. Res.* **12(2)** (1997) 355
- [129] N. Tsujii, H. Kitazawa and G. Kido *Phys. Stat. Sol. (a)* **189 (3)** (2002) 951
- [130] A. Weidinger, J. Krauser, Th. Riedle, R. Klenk, M. Ch. Lux Steiner and M. V. Yakushev *Proc. Mat. Res. Soc.* **513** (1998) 177
- [131] G. Lippold, K. Otte, H. Schlemm and W. Grill *Proc. Mat. Res. Soc.* **513** (1998) 269
- [132] K. Otte, G. Lippold, D. Grambole, F. Herrmann, H. Schlemm, A. Schindler and F. Bigl *Proc. Mat. Res. Soc.* **513** (1998) 275
- [133] T. M. Hsu *Phys. Lett. A* **133** (1988) 79
- [134] J. M. Gil, P. J. Mendes, L. P. Ferreira, H. V. Alberto, R. C. Vilao, N. Ayres de Campos, A. Weidinger, Y. Tomm, Ch. Niedermayer, M. V. Yukushev, R. D. Tomlinson, S. P. Cottrell and S. F. J. Cox *Physical Review B* **59 (3)** (1999) 1912
- [135] K. Töpfer, J. Krauser, J. Bruns, R. Scheer, A. Weidinger and D. Bräunig *Sol. Energy Mater. Sol. Cells* **49** (1997) 383
- [136] R. P. Vijaya Lakshmi, R. Venugopal, D. R. Reddy and B. K. Reddy *Solid State Commun.* **82 (12)** (1992) 997
- [137] K. Wakita, N. Nakayama, M. Matsuo and N. Yamamoto *Analytical Sciences* **17** (2001) s299
- [138] M. Nanu, J. Schoonman and A. Goossens *Thin Solid Films* **451–452** (2004) 193
- [139] T. Yamamoto and H. K. Yoshida *Jpn. J. Appl. Phys.* **34** (1995) L 1584
- [140] K. Wakita, M. Matsuo, G. Hu, M. Iwai and N. Yamamoto *Thin Solid Films* **431–432** (2003) 184
- [141] J. J. M. Binsma, L. J. Giling and J. Bloem *J. Lumin.* **27** (1982) 35
- [142] H. Y. Ueng and H. L. Hwang *J. Phys. Chem. Solids* **50 (12)** (1989) 1297
- [143] H. Y. Ueng and H. L. Hwang *J. Phys. Chem. Solids* **51** (1990) 11

- [144] J. Krustok, J. Raudoja, J. H. Schön, M. Yakushev and H. Collan *Thin Solid Films* **361-362** (2000) 406
- [145] G. Massé, N. Lahlou and C. Butti *J. Phys. Chem. Solids* **42** (1981) 449
- [146] K. Töpper, J. Bruns, R. Scheer, M. Weber, A. Weidinger and D. Bräunig *Appl. Phys. Lett.* **71** (4) (1997) 482
- [147] J. H. Schön and E. Bucher *Phys. Stat. Sol. (a)* **171** (1999) 511
- [148] H. J. Lewerenz *Sol. Energy Mater. Sol. Cells* **83** (2004) 395
- [149] P. Würfel *Physica E* **14** (2002) 18
- [150] J. M. Meese, J. C. Manthuruthil and D. R. Locker *Bull. Amer. Phys. Soc.* **20** (1975) 696
- [151] K. L. Chopra and S. R. Das *Thin Film Solar Cells*, Plenum Press, New York (1983) 83
- [152] L. L. Kazmerski, F. R. White, M. S. Ayyagari, Y. J. Juang and R. P. Patterson *J. Vac. Sci. Technol.* **14**(1) (1977) 65
- [153] L. L. Kazmerski and G. A. Sanborn *J. Appl. Phys.* **48** (7) (1977) 3178
- [154] S. Kumar, A. N. Tiwari, O. S. Sastry, D. K. Pandya and K. L. Chopra *Bull. Mater. Sci.* **8** (3) (1986) 285
- [155] S. Uenishi, K. Tohyama and K. Ito *Sol. Energy Mater. Sol. Cells* **35** (1994) 231
- [156] K. Subbaramaiah and V. S. Raja *Sol. Energy Mater. Sol. Cells* **32** (1994) 1
- [157] T. Watanabe and M. Matsui *Jpn. J. Appl. Phys.* **35** (1996) 1681
- [158] D. Braunger, D. Hariskos, T. Walter and H. W. Schock *Sol. Energy Mater. Sol. Cells* **40** (1996) 97
- [159] H. Metzner, Th. Hahn, Chr. Schmiga, J. H. Bremer, D. Borchert, W. R. Fahrner and M. Seibt *Sol. Energy Mater. Sol. Cells* **49** (1997) 337
- [160] T. Negami, Y. Hashimoto, M. Nishitani and T. Wada *Sol. Energy Mater. Sol. Cells* **49** (1997) 343
- [161] R. Klenk, U. Blieske, V. Dieterle, K. Ellmer, S. Fiechter, I. Hengel, A. Jäger-Waldau, T. Kampschulte, Ch. Kaufmann, J. Klaer, M. Ch. Lux-Steiner, D.

- Braunger, D. Hariskos, M. Ruckh and H. W. Schock *Sol. Energy Mater. Sol. Cells* **49** (1997) 349
- [162] T. Watanabe, H. Nakazawa, M. Matsui, H. Ohbo and T. Nakada *Sol. Energy Mater. Sol. Cells* **49** (1997) 357
- [163] G. C. Park, H. D. Chung, C. D. Kim, H. R. Park, W. J. Jeong, J. U. Kim, H. B. Gu and K. S. Lee *Sol. Energy Mater. Sol. Cells* **49** (1997) 365
- [164] T. Nakabayashi, T. Miyazawa, Y. Hashimoto and K. Ito *Sol. Energy Mater. Sol. Cells* **49** (1997) 375
- [165] R. Scheer, M. Alt, I. Luck and H. J. Lewerenz *Sol. Energy Mater. Sol. Cells* **49** (1997) 423
- [166] D. Gal, G. Hodes, D. Hariskos, D. Braunger and H. W. Schock *Appl. Phys. Lett.* **73** (21) (1998) 3135
- [167] A. Ennaoui, M. Weber, R. Scheer and H. J. Lewerenz *Sol. Energy Mater. Sol. Cells* **54** (1998) 277
- [168] J. Klaer, J. Bruns, R. Henninger, K. Siemer, R. Klenk, K. Ellmer and D. Bräunig *Semicond. Sci. Technol.* **13** (1998) 1456
- [169] T. Watanabe, H. Nakazawa and M. Matsui *Jpn. J. Appl. Phys.* **37** (1998) L 1370
- [170] T. Watanabe and M. Matsui *Jpn. J. Appl. Phys.* **38** (1999) L 1379
- [171] J. Kneisel, K. Siemer, I. Luck and D. Bräunig *J. Appl. Phys.* **88** (9) (2000) 5474
- [172] K. Ito, N. Matsumoto, T. Horiuchi, K. Ichino, H. Shimoyama, T. Ohashi, Y. Hashimoto, I. Hengel, J. Beier, R. Klenk, A. Jäger-Waldau and M. Ch. Lux-Steiner *Jpn. J. Appl. Phys.* **39** (2000) 126
- [173] I. Hengel, A. Neisser, R. Klenk and M. Ch. Lux-Steiner *Thin Solid Films* **361-362** (2000) 458
- [174] K. Siemer, J. Klaer, I. Luck, J. Bruns, R. Klenk and D. Bräunig *Sol. Energy Mater. Sol. Cells* **67** (2001) 159
- [175] J. Wienke, V. Groen-Smit, M. Burgelman, S. Degrave and J. Penndorf *Thin Solid Films* **387** (2001) 165

- [176] J. Klaer, K. Siemer, I. Luck and D. Bräunig *Thin Solid Films* **387** (2001) 169
- [177] A. M. Chaparro, C. Maffiotte, M. T. Guliérrez, J. Herrero, J. Klaer, K. Siemer and D. Bräunig *Thin Solid Films* **387** (2001) 104
- [178] Y. Onuma, K. Takeuchi, S. Ichikawa, M. Harada, H. Tanaka, A. Koizumi and Y. Miyajima *Sol. Energy Mater. Sol. Cells* **69** (2001) 261
- [179] I. Luck, J. Kneisel, K. Siemer, J. Bruns, R. Scheer, R. Klenk, N. Janke and D. Bräunig *Sol. Energy Mater. Sol. Cells* **67** (2001) 151
- [180] A. M. Chaparro, M. T. Guliérrez, J. Herrero, J. Klaer, M. J. Romero and M. M. Al-Jassim *Prog. Photovolt: Res. Appl.* **10** (2002) 465
- [181] A. Mere, O. Kijattina, H. Rebane, J. Krustok and M. Krunka *J. Phys. Chem. Solids* **64** (2003) 2025
- [182] E. Rudigier, Ch. Peitzker, M. Wimbor, I Luck, J. Klaer, R. Scheer, B. Barcones, T. J. Colin, J. A. Garcia, A. P. Rodriguez and A. R. Rodriguez *Thin Solid Films* **431-432** (2003) 110
- [183] N. Barreau, J. C. Bernède, S. Marsillac, C. Amory and W. N. Shafarman *Thin Solid Films* **431-432** (2003) 326
- [184] S. Nakamura and A. Yamamoto *Sol. Energy Mater. Sol. Cells* **75** (2003) 81
- [185] R. P. Wijesundara and W. Siripala *Sol. Energy Mater. Sol. Cells* (in Press)
- [186] J. Verschraegen, M. Burgelman and J. Penndorf *Thin Solid Films* **451-452** (2004) 179
- [187] H. Goto, Y. Hashimoto and K. Ito *Thin Solid Films* **451-452** (2004) 552

Chapter 3**STUDIES ON INDIUM SULFIDE THIN FILMS PREPARED USING CHLORIDE BASED PRECURSOR SOLUTION****3.1 Introduction**

Thin film solar cells based on Cu (In,Ga) Se₂, CuInSe₂ and CuInS₂ absorber layers showed promising solar energy conversion efficiencies (>10%) [1-3] using CdS as buffer layer. Nowadays a lot of research is going on for Cd- free CIS based solar cells. The motivation of searching for an alternative buffer layer is not only to eliminate toxic cadmium but also to improve light transmission in the blue wavelength region by using a material with a wider band gap compared to CdS [4]. Recently Nakada and Mizutani [5] showed that use of CBD-ZnS ($E_g > 3$ eV) as buffer layer allowed reaching a conversion efficiency of 18.1%. Other materials like ZnO, ZnSe, In₂Se₃, In_x(OH,S)_y were also used to replace CdS effectively [6-9]. ZnO buffer layer, deposited using CBD technique yielded comparable values of fill factor and photocurrent (as in the case of CdS) for CuInS₂ based solar cell even though the efficiency was only 4% [6]. The solar cell structure Mo/CIS/In₂Se₃/ZnO in which In₂Se₃ is the buffer layer, yielded an efficiency of 8.3% [8]. An active area efficiency of 11.4% was obtained for a CuInS₂ based solar cell in which CdS was replaced by In_x(OH,S)_y [9]. In₂S₃ is another such material. Indium sulfide is an important semiconductor material for optoelectronic and photovoltaic applications [10, 11] and is a promising candidate for many technological applications due to its stability, wider band gap and photoconductive behaviour [12]. A number of techniques have been used to prepare this compound such as CBD [13], organometallic chemical evaporation [14], spray pyrolysis [11, 12, 15], thermal evaporation [16], reactive evaporation [17], rf sputtering [18] and atomic layer epitaxy [19].

Chemical Spray Pyrolysis (CSP) technique, one of the chemical methods for the preparation of thin films, is widely used to deposit a variety of thin films. It involves spraying a solution, usually aqueous, containing soluble salts of constituents of the desired compound, onto a heated substrate. It is quite suitable for depositing large area thin films using simple apparatus with good reproducibility. In CSP technique it is quite easy to vary the stoichiometry of the film or the doping profile. Stoichiometry can be varied by changing molarity of the solution while dopant concentration in the film can be varied by changing the quantity of dopant dissolved in the solution. These parameters can be varied along film thickness itself. A major shortcoming of this technique is that sometimes films prepared using this may have voids/pinholes.

CSP was developed in the early 1960's by Hill and Chamberlin and preparation of thin films of certain inorganic sulfides and selenides using this technique was first reported by Chamberlin and Skarman [20]. At present, this method is used for preparation of binary and ternary compounds, and their quaternary alloys. Optical energy band gaps of β - In_2S_3 thin films grown by spray pyrolysis was studied by Kim et al [15]. They also studied $\text{Co}_x\text{In}_2\text{S}_{3+x}$ thin films having various compositions with x varying from 0.0 to 0.6 [21]. L. Bhira et al used this technique for the preparation of indium sulfide films and they studied the structural and photoelectrical properties [12]. Optical properties of InS layers with In/S composition ratio varying from 0.4 to 0.6 deposited using an airless spray technique had been studied by Kamoun et al [22]. They also studied the effect of the nature of the substrate on β - In_2S_3 and introduction of small amounts of Al (β - $\text{In}_{2-x}\text{Al}_x\text{S}_3$) on the properties of the film [23]. Acoustic properties of indium sulfide thin films prepared by spray technique were also reported [11]. But the effect of substrate temperature and variation of composition of indium on the structural compositional, optical and electrical properties of indium sulfide films prepared using CSP has not been studied yet.

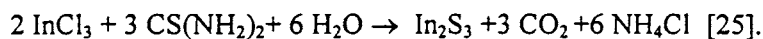
Our intension was to use In_2S_3 films prepared using CSP technique, for fabricating pn junction with CuInS_2 for solar cell application. We were interested in depositing In_2S_3 film having suitable photosensitivity and electrical resistivity for this application. Hence photoconductive $\beta\text{-In}_2\text{S}_3$ thin films were prepared using CSP technique at different substrate temperatures and various indium to sulfur ratios. Knowledge of variation of photosensitivity of this material with deposition, structural or stoichiometric parameters are very much essential for photovoltaic device application. It is to be specifically noted that in CSP technique, it is comparatively easy to make variation in stoichiometry of the sample. A detailed study on the variations in structural, compositional, optical and electrical properties of In_2S_3 films due to changes in molarity ratio of spray solution, substrate temperature and sample thickness was done as we could not find out such an exhaustive study on this important material from earlier publications.

3.2 Experimental Details

Experimental set-up for the deposition is schematically shown in Fig. 3.1. Cleaned glass slides ($37 \times 12 \times 1.4 \text{ mm}^3$) were placed on a thick iron block ($15 \times 9 \times 1 \text{ cm}^3$), which can be heated to the required temperature with a controlled heater. Temperature of substrate holder was measured using a digital thermometer (Thermis, series 4000) and temperature control was achieved using a variable transformer. Spray head and heater with substrate were kept inside a chamber provided with an exhaust fan for removing gaseous by-products and vapour of the solvent (here water). During spray, the temperature of substrate was kept constant with an accuracy of $\pm 5^\circ\text{C}$. Pressure of carrier gas was noted using a manometer and was kept at $90 \pm 0.5 \text{ cm}$ of Hg. Spray rate was 20 ml/min , and the distance between spray head and substrate was $\sim 15 \text{ cm}$. In order to get uniform composition and thickness, the spray head was moved to either side manually with uniform speed. At a time we usually kept three

substrates spread over the heater for sample preparation. All these samples were found to be good for further studies.

In₂S₃ thin films were deposited by spraying aqueous solutions of indium chloride (InCl₃) and thio-urea (CS(NH₂)₂) using compressed air as carrier gas. Thiourea was chosen as the source of sulfur ions in spray solution because it avoids precipitation of metallic sulfides and hydroxides since it forms complexes with indium ions easily [24]. Aqueous solutions of these salts were prepared in distilled water. Indium to sulfur ratio in the solution was varied by varying molar concentration of InCl₃ and CS (NH₂)₂. Formation of In₂S₃ results from the chemical reaction:



Total volume of the solution sprayed was 400 ml in all cases. Samples were prepared at different substrate temperatures in the range 150°C to 380°C with an accuracy of ± 5°C keeping In/S ratio at 2/3. Then the molar concentration of sulfur in the solution was varied by keeping the indium concentration at 2 so that In/S ratio varied from 2/1 to 2/8. For this, molarity of indium chloride was kept at 0.025 M and that of thiourea was varied. Later keeping the sulfur concentration at 3, 6 and 8, the concentration of indium was varied from 1.2 to 2.5 with the aim of studying the variation in photoresponse of the sample. Samples having different thicknesses were also prepared by varying the total volume of the solution sprayed as 400 ml, 600 ml, 800 ml and 1000 ml. In all these cases substrate temperature was kept at 300°C. Details of changes in the properties of the films due to variation in stoichiometry, substrate temperature and volume of solution will be discussed in the following section.

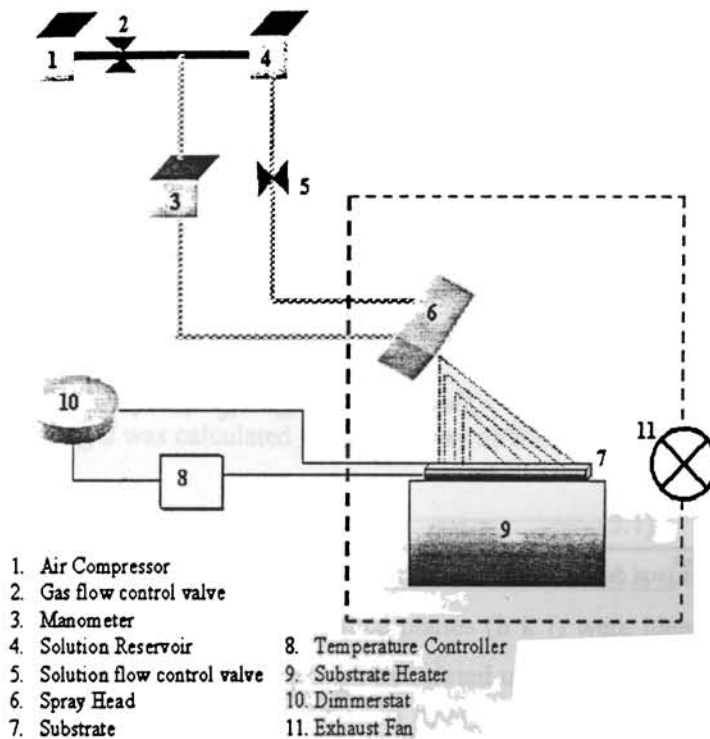


Fig. 3.1 Experimental set-up for spray pyrolysis system

3.3 Results and Discussion

3.3.1 Effect of Variation of Substrate Temperature

Samples were prepared at different substrate temperatures in the range 150°C to 380°C keeping the In/S ratio at 2/3. The samples prepared were found to be very uniform for all the substrate temperatures except at 150°C. Thickness of the films prepared at 300°C was found to be 1 μm from Stylus measurement [Fig.3.2]. Conductivity of all the samples was determined to be n-type using Hot Probe method.

3.3.1.1 Structural Analysis

X-Ray Diffraction (XRD) is an extremely important technique in the field of material characterization to obtain information on an atomic scale from both crystalline and non crystalline (amorphous) materials.

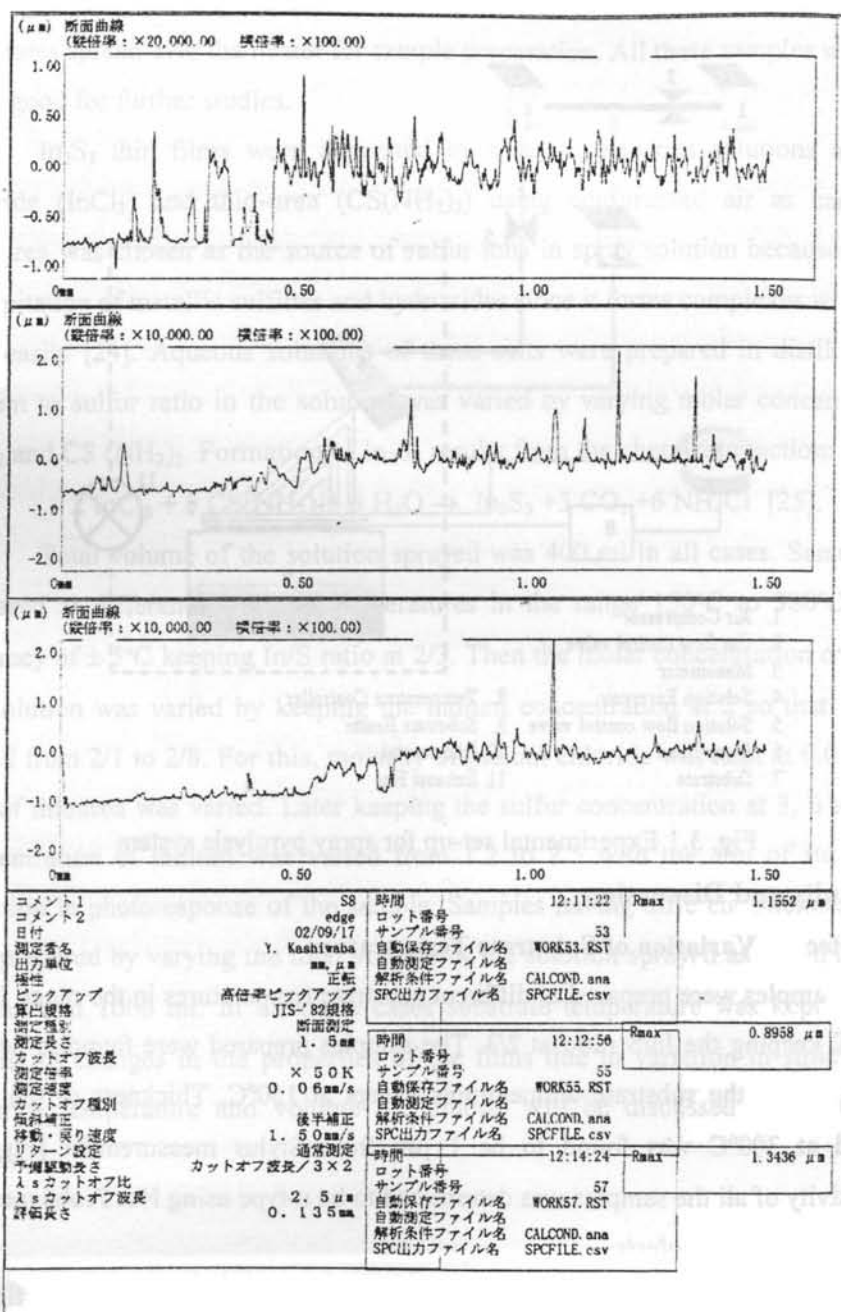


Fig. 3.2 Stylus measurement of In_2S_3 film

It can be used to determine the phase content in many minerals and materials. It requires no elaborate sample preparation and is essentially non-destructive. Generally, it gives a whole range of information about the crystal structure, orientation, crystallite size, composition (with the help of standards), defects and stresses in thin films. Experimentally obtained diffraction pattern of the sample is compared with Joint Council Powder Diffraction (JCPDS) data for Standards. This gives information of different crystallographic phases, the relative abundance and preferred orientations. From the width of the diffraction peak, average grain size in the film can also be estimated.

Interplanar spacing d was calculated from the X-ray diffraction profiles using the formula,

$$2d \sin \theta = n\lambda \dots\dots\dots(3.1)$$

where θ is the Bragg angle, n is the order of the spectrum and λ is the wavelength of X-rays. Using the d values the set of lattice planes (h k l) were identified from the standard data and the lattice parameters are calculated using the following relations.

For the tetragonal systems,

$$\frac{1}{d^2} = \frac{(h^2 + k^2)}{a^2} + \frac{l^2}{c^2} \dots\dots\dots(3.2)$$

and for hexagonal systems,

$$\frac{1}{d^2} = \frac{4(h^2 + hk + k^2)}{3a^2} + \frac{l^2}{c^2} \dots\dots\dots(3.3)$$

where a and c are lattice parameters. The grain size (D) can be evaluated using Scherrer's formula,

$$D = \frac{k\lambda}{\beta \cos \theta} \dots\dots\dots(3.4)$$

where k is a constant which is nearly equal to one and β is the "full width at half maximum (FWHM)", usually measured in radians.

In the present study, XRD analysis was done using Rigaku (D.Max.C) X-Ray Diffractometer, with Cu K α ($\lambda = 1.5405 \text{ \AA}$) radiation and a Ni filter operated at 30 kV and 20 mA. Fig.3.3 shows the X-ray diffraction pattern of the films deposited at different substrate temperatures. All figures have the same scale on Y-axis.

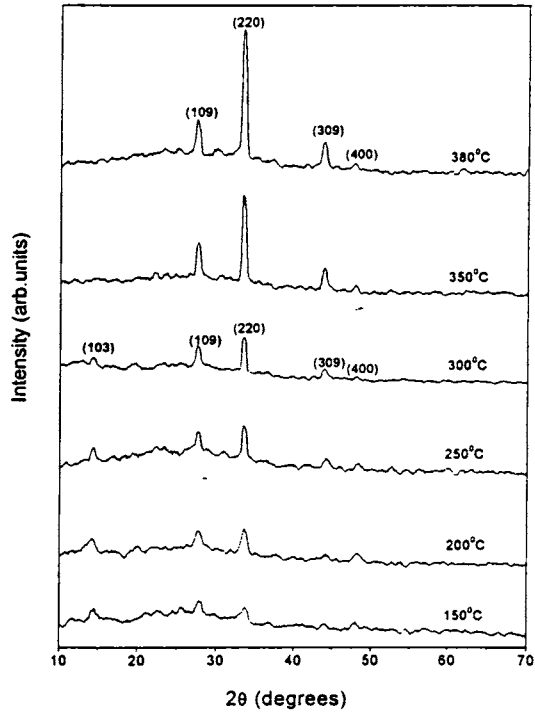


Fig.3.3 XRD pattern of β -In $_2$ S $_3$ films prepared at different substrate temperatures

The d values coincided with that of β -In $_2$ S $_3$ in standard JCPDS data card (25-390) with preferential orientation along the (220) plane at $2\theta = 33.45^\circ$. Eventhough samples prepared at 380°C showed better crystallinity, maximum photoresponse was observed for samples prepared at 300°C and this temperature was maintained for

various In/S ratios. The d values and the relative intensities are compared in Table 3.1 for β - In_2S_3 films deposited at 300°C.

As the temperature was increased from 150°C to 200°C the intensity of the peak corresponding to (220) plane increased. At still higher temperatures the small peak corresponding to (103) plane disappeared but the intensity of the peak corresponding to the (309) plane increased. It is worth mentioning here that for the sample prepared at 150°C, peaks of (103) plane, (109) plane and (220) plane were all having almost the same intensity.

Table 3.1 X-ray data of β - In_2S_3 film

2θ (degrees)	d [Å] (observed)	d [Å] (standard)	hkl	I/I_0 (observed)	I/I_0 (standard)
14.30	6.19	6.21	103	29.85	30
27.55	3.24	3.249	109	55.85	100
33.45	2.68	2.694	220	100	50
43.90	2.06	2.074	309	23.96	45
47.97	1.89	1.905	400	19.60	65

Grain size of the film was calculated from the peak at $2\theta = 33.45^\circ$ using the Debye-Scherrer formula $D = 0.9\lambda/\beta \cos\theta$, where D is the diameter of the crystallites forming the film, λ is the wavelength of CuK_α line, β is FWHM in radians and θ is the Bragg angle. The grain sizes are compared in Table 3.2. The grain size was found to increase from 8.48 nm to 24.91 nm as the substrate temperature was increased from 200°C to 380°C.

Table 3.2 Grain size of β - In_2S_3 film

Temperature ($^{\circ}\text{C}$)	FWHM (Degrees)	Grain Size (nm)
200	0.979	8.48
250	0.523	15.87
300	0.462	17.96
350	0.336	24.69
380	0.333	24.91

3.3.1.2 Scanning Electron Micrograph [SEM]

SEM is a method for high resolution imaging of surfaces. It is the most widely used instrument for obtaining micro structural and surface features of thin films. The SEM uses electrons for imaging, much as a optical microscope uses visible light. The advantages of SEM over optical microscopy include much higher magnification (>100,000X) and depth of field upto 100 times that of light microscopy. A finely focused electron beam is scattered over the surface of the specimen and the secondary electrons emanating from the specimen are used for imaging the surface. Since secondary electrons come from the surface layer, the picture obtained is a faithful reproduction of the surface features. Secondary electron imaging can provide high-resolution imaging of fine surface morphology. Quantitative and qualitative chemical analysis information can also be obtained using Energy Dispersive X-ray spectrometer (EDAX) with the SEM [26].

SEM (Oxford Model 7060) was used to find out the uniformity of indium sulfide films prepared. Surface morphology of the In_2S_3 film prepared at 300°C is shown in Fig.3.4. The film was found to be dense with no pinholes or cracks.

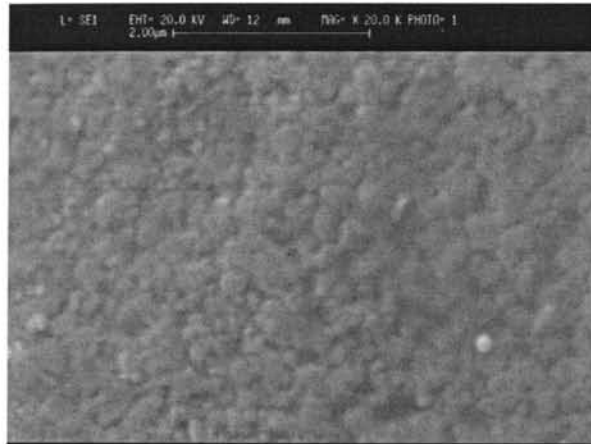


Fig. 3.4 Surface Morphology of In₂S₃ film prepared at 300°C

3.3.1.3 Atomic Force Microscopy (AFM)

AFM is a form of Scanning Probe Microscopy (SPM) where a small probe is scanned across the sample to obtain information about the sample's surface. The information gathered from the probe's interaction with the surface can be as simple as physical topography or as diverse as measurements of the material's physical, magnetic or chemical properties. These data are collected as the probe is scanned in a raster pattern across the sample to form a map of the measured property relative to the X-Y position.

The AFM probe has a very sharp tip, often less than 100 Å diameter, at the end of a small cantilever beam. The probe is attached to a piezoelectric scanner tube, which scans the probe across a selected area of the sample surface. Interatomic forces between the probe tip and the sample surface cause the cantilever to deflect as the sample's surface topography (or other properties) changes. A laser light reflected from the back of the cantilever measures the deflection of the cantilever. This information is fed back to a computer, which generates a map of the topography and/or other

properties of interest. Areas as large as 100 μm square to less than 100 nm square can be imaged.

The 2D and 3D images (recorded using Molecular Imaging Picoscan) of 6 micrometer square area of In_2S_3 film prepared at 300°C is given in Fig. 3.5 (a) and (b). AFM scan showed a dense microstructure but the grains were not uniform in size. Fig. 3.5b showed that In_2S_3 nucleated as individual, pyramidal islands. This kind of a surface structure has potential application in enhanced light trapping [27].

3.3.1.4 XPS Analysis

X-Ray Photoelectron Spectroscopy (XPS) [Electron Spectroscopy for Chemical Analysis (ESCA)] is one of the major techniques for studying thin films. It provides information on the elemental composition of a sample as well as on the chemical state of the observed atoms.

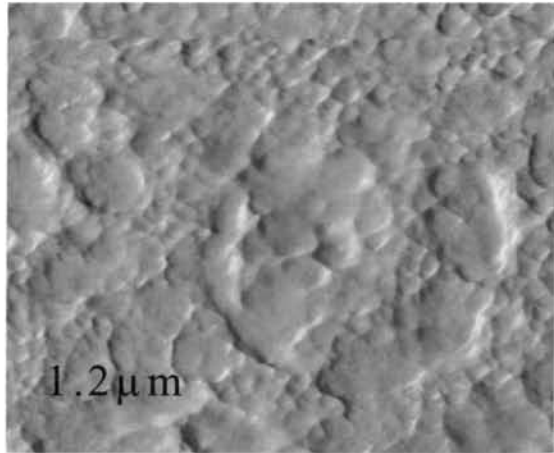
In this technique, the sample is irradiated using electromagnetic radiation of energy $h\nu$. Due to the photoelectric effect, electrons are emitted with kinetic energy

$$E_{kin} = h\nu - E_B - \phi \dots\dots\dots(3.5)$$

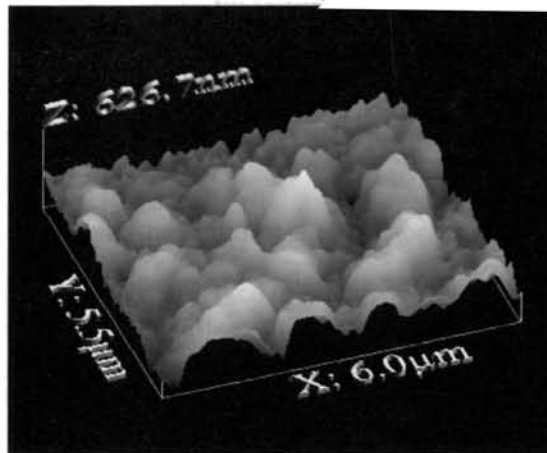
where E_B is the binding energy (BE) of a particular electron shell and Φ is the sample work function. Photoelectrons are energy-analyzed in the spectrometer and, since the photon energy is known, one can determine characteristic binding energies of valence electrons coming from different elements present in the sample. Depending on the energy of the incident radiation, this technique is called either “Ultra Violet Photoelectron Spectroscopy (UPS)” for lower photon energies (≤ 50 eV) or “X-ray Photoelectron Spectroscopy (XPS)” for higher photon energies (≥ 1 keV) [28].

The chemical composition of the films was evaluated using XPS technique in the present work. XPS spectra of the samples were recorded using an ULVAC-PHI unit (model: ESCA 5600 CIM) employing argon ion sputtering (Voltage = 3 kV,

Raster size = $3 \times 3 \text{ mm}^2$, pressure 10^{-8} m bar). Al K_{α} X-ray (1486.6 eV) with a beam diameter of 0.8 mm and power of 400 W was used as the incident beam.



(a)



(b)

Fig. 3.5 AFM image of indium sulfide film prepared at 300°C (a) 2D and (b) 3D image

In order to know the variation in stoichiometry as well as the chemical state of the elements along the thickness of the samples, we performed XPS depth profile of the samples. Here the presence of the elements In, S, O, and Si was checked along the sample thickness. In order to get this information, first XPS analysis was done on surface of the sample. After this the sample was etched using Ar ion sputtering for 0.88 min and the analysis was repeated. Each line in the spectra shown in Fig. 3.6 represents the result of such analysis and one line is called 'one cycle'. The spectra were calibrated against shifts due to machine errors, using the C 1s line of the hydrocarbon contamination on the films as the standard (Binding energy of C 1s is 284.5 eV). The bottom portion of the spectra represented the surface of the film and the top, the substrate. After 12 cycles, peaks corresponding to O and Si could be seen indicating the beginning of the glass substrate (SiO_2). XPS analysis indicated that indium and sulfur are uniformly distributed throughout the depth of the sample [Fig.3.6]. The binding energy values [Table 3.3] were in agreement with the reported values [29].

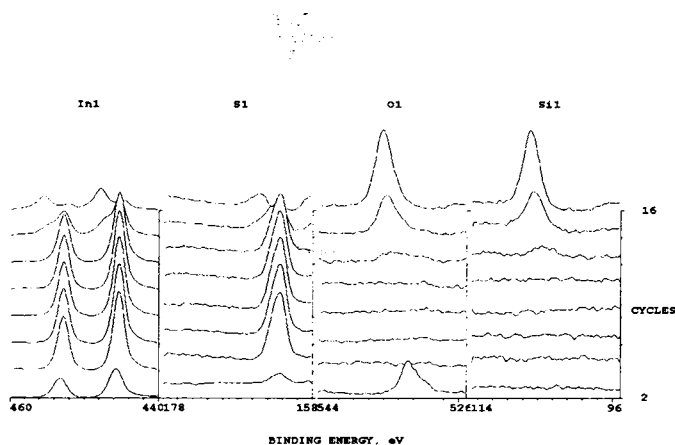


Fig. 3.6 XPS depth profile of sample with In/S = 2/3

Table 3.3 Binding energies of indium and sulfur in β -In₂S₃ film

Element	Binding Energy (eV)
In 3d _{5/2}	444.99
In 3d _{3/2}	453.06
S 2p	162.23

From the XPS pattern no obvious peaks for indium oxides (529.8 eV-530.5 eV for O 1s in In₂O₃) and In(OH)₃ (531.8 eV for O1s in In(OH)₃) or sulfur (164.5 eV) were observed [12, 29]. The binding energy of free oxygen is 531 eV. Binding energy peak corresponding to oxygen in the sample was at 532.49 eV. This could be attributed to the surface contamination of the sample in the form of sulfate [12]. The decrease in the peak height of sulfur at the surface of the film indicated that this oxygen substitutes sulfur in the top layer. The exact relative atomic proportion of each element in the films could not be determined accurately by XPS because of the different etching rates of indium, sulfur and oxygen.

3.3.1.5 Optical Studies

The most direct and the simplest method for probing the band structure of semiconductors are measuring the absorption spectrum. Absorption is expressed in terms of a coefficient $\alpha(h\nu)$ which is defined as the relative rate of decrease in light energy $L(h\nu)$ along its propagation path: [30]

$$\alpha = \frac{1}{L(h\nu)} \frac{d[L(h\nu)]}{dx} \dots\dots\dots(3.6)$$

the absorption coefficient α is related to the energy gap E_g according to the equation

$$\alpha h\nu = A(h\nu - E_g)^n \dots\dots\dots(3.7)$$

where A is a constant, h is the Plank's constant, ν the frequency of the incident beam and n is equal to $\frac{1}{2}$ for a direct gap and 2 for an indirect gap.

Absorption spectra of the samples were recorded using UV-Vis-NIR spectrophotometer (Hitachi U-3410) model. From the plot of $(\alpha h\nu)^2$ vs $h\nu$ [Fig.3.7], a direct band gap of 2.67 eV was obtained for films prepared at 300°C while band gap dropped to 2.58 eV for samples prepared at high temperature (380°C). It was found that the band gap has a higher value than that reported earlier [12, 15, 19] and it varied with the composition of the film [15]. A band gap of 2.639 eV [31] for β - In_2S_3 single crystals and 2.75 eV for indium sulfide prepared using CBD technique was reported [13]. The wider band gap obtained in the present study may be due to the presence of oxygen in the film as indicated by XPS analysis and also due to smaller grain size [32].

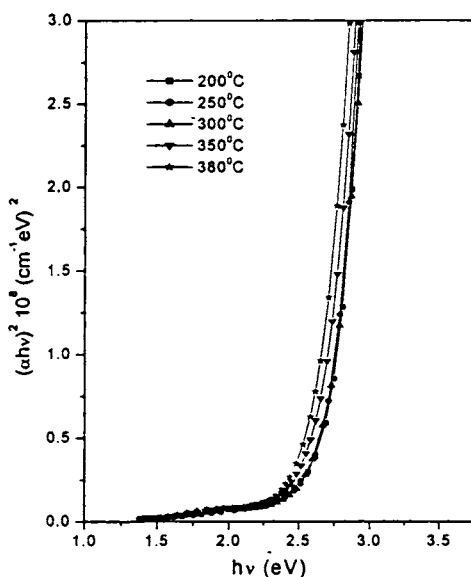


Fig.3.7 Variation of band gap with substrate temperature

Fig.3.8 shows transmission spectra obtained for In₂S₃ thin films obtained for different substrate temperatures. The films showed 78-85% transmission in the wavelength range 350-2500 nm. Presence of interference fringes due to multiple reflections showed fairly homogeneous film [12,17]. This happens when the film surface is reflecting and there is not much scattering/absorption in the bulk of the film [17].

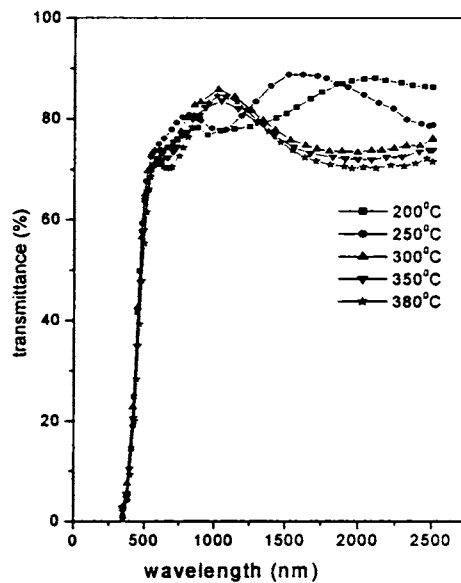


Fig. 3.8 Variation of optical transmittance with substrate temperature

The index of refraction $n(\lambda)$ at different wavelengths was calculated using the envelope curve for T_{max} (T_M) and T_{min} (T_m) in the transmission spectra [33]. The expression for refractive index is given by

$$n = \left[N + (N^2 - s^2)^{1/2} \right]^{1/2} \dots\dots\dots (3.8)$$

$$\text{where } N = 2s \frac{T_M - T_m}{T_M T_m} + \frac{s^2 + 1}{2} \dots\dots\dots(3.9)$$

and s is the refractive index of the substrate (in our case $s = 1.5$ (glass)). Fig. 3.9 depicts refractive index as a function of wavelength for films prepared at various temperatures and Fig. 3.10 shows refractive index of the films at a wavelength of 750 nm as a function of substrate temperature.

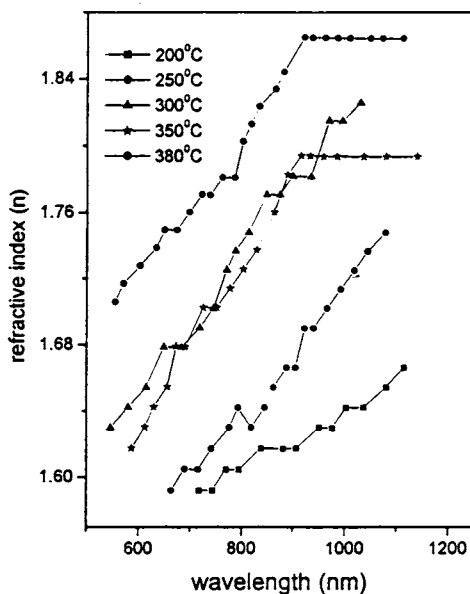


Fig. 3.9 Refractive index vs wavelength for films prepared at various substrate temperatures

The value was found to be in the range 1.6-1.86 (with wavelength) for temperatures ranging from 200°C to 380°C. The values of refractive index for films deposited at lower temperature were found to be less than those deposited at higher substrate temperature. J. George et al [17] reported similar observation in indium sulfide thin films deposited by the reactive evaporation of indium in sulfur atmosphere at different substrate temperatures. They related this effect to the concept of critical

optimization of Vincett [34]. He has concluded from many experimental results that when the substrate temperature approaches about 0.33 of the boiling point of the material, the film qualities (surface smoothness, optical transmission, carrier mobility etc) improve considerably. Hence for indium sulfide the critical temperature should be around 440 K. George et al found that the value of refractive index went through a maximum at about 410 K and then decreased. In our case, refractive index was found to increase with substrate temperature, but did not reach a maximum value, as we have not gone upto the critical value. For any particular wavelength the value of refractive index was found to increase with temperature.

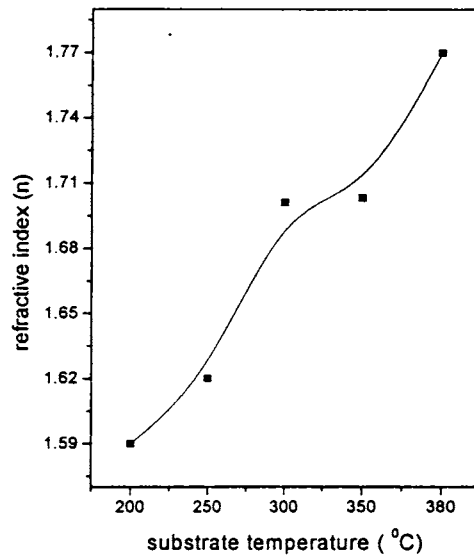


Fig. 3.10 Refractive index at 750 nm vs substrate temperature

The extinction coefficient could be calculated from the equation $k = \alpha\lambda/4\pi$ once the values of absorption coefficient (α) was known. The value was found to be in the range 0.005 to 0.045 [Fig. 3.11] [35]. As the value of absorption coefficient

slightly increased for samples prepared at higher temperatures, the value of k also was found to increase accordingly.

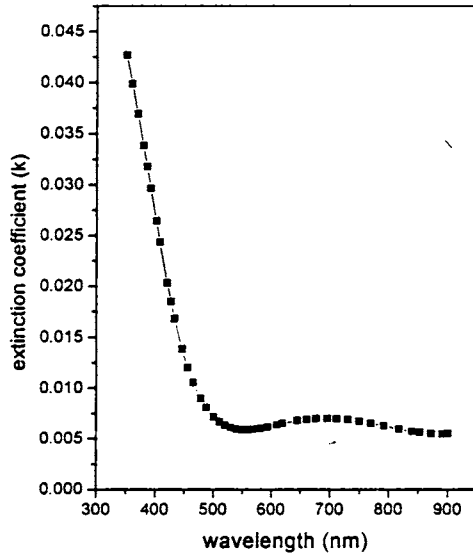


Fig. 3.11 Extinction coefficient vs wavelength
for sample prepared at 300°C

3.3.1.6 Photosensitivity Measurements

Photosensitivity measurements were done using the Keithley 236 Source Measure Unit. The sample was illuminated using a tungsten halogen lamp. The intensity of the source of light used was 60 mW/cm^2 with an IR filter and a water column in between to avoid heating of the sample. Silver electrodes were painted on the surface of the film keeping a distance of 5 mm in between the electrodes for photosensitivity measurements.

A graph plotted between photosensitivity ($(I_L - I_D)/I_D$) and substrate temperature is depicted in Fig.3.12. I_L is the current when the sample is illuminated with light and I_D is the dark current.

The value of maximum photosensitivity was 191.08 and this was obtained for samples prepared at 300°C [36]. This means that the photocurrent was 191 times larger than the dark current for the sample prepared at 300°C. So the substrate temperature during growth was maintained at 300°C for different In/S ratios. But on further increasing the substrate temperature, photosensitivity decreased considerably. This might be linked with crystallinity of the samples [Fig.3.3]. Due to better crystallinity (for samples prepared at temperature >350°C) dark resistivity was found to be low and hence low photosensitivity.

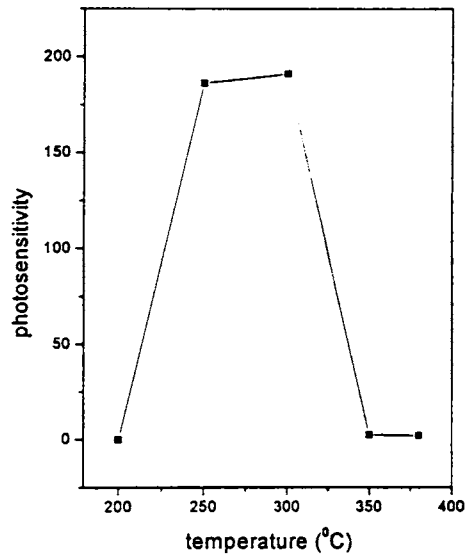


Fig. 3.12 Variation of photosensitivity with substrate temperature

3.3.2 Effect of Variation of Sulfur Concentration

In/S ratio was varied by varying the molar concentrations of InCl_3 and thiourea taken in the spray solution. The molarity of InCl_3 was kept at 0.025 M and the concentration of thiourea was varied to get In/S ratio ranging from 2/1 to 2/8.

3.3.2.1 Structural Analysis

The samples showed β - In_2S_3 phase with good crystallinity and preferential orientation along the (220) plane except for those having very low sulfur concentration [Fig.3.13]. All figures have the same scale on Y- axis.

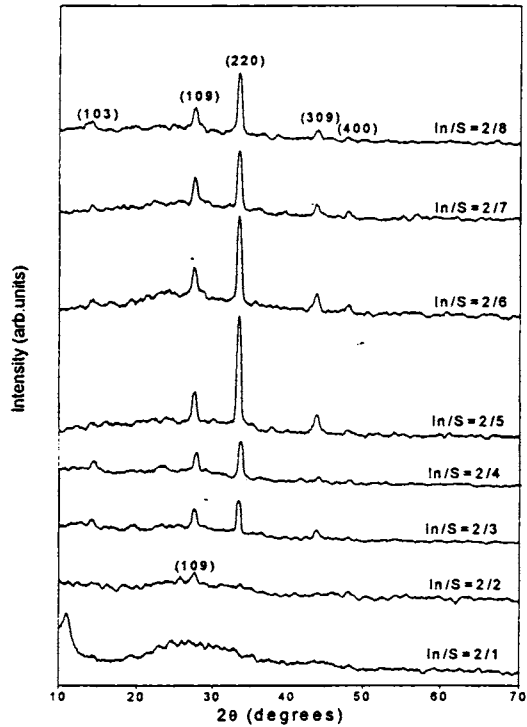


Fig. 3.13 Variation of XRD with sulfur concentration ($\text{In/S}=2/1$ to $2/8$)

The characteristic peaks of β - In_2S_3 , were begin to grow for samples having In/S ratio $2/2$. The sample with $\text{In/S} = 2/3$ ratio showed good crystallinity and orientation along (220) plane. As the sulfur concentration increased the intensity of the peak corresponding to the (220) plane increased up to indium to sulfur molar ratio

2/5 [37]. On further increasing the sulfur concentration, the intensity of this peak decreased.

3.3.2.2 Energy Dispersive X-Ray Analysis (EDAX)

Here the sample is irradiated by electron beam and the emitted x-rays are directly measured using energy dispersive X-ray spectrometer, producing a spectrum of counts versus energy. As each x-ray photon enters the detector, it produces photoelectrons, whose total number is linearly proportional to the energy of the entering X-rays. The charge collected from the detector is very small since only a few hundreds or thousands of electrons are produced by each X-ray photon. Hence it is amplified by a pre-amplifier whose output voltage is proportional to the X-ray energy [38].

The atomic concentration of the elements present in the In_2S_3 sample was determined using EDAX measurements (Oxford Model 7060). The percentage of atomic concentration of the elements In, S and Cl for samples having In/S ratio 2/3 and 2/8 are shown in Table 3.4.

Table 3.4 Atomic concentrations of In_2S_3 samples having In/S ratio 2/3 and 2/8

Sample	In (%)	S (%)	Cl (%)
2/3	37.34	47.27	15.39
2/8	35.65	55.71	8.65

As the concentration of sulfur in the solution was increased, that in the film also increased even though the value was still less than the stoichiometric composition of 60%. It could also be observed that, as the concentration of indium increased the concentration of chlorine also increased, which might be coming from indium chloride (InCl_3) that was used as one of the precursor solutions. Because of the

presence of chlorine in In_2S_3 the atomic ratio in the film did not exactly follow that in the spray solution.

3.3.2.3 XPS Analysis

Depth profile of the sample having In/S ratio 2/2 showed the presence of oxygen throughout the depth of the sample [Fig.3.14]. Binding energies of oxygen (531.5 eV to 532.6 eV) and sulfur (166.9 eV, on the surface) indicated the formation of a mixed phase of sulfate and sulfite. Binding energies were so close for these two that it was difficult to distinguish between sulfate and sulfite. Shift in the binding energies of indium and sulfur might be due to the presence of oxygen in the sample. Chlorine was also present in the film (201 eV) in elemental form.

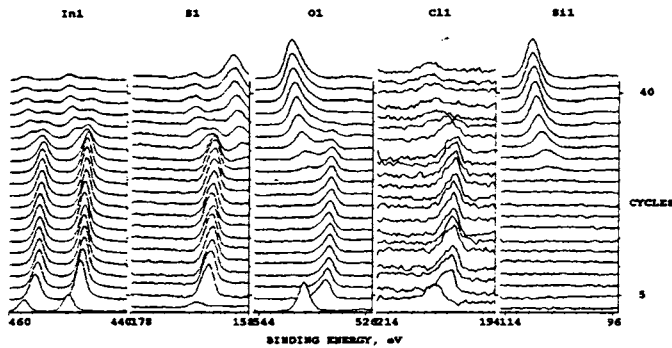


Fig.3.14 XPS depth profile of sample with In/S = 2/2

On increasing the sulfur concentration to 2/4 and then to 2/8 [Fig.3.15 and 3.16] indium and sulfur were uniformly distributed throughout the depth from the top surface itself. Oxygen was present as a surface contaminant (532.5 eV) only, which corresponds to sulfate. The binding energies of indium and sulfur clearly indicated the formation of indium sulfide (162.5 eV for S2p, 444.9 eV and 452.9 eV for $\text{In}3d_{5/2}$ and

$\text{In}_3\text{d}_{3/2}$ respectively). Peaks corresponding to indium and sulfur at the surface of the sample was more predominant when the In/S ratio became 2/8. There was a shift in the binding energy (199.1 eV) of chlorine.

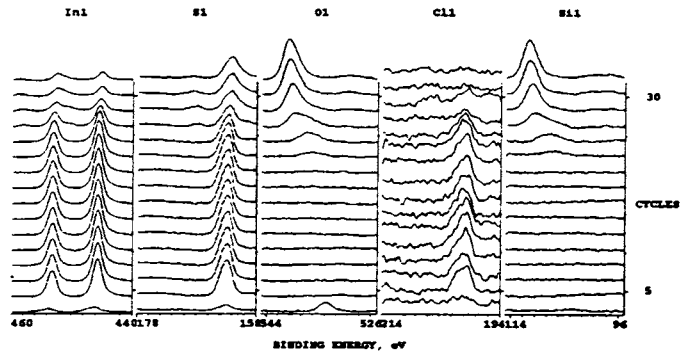


Fig.3.15 XPS depth profile of sample with In/S = 2/4

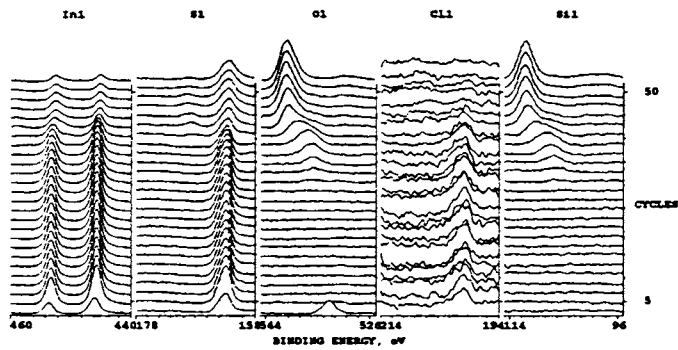


Fig.3.16 XPS depth profile of sample with In/S = 2/8

3.3.2.4 Optical Studies

Energy band gap was calculated from the plot $(\alpha h\nu)^2$ vs $h\nu$. The band gap of the sample having $\text{In/S} = 2/3$ was found to be 2.67 eV. On decreasing the sulfur concentration (2/1) the band gap increased to 2.81 eV [Fig.3.17].

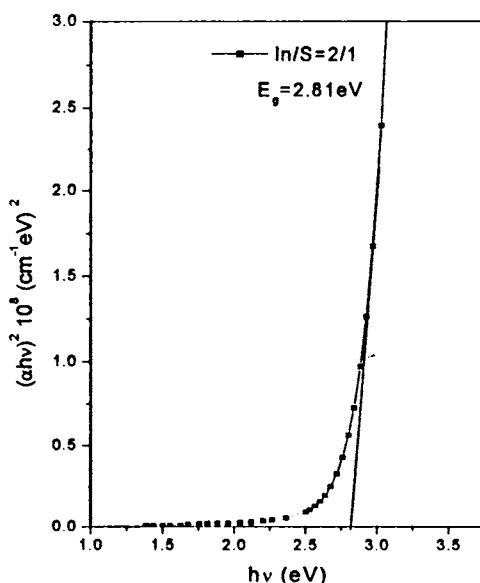


Fig. 3.17 Band gap of In_2S_3 sample having In/S ratio 2/1

The wider band gap might be due to low crystallinity and presence of oxygen [32]. In samples having very low sulfur concentration there was more oxygen and the crystallinity was also not good. Hence wider band gap was obtained in samples with low sulfur content. The presence of oxygen throughout the depth was observed from XPS analysis for samples with In/S ratio 2/2 [Fig.3.14].

On increasing the sulfur concentration (2/8) the band gap reduced to 2.64 eV [Fig.3.18]. The atomic concentration of oxygen was very low in the sample having high sulfur ratio 2/8; oxygen was present only on the surface for this film [Fig. 3.16].

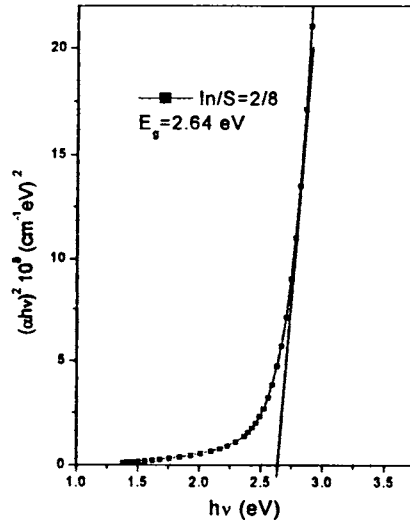


Fig.3.18 Band gap of In_2S_3 sample having In/S ratio 2/8

The percentage of transmittance decreased from 85% to 55% when indium to sulfur ratio varied from 2/1 to 2/8 [Fig.3.19] in the wavelength range 350-2500 nm. The high value of transmittance for samples having low sulfur concentration might be due to the presence of oxygen in the sample. The amplitude of interference fringes is a measure of film quality, larger the amplitude better the film. It was clear from the transmission spectra that the interference pattern almost disappeared on increasing the sulfur concentration. This might be due to the increase in the surface roughness of the film. Refractive index was calculated using the envelope method and the value was found to vary in the range 1.6 to 1.8 with wavelength. The refractive index may depend on stoichiometry of the films [39], but here the value was found to follow the variation observed in XRD pattern [Fig.3.13] and hence the effect due to variation in crystallinity might be prominent. The value was found to decrease with improvement

in crystallinity [22]. Upto In/S ratio 2/5 (maximum crystallinity), value of refractive index decreased and then it started increasing with further increase in sulfur concentration [Fig. 3.20].

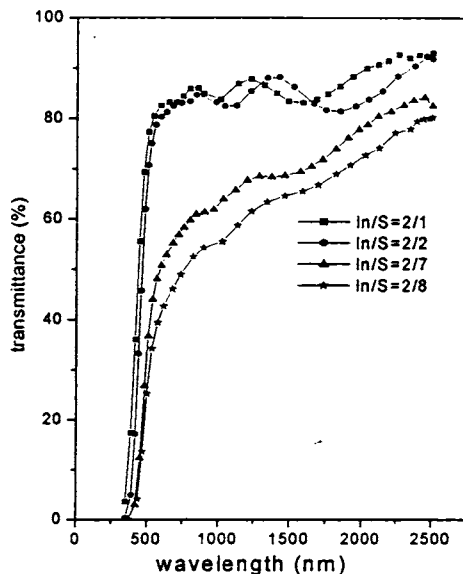


Fig. 3.19 Variation of optical transmittance with In/S ratio (In/S=2/1 to 2/8)

Variation of extinction coefficient with wavelength for sample having In/S ratio 2/8 is given in Fig. 3.21. As the value of absorption coefficient was higher for greater sulfur concentrations [Fig. 3.18], value of k also was found to increase (in the range 0.02 to 0.12) [35]. See Fig. 3.17 for lower sulfur concentration.

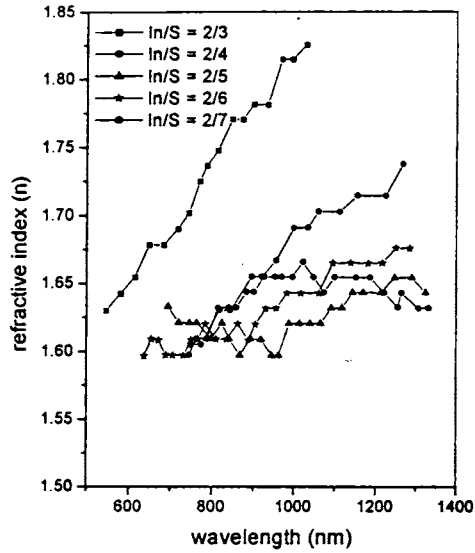


Fig. 3.20 Variation of refractive index with In/S ratio

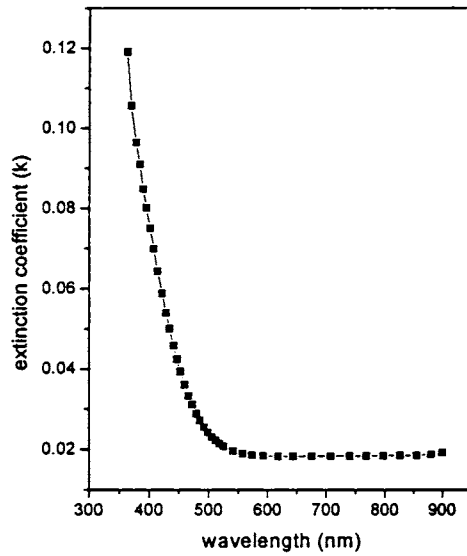


Fig. 3.21 Variation of k with λ for In/S ratio 2/8

3.3.2.5 Photosensitivity Measurements

Fig.3.22 shows the variation of photoresponse with concentration of sulfur in the solution. The sample having In/S ratios 2/1 and 2/8 showed good response, the latter having maximum response. The response of the samples decreased with increase in sulfur concentration from 2/2 to 2/5 and it was minimum for In/S= 2/5. This could be attributed to the improvement in crystallinity with increase in sulfur concentration as indicated in the XRD analysis [Fig.3.13]. Photosensitivity increased on further increasing sulfur concentration. Moreover there is another point also worth mentioning here. As sulfur concentration increased, naturally indium concentration decreased, causing a drastic decrease in majority carrier concentration. This will lead to survival of minority carriers and hence there was considerable increase of photosensitivity for samples having higher sulfur concentration.

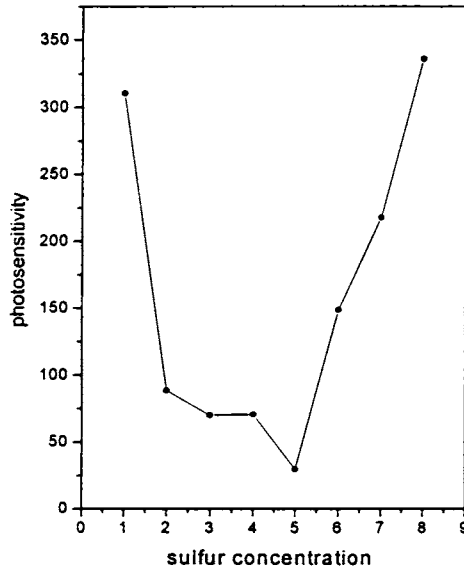


Fig.3.22 Variation of photosensitivity with sulfur concentration for In = 2

3.3.2.6 Electrical Conductivity

Dark conductivity of the samples was measured at room temperature. Silver was painted on the top of the film, which served as the electrode. The value was found to increase with the increase of the sulfur concentration upto In/S ratio 2/5. On further increasing the sulfur concentration conductivity decreased [Fig.3.23]. We observed the same variation with XRD [Fig. 3.13] also. Samples showed better crystallinity on increasing the sulfur concentration till In/S ratio 2/5 and then it decreased. Hence we could observe an enhancement in conductivity with improvement in crystallinity.

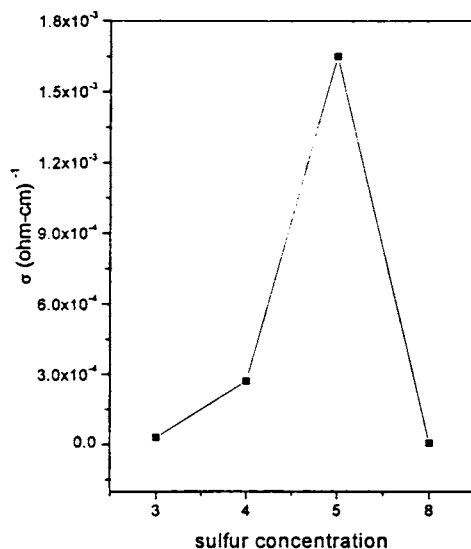


Fig. 3.23 Variation of electrical conductivity with sulfur concentration at room temperature

3.3.3 Effect of Variation of Indium Concentration

By fixing the sulfur concentration at 3, 6 and 8 the concentration of indium in the solution was varied from 1.2 to 2.5. For this the molarity of thiourea was fixed at 0.0375 M (S = 3), 0.0758 M (S = 6) and 0.1 M (S = 8) respectively and that of InCl₃

solution was varied. The aim was to see the variation in photosensitivity with variation in indium concentration.

3.3.3.1 Structural Analysis

Fig.3.24 shows the variation in XRD with the variation in indium concentration for sulfur concentration, S = 8. The sample showed characteristic peaks of β - In_2S_3 even for low indium concentration (1.2/8). But the intensity of the peak corresponding to (220) plane was very low. As the indium to sulfur ratio was increased, the sample showed better crystallinity. This could be compared with the samples in which sulfur concentration was varied [Fig.3.13]. There also, the intensity of the peak corresponding to the (220) plane decreased when the sulfur ratio was very high in the solution. Same was the case with the variation in indium concentration keeping the sulfur concentration at 3 & 6.

3.3.3.2 XPS Analysis

Binding energies of indium and sulfur indicated the formation of indium sulfide. Depth profile of the sample having In/S ratio 1.2/8 is shown in Fig.3.25. Atomic concentration of chlorine in sample having In/S ratio 1.2/8 was less when compared to the sample having the ratio 2.5/8 [40]. This might be due to the low molarity of InCl_3 in the spray solution. This was clear from the EDAX measurements also, where the atomic percentage of chlorine was 10.78 for the In/S ratio 1.2/8 and 11.52 for the ratio 2.5/8. Atomic concentration of the constituent elements, along the thickness of the samples with In/S ratio 1.2/8 and 2.5/8 are shown in figures 3.26 (a) and (b). Atomic concentration of sulfur was much less than that obtained from EDAX. For In/S ratio 1.2/8, the concentration of sulfur was 53.02% (measured using EDAX) while it was ~ 40% only in the case of XPS. This might be probably due to the preferred sputtering of group VI elements such as sulfur and selenium.

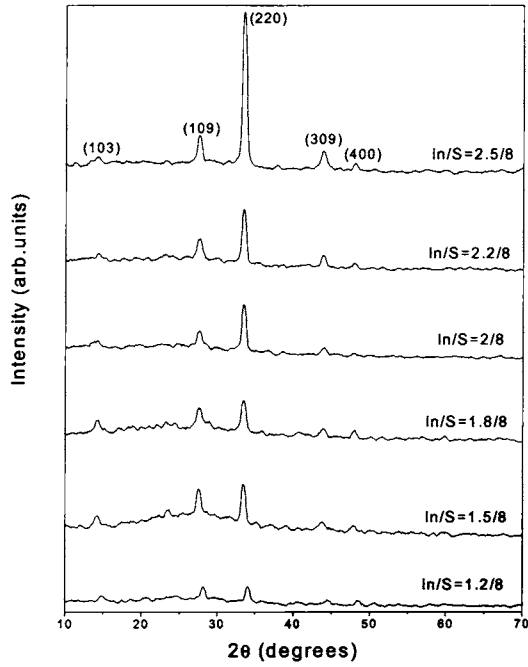


Fig. 3.24 Variation of XRD with In/S ratio from 1.2/8 to 2.5/8

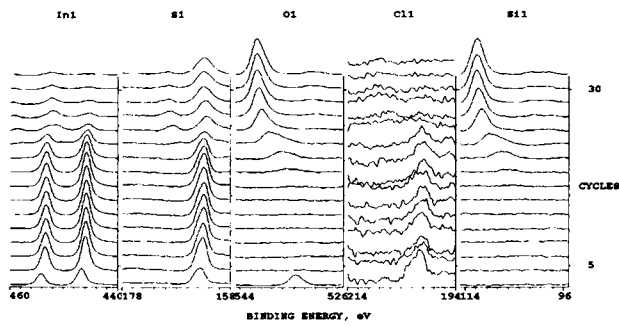
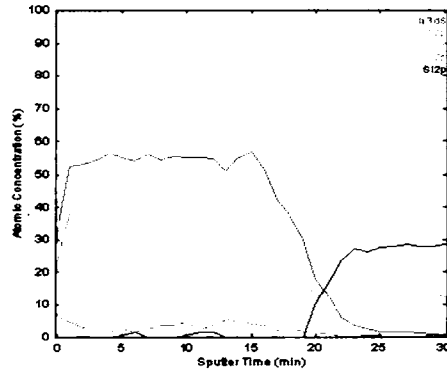
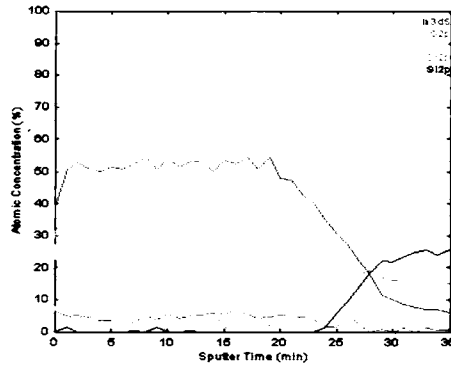


Fig. 3.25 Depth profile of the sample with In/S ratio 1.2/8



(a)



(b)

Fig. 3.26 Atomic concentration vs Sputter time graph of samples with In/S ratio (a) 1.2/8 (b) 2.5/8

3.3.3.3 Optical Studies

The band gap of the sample was found to decrease with increase in indium concentration, 1.2/8 to 2.5/8 [Fig.3.27]. This was because the sample showed better crystallinity on increasing indium concentration [Fig. 3.24]. Optical transmittance spectrum is given in Fig.3.28. Absence of interference fringes in the transmission spectra showed that surface roughness (not reflecting) of the film increased on increasing sulfur concentration. Hence we were unable to calculate the value of refractive index (n). Extinction coefficients calculated was found to vary in accordance with the values of absorption coefficient α . The variation with wavelength for In/S ratio 2.5/8 is shown in Fig. 3.29. The value was found to vary in the range 0.02 to 0.19 [35].

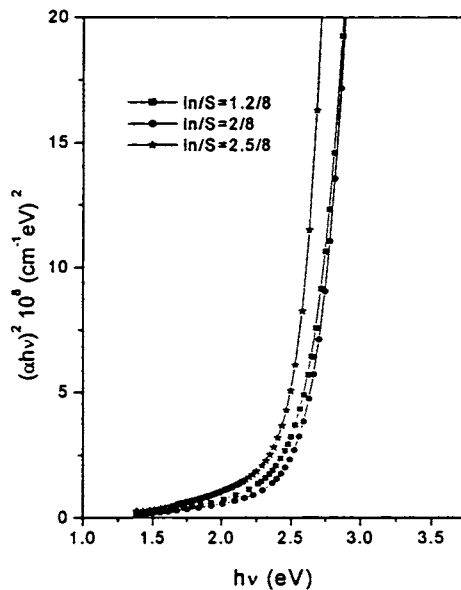


Fig.3.27 Variation of band gap with In/S ratio (In/S=1.2/8 to 2.5/8)

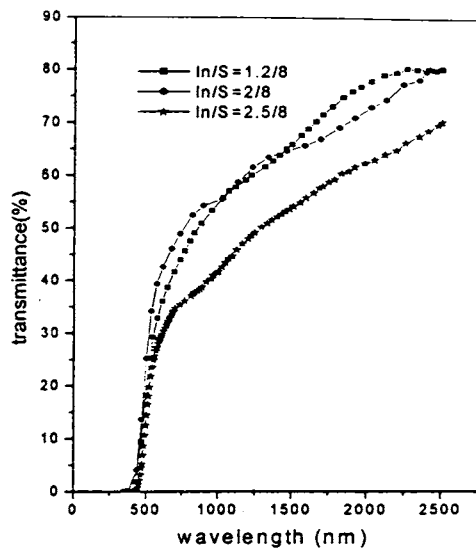


Fig.3.28 Variation of optical transmittance with In/S ratio (In/S=1.2/8 to 2.5/8)

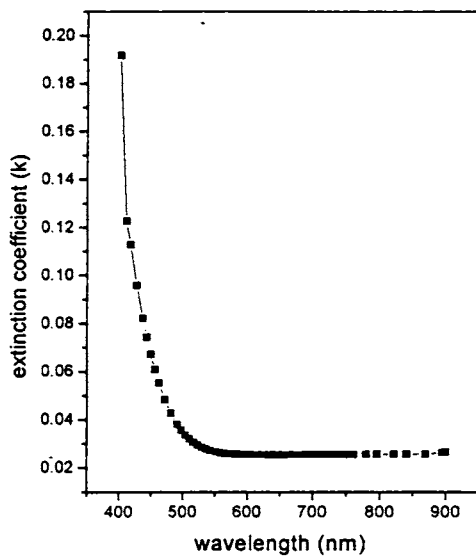


Fig. 3.29 k vs λ for In/S ratio 2.5/8

3.3.3.4 Photosensitivity Measurements

Fig.3.30 shows the variation of photosensitivity with indium concentration for sulfur ratios 3, 6 and 8. The figures clearly indicated that the response of the samples improved with decrease in the indium concentration in the solution. The sample having In/S ratio 1.2/8 showed maximum photosensitivity. The value of photosensitivity $\Delta I/I_D$ (949.97) was found to be much higher than that for samples prepared at different substrate temperatures (191.08 at 300°C) and by varying sulfur ratio (335.84 for In/S ratio 2/8). Here also we can see that the increase in photosensitivity was due to the reduction in majority carrier density. When the In/S ratio of the sample was equal to 1.2/8, the concentration of indium was very low and that of sulfur was very high. Both these conditions caused considerable reduction in majority carrier concentration (here electron) inside the material. Naturally recombination will be low and hence more minority carriers will survive giving higher photosensitivity.

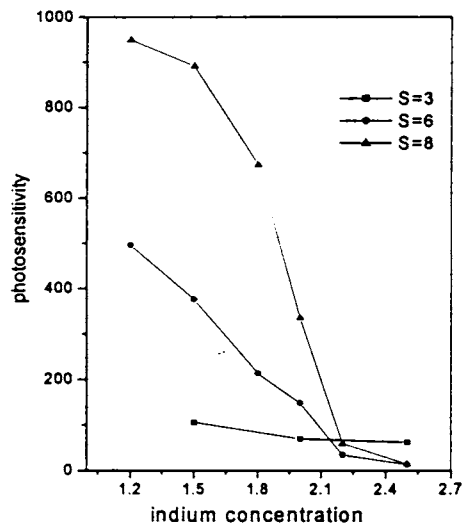


Fig.3.30 Variation of photosensitivity with indium concentration for S = 3, 6, 8

3.3.4 Thermally Stimulated Current (TSC) Measurements

Thermally Stimulated Current, TSC (also called thermally stimulated conductivity) has been studied extensively as a defect characterization technique. This technique helps the identification and determination of the traps or defects and trap parameters of a material.

The details of TSC measurements are given elsewhere [41]. The TSC spectra of the In_2S_3 films having different In/S ratios are shown in Fig.3.31 a-f.

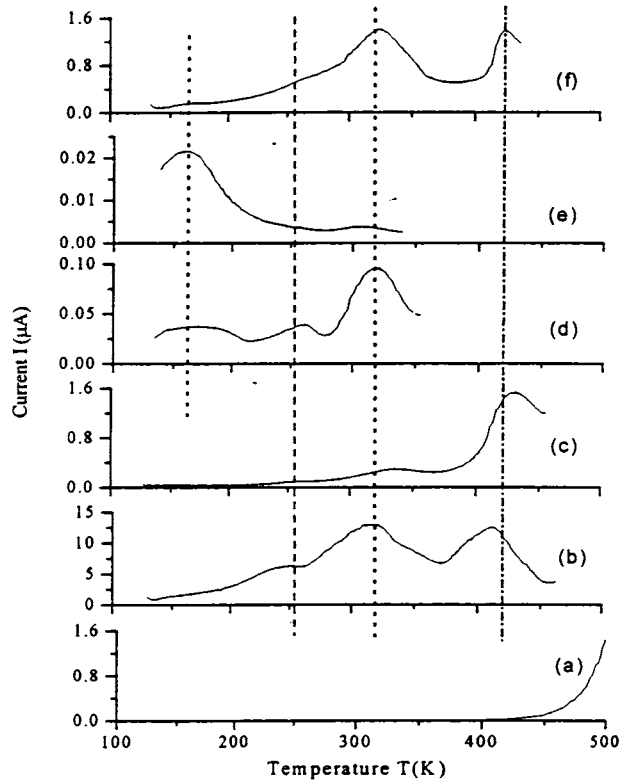


Fig. 3.31 TSC spectra of $\beta\text{-In}_2\text{S}_3$, (a) In/S=2/1 (b) In/S=2/3 (c) In/S=2/6 (d) In/S=2/8 (e) In/S=1.2/8 (f) In/S=2.5/8

TSC curve for sample with In/S ratio 2/1 showed no peak. The sample was amorphous and highly resistive [Fig. 3.13]. TSC study on different samples of $\beta\text{-In}_2\text{S}_3$

could reveal the existence of four major traps in the material [42]. A defect level at 160 K corresponding to 0.1 eV was detected whose prominence increased with the decrease in indium concentration. It was observed only for samples having lower indium concentration, for In/S ratios 2/8 and 1.2/8. It could be clearly seen that this peak intensity was greatest for the sample with In/S ratio 1.2/8 and it vanished for the ratio 2.5/8. This indicated that this level corresponds to indium vacancy or deficiency of indium. This did not appear in other samples.

Another trap level at 0.26 eV (around 230 K) existed in all samples except for the one having In/S ratio 1.2/8. As the concentration of indium was the least, a high percentage of indium vacancy existed in this sample. High percentage of chlorine was present in all the other samples, except this one as revealed through XPS studies [Fig.3.26a]. Hence a weak signal of this defect was seen in the TSC spectra for the sample with In/S ratio 1.2/8. This indicated that probably this defect at 0.26 eV arises due to chlorine impurity.

Another trap level was identified just above room temperature, 320 K corresponding to 0.43 eV. This level was present in all the spectra with varying peak intensities depending on the In/S concentration ratio, revealing that this was a native defect. Its prominence decreased when the sulfur concentration was increased or indium concentration was decreased. The highest prominence was for the sample whose concentration ratio was 2/3 while it decreased when the ratio was changed to 2/8. Further decrease of indium concentration or increase of sulfur concentration led to negligible contribution of this defect indicating that this defect decreased with increase of sulfur, hence must be a sulfur vacancy.

A high temperature peak at 450 K could be detected with activation energy 0.82 eV. Activation energy of 0.84 eV with a carrier density of $5.88 \times 10^{-21} \text{ m}^{-3}$ was reported using electrical resistivity measurements and space charge limited current by Seyama [21]. The effect of this level was observed to be most prominent for the sample having In/S ratio 2/3. XPS studies showed the highest percentage of oxygen in

this sample. It was observed that the TSC peak corresponding to 0.82 eV decreased with increase in sulfur. Thus perhaps it might be the replacement of sulfur by oxygen that created such a deep impurity level in indium sulfide thin films.

3.3.5 Variation of Thickness

Thickness of the indium sulfide thin films was varied by varying the total volume of the solution sprayed. Volume of the solution was varied as 400 ml, 600 ml, 800 ml and 1000 ml. For this the molarity of InCl_3 solution was kept at 0.025 M and that of thiourea at 0.0375 M so that the In/S ratio became 2/3.

3.3.5.1 Structural Analysis

The XRD spectra of the samples are shown in Fig.3.32. It was observed that the crystallinity of the samples increased on increasing the thickness. The intensity of all the peaks corresponding to the planes (109), (220) and (309) was found to increase with the increase in thickness. Due to the high intensity of the peak corresponding to the (220) plane the peak corresponding to the (103) plane became invisible on increasing the thickness. The grain size, calculated using (220) plane is tabulated in Table 3.5.

Table 3.5 Variation of grain size with volume of the solution

Volume of the solution (ml)	Grain Size (nm)
400	17.96
600	22.11
800	23.14
1000	25.53

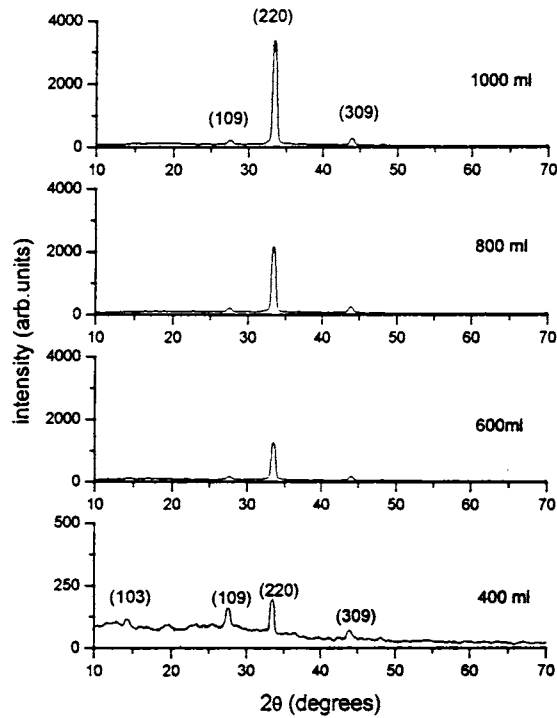


Fig. 3.32 Variation in XRD with thickness of In₂S₃ films

3.3.5.2 Measurement of Thickness

Thicknesses of the samples were measured using Stylus method. The values are compared in Table 3.6. Samples were found to be uniform without any pinholes.

Table 3.6 Variation in thickness with volume of the solution sprayed

Volume of the solution (ml)	Thickness (μm)
400	1.00
600	2.05
800	2.11
1000	4.10

3.3.5.3 Optical Studies

The variation in band gap of the samples was studied using optical absorption spectra. Absorbance vs wavelength graph is shown in Fig. 3.33.

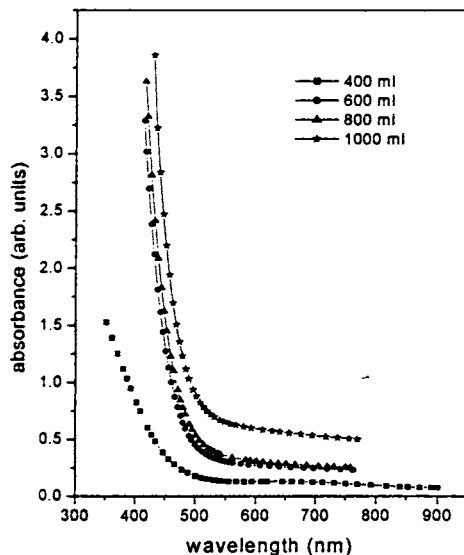


Fig. 3.33 Variation in absorbance with wavelength for different volumes of the solution sprayed

Absorbance was found to increase with the increase in the thickness of the samples. The band gap value decreased from 2.67 eV for 400 ml of the solution to 2.49 eV for 1000 ml of the solution. Variation in band gap is given in Fig.3.34. The thickness dependence of band gap may arise due to one or combined effect of the following cause [43] (i) large density of dislocation (ii) quantum size effect and (iii) change in the barrier height due to change in grain size in polycrystalline films. Quantum size effect and density of dislocation could be neglected due to large film thickness [43]. Hence the reduction in band gap may be due to the change in the barrier height due to increase in grain size and the crystallinity [Fig.3.32] of the samples.

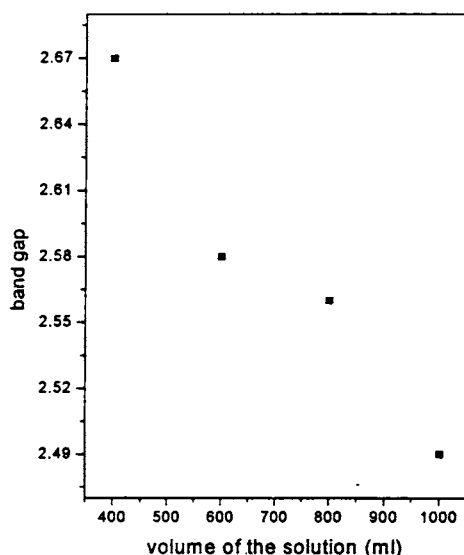


Fig.3.34 Variation in band gap with the volume of the solution sprayed

Transmission spectra were taken in the wavelength range 450-2500 nm. The percentage of transmittance decreased from $\sim 80\%$ to $\sim 40\%$ on increasing the thickness of the films. The variation in transmittance for different volumes of the solution sprayed is shown in Fig.3.35. Decrease in the amplitude of interference fringes showed increase in the surface roughness of the film with increasing thickness. For $4\ \mu\text{m}$ thick film there was no interference fringe at all, might be due to large film thickness. The value of refractive index was found to decrease with increase in film thickness. This might be due to the improvement in crystallinity of the film [22]. For lower thickness of the film the value was found to increase with wavelength while for higher thicknesses it was almost constant. The reason for this variation is unknown. Fig. 3.36 shows the variation of refractive index with wavelength for different film thicknesses.

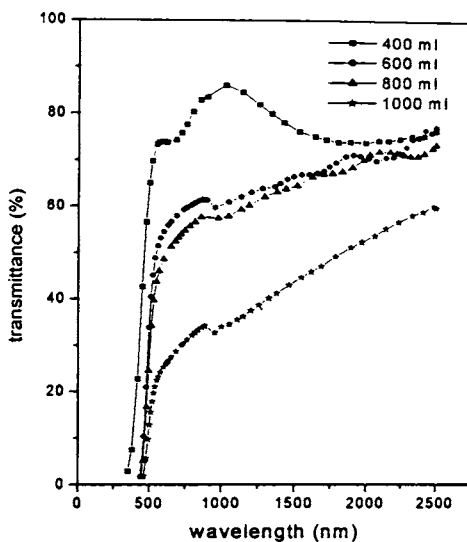


Fig.3.35 Variation in transmittance for various volumes of the solution sprayed

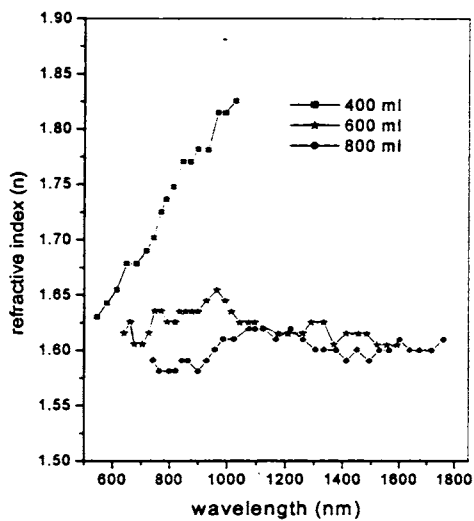


Fig. 3.36 Variation of refractive index with wavelength for various film thicknesses

Absorption coefficient of the samples increased with increase in the thickness and hence the value of extinction coefficient also increased. The value varied in the range 0.03 to 0.13 with wavelength for the sample maximum thickness (1000 ml) [Fig. 3.37].

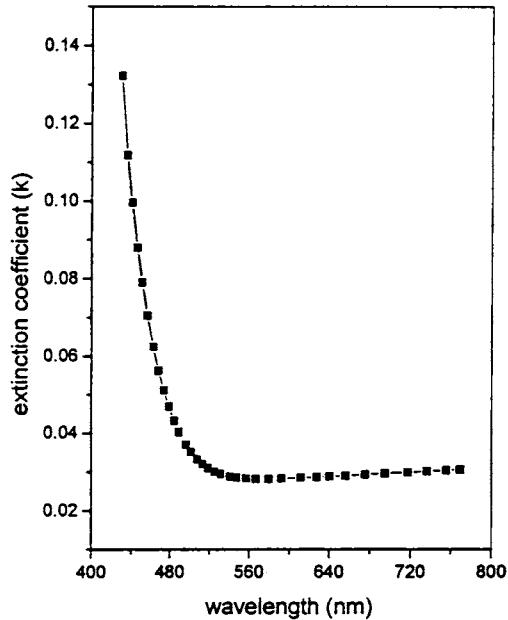


Fig. 3.37 Extinction coefficient with wavelength for maximum thickness of the sample

3.3.5.4 Electrical Resistivity

Resistivity of the samples was found to decrease with the increase in thickness. The values are compared in Table 3.7. This might be due to the improvement in the crystalline quality of the film.

Table 3.7 Variation in resistivity with the volume of the solution

Volume of the solution (ml)	Resistivity (ohm-cm)
400	33.30×10^3
600	59.70×10^2
800	13.03×10^2
1000	12.46×10^2

3.3.6 Effect of Annealing

Indium sulfide samples having In/S ratio 2/3 (400 ml) were annealed in vacuum at 300°C and 400°C to study the effect of annealing on the samples keeping the pressure at 10^{-5} Torr. Structural analysis of the samples was done using XRD and optical studies were done using optical absorption and transmission.

3.3.6.1 Structural Analysis

Samples showed better crystallinity on annealing. The intensity of all the three peaks corresponding to (109), (220) and (309) planes increased as an effect of annealing. The peak corresponding to (103) plane almost disappeared when the annealing temperature was increased to 400°C. XRD spectra of the as prepared and annealed samples are compared in Fig.3.38. Grain sizes calculated from Debye-Scherrer formula are tabulated in Table 3.8.

Table 3.8 Variation in grain size with temperature of annealing

Annealing Temperature (°C)	Grain Size (nm)
As prepared	17.96
300	18.10
400	21.84

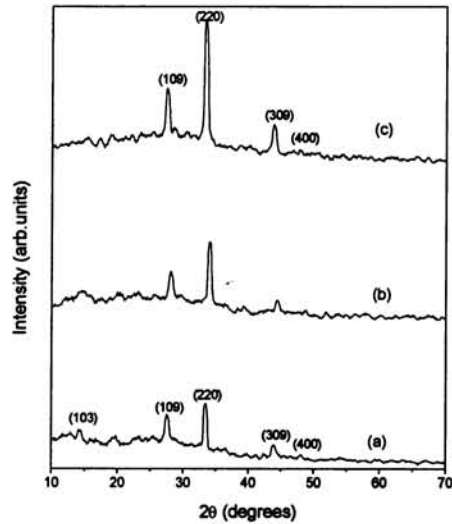


Fig. 3.38 XRD spectrum of samples (a) as prepared
(b) annealed at 300°C and (c) annealed at 400°C

3.3.6.2 Surface Morphology

Fig. 3.39 shows SEM micrograph of In₂S₃ film annealed at 300°C. It was clear that the surface became dense and the grains were uniform in size compared to the as

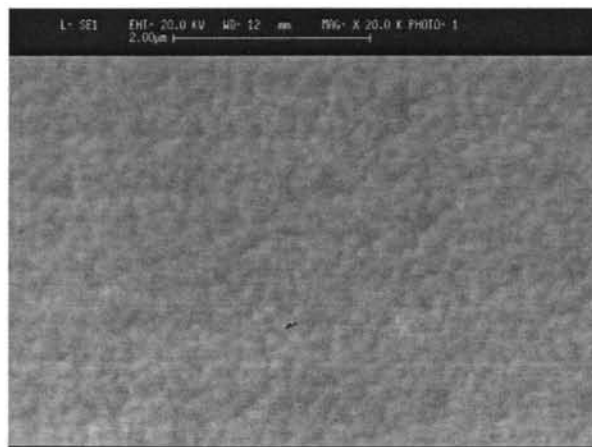


Fig. 3.39 Surface morphology of In₂S₃ film annealed at 300°C

prepared sample [Fig. 3.4]. No voids or pinholes were also detected. XRD also indicated improvement in crystalline structure [Fig.3.38].

3.3.6.3 XPS Analysis

XPS depth profile of the sample annealed at 300°C is shown in Fig.3.40. Oxygen was detected throughout the depth of the sample after annealing while there was no oxygen in the depth of the sample before annealing. But there was no shift in the binding energies of indium or sulfur. Oxygen at the surface could be attributed to surface contamination in the form of sulfate. Chlorine was also present throughout the depth of the sample. Sulfur and indium were diffused much into glass after annealing. The atomic concentration of the elements throughout the depth of the film after annealing (300°C) is shown in Fig.3.41.

Silicon was also found to have diffused throughout the depth of the sample, but we were unable to identify the chemical state from the BE values. There was no considerable variation in the concentration of chlorine in the film.

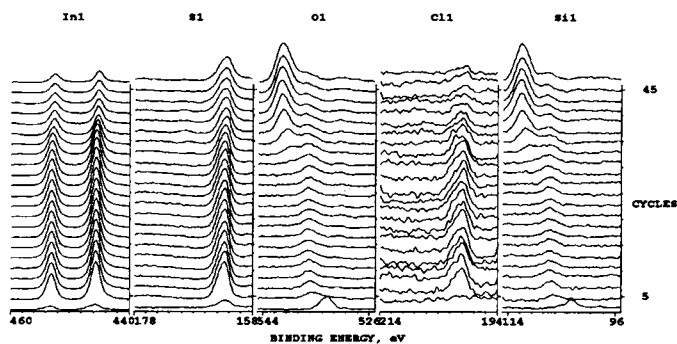


Fig.3.40 XPS depth profile of In_2S_3 sample annealed at 300°C

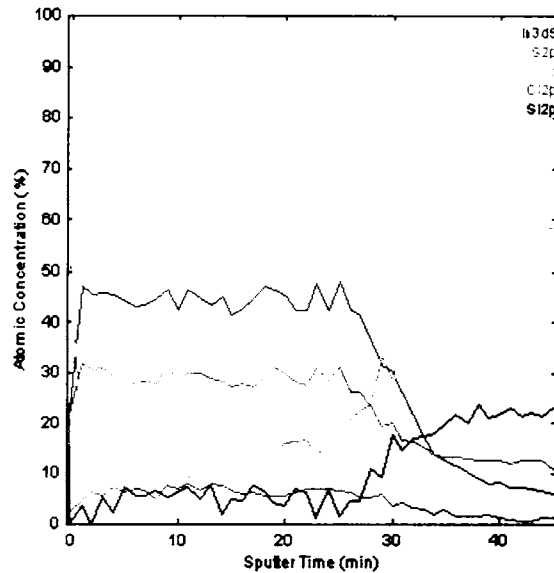


Fig. 3.41 Atomic concentration along the depth of the sample annealed at 300°C

3.3.6.4 Optical Studies

On annealing, band gap was slightly reduced from 2.67 eV of as prepared samples to 2.62 eV for samples annealed at 400°C. From the structural analysis, one could expect a significant reduction in band gap due to improvement in crystallinity on increasing the annealing temperature to 400°C. But oxygen in the bulk of the sample [Fig. 3.40] might be contributing to the widening of band gap [32] and as a result the band gap did not show much variation. Wavelength dependence of optical absorbance for the as prepared and annealed samples is shown in Fig. 3.42 and Fig.3.43 depicts the variation in transmittance.

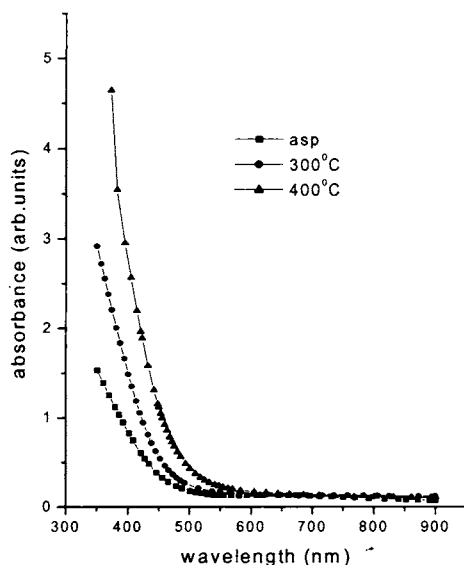


Fig. 3.42 Absorbance vs wavelength for the as prepared and annealed samples

The excellent surface quality of the film was confirmed from the appearance of interference fringes in the transmission spectra. The value of refractive index was found to increase with wavelength for as prepared as well as annealed films. It was found to be in the range 1.6-1.84. Meanwhile the value decreased with increase in annealing temperature [Fig. 3.44].

Dietrich et al found that if lattice contraction is the main cause in the variation of refractive index, a continuous decrease in the refractive index must be observed with increasing annealing temperature, as lattice constant c decreases [44]. Same variation was observed in our case also, the lattice constant c decreased from 3.23 Å to 3.20 Å, and hence lattice contraction might be the reason for the reduction in the value of refractive index with annealing temperature. Variation of extinction coefficient with wavelength for sample annealed at 400°C is given in Fig. 3.45.

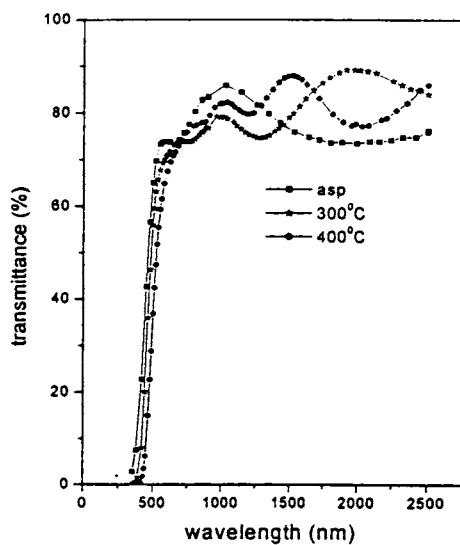


Fig. 3.43 Variation transmittance for the as prepared and annealed samples

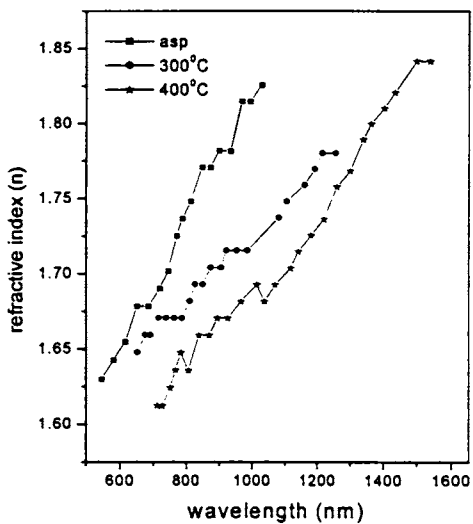


Fig. 3.44 Variation of refractive index with wavelength for as prepared and annealed films

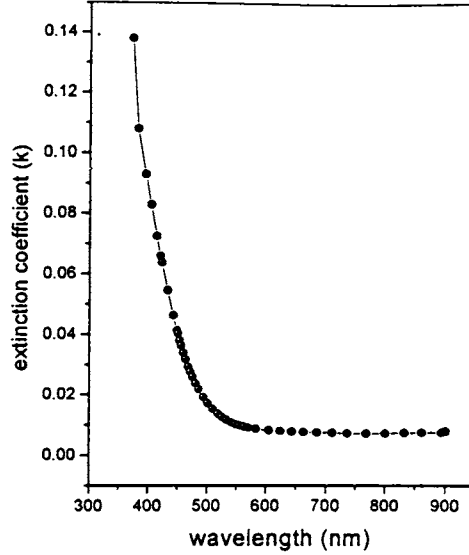


Fig. 3.45 Extinction coefficient vs wavelength
for sample annealed at 400°C

3.3.6.5 Variation of Sheet Resistance

Electrical measurements showed that the sheet resistance of the films reduced considerably (from mega ohm range to few kilo ohms) due to annealing. It is well known that the electrical properties of polycrystalline thin films are limited by the potential barriers created by grain boundaries. Presence of oxygen in the thin films could strongly modify the properties of the grain boundaries, and this probably caused an increase of the electrical conductivity of the films. The high increase of the electrical conductivity of the films studied could be attributed to the modification of the properties of the grains or their boundaries when oxygen was introduced in the films [45]. All the films exhibited n-type conductivity, which meant that introduction of oxygen did not change the type of the majority carriers. Improvement in crystallinity due to annealing may also contribute to enhancement in conductivity.

3.4 Conclusion

Indium sulfide thin films were prepared using CSP technique by varying substrate temperature, In/S ratio and thickness. The samples were characterized using XRD, SEM, AFM, EDAX, XPS, optical absorption and transmission, photosensitivity, electrical resistivity and TSC measurements. The samples showed β - In_2S_3 phase. The band gap was found to be 2.67 eV for the In/S ratio 2/3. We could get good control over the photosensitivity of the material by varying the substrate temperature or In/S ratio and the sample having In/S ratio 1.2/8 gave the maximum response ($\Delta I/I_D = 949.97$). But the sheet resistance of the sample was found to be $>2000 \text{ M}\Omega/\square$. On increasing the indium concentration (2.5/8) the sheet resistance as well as the photosensitivity of the sample decreased, and hence we have to have a compromise between the photosensitivity and resistance of the sample. Here it was observed that in terms of crystallinity, band gap and photoresponse, the sample with In/S ratio 1.2/8 is quite suitable for any photovoltaic applications. But the high resistivity of the samples with In/S ratio 1.2/8 may increase the series resistance and reduce the Fill Factor (FF) on coming to solar cell applications. Hence there should be doping (In, Sn) at top layer of In_2S_3 to have a moderate resistance and photosensitivity. Presence of chlorine also resulted in the increase of resistivity of the samples and hence it was planned to try nitrate based precursor solutions instead of chloride based ones for preparing the samples. Thermally stimulated conductivity studies revealed four trap levels with activation energies 0.1 eV, 0.26 eV, 0.43 eV and 0.82 eV in the band gap of this material. Thickness of the film could be varied by varying the volume of the spray solution and we obtained a maximum of 4 μm by spraying 1000 ml of the solution.

References

- [1] M. A. Contreras, B. Egaas, K. Ramanathan, J. Hiltner, A. Swartzlander, F. Hasoon and R. Noufi *Prog. Photovolt: Res. Appl.* **7** (1999) 311
- [2] J. R. Tuttle, M. Ruth, D. Albin, A. Mason and R. Noufi *Conf. Rec. 20th IEEE Photov. Spec. Conf.* (1988) 1525
- [3] K. Siemer, J. Klaer, I. Luck, J. Bruns, R. Klenk and D. Bräunig *Sol. Energy Mater. Sol. Cells* **67** (2001) 159
- [4] D. Hariskos, M. Ruckh, U. Rühle, T. Walter, H. W. Schock, J. Hedström and L. Stolt *Sol. Energy Mater. Sol. Cells* **41/42** (1996) 345
- [5] T. Nakada and M. Mizutani *Jpn. J. Appl. Phys.* **41** (2002) 165
- [6] A. Ennaoui, M. Weber, R. Scheer and H. J. Lewerenz *Sol. Energy Mater. Sol. Cells* **54** (1998) 277
- [7] Y. Ohtake, K. Kushiyai, M. Ichikawa, A. Yamada and M. Konagai *Jpn. J. Appl. Phys.* **37** (1998) 3220
- [8] G. Gordillo and C. Calderón *Sol. Energy Mater. Sol. Cells* **77** (2003) 163
- [9] D. Braunger, D. Hariskos, T. Walter and H. W. Schock *Sol. Energy Mater. Sol. Cells* **40** (1996) 97
- [10] P. O' Brien, D. J. Octway and J. R. Walsh *Thin Solid Films* **31** (1998) 5761
- [11] M. Amlouk, M. A. Ben Said, N. Kamoun, S. Belgacem, N. Brunet and D. Barjon *Jpn. J. Appl. Phys.* **38** (1999) 26
- [12] L. Bhira, H. Essaidi, S. Belgacem, G. Couturier, J. Salardenne, N. Barreau and J. C. Bernède *Phys. Stat. Sol. (a)* **181** (2000) 427
- [13] C. D. Lokhande, A. Ennaoui, P. S. Patil, M. Giersig, K. Diesner, M. Muller and H. Tributsch *Thin Solid Films* **340** (1999) 18
- [14] R. Nomura, K. Konishi and H. Matsuda *Thin Solid Films* **198** (1990) 339
- [15] W. T. Kim and C. D. Kim *J. Appl. Phys.* **60(7)** (1986) 2631

- [16] A. A. El Shazly, D. Abdelkady, H. S. Metoually and M. A. M. Segmam *J. Phys: Condens. Mater.* **10** (1998) 5943
- [17] J. George, K. S. Joseph, B. Pradeep and T. I. Palson *Phys. Stat. Sol. (a)* **106** (1988) 123
- [18] H. Ihara, H. Abe, S. Endo and T. Irie *Solid State Commun.* **28** (1970) 563
- [19] T. Asikainen, M. Ritala and M. Leskelä *Appl. Surf. Sci.* **82/83** (1994) 122
- [20] R. R. Chamberlin and J. S. Skarman *J. Electrochem. Soc.* **113** (1966) 86
- [21] W. T. Kim and C. S. Yun *J. Appl. Phys.* **60**(7) (1986) 2357
- [22] N. Kamoun, R. Bennaceur, M. Amlouk, S. Belgacem, N. Mikli, J. M. Frigerio and M. L. Theye *Phys. Stat. sol. (a)* **169** (1998) 97
- [23] N. Kamoun, S. Belgacem, M. Amlouk, R. Bennaceur, J. Bonnet, F. Touhari, M. Nouaoura and L. Lassabatere *J. Appl. Phys.* **89** (5) (2001) 2766
- [24] M. Ortega – Lopez and A. Morales- Acevedo *Thin Solid Films* **330** (1998) 96
- [25] N. Bouguila, H. Bouzouita, E. Lacaze, A. B. Amara, H. Bouchriha and A. Dhoub *J. de Physique III* **7** (1997) 1647
- [26] *Hand Book of Analytical Methods for Materials, Materials Evaluation and Engineering*, INC (2000)
- [27] P. M. Verghese and D. R. Clarke *J. Mater. Res.* **14** (3) (1999) 1039
- [28] Rosenberg and Tu *Treatise on Materials Science and Technology*, Academic Press **27** (1988) 65
- [29] S. H. Yu, L. Shu, Y. S. Wu, J. Yang, Y. Xie and Y. T. Qian *J. Am. Ceram. Soc.* **82** (2) (1999) 457
- [30] J. I. Pankov *Optical Processes in Semiconductors*, Dover publications, New York (1971) 34
- [31] S. H. Choe, T. H. Bang, N. O. Kim, H. G. Kim, C. I. Lee, M. S. Jin, S. K. Oh and W. T. Kim *Semicond. Sci. Technol.* **16** (2001) 98
- [32] N. Barreau, J. C. Bernède, H. El Maliki, S. Marsillac, X. Castel and J. Pinel *Solid State Commun.* **122** (2002) 445

- [33] R. Swanepoel *J. Phys. E: Sci. Instrum.* **16** (1983) 1214
- [34] P. S. Vincett *Thin Solid Films* **100** (1983) 371
- [35] N. Barreau, S. Marsillac, J. C. Bernède, T. Ben Nasrallah and S. Belgacem
Phys. Stat. Sol. (a) **184** (1) (2001) 179
- [36] Teny Theresa John, S. Bini, Y. Kashiwaba, T. Abe, Y. Yasuhiro, C. Sudha Kartha and K. P. Vijayakumar *Semicond. Sci. Technol.* **18** (2003) 491
- [37] Teny Theresa John, S. Bini, C. Sudha Kartha, K. P. Vijayakumar, T. Abe and Y. Kashiwaba *Proc. International Symposium on Recent Advances in Inorganic Materials (RAIM-2002)* Mumbai, India (2002) 106
- [38] J. H. Richardson and R.V. Peterson (Ed), *Vol II Systematic Materials Analysis*, Academic Press, New York (1974)
- [39] V. Gupta and A. Mansingh *J. Appl. Phys.* **80** (2) (1996) 1063
- [40] Teny Theresa John, K. P. Vijayakumar, C. Sudha Kartha, T. Abe and Y. Kashiwaba *Proc. World Conference on Photovoltaic Energy Conversion (WCPEC-3)* Osaka, Japan (2003) 1P-C3-24
- [41] Rupa R Pai *PhD Thesis*, Department of Physics, Cochin University of Science and Technology, Kochi-22, India (2004)
- [42] Rupa R Pai, Teny Theresa John, Y. Kashiwaba, T. Abe, K. P. Vijayakumar and C. Sudha Kartha *J. Mater. Sci.* **39** (2004) 1
- [43] P. Tyagi and A. G. Vedeshwar *Bull. Mater. Sci.* **24** (2001) 297
- [44] A. Dietrich, K. Schmalzbauer and H. Hoffmann *Thin Solid Films* **122** (1984) 19
- [45] N. Barreau, S. Marsillac, D. Albertini and J.C Bernède *Thin Solid Films* **403-404** (2002) 331

Chapter 4**PROPERTIES OF INDIUM SULFIDE THIN FILMS PREPARED USING NITRATE BASED PRECURSOR SOLUTION****4.1 Introduction**

In recent years, there has been a significant increase in the research works on III-VI materials because they find great use in the electronic industry in optoelectronic or photovoltaic applications [1, 2]. Indium sulfide is a III-VI compound, which can be prepared using different chemical methods like organometallic chemical vapour deposition [3], chemical bath deposition, atomic layer epitaxy and chemical spray pyrolysis. Indium sulfate $\text{In}_2(\text{SO}_4)_3$, 80% hydrazine hydrate, thioacetamide, triethanolamine and ammonium chloride were used for the deposition of indium sulfide using chemical bath [4]. In atomic layer epitaxy In_2S_3 films were deposited using InCl_3 and H_2S as precursors [5]. In all the reports using spray pyrolysis, dealing with deposition of indium sulfide, indium chloride and thiourea were used as the precursor solutions and their structural, optical, photoelectrical and acoustic properties had been studied [6, 7, 8, 9].

In the previous chapter we described preparation of indium sulfide films using indium chloride as one of the precursor solutions. The properties of the films depend upon the precursor solution used for deposition. This chapter describes the effect of indium nitrate as one of the precursor solutions, on the properties of indium sulfide thin films. One of the advantages of indium nitrate is that it can be pyrolysed at relatively low temperature. Moreover there is no chance of inclusion of any impurities like chlorine in the film unlike the films prepared using indium chloride.

Our motivation behind the replacement of the precursor was to remove chlorine, which caused high enhancement of electrical resistivity of In_2S_3 films. At the same time we were interested in seeing whether we could get high photosensitivity and good crystallinity in these films prepared using nitrate precursor solution. Then it

will be a great achievement as one can control both electrical resistivity and photosensitivity as these are very important factors for solar cell fabrication. If this was found to be possible, we also aimed at optimizing the preparation condition so as to get the required values of these parameters for solar cell fabrication.

4.2 Experimental Details

β - In_2S_3 thin films were prepared using CSP technique with indium nitrate ($\text{In}(\text{NO}_3)_3$) and thiourea ($\text{CS}(\text{NH}_2)_2$) as precursor solutions. Indium nitrate was prepared by dissolving high purity (99.99%) indium in concentrated HNO_3 . Micro glass slides, having dimensions of $37 \times 12 \times 1.4 \text{ mm}^3$ were used as substrates. Indium to sulfur ratio was varied by varying molar concentrations of the precursor solutions. For this, the molarity of indium nitrate was kept at 0.025 M and that of thiourea was varied to have In/S ratios ranging from 2/1 to 2/8. The total volume of the solution sprayed was 400 ml and the rate of spray was 20 ml/min in all cases keeping the substrate at 300°C . Air was used as the carrier gas. These films were yellowish in colour. Samples having In/S ratio from 2/1 to 2/8 were named S1, S2, S3, S4, S5, S6 and S8 respectively. Samples were also prepared by varying indium concentration keeping sulfur concentration at 8 to get In/S ratio 1.2/8 and 2.5/8. These samples were named S12 and S25.

4.3 Results and Discussion

4.3.1 Effect of Variation of Sulfur Concentration

4.3.1.1 Structural Analysis

Structural analysis was done using X-Ray Diffraction (XRD) (Philips X'Pert-Pro. X-Ray Diffractometer having $\text{CuK}\alpha$; $\lambda=1.5405 \text{ \AA}$ radiation). In_2S_3 thin films prepared from indium nitrate showed an interesting property in the XRD analysis. Only the sample prepared using solution having In/S ratio 2/3 (S3) exhibited good crystalline property. This sample had five peaks corresponding to (103), (109), (220), (309) and (400) orientations [Fig.4.1].

On decreasing the sulfur concentration, the sample became amorphous (S1). But on increasing the sulfur concentration the sample showed a very small peak along the (103) plane. Further increase resulted in change of preferential orientation to (109) plane for the samples S6 and S8. Other than this, two peaks corresponding to (103) and (400) also appeared on increasing the sulfur concentration. The grain size of the film was calculated using the Debye-Scherrer formula $D = 0.9\lambda/\beta\cos\theta$, where D is the diameter of the crystallites forming the film, λ is the wavelength of CuK_α line, β is FWHM in radians and θ is the Bragg angle. It was found to be 28 nm for the sample S3 that reduced to 20.8 nm for S8.

Lattice constants a and c for the samples were calculated from the results of x-ray diffraction patterns using the (103) and (109) planes. For the sample S3, the values were found to be $a = b = 7.58 \text{ \AA}$, $c = 32.08 \text{ \AA}$. As the In/S ratio decreased, the lattice constants increased slightly (for the ratio 2/8 $a = b = 7.6 \text{ \AA}$, $c = 32.4 \text{ \AA}$) [7]. These values are comparable with those for $\beta\text{-In}_2\text{S}_3$ shown in JCPDS card (25-390).

Samples prepared using indium chloride also showed $\beta\text{-In}_2\text{S}_3$ phase with preferential orientation along the (220) plane. On increasing the sulfur concentration from 2/3 to 2/5, the intensity of the peak corresponding to this plane increased, but a further increase of sulfur concentration (2/8) resulted in the decrease of the peak intensity [10, 11]. There was no change in preferential orientation.

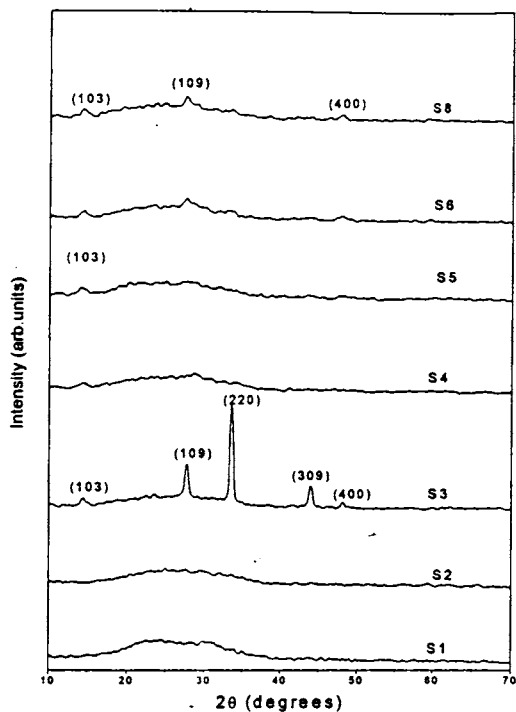


Fig. 4.1 XRD pattern of In₂S₃ samples, S1 to S8

4.3.1.2 Surface Morphology

Surface morphology was examined using Scanning Electron Microscopy (SEM). It revealed a dense structure and no cracks or voids were observed on the sample S3 [Fig.4.2a]. Fig.4.2 (b) show that granularity was lost on decreasing (S1) or on increasing (S4) [Fig. 4.3a] the sulfur concentration. The sample regained its granular structure [Fig.4.3b] when the ratio became 2/8 (S8). However the grain size was small even in this case. This was clearly observed in structural analysis (XRD) also [Fig.4.1].



(a)



(b)

Fig. 4.2 SEM micrographs of (a) S3 and (b) S1



(a)

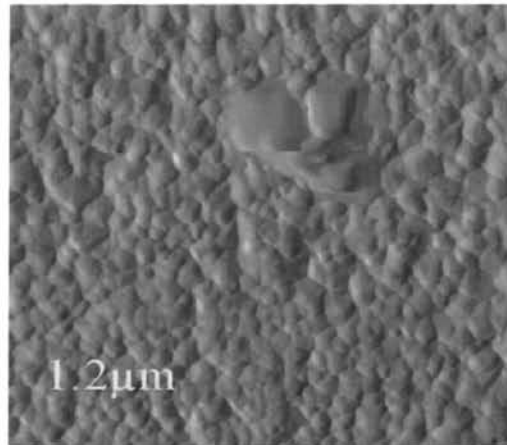


(b)

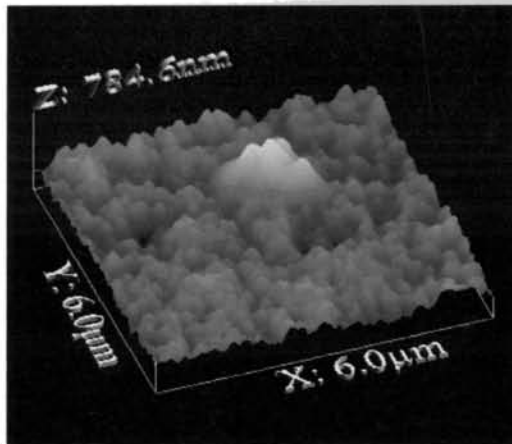
Fig. 4.3 Surface morphology of samples (a) S4 and (b) S8

4.3.1.3 AFM

Fig. 4.4 (a) and (b) depicts the AFM image (2D and 3D) of 6 micrometer square area of the sample S3. The sample was dense and grains were found to be uniform in size.



(a)



(b)

Fig. 4.4 AFM image of sample S3 (a) 2D and (b) 3D

4.3.1.4 EDAX Measurements

Concentration of sulfur was found to be low for samples S1 and S2 (~38%), but it exceeded 60% on increasing the sulfur concentration in solution. Atomic

concentrations of indium and sulfur were found to be almost equal for S3. This sample was found to be better in electrical conductivity ($232 \Omega\text{-cm}$) compared to S2, S4 and S5. Hence excess of indium indicated by EDAX analysis, might be occupying interstitial position. It had been reported that in relatively low resistive In_2S_3 , donor concentrations are high (In interstitials) [12]. Variation of atomic concentration with In/S ratios is given in Fig.4.5. Thus it was clear that the In/S ratio in the initial precursor solution determined the composition of the samples.

Concentration of sulfur in the sample never reached 60% when indium chloride was used to prepare the samples. Nevertheless an increase in the concentration of indium resulted in a corresponding increase in the concentration of chlorine in the sample. Stoichiometric films were obtained only when indium chloride was replaced by indium nitrate.

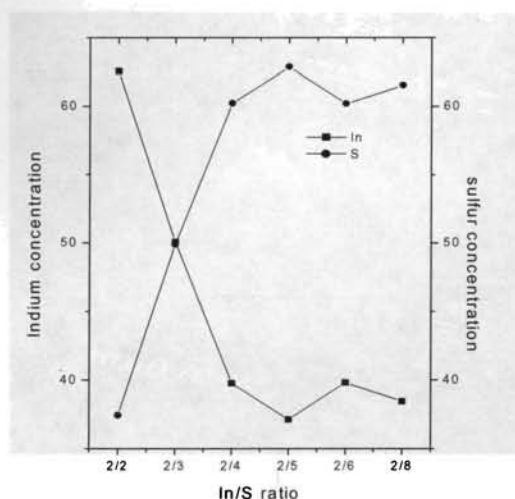


Fig.4.5 Variation of atomic concentration with In/S ratio

4.3.1.5 XPS Analysis

Depth profile of the sample S3 [Fig.4.6] showed that indium and sulfur were uniformly distributed throughout the depth of the sample. Binding energies of indium and sulfur clearly indicated the formation of indium sulfide. The values are compared in Table 4.1.

Table 4.1 Binding energies of indium and sulfur in indium sulfide

Element	Binding Energy (eV)
In3d _{5/2}	444.7
In3d _{3/2}	452.7
S2p	162

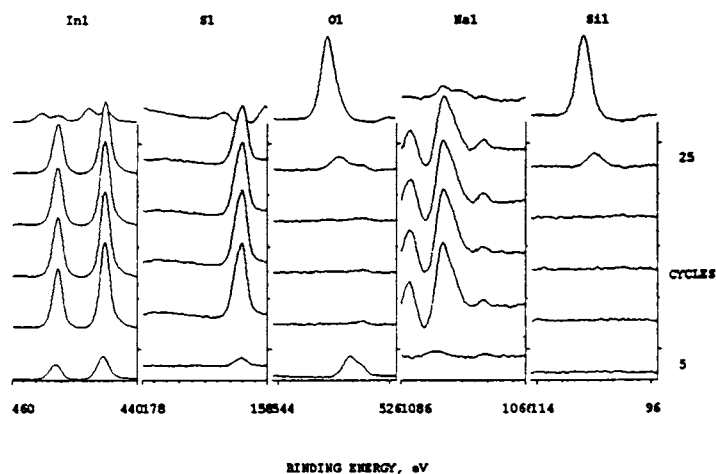
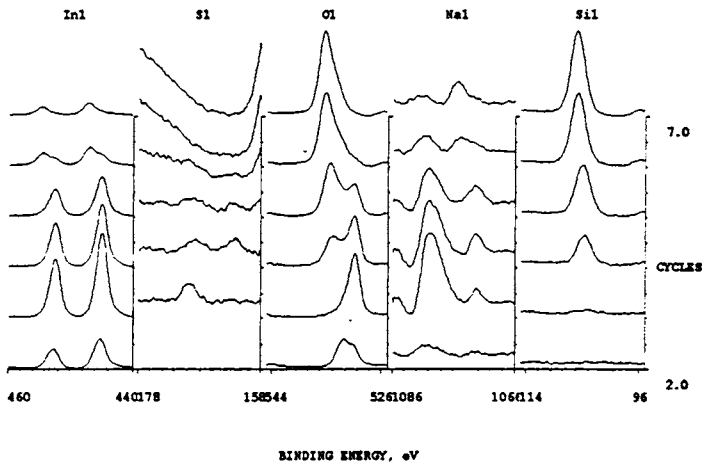


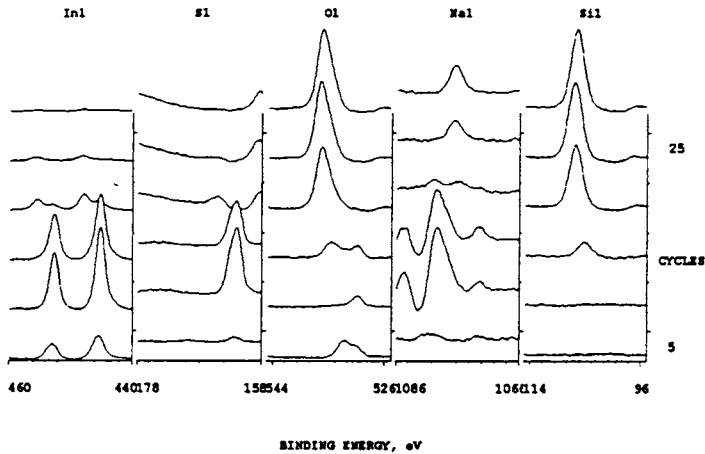
Fig. 4.6 XPS profile montage of sample S3

Oxygen was present only as a surface contaminant having binding energy 532 eV that corresponds to oxygen in the form of sulfate [13]. But sodium was present throughout the depth of the sample, which might be diffusing from the glass substrate, as the substrate was kept at high temperature (300° C). Moreover there was no sodium in any of the chemicals used for the preparation of the sample.

On decreasing the sulfur concentration (S1) [Fig.4.7] there was a shift in the binding energy of sulfur (170 eV), which corresponds, to that of sulfate. There was also oxygen present in the bulk of this sample with binding energy 530 eV. This corresponds to O1s in In_2O_3 . The sample S1 is suspected to be In_2O_3 eventhough we could not identify any In_2O_3 phase from XRD.



(a)



(b)

Fig. 4.7 XPS depth profile of samples (a) S1 and (b) S4

On increasing sulfur concentration (S4) the binding energies of indium and sulfur indicated the formation of indium sulfide, but the presence of In₂O₃ also was observed from the shift in the binding energy of oxygen in the bulk of the sample [Fig.4.7b]. BE of oxygen on the surface of the sample corresponds to that of surface contamination in the form of sulfate (532 eV). The sulfur atoms in sample S4 situated near film substrate interface or diffused into the substrate exhibited BE of 164 eV. This corresponds to that of elemental sulfur. These samples were amorphous, and there are earlier reports on amorphous nature of samples having excess sulfur [14].

On further increasing the sulfur concentration (S8), oxygen was found to be present only on the surface of the sample [Fig.4.8]. There was no In₂O₃ phase in samples S6 and S8. Presence of sodium in the bulk was observed for all the samples.

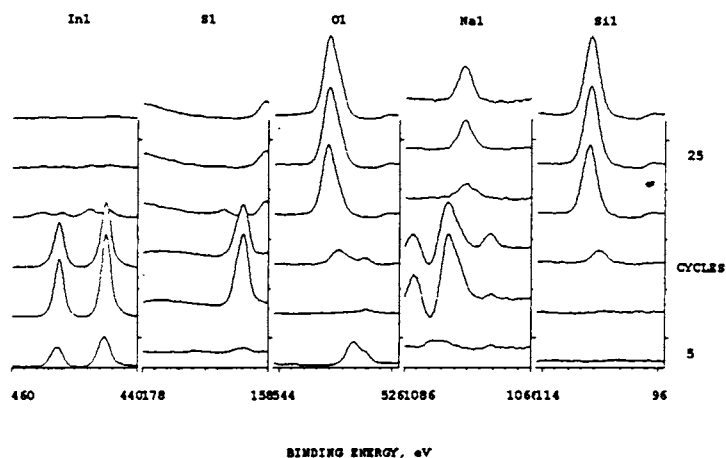


Fig. 4.8 Profile montage of sample S8

4.3.1.6 Optical Studies

From the plot of $(\alpha h\nu)^2$ vs $h\nu$ [Fig.4.9], a direct band gap of 2.66 eV was obtained for the sample S3. On decreasing sulfur concentration (S1) the band gap increased to 2.95 eV [Fig.4.10]. Increase in the band gap for smaller sulfur concentration could be ascribed both to the presence of secondary phases and to a more disordered structure. Incorporation of oxygen might be another reason for the widening of the band gap [14]. Band gap decreased to 2.73 eV on increasing the sulfur concentration (S8). Thus the band gap was found to vary with crystalline structure [Fig.4.1] of the sample.

Transmittance measurements were performed in the spectral range 400 nm to 1200 nm [Fig.4.11]. Sample S1 showed better transparency (might be due to the formation of In_2O_3 as observed from XPS). The band gap of this sample was also close to that of In_2O_3 [15].

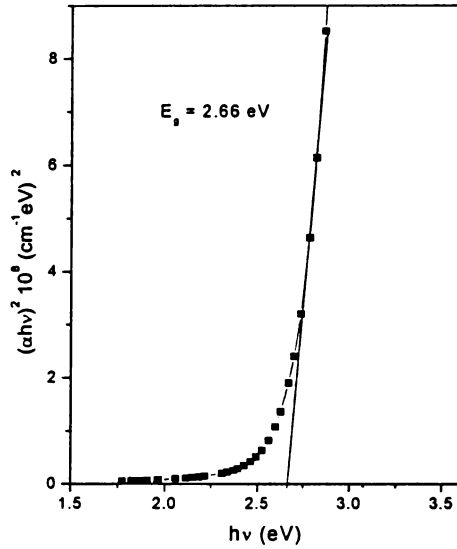


Fig. 4.9 $(\alpha h\nu)^2$ vs $h\nu$ plot of sample S3

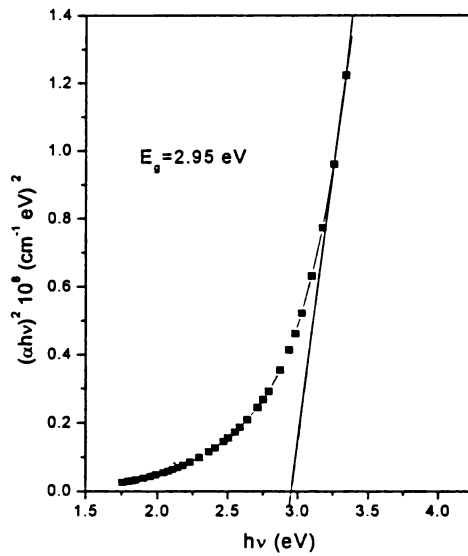


Fig.4.10 Band gap of sample S1

Refractive index was calculated using the envelope method from transmission spectra for samples S3 and S8. The value was found to vary in the range 1.57 to 1.77 with wavelength [Fig. 4.12]. Increase in the value of refractive index with the concentration of sulfur in the film might be due to diminishing crystallinity [16]. For sample S3, variation of extinction coefficient with wavelength is shown in Fig. 4.13.

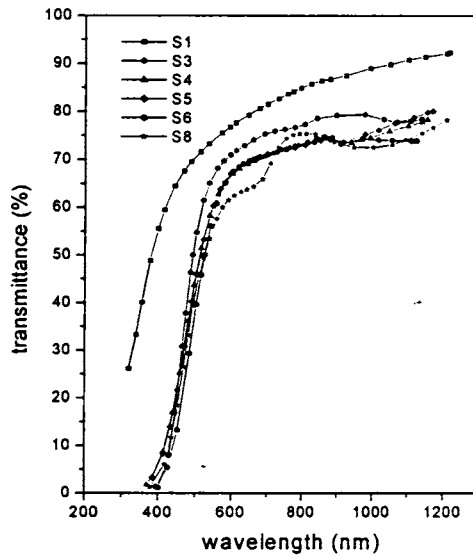


Fig. 4.11 Variation of transmittance with In/S ratio

When indium chloride was used as the precursor solution, band gap was found to be almost the same (2.67 eV) for the sample S3. It increased to 2.81 eV on decreasing the sulfur concentration (S1) and reduced to 2.64 eV on increasing the same in that case [10]. Here also widening of the band gap on reducing the sulfur concentration might be due to presence of oxygen in the sample. But In_2O_3 phase was not detected either from XRD or from XPS.

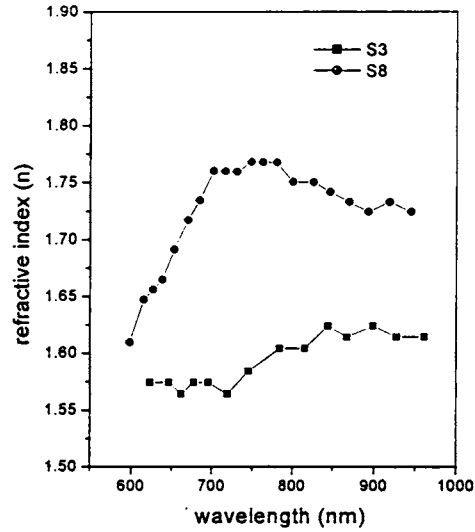


Fig. 4.12 Variation in refractive index with wavelength for samples S3 and S8

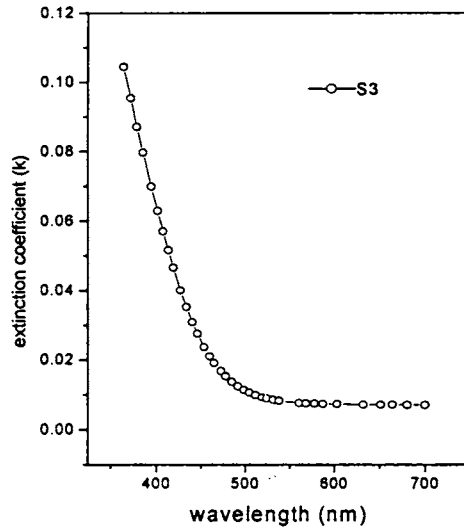


Fig. 4.13 Extinction coefficient with wavelength for sample S3

4.3.1.7 Resistivity and Photosensitivity

Resistivity of the sample S1 was found to be $9.6 \Omega\text{-cm}$, which was very low when compared with that of samples having higher sulfur concentration, indicating the presence of mainly In_2O_3 . But it was observed that small quantity of In_2O_3 phase in In_2S_3 films decreased the conductivity very much. This was true for samples S2 and S4 ($\rho = 1.8 \times 10^4 \Omega\text{-cm}$) in which In_2O_3 phase was found to exist along with In_2S_3 from XPS profile montage [17]. On increasing the sulfur concentration (S8) the sample showed maximum conductivity ($\rho = 59.4 \Omega\text{-cm}$). This was actually against the expectation as we feel that increase in sulfur concentration might decrease electrical conductivity as observed in the case of chloride samples. This might be because of the slightly better stoichiometry and the change of preferential orientation to the (109) plane [as per JCPDS data (25-390) this is the maximum intensity peak for $\beta\text{-In}_2\text{S}_3$]. Fig. 4.14 depicts the variation of resistivity with sulfur concentration.

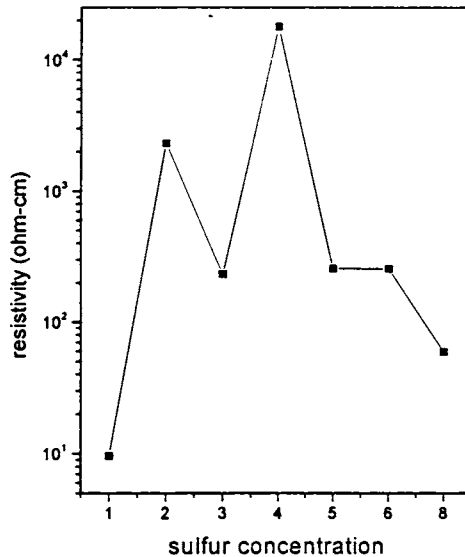


Fig. 4.14 Variation of resistivity with sulfur concentration

Fig.4.15 shows the variation of the photosensitivity with In/S ratio. Sample S4 showed maximum photosensitivity. High resistivity of samples S2 and S4 indicated a reduction in the number of majority carriers. So, probably the minority carriers, surviving to contribute to photoconductivity for these two samples might be more, indicating high photosensitivity.

However photosensitivity was low for samples prepared using nitrate based precursor solution when compared to that prepared using chloride based precursor solution. We suspect that the chlorine present in the sample, prepared using indium chloride, might be the reason for the decrease in dark conductivity (and hence increase in photosensitivity) of those samples [10].

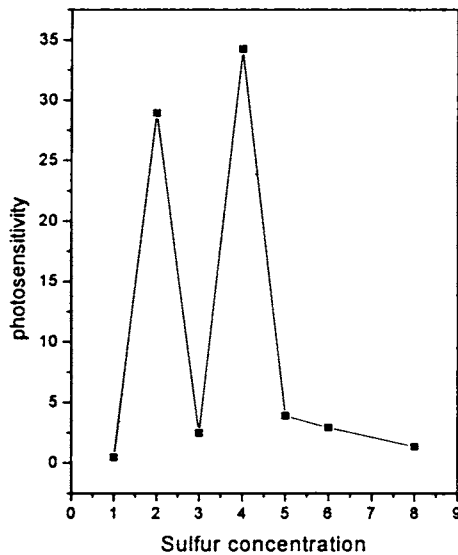


Fig. 4.15 Variation in photosensitivity with In/S ratio

4.3.2 Effect of Variation of Indium Concentration

The concentration of indium in the solution was varied by keeping the sulfur concentration at 8. For this the molarity of thiourea was kept at 0.1 M and that of indium nitrate was varied.

4.3.2.1 Structural Analysis

Four peaks were observed in the XRD spectra corresponding to the planes (103), (109), (220) and (400) with preferential orientation along the (109) plane for sample S25 [Fig. 4.16c].

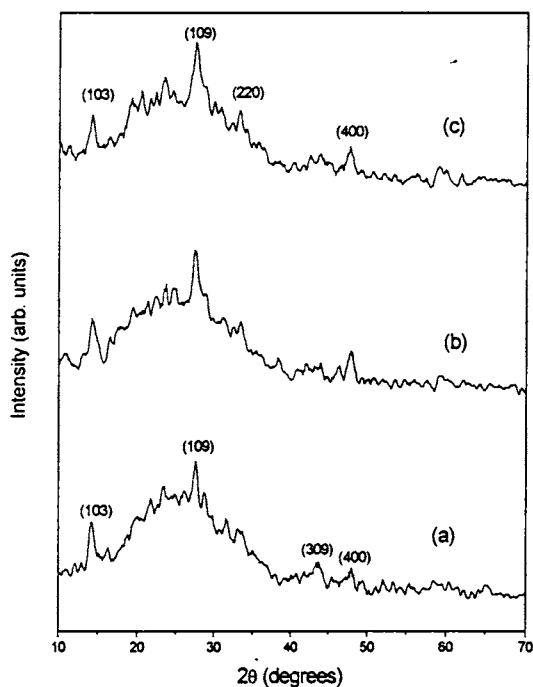


Fig.4.16 XRD spectra of (a) S12 (b) S8 and (c) S25 samples

The intensity of preferentially oriented (109) plane increased on increasing the indium concentration (S12 to S25). The small peak corresponding to the (309) plane disappeared in the case of sample S25, while that corresponding to (400) plane gained intensity. In the case of samples prepared using indium chloride as one of the precursor solutions, all these samples showed preferential orientation along (220) plane.

4.3.2.2 Optical Studies

Band gap varied from 2.77 eV for sample S12 to 2.67 eV for sample S25. The wavelength dependence of absorbance on these samples is shown in Fig. 4.17. The decrease in band gap might be due to the improvement in crystalline structure of the samples on increasing indium concentration. Transmittance spectrum of the samples on increasing indium concentration. Transmittance spectrum of the samples in the wavelength range 350-1400 nm is shown in Fig. 4.18.

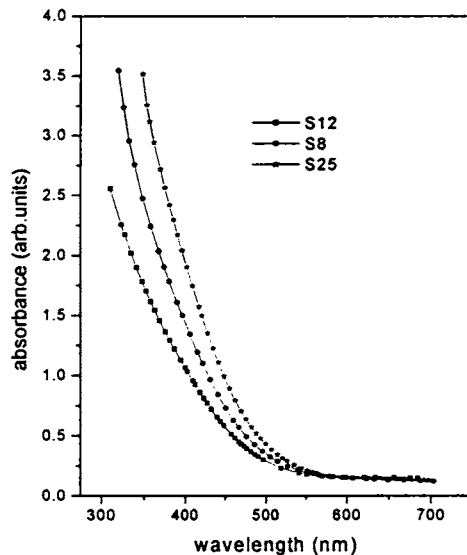


Fig. 4.17 Wavelength dependence of absorbance for samples S12, S8 and S25

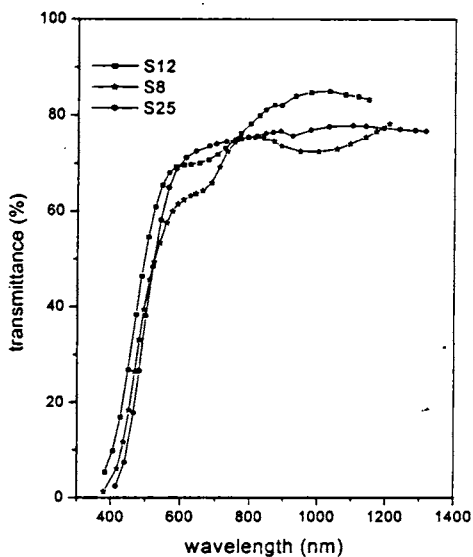


Fig. 4.18 Transmittance spectra of samples S12, S8 and S25

4.3.2.3 Photosensitivity Measurements

Photosensitivity of the samples decreased on increasing the indium concentration. Among the three samples S12, S8 and S25, the sample S12 showed maximum sensitivity. But the value was found to be much less than those samples prepared using chloride based precursor solution. Variation of photosensitivity is given in Fig. 4.19.

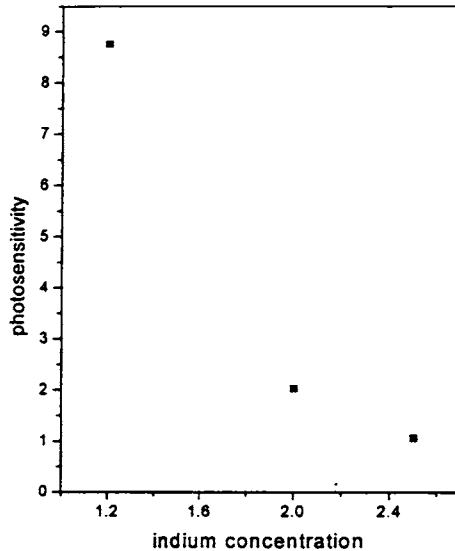


Fig. 4.19 Variation in photosensitivity: S12, S8 and S25

4.4 Conclusion

Indium nitrate, instead of indium chloride, could be used as the precursor solution for preparing β - In_2S_3 thin films using CSP technique. Interestingly only the sample having In/S ratio 2/3 in the solution showed good crystallinity with band gap 2.66 eV, while chloride samples showed better crystallinity on increasing the sulfur concentration. We could get better control over stoichiometry of the films by varying In/S ratio taken in the solution, using nitrate-based precursor. Concentration of sulfur exceeded 60% on increasing sulfur concentration in the solution. Moreover presence of chlorine in the sample could be avoided using indium nitrate as precursor. When indium chloride was used, increasing concentration of indium resulted in a corresponding increase in chlorine also. Because of this the In/S ratio in the film was found not to follow the variation of In/S ratio in the solution. Another important point worth mentioning here is the variation of electrical conductivity with increase of

sulfur concentration in the sample. Unlike in the case of samples prepared from chloride precursor, here conductivity increased considerably for samples having In/S ratio 2/6 and 2/8. This might be due to the structural changes for these samples as revealed by XRD or due to carriers released from defects. Thus indium nitrate proved to be a good precursor for preparing In_2S_3 films. However, there was considerable decrease in photosensitivity for In_2S_3 prepared using indium nitrate. Maximum photosensitivity was obtained for the sample having In/S ratio 2/4 (34.23) among nitrate based samples, while it was for 1.2/8 (949.97) in chloride-based samples. But this sample had very high sheet resistance ($>2000 \text{ M}\Omega/\square$) when compared with nitrate sample having In/S ratio 2/4 ($99 \text{ M}\Omega/\square$). Nitrate based samples were found to be more conducting compared to chloride samples. Presence of chlorine might be the reason for the high resistivity of chloride-based samples. But because of the low photosensitivity of nitrate samples, it may not be as good as chloride samples for fabricating solar cells.

References

- [1] A. R. Barron *Adv. Mater. Opt. Electro.* **5** (1995) 245
- [2] M. Amlouk, M. A. Ben Said, N. Kamoun, S. Belgacem, N. Brunet and D. Barjon
Jpn. J. Appl. Phys. **38** (1999) 26
- [3] R. Nomura, K. Konishi and H. Matsuda *Thin Solid Films* **198** (1990) 339
- [4] C. D. Lokhande, A. Ennaoui, P. S. Patil, M. Giersig, K. Diesner, M. Muller and H. Tributsch *Thin Solid Films* **340** (1999) 18
- [5] T. Asikainen, M. Ritala and M. Leskelä *Appl. Surf. Sci.* **82/83** (1994) 122
- [6] N. Kamoun, S. Belgacem, M. Amlouk, R. Bennaceur, J. Bonnet, F. Touhari, M. Nouaoura and L. Lassabatere *J. Appl. Phys.* **89(5)** (2001) 2766
- [7] W. T. Kim and C. D. Kim *J. Appl. Phys.* **60(7)** (1986) 2631
- [8] L. Bhira, H. Essaidi, S. Belgacem, G. Couturier, J. Salardenne, N. Barreaux and J. C. Bernède *Phys. Stat. Sol. (a)* **181** (2000) 427
- [9] M. Amlouk, M. A. Ben Said, N. Kamoun, S. Belgacem, N. Brunet and D. Barjon
Jpn. J. Appl. Phys. **38** (1999) 26.
- [10] Teny Theresa John, S. Bini, Y. Kashiwaba, T. Abe, Y. Yasuhiro, C. Sudha Kartha and K. P. Vijayakumar *Semicond. Sci. Technol.* **18** (2003) 491
- [11] Teny Theresa John, S. Bini, C. Sudha Kartha, K. P. Vijayakumar, T. Abe and Y. Kashiwaba *Proc. International Symposium on Recent Advances in Inorganic Materials (RAIM-2002)* Mumbai, India (2002) 106
- [12] R. S. Becker, T. Zheng, J. Elton and M. Saeki *Sol. Energy. Mater.* **13** (1986) 97
- [13] Teny Theresa John, K. P. Vijayakumar, C. Sudha Kartha, T. Abe and Y. Kashiwaba *Proc. World Conference on Photovoltaic Energy Conversion (WCPEC-3)* Osaka, Japan (2003) 1P-C3-24
- [14] N. Barreau, J. C. Bernède, H. El Maliki, S. Marsillac, X. Castel and J. Pinel *Solid State Commun.* **122** (2002) 445
- [15] K. Hara, K. Sayama and H. Arakawa *Sol. Energy Mater. Sol. Cells* **62** (2000) 441

- [16] N. Kamoun, R. Bennaceur, M. Amlouk, S. Belgacem, N. Mikli, J. M. Frigerio and M. L. Theye *Phys. Stat. Sol. (a)* **169** (1998) 97
- [17] Teny Theresa John, C. Sudha Kartha, K. P. Vijayakumar, T. Abe and Y. Kashiwaba *Appl. Surf. Sci.* (under revision)

Chapter 5**STUDIES ON CuInS₂ THIN FILMS PREPARED USING CHLORIDE AND NITRATE BASED PRECURSOR SOLUTIONS****5.1 Introduction**

High conversion efficiency and low fabrication costs are the two principal requirements of thin film solar cells for terrestrial applications. Several promising materials are currently being investigated in an effort to improve properties and reduce process costs; CuInS₂ is particularly a promising candidate because of its optimum direct band gap ($E_g = 1.5$ eV) [1] and its controllable conversion type [2]. This is one of the I-III-VI₂ type semiconductors that crystallize in chalcopyrite structure. Thin film solar cells based on CuInS₂ have reached efficiency above 10% that make them a promising candidate for future energy requirements [3]. Wider band gap of CuInS₂ compared to other widely used chalcopyrites such as CuInSe₂ and Cu(In,Ga)Se₂ has an advantage of potentially higher open circuit voltages. It is also important that sulfur is less toxic than selenium. It has been predicted theoretically that homojunction fabricated using this material can yield an efficiency of 27 to 32% [4].

A variety of techniques have been applied to deposit CuInS₂ thin films [5-9] including molecular beam epitaxy, flash evaporation, r f sputtering, chemical vapor deposition and chemical spray pyrolysis (CSP). One of the major problems of this class of materials is the control of stoichiometry ie, control of the excess copper content and of the copper to indium and metal to chalcogen ratios. Because of the large difference in the vapor pressures of copper, indium and chalcogen, the stoichiometry is controlled by means of sophisticated vapor monitoring techniques. Unlike the case of physical vapor deposition techniques, in CSP technique, ratios of the constituents in the sample are directly linked to their concentrations in the spray solution. Hence this technique is ideally suited for deposition of large area films with

controlled stoichiometry and dopant profiles [10]. One can even think of varying stoichiometry along film thickness by making appropriate changes in molarity ratio of the solution.

Also, for economic reasons, it should be very interesting to deposit these films using a cheap deposition technique. In that case, spray pyrolysis appears very promising since CuInS₂ films with good crystalline properties were grown. In most of the cases CuInS₂ thin films were deposited from aqueous solution containing CuCl₂, InCl₃ and thiourea [11-14]. Pamplin et al prepared CuInS₂ thin films using cuprous chloride, cupric acetate and cupric chloride as sources of copper. It was also found that N, N-dimethyl thiourea gave better quality layers than those obtained from thiourea [15].

In this chapter, properties of CuInS₂ thin films prepared using chloride and nitrate based precursor solutions are described. Nitrate based precursor solutions were used to avoid formation of chlorine impurity phase in the films. There were no earlier reports on sample preparation using nitrate-based precursors. The structural and optical properties of sprayed films were determined mainly by growth temperature and Cu/In ratio in the spraying solution. We have obtained information about the dependence of the composition of the elements in the films as a function of the composition in the spray solution. Nitrate based CuInS₂ films showed better stoichiometry. It could be seen that chemical composition in the solution controlled film resistivity in a wide range, a fact that might be useful when designing solar cells made from this material. Crystallinity, photosensitivity and band gap of the samples are also important as far as solar cells are concerned. The surface morphology, structural and optical properties, depth analysis (XPS) and temperature dependent conductivity of both the set of samples are also discussed.

5.2 Experimental Details

CuInS_2 thin films were prepared using chloride and nitrate based precursor solutions using CSP. In the first case aqueous solutions of CuCl_2 , InCl_3 and thiourea ($\text{CS}(\text{NH}_2)_2$) were used as the precursors, while in the second case $\text{Cu}(\text{NO}_3)_2$, $\text{In}(\text{NO}_3)_3$ and thiourea were used as precursors. Indium chloride was prepared by dissolving high purity indium (99.99%) in concentrated HCl and indium nitrate was prepared by dissolving the same in concentrated HNO_3 . All the solutions were prepared in distilled water. 375 ml of the solution was sprayed onto glass substrates kept at 300°C . The maximum volume of the solution that could be sprayed in a single stretch for getting uniform good films without any pinholes was 375 ml. On further increasing the volume, it resulted in the development of pinholes in the sample. Thus in a single spray we could not increase the film thickness beyond a limit. Equal volumes of the solutions were mixed in appropriate molar concentrations to get different Cu/In ratios. Cu/In ratio was varied from 0.5 to 1.5 keeping S/Cu ratio at 5. For this, the molarity ratio of CuCl_2 (or $\text{Cu}(\text{NO}_3)_2$) and thiourea was kept at 0.0125 M and 0.0625 M respectively while molarity of InCl_3 (or $\text{In}(\text{NO}_3)_3$) was varied. Air was used as the carrier gas and the spray rate was kept at 20 ml/min in all cases. Samples prepared using chloride based precursor solution were named C1, C2, C3, C4 and C5 having Cu/In ratio 0.5, 0.7, 1, 1.2 and 1.5 respectively, keeping S/Cu ratio at 5. For nitrate based precursor solutions samples were represented as N1, N2, N3, N4 and N5 having Cu/In ratio 0.5, 0.7, 1, 1.2 and 1.5 respectively with S/Cu ratio 5.

5.3 CuInS_2 from Chloride Based Precursor Solution

5.3.1 Structural Analysis

XRD spectrum of the samples is depicted in Fig 5.1. Crystallinity of the samples was found to increase with increase in Cu/In ratio. Four characteristic peaks corresponding to planes (112), (220), (312) and (224) appeared for sample C5 (JCPDS-270159) with preferential orientation along (112) plane. The improvement in

crystallinity when Cu/In ratio was increased was an effect, which had been attributed to copper mobility [16]. The d values and peak intensities are compared in Table 5.1. Peak corresponding to (220) plane of CuInS₂ indicated formation of CuInS₂ phase in both Cu-poor C1 and C2 samples. A broad peak with a shoulder was obtained for Cu-poor C1 sample at around 26.5° and another one at 64°. This might be due to some impurity phase formation in the sample. The diffraction peak at $2\theta = 26.5^\circ$ could be related to the formation of In₂S₃ phase (JCPDS-330623), due to presence of excess indium as observed from EDAX analysis. Films with excess indium did not show good crystallinity due to the presence of secondary chemical phases of In₂S₃ and InS, and very likely due to the lattice deformation by copper vacancies being occupied by indium atoms. The peak at 64° corresponds to the formation of InS phase (JCPDS-190588).

Table 5.1 XRD data of CuInS₂ film

2θ (degrees)	d [Å] (observed)	d [Å] (standard)	hkl	I/I_0 (observed)	I/I_0 (standard)
27.91	3.1932	3.198	112	100	100
46.27	1.9603	1.952	220	10.54	10
54.88	1.6716	1.666	312	2.80	12
57.70	1.5962	1.601	224	16.51	4

Grain size was calculated from the Debye-Scherrer formula for samples C3, C4 and C5 since they only showed maximum intensity peak along the same plane. The value was found to increase from 5.8 nm to 21.23 nm with increase in the Cu/In ratio. Lattice parameters were calculated to be $a = b = 5.54$ Å and $c = 11.01$ Å which was in good agreement with the standard values of $a = b = 5.523$ Å and $c = 11.141$ Å.

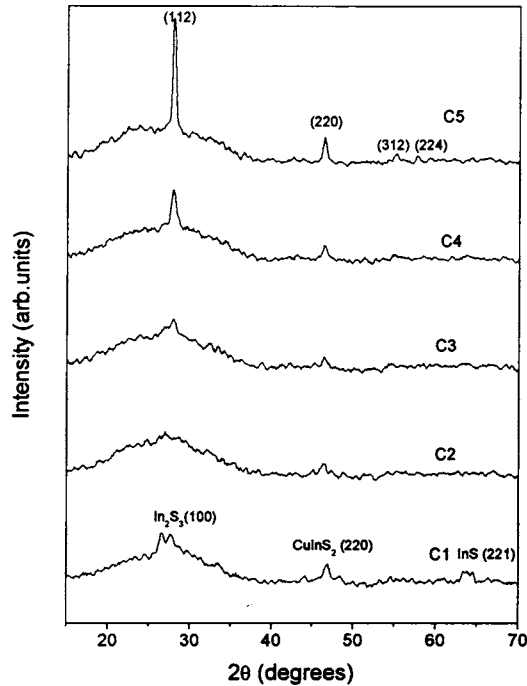


Fig. 5.1 XRD pattern of samples C1, C2, C3, C4 and C5

5.3.2 Surface Morphology

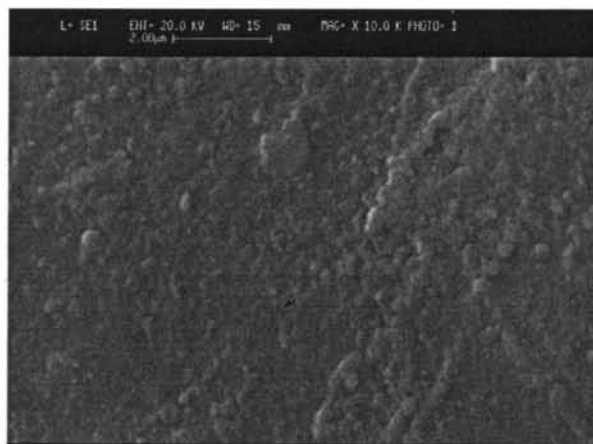
Surface morphology was examined using SEM. In-rich solutions produced films (C1) with smooth surface and small grains. SEM micrographs showed agglomerated areas in Cu-rich films. The number as well as size of the agglomerated area increased with increasing copper concentration in the solution. Chemical composition of the agglomerated area was different from composition of the flat region. The copper content in this area was higher than that in the flat region and indium content was essentially decreased [17]. SEM micrographs are compared in Fig.5.2 (a), (b) and (c).



(a)



(b)



(c)

Fig. 5.2 Surface morphology (a) C1 (b) C4 (c) C5

5.3.3 EDAX Measurements

Composition of CuInS_2 films was studied using EDAX measurements. Atomic concentration of Cu, In and S in the film is compared in Table 5.2. Cu/In and S/Cu ratios were found to be always less than that taken in the solution. The EDAX spectrum of sample C1 is shown in Fig.5.3.

Table 5.2 Atomic concentrations of Cu, In and S

Sample	Cu (%)	In (%)	S (%)	Cu/In ratio in film
C1 (Cu/In = 0.5)	11.27	25.65	54.52	0.44
C3 (Cu/In = 1.0)	16.36	23.75	56.33	0.69
C4 (Cu/In = 1.2)	15.47	16.68	59.12	0.93
C5 (Cu/In = 1.5)	15.72	12.58	59.08	1.25

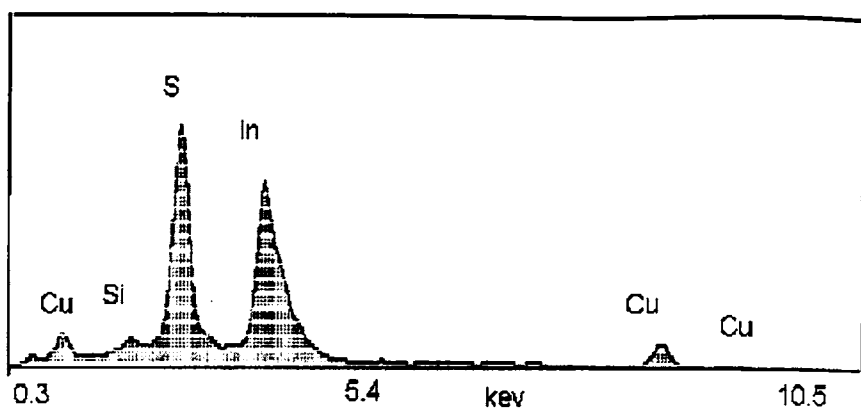


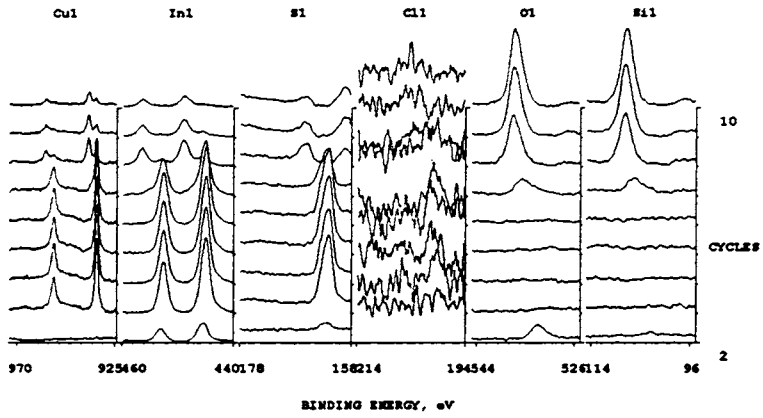
Fig. 5.3 EDAX spectrum of sample C1

5.3.4 XPS Analysis

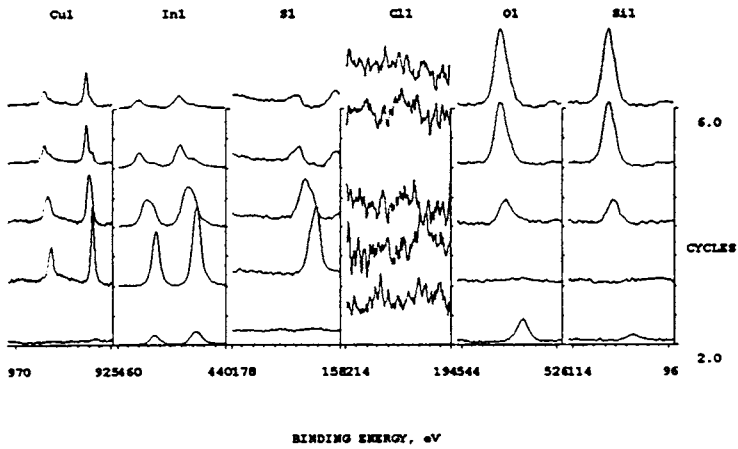
In order to know the chemical state of the elements along the thickness of the samples, we performed XPS depth profile of the samples. Here the presence of the elements Cu, In, S, O and Si was checked along the thickness of the samples. It could be seen that all the elements diffused slightly into the glass substrate, probably due to the high temperature at which spraying was done. Oxygen was present only at the surface of these samples. This was very much evident in Fig.5.4 (a) and (b). The BE value of surface oxygen was found to be 532 eV, which was due to surface contamination [18]. BE values of Cu, In and S indicated formation of CuInS_2 and these are compared in Table 5.3. Interestingly chlorine was absent in these samples.

Table 5.3 BE value of Cu, In and S as observed from XPS Analysis

Element	Binding Energy (eV)
$\text{Cu}2p_{3/2}$	932.5
$\text{Cu}2p_{1/2}$	952.5
$\text{In}3d_{5/2}$	444.7
$\text{In}3d_{3/2}$	452.7
$\text{S}2p$	162.0



(a)



(b)

Fig. 5.4 Depth profile of sample (a) C1 (b) C5

5.3.5 Optical Studies

We obtained band gap from the plot of $(\alpha h\nu)^2$ vs $h\nu$ [Fig.5.5] and was found to decrease from 1.51 eV to 1.32 eV for sample C1 to C5 [Fig.5.6]. This variation was in accordance with the variation in crystallinity of the samples as observed from XRD [Fig. 5.1]. Another possible cause for this effect might be carrier degeneracy in CuInS_2 due to defects in the crystal lattice [12] and/or due to the increase in Cu/In ratio. This was evident from the high conductivity of sample C5.

Transmittance spectra of the samples in the wavelength range 400 – 1200 nm are shown in Fig.5.7. Percentage of transmittance was found to decrease with increase in Cu/In ratio.

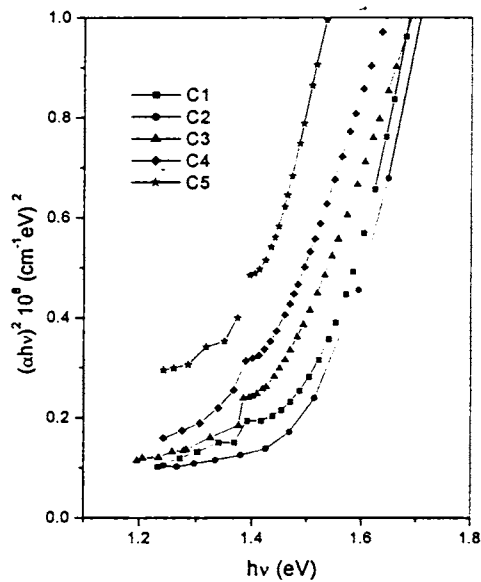


Fig.5.5 $(\alpha h\nu)^2$ vs $h\nu$ for samples C1 to C5

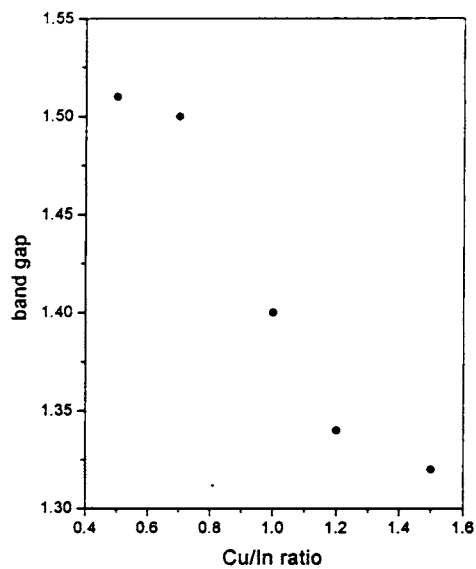


Fig. 5.6 Variation in band gap (C1 to C5)

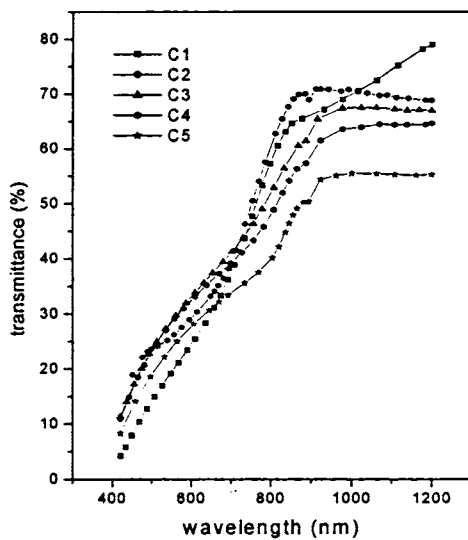


Fig. 5.7 Wavelength dependence of transmittance for samples C1 to C5

5.3.6 Photosensitivity Measurements

Figure 5.8 shows variation in photosensitivity with Cu/In ratio. The value decreased drastically with increase in the Cu/In ratio. Thus the sample C1 was found to have maximum photoresponse. High resistivity of sample C1 indicated a reduction in the number of majority carriers. So, probably the minority carriers, surviving to contribute to photoconductivity for this sample might be more, indicating high photosensitivity.

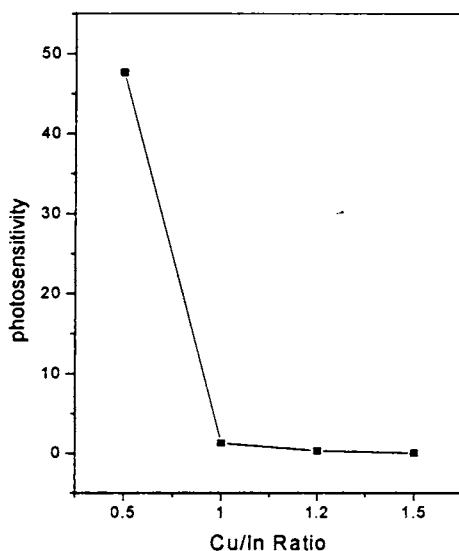


Fig.5.8 Variation in photosensitivity with Cu/In ratio

5.4 CuInS_2 from Nitrate Based Precursor Solution

5.4.1 Structural Analysis

It was obvious from the XRD spectra that the crystallinity of the samples increased with increase in Cu/In ratio [Fig.5.9]. All the samples showed preferential orientation along (112) plane. Cu-poor nitrate based CuInS_2 films seem to be more crystalline when compared to that of samples prepared from chloride based solutions. Grain sizes are compared in Fig.5.10. Grain size increased from 6.64 nm for N1

(Cu/In=0.5) to 20.6 nm for N5 (Cu/In=1.5). Thus the grain size was found to depend on the content of copper and indium in the films.

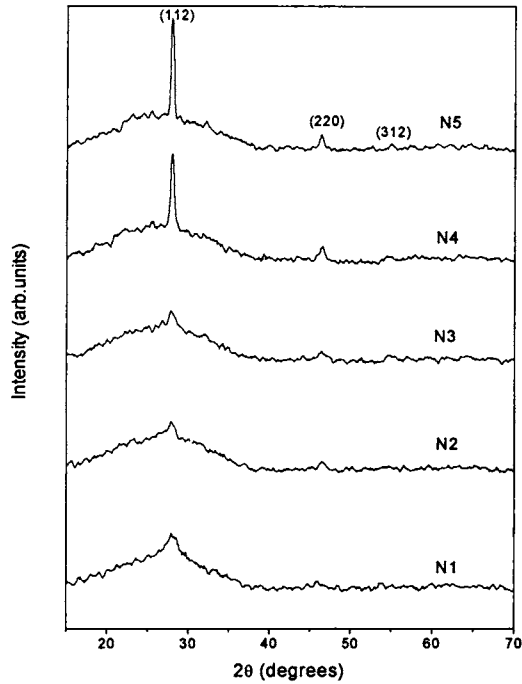


Fig. 5.9 XRD pattern of samples N1 to N5

5.4.2 Surface Morphology

CuInS_2 layer was characterized by means of scanning electron microscopy (JEOL Scanning Microscope Model JSM-8404) for surface observation. No surface feature was observed in the film and the film appeared to be uniform. This improved on increasing Cu/In ratio. SEM micrographs of samples N1 and N4 are shown in Fig. 5.11 (a) and (b). Both Cu-rich and In-rich films had fairly smooth structure, consisting of non-featured grains.

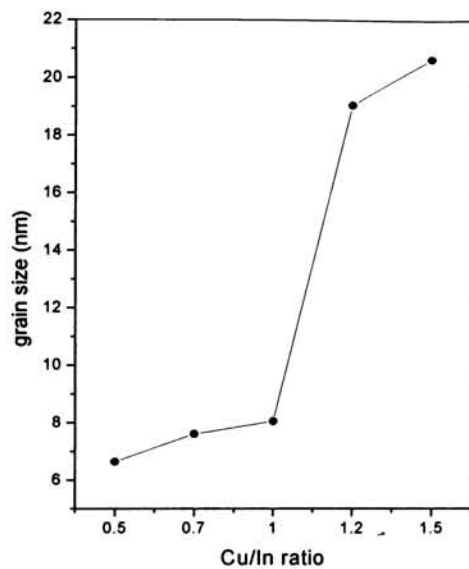
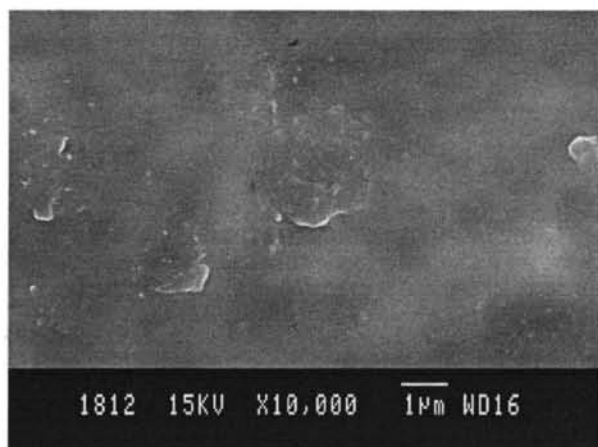
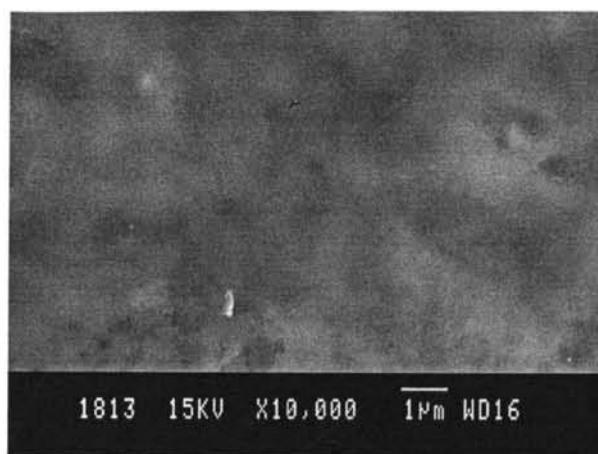


Fig. 5.10 Grain sizes of nitrate based CuInS_2 films



(a)



(b)

Fig. 5.11 SEM micrographs of samples (a) N1 and (b) N4

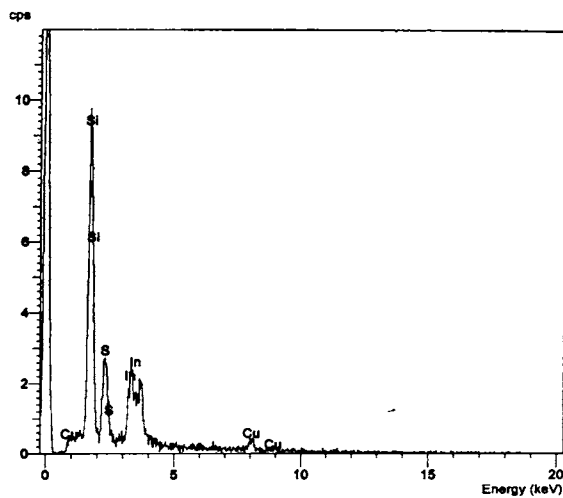
5.4.3 EDAX Measurements

Chemical composition of the samples was determined with EDAX measurements [Oxford systems, Model 6211 attached to JEOL Scanning Microscope (JSM-840A)]. Cu/In ratio followed the variation that had been made in the solution [Table 5.3]. Samples were found to be more stoichiometric when compared to that of chloride based films. Moreover Cu/In ratio in the sample was almost equal to that of the solution. This did not happen in the case of samples C1-C5.

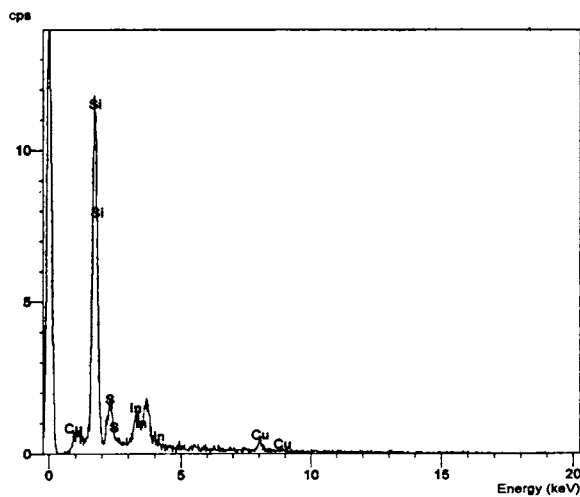
Table 5.3 Variation in atomic concentration as observed from EDAX measurements

Sample	Cu (%)	In (%)	S (%)	Cu/In ratio in film
N1 (Cu/In = 0.5)	15.49	32.09	52.42	0.48
N3 (Cu/In = 1.0)	22.75	25.16	52.09	0.91
N4 (Cu/In = 1.2)	26.26	21.43	52.31	1.23

EDAX spectrum for samples N1 and N4 are given in Fig.5.12 (a) and (b). From the spectrum it was observed that the concentration of indium was high in sample N1 compared to sample N4.



(a)

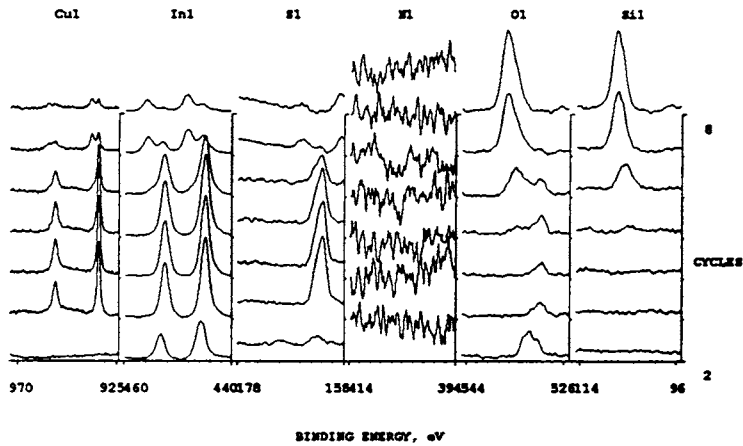


(b)

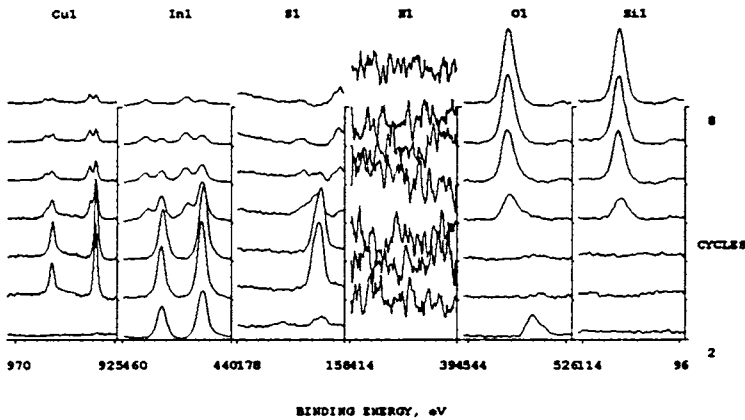
Fig. 5.12 EDAX spectrum of sample (a) N1 (b) N4

5.4.4 XPS Analysis

BE values of 932.5 eV, 952.5 eV, 444.74 eV, 452.7 eV and 162 eV for $\text{Cu}2p_{3/2}$, $\text{Cu}2p_{1/2}$, $\text{In}3d_{5/2}$, $\text{In}3d_{3/2}$ and $\text{S}2p$ indicated formation of CuInS_2 . Depth analysis of samples N1 and N3 are given in Fig. 5.13 (a) and (b) respectively.



(a)



(b)

Fig. 5.13 Depth analysis of samples (a) N1 (Cu/In=0.5) (b) N3 (Cu/In=1)

Cu, In and S were uniformly distributed along the depth of the samples. BE peak at 532 eV of oxygen at the surface corresponds to surface contamination of the samples. Unlike in the case of sample C1 here in N1 oxygen was present throughout the depth of the sample, indicating that oxygen was not only chemisorbed on the surface, but oxygen-containing phase was formed during film growth. The binding energy of oxygen in the bulk (530 eV) corresponds to that of indium oxides (529.8 eV-530.5 eV for O 1s in In_2O_3). But as the film become stoichiometric, we could not observe any oxygen in the bulk of the sample (N3). Moreover nitrogen or its oxides were also not present in any of these samples.

5.4.5 Optical Studies

Band gap was found to be decreasing with increase in Cu/In ratio. The value decreased from 1.44 eV for sample N1 to 1.3 eV for sample N5. $(\alpha h\nu)^2$ vs $h\nu$ plot for the samples are shown in Fig. 5.14. The percentage of transmittance decreased with increase in Cu/In ratio in the wavelength range 400 nm-1200 nm [Fig.5.15].

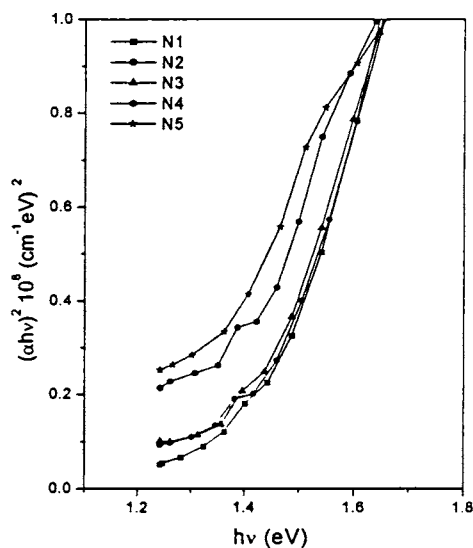


Fig. 5.14 Variation of band gap with Cu/In ratio

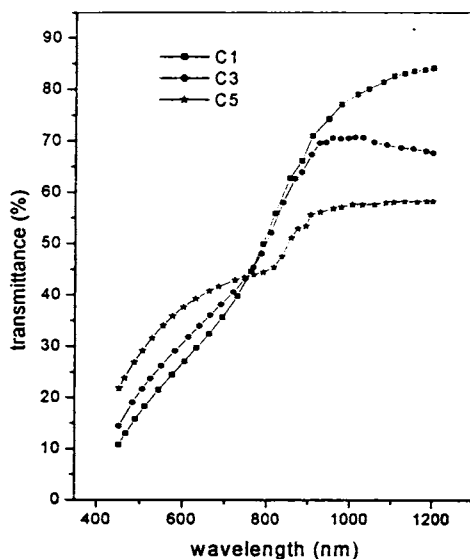


Fig. 5.15 Transmittance spectra of samples N1, N3 and N5

5.4.6 Photosensitivity Measurements

Photosensitivity of nitrate-based samples was found to be less than that of chloride-based samples except for sample N5. Sample N5 was found to be less conducting compared to sample C5. Here the number of majority carriers was less, and hence more minority carriers might be surviving to contribute to sensitivity. High sensitivity of sample C1 in comparison with N1 might be due to the presence of photosensitive In_2S_3 phase [19] as observed from XRD [Fig.5.1].

Here the maximum value of photosensitivity was found to be 18.9. But in the case of chloride sample this was 47.7. Similar observation was made in In_2S_3 prepared from chloride and nitrate precursor solutions. Fig. 5.16 depicts variation in photosensitivity with Cu/In ratio. When copper concentration was increased, naturally majority carrier concentration in the sample increased and hence minority carrier concentration will be decreased leading to decrease in photosensitivity.

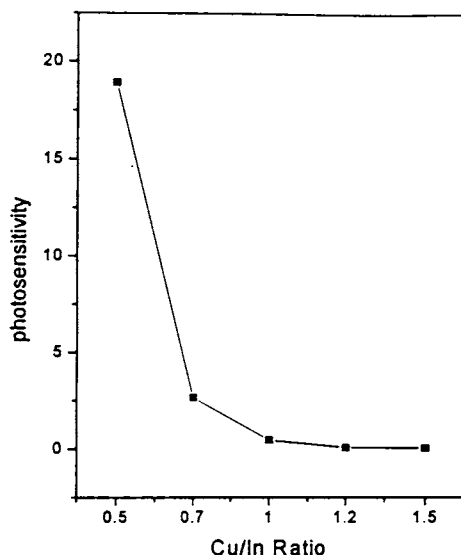


Fig. 5.16 Variation in photosensitivity with Cu/In ratio

5.5 Temperature Dependent Conductivity of Chloride and Nitrate Based CuInS_2 Films

Temperature dependent conductivity measurements in the temperature range 100 K- 300 K for both chloride and nitrate based samples (C1, C3, C5 and N1, N3, N5) were done using liquid helium cryostat having autotuning temperature controller (Lakeshore 321 model). Current and voltage were measured using a source measure unit (SMU) (Model: Keithley 236) interfaced by GPIB card and ICS software. Electrical contacts were given using silver paste painted on the surface of the sample at a separation of 0.5 cm.

Conductivity of the samples was found to increase with increase in Cu/In ratio. Of all the samples, N1 was highly resistive (more than C1), and this might be due to the high indium content in the sample as observed from EDAX [Table 5.3]. In fact indium rich samples (C1 and N1) were found to be n-type from Hot Probe

measurements. The high resistivity of indium rich films (C1 and N1) could also be due to poor crystallinity of these samples [Fig.5.1 and Fig. 5.9]. But on increasing Cu/In ratio, sample N3 was found to be more conducting compared to C3 and the samples were p-type. Sample N3 maintained better stoichiometry (in the film, EDAX) than sample C3. Conductivity values at room temperature are compared in Table 5.4.

Table 5.4 Comparison of conductivity at room temperature

Chloride	σ ($\Omega\text{-cm}$) ⁻¹	Nitrate	σ ($\Omega\text{-cm}$) ⁻¹
C1	3.78×10^{-6}	N1	6.40×10^{-7}
C3	3.88×10^{-5}	N3	1.98×10^{-4}
C5	15.86	N5	5.65

Log ρ versus Cu/In ratio for films grown from chloride and nitrate based precursor solutions are shown in Fig.5.17. From the graph it was clear that the film resistivity showed a big decrease of around seven orders of magnitude when the Cu/In ratio was increased from 0.5 to 1.5. These results indicated that excess copper caused hole degeneracy in the deposited films. Moreover the ratio Cu/In was found to have an important role in controlling the electrical properties of the CuInS_2 films. Interestingly this ratio could be easily controlled in samples prepared using CSP technique by adjusting molarity ratio in the spray solution.

From the Arrhenius plot of conductivity, samples C3 and N3 were having comparable activation energies and C5 and N5 exhibited low activation energies. Combining the results of electrical and stoichiometric analysis, the energy levels of the defects could be identified. The $\ln\sigma$ vs $1000/T$ graph for sample C1 is shown in Fig.5.18.

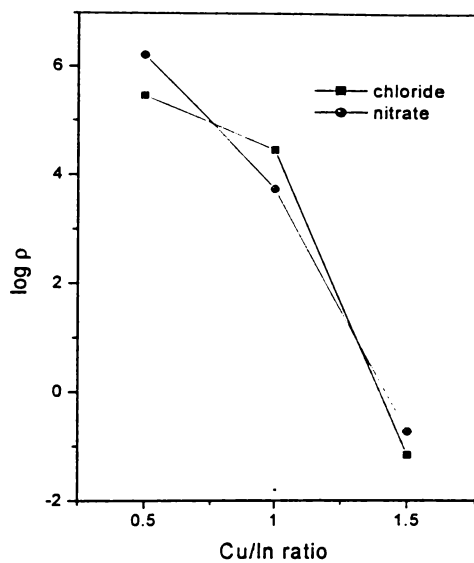


Fig 5.17 $\log \rho$ vs Cu/In ratio for chloride and nitrate based films

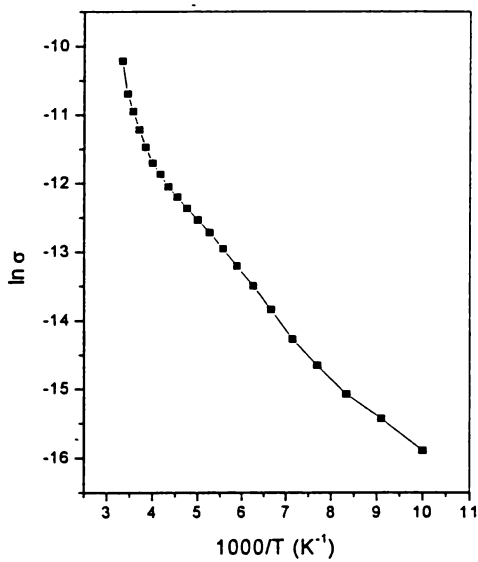
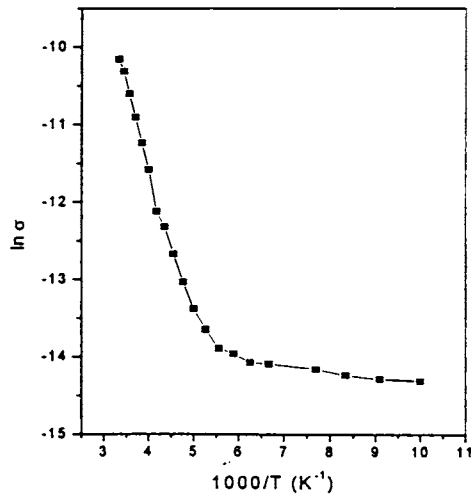


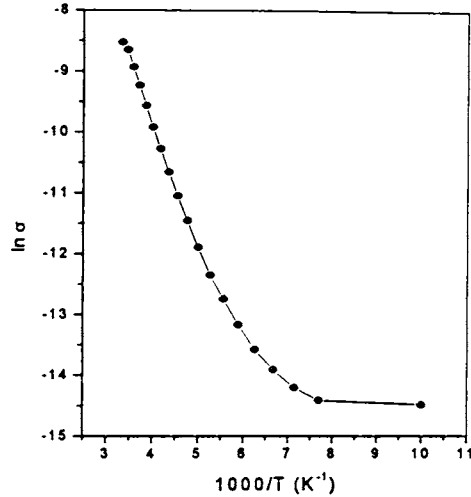
Fig. 5.18 Arrhenius plot of sample C1

For sample C1 we could identify three defect levels corresponding to activation energies 183.5 meV, 66.4 meV and 48.2 meV. From the EDAX measurements, indium was found to be in excess for sample C1. Thus the donor level at 183.5 meV could be ascribed to In at the interstitial position (In_i , 180 meV) [20]. Moreover the sample showed n-type conductivity, which also supported the existence of this level. Other two activation energies (66.4 meV and 48.2 meV- donor levels) were so close to each other, and might be due to indium occupying copper vacancy In_{Cu} (75 meV and 35 meV) [20, 21]. This level also might be contributing to the n-type conductivity of the sample. Indium sulfide (n-type) phase was also observed in the sample [Fig. 5.1]. Atomic concentration of indium was very high for sample N1 compared to C1 and thus it showed high resistivity. In fact we were unable to take conductivity measurements at low temperature because of high resistivity.

For samples C3 and N3 also, we could identify three defect levels corresponding to 189 meV, 125.6 meV and 6 meV and 183 meV, 123 meV and 6.7 meV respectively. Arrhenius plot for samples C3 and N3 are shown in Fig. 5.19 (a) and (b).



(a)



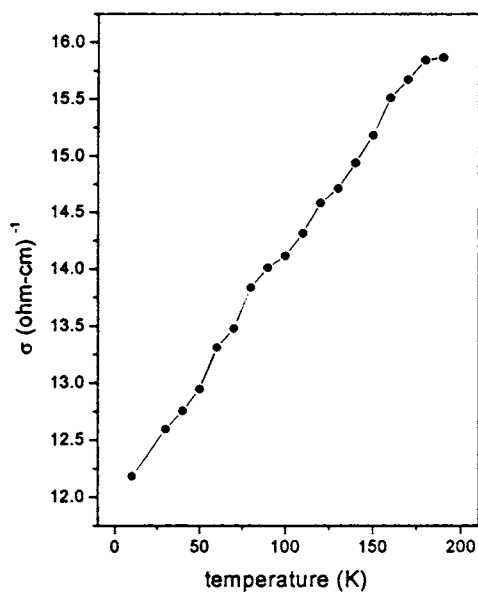
(b)

Fig.5.19 Arrhenius plots for (a) C3 (b) N3

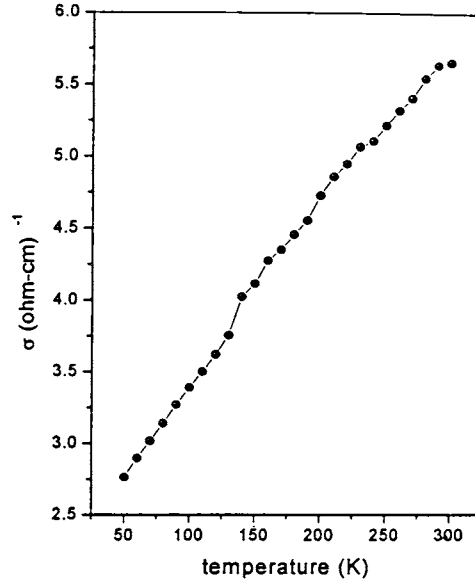
Here the samples showed p-type conductivity and were found to have excess sulfur (>50%) and thus the level at ~ 180 meV (above the valence band) could be arising due to sulfur at the interstitial position (S_i) [22]. The level at ~ 120 meV could be linked to vacancy of Cu (V_{Cu}) which is the most probable defect in a sample having excess indium [23]. This is an acceptor level. The level corresponding to activation energy of ~ 6 meV might be contributing to conductivity, as samples C3 and N3 were found to have better conductivity compared to C1 and N1. The observed slopes (C3 and N3) were always increasing with temperature, which was compatible with grain boundary scattering mechanisms [24]. The classical grain boundary trapping theory assumes the presence of trapping states at the grain boundaries, which capture free carriers. These charged states at the grain boundaries create depleted regions and potential barriers, which provide a resistance to the passage of carriers from a grain to a neighboring one.

Temperature dependent conductivity measurements for samples C5 and N5 are given in Fig. 5.20 (a) and (b). It was very clear from the graph that the conductivity of the samples increased linearly with temperature even from low temperature itself.

We could identify only shallow levels 2.3 meV, 0.81 meV and 0.17 meV for sample C5 and 8.7 meV, 3.4 meV and 1.4 meV for sample N5. Samples C5 and N5 were highly conducting in comparison to the other samples (C1, N1 and C3, N3). Thus these shallow levels might be contributing to the conductivity of the samples.



(a)



(b)

Fig. 5.20 Temperature dependent conductivity for samples (a) C5 (b) N5

5.6 Conclusion

CuInS_2 thin films were prepared using chloride and nitrate based precursor solutions. In single spray we could not increase volume of the solution beyond 375 ml as the film got damaged. Nitrate based CuInS_2 samples showed better crystalline structure and better stoichiometry in comparison. The band gap of the samples decreased with increase in Cu/In ratio in both cases. BE values from XPS studies indicated formation of CuInS_2 . Conductivity of both set of samples increased with increase in Cu/In ratio. Chloride based samples showed better photosensitivity for Cu poor samples (but n-type), but for samples having higher Cu/In ratio photosensitivity decreased drastically. Nitrate based samples show better crystallinity, stoichiometry, conductivity (N3) and a slightly low photosensitivity. These samples may show better

characteristics if they are used for fabricating solar cells. Defect levels were identified using the temperature dependent conductivity measurements and composition analysis. It is worth mentioning here that there are no publication giving results of similar studies in this material, to the best of our knowledge. Through this study we could establish that in CSP technique one can control electrical properties by adjusting molarity ratio of spray solution. Another important point was that Cu/In ratio was the controlling parameter as far as the electrical properties of the film was concerned. Major difficulty we observed was the preparation of thick films. We could not spray large volume of solution (> 375 ml) at a single stretch. This has to be solved.

References

- [1] J. L. Shay and J. H. Wernick *Ternary Chalcopyrite Semiconductors: Growth, Electronic Properties and Applications*, Pergamon Press, New York (1975)
- [2] D. C. Look and J. C. Manthuruthil *J. Phys. Chem. Solids* **37** (1976) 173
- [3] J. Klaer, J. Bruns, R. Henninger, K. Siemer, R. Klenk, K. Ellmer and D. Bräunig *Semicond. Sci. Technol.* **13** (1998) 1456
- [4] J. M. Meese, J. C. Manthuruthil and D. R. Locker *Bull. Amer. Phys. Soc.* **20** (1975) 696
- [5] F. R. White, A. H. Clark, M. C. Grey and L. L. Kazmerski *J. Appl. Phys.* **50** (1979) 544
- [6] H. L. Hwang, C. C. Tu, J. S. Maa and C. Y. Sun *Sol. Energy Mater.* **2** (1980) 433
- [7] H. L. Hwang, C. L. Cheng, L. M. Liu and C. Y. Sun *Thin Solid Films* **67** (1980) 83
- [8] S. P. Gindle, C. W. Smith and S. D. Mittlem *Appl. Phys. Lett.* **35** (1979) 24
- [9] H. Bihri and M. Abd-Lefdil *Thin Solid Films* **354** (1999) 5
- [10] A. N. Tiwari, D. K. Pandya and K. L. Chopra *Thin Solid Films* **130** (1985) 217
- [11] H. Bihri, C. Messaoudi, D. Soyah, A. Boyer, A. Mzerd and M. Abd-Lefdil *Phys. Stat. Sol. (a)* **129** (1992) 193
- [12] M. Ortega-Lopez and A. Morales-Acevedo *Thin Solid films* **330** (1998) 96
- [13] M. Krunk, O. Bijakina, V. Mikli, H. Rebane, T. Varema, M. Altosaar and E. Mellikov *Sol. Energy Mater. Sol. Cells* **69** (2001) 93
- [14] J. González-Hernández, P. M. Gorley, P. P. Horley, O. M. Vartsabyuk and Yu V. Vorobiev *Thin Solid Films* **403-404** (2002) 471
- [15] B. Pamplin and R. S. Feigelson *Thin Solid Films* **60** (1979) 141
- [16] R. Klenk, T. Walter, H. W. Schock and D. Cahen *Adv. Mater.* **5** (1993) 114
- [17] M. Krunk, V. Mikli, O. Bijakina and E. Mellikov *Appl. Surf. Sci.* **142** (1999) 256
- [18] Teny Theresa John, K. C. Wilson, P. M. Ratheesh Kumar, C. Sudha Kartha, K.P. Vijayakumar, Y. Kashiwaba, T. Abe and Y. Yasuhiro *Phys. Stat. Sol. (a)*

202 (1) (2005) 79

- [19] Teny Theresa John, S. Bini, Y. Kashiwaba, T. Abe, Y. Yasuhiro, C. Sudha Kartha and K. P. Vijayakumar *Semicond. Sci. Technol.* **18** (2003) 491
- [20] J. H. Schön and E. Bucher *Phys. Stat. Sol. (a)* **171** (1999) 511
- [21] I. A. Aksenov, N. A. Sobolev and V. A. Sheraukhov *Phys. Stat. Sol. (a)* **123** (1991) K171
- [22] H. J. Lewerenz *Sol. Energy Mater. Sol. Cells* **83** (2004) 395
- [23] J. J. M. Binsma, L. J. Giling and J. Bloem *J. Lumin.* **27** (1982) 35
- [24] S. Marsillac, M. C. Zouaghi, J. C. Bernède, T. Ben Nasrallah and S. Belgacem *Sol. Energy Mater. Sol. Cells* **76 (2)** (2003) 125

Chapter 6**PROPERTIES OF CuInS₂ FILMS PREPARED USING REPEATED
SPRAY PYROLYSIS TECHNIQUE****6.1 Introduction**

Techniques for making both n- and p-type CuInS₂ were discovered several years ago [1]. Since then, a number of papers were published concerning CuInS₂ and its potential device applications, particularly as a photovoltaic detector or solar cell [2-4]. Efficiencies of more than 12% have been reached with a Mo/CuInS₂/CdS/ZnO cell structure [5]. Deposition of CuInS₂ is based on a sequential process using d.c magnetron sputtering of the metals and sulfurization in elemental sulfur vapor, and CuInS₂ layer thickness was 3 μm. Scheer et al reported 10.2% efficiency solar cell which also was having 3 μm thick CuInS₂ layer [6]. For CuInS₂ based solar cell using a Cd-free buffer layer (11.4% efficiency) also the thickness was maintained in the same order [7]. Chemically etched CuInS₂ absorber layer with 4 μm thickness yielded an efficiency of 12% as reported by Onuma et al [8]. A four layer structure of solar cell of low ρ- CuInS₂/high ρ- CuInS₂/high ρ- CdS/low ρ- CdS has been fabricated by Park et al in order to form back surface field and internal electric field by graded band gap [9]. The thickness of the low resistive CuInS₂ film was about 1.5 μm and that of high resistivity layer was 0.2 μm so that the total layer thickness is 1.7 μm. They obtained an efficiency of 8.25%. Thick absorber layer naturally improves light absorption and hence photogenerated carriers in the layer.

One of the difficulties in using CSP technique is in the preparation of thick (>1 μm) films by spraying large volumes of solution in a single stretch. It was observed that when large volumes of the solution (say 600 ml) was sprayed in a single stretch, it always resulted in the formation of CuInS₂ film with a lot of pinholes resulting in the wastage of large number of samples. But in spite of this difficulty there are certain advantages in using this technique for film preparation. As stated

earlier it is rather easy to vary stoichiometry of samples when prepared using CSP. This is very useful in the case of CuInS₂. For example by varying Cu/In and/or S/Cu ratio we could adjust carrier concentration, photosensitivity and also crystallinity. This is important for solar cell fabrication. Moreover this same technique could be used for the deposition of lower electrode (transparent conducting oxide), absorber layer and buffer layer without any break. This is quite useful for large-scale production of solar cells. We tried to modify the technique for the preparation of thick CuInS₂. Hence a trial was made to prepare the film by 'repeated spraying' of small quantities of solution and this resulted in improving the thickness of the film without pinholes. Nobody earlier tried this 'multiple spray technique' to increase CIS thickness. Structural, compositional, optical and electrical characterizations were done for films prepared in this way (with different Cu/In molar ratio in spray solution) and the results are presented in this chapter. This was purposefully done to see the variation in photosensitivity with the change in Cu/In ratio. This is important for cell fabrication, as we are varying mainly the majority carrier concentration by changing Cu/In ratio.

6.2 Experimental Details

CuInS₂ thin films were deposited onto glass substrates from aqueous solutions of CuCl₂, InCl₃ and thiourea (CS(NH₂)₂) by means of CSP technique using compressed air as carrier gas. Equal volumes of the solutions were mixed in appropriate molar concentrations to get different Cu/In ratios. Cu/In ratio was varied from 0.5 to 1.5 keeping S/Cu ratio at 5. Here the molarity of CuCl₂ was fixed at 0.025 M, that of thiourea at 0.125 M and the molarity of InCl₃ was varied to get different Cu/In ratios. 225 ml of the solution was sprayed onto the glass substrates kept at 300°C. The samples were kept at the same temperature for half an hour after each spray, and then the temperature was reduced to room temperature. The process was repeated four times and thus the total volume of the solution sprayed was 900 ml. Spray rate was kept at 20 ml/min for all cases. Samples were found to be uniform

without any pinholes and were named CIS1, CIS2 and CIS3 having Cu/In ratio 0.5, 1 and 1.5 respectively with S/Cu ratio fixed at 5.

6.3 Results and Discussion

6.3.1 Structural Analysis

XRD pattern of the films deposited with different Cu/In ratio are given in Fig.6.1. The d values coincided with that of $CuInS_2$ (JCPDS-270159) with preferential orientation along (112) plane at $2\theta = 27.75^\circ$. For Cu deficient CIS1 sample, peak at 33.4° corresponds to (220) plane of β - In_2S_3 [10]. There was no such impurity phase for CIS2 and CIS3 samples. Crystallinity of the film improved on increasing the Cu/In ratio. The grain size of the film was calculated from Debye - Scherrer formula. Variation of grain size with Cu/In ratio is given in Table 6.1. Grain size of the films increased with increase in Cu/In ratio. Lattice parameters were calculated to be $a = b = 5.55 \text{ \AA}$ and $c = 11.55 \text{ \AA}$ which was in good agreement with the standard values of $a = b = 5.523 \text{ \AA}$ and $c = 11.141 \text{ \AA}$. The thickness of the films was found to be $1.17 \mu\text{m}$ using Stylus method [Fig.6.2].

Table 6.1 Variation of grain size with Cu/In ratio

Sample	Grain Size (nm)
CIS1	7.85
CIS2	11.69
CIS3	24.36

Lattice strain was calculated from the plot of $\beta \cos\theta$ versus $4 \sin\theta$ graph, where β represents FWHM. The value was found to decrease from 1.32 to 0.168 for sample CIS1 to sample CIS3. Thus it was clear that as the sample became more stoichiometric, lattice strain decreased considerably.

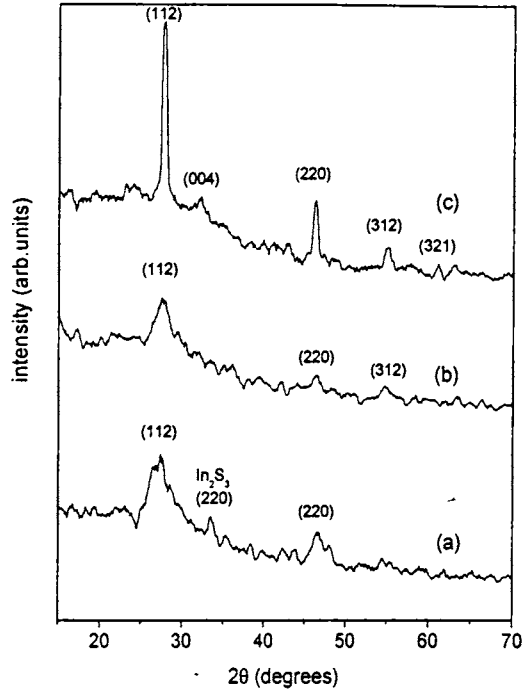


Fig. 6.1 XRD pattern: (a) CIS1 (b) CIS2 (c) CIS3

6.3.2 Surface Morphology

Analysis of surface topography using SEM was done on the samples. Surface was not dense and grains were not uniform for Cu-poor films. SEM micrographs showed some agglomerated areas on increasing Cu concentration and surface was denser compared to Cu-poor films. In all cases the surface was found to be rough. SEM micrographs of samples CIS1, CIS2 and CIS3 are given in Fig. 6.3 (a), (b) and (c).

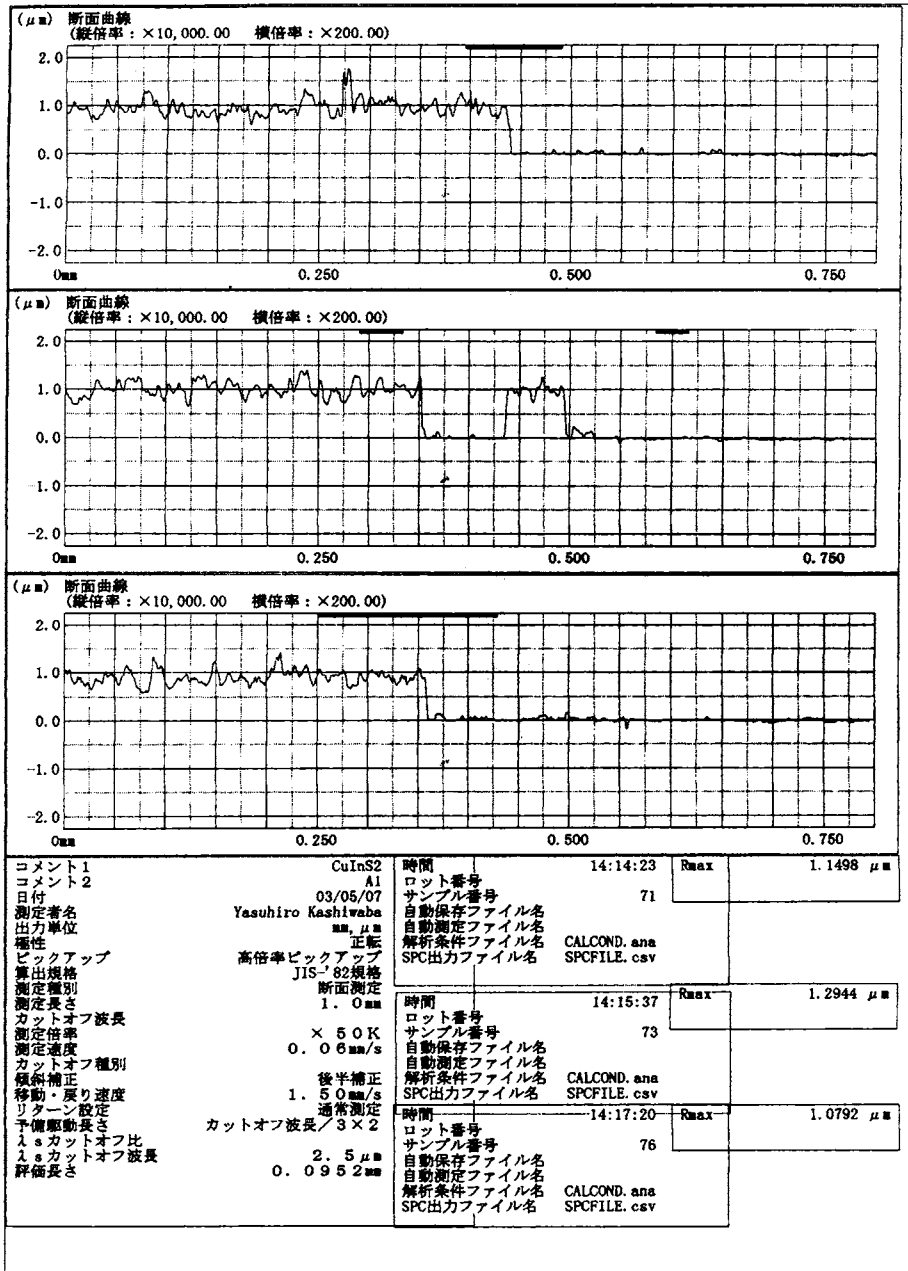
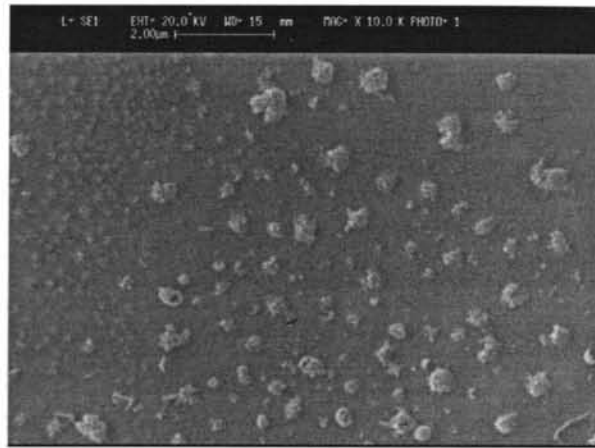
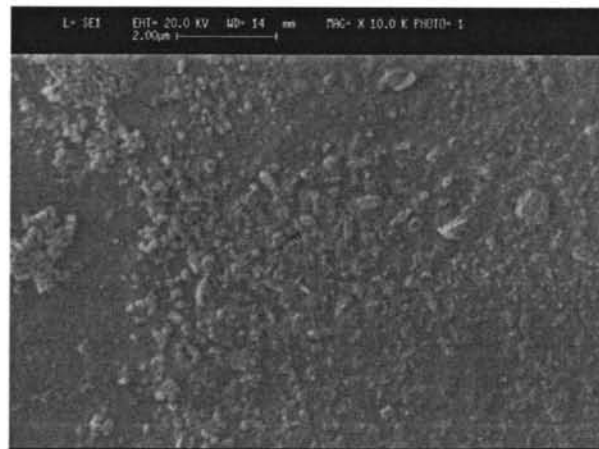


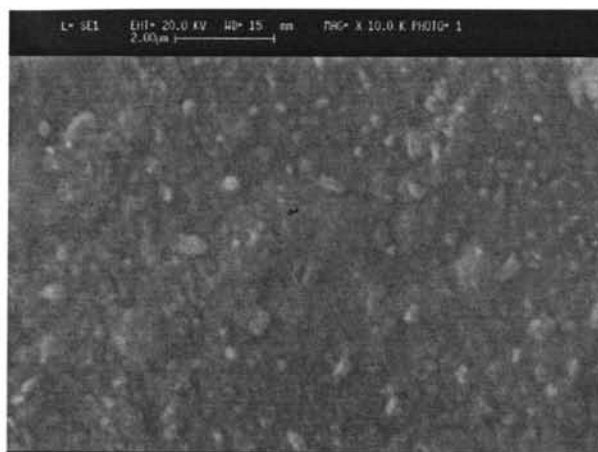
Fig. 6.2 Stylus measurement of CuInS_2 film



(a)



(b)



(c)

Fig. 6.3 Scanning Electron Micrograph of
(a) CIS1 (b) CIS2 (c) CIS3 samples

6.3.3 EDAX Measurements

Atomic concentration of Cu, In and S in samples CIS1, CIS2 and CIS3 obtained from EDAX measurements are given in Table 6.2. It had been seen that the Cu/In ratio in the film was always less than that taken in the solution.

Table 6.2 Atomic concentrations from EDAX measurements

Samples	Cu (%)	In (%)	S (%)	Cu/In ratio in film
CIS1 (Cu/In=0.5)	11.56	34.45	53.99	0.34
CIS2 (Cu/In=1)	17.95	26.69	55.36	0.67
CIS3 (Cu/In=1.5)	23.21	20.63	56.16	1.12

6.3.4 XPS Analysis

XPS depth profile of the sample CIS2 is given in Fig. 6.4. Binding Energies (BE) of copper, indium and sulfur indicated the formation of CuInS_2 [11]. BE values are given in Table 6.3.

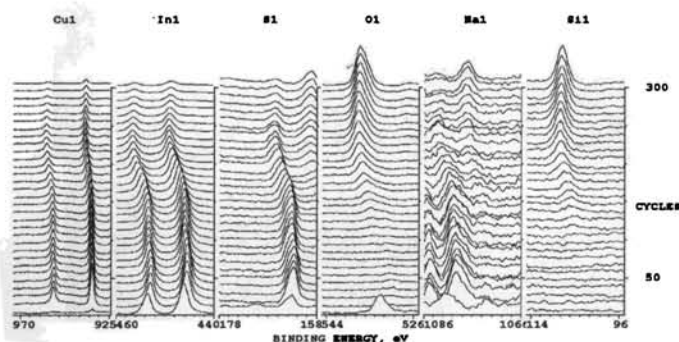


Fig. 6.4 XPS depth profile of CIS2

Table 6.3 BE values of Cu, In and S as observed from XPS analysis

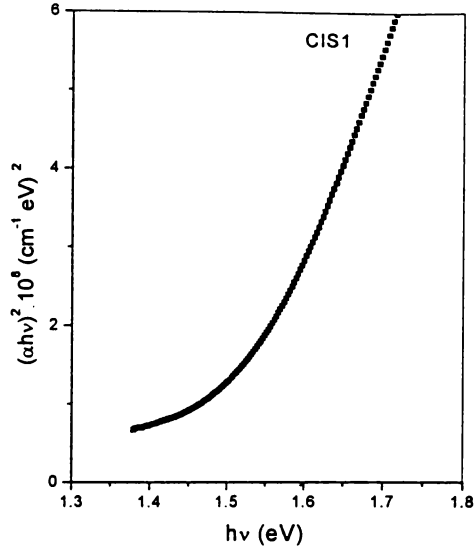
Element	Binding Energy (eV)
$\text{Cu}2p_{3/2}$	932.7
$\text{Cu}2p_{1/2}$	952.7
$\text{In}3d_{5/2}$	445.1
$\text{In}3d_{3/2}$	452.5
$\text{S}2p$	162.5

It had been found that there was a small quantity of oxygen in the sample near the substrate-film interface, which caused BE shift for copper, indium and sulfur

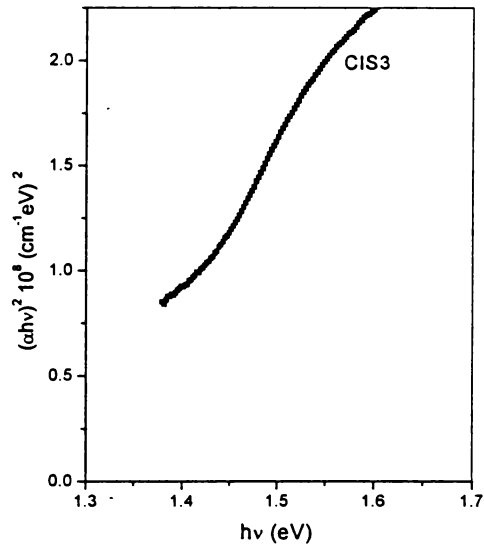
in that area (after 160 cycles of etching). Multiple heating might have caused O₂ diffusing out of glass. However there was no shift in the BE value in the bulk of the sample where there was no oxygen. BE of oxygen (532.5 eV) at the surface indicated surface contamination in the form of sulfate and this was only for ~750 Å (ten cycles) thickness of the film (Binding energy of free oxygen is 531 eV). Decrease in the peak height of sulfur at the surface of the film indicated that this oxygen substituted sulfur in the top layer. But it should be noted that oxygen was not present in the bulk of the sample even after successive heating. But sodium was present throughout the depth of the sample, which might have diffused from the glass substrate, associated with sodium silicate, as there was no sodium content in any of the chemicals used for sample preparation. Decrease in the peak height of Na in glass near film interface proved this. Enhancement in conductivity, crystalline quality and device performance due to incorporation of Na in CuInS₂ had been reported [12].

6.3.5 Optical Studies

To determine energy band gap, $(\alpha h\nu)^2$ vs $h\nu$ graph was drawn for all the samples and is represented in Fig.6.5 (a) and (b). It was found that E_g value decreased with increase in Cu/In ratio, from 1.49 eV of sample CIS1 to 1.31 eV of sample CIS3 [13]. This was in accordance with the improvement in crystallinity of the samples with increase in Cu/In ratio [Fig. 6.1].



(a)



(b)

Fig.6.5 Energy band gap of samples (a) CIS1 (b) CIS3

6.3.6 Resistivity and Photosensitivity

Photosensitivity ($(I_L - I_D)/I_D$, where I_L is the current when the sample is illuminated with light and I_D is the dark current) of the samples was also found to decrease with increase in Cu/In ratio. Variation in photosensitivity is shown in Fig.6.6. As Cu/In ratio increased crystallinity of the sample was improved [Fig. 6.1] leading to increase in dark conductivity. Correspondingly number of majority carriers increased and hence the minority carriers surviving to contribute to photosensitivity decreased resulting in reduced photoresponse.

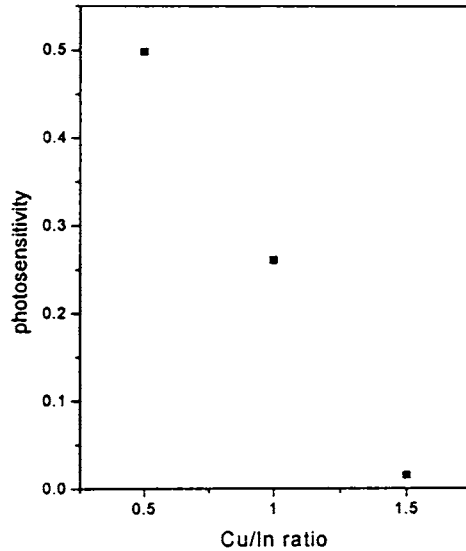


Fig.6.6 Variation in photosensitivity with Cu/In ratio

Resistivity of the samples decreased with increase in Cu/In value. Very high resistivity of samples with excess of indium ($\text{Cu/In} < 1$) could be explained by the poor crystallinity (XRD) and due to the reduction in majority carriers caused by the low value of Cu/In ratio. Films with excess copper ($\text{Cu/In} > 1$), showed good crystallinity. Here majority carrier concentration also increased with increase in the concentration

of copper and hence increase in conductivity. Resistivity values are compared in Table 6.4.

Table 6.4 Variation of resistivity (ρ) with Cu/In ratio

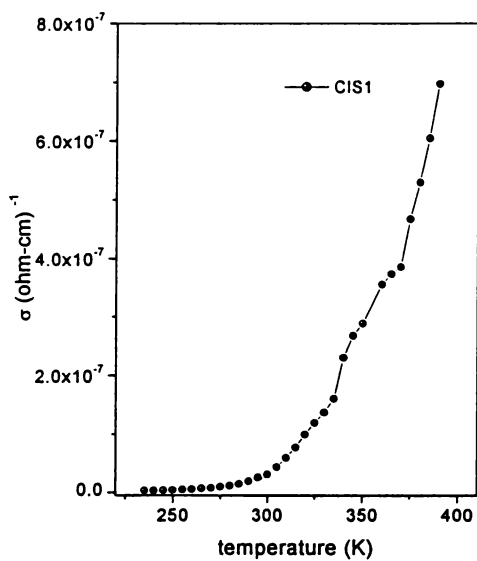
Sample	ρ (ohm-cm)
CIS1	7.56×10^3
CIS2	6.36×10^3
CIS3	1.13×10^{-1}

6.3.7 Temperature Dependent Conductivity Measurements

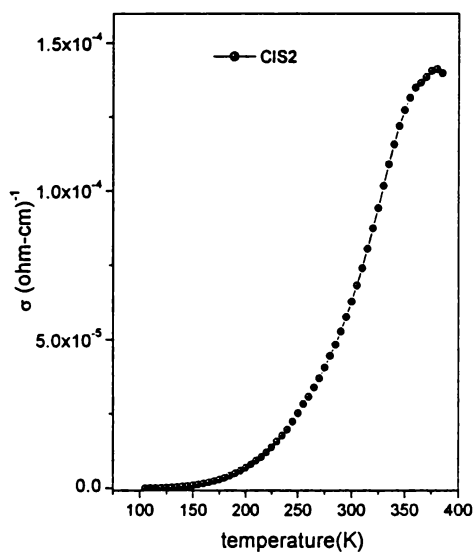
Temperature dependence of conductivity (from 100 K) of the samples was measured using computerized setup (IMS 2000, Lab Equip). Measurements at still lower temperatures (from 10 K) were done using liquid helium cryostat having autotuning temperature controller (Lakeshore 321 model). Current and voltage were measured using source measure unit (SMU) (Model: Keithley 236) interfaced by GPIB card and ICS software. Electrical contacts were given using silver paste, painted on surface of the sample at a separation of 0.5 cm.

Figure 6.7 (a), (b) and (c) represent temperature dependent conductivity of samples CIS1, CIS2 and CIS3. It could be seen that the conductivity of CIS3 was much higher than that of CIS1 and CIS2. Conductivity of CIS3 increased steadily from low temperature (100 K) itself unlike the other two samples.

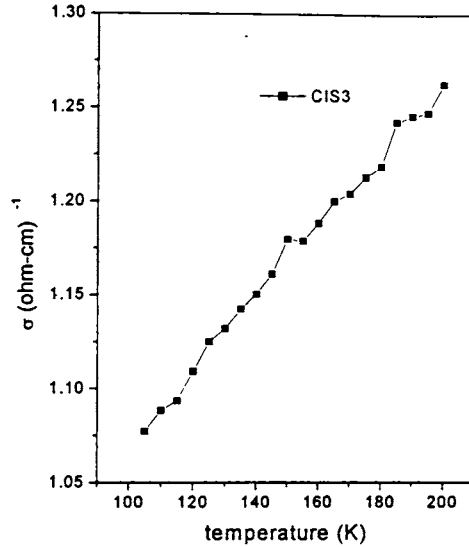
Using Hot Probe, we found that sample CIS1 showed fluctuating nature between n and p while CIS2 and CIS3 showed clearly p -type conductivity. Arrhenius plot of conductivity of the samples are given in Fig.6.8. Enhanced conduction of CIS2 and CIS3 is apparent from the upward shift of the Arrhenius plots.



(a)



(b)



(c)

Fig. 6.7 Temperature dependent conductivity of samples (a) CIS1 (b) CIS2 (c) CIS3

Sample CIS1 indicated two distinct slopes from which activation energies (E_a) were calculated as 390 meV and 196 meV. The plots of CIS2 and CIS3 indicated only one slope whose E_a values were 90 meV and 3 meV respectively. Cu deficient CuInS_2 (CIS1) had a deep level at 390 meV, which may be another reason for the decrease in conductivity of the sample. This may be acting as majority carrier trap for the sample as described by Kneisel et al [14]. The activation energy of 196 meV correspond to interstitial In (In_i) or In_{Cu} [15, 16]. Presence of indium at the interstitial site (In_i) or at the Cu vacancy (In_{Cu}) might be the reason for the fluctuating nature of conductivity exhibited by the sample. Vacancy of copper created the 90 meV level for CIS2 sample [17].

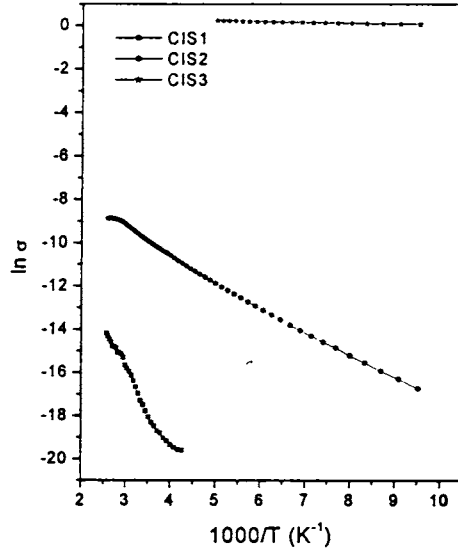


Fig. 6.8 Arrhenius plot of samples CIS1, CIS2 and CIS3

We could find a very shallow level at 3 meV for CIS3 samples, which might be the reason for the high conductivity of the sample. In the first experiment, temperature was varied from 100 K to 200 K using liquid nitrogen cryostat (IMS 2000, Lab Equip). Activation energy was calculated and was found to be 3 meV. Using liquid helium cryostat the temperature was brought down to 10 K and the same experiment was repeated. Even at low temperature the conductivity increased steadily with temperature for CIS3 sample. The result agreed with that of the previous experiment and the activation energy was calculated to be the same. But we could not identify the defect/impurity causing this shallow level in CIS3.

6.4 Conclusion

CuInS_2 films having thickness of $>1 \mu\text{m}$ could be prepared using multiple spray pyrolysis technique. Greater Cu/In ratio in the solution resulted in larger crystallites and the band gap decreased from 1.49 eV to 1.3 eV. BE values clearly

indicated the formation of CuInS₂. Depth profiling of the sample revealed presence of oxygen (only at the film substrate interface) and Na in the sample. The Cu/In ratio in the film was slightly less than that in the solution as observed from EDAX measurements. Temperature dependence of dark conductivity of the samples was also investigated. Two distinct slopes corresponding to activation energies 390 meV (contributing to enhancement of resistivity) and 196 meV (In_i or In_{Cu}) were obtained for sample CIS1. Activation energy corresponding to a level of 90 meV (V_{Cu}) for CIS2 and 3 meV (contributing to the high conductivity) for CIS3 was also identified. However the reason for the shallow level in CIS3 could not be found out.

References

- [1] B. Tell, J. L. Shay and H. M. Kasper *Phys. Rev. B* **4** (1971) 2463
- [2] L. L. Kazmerski, M. S. Ayyagari and G. A. Sanborn *J. Appl. Phys.* **46** (1975) 4865
- [3] Y. Ogawa, A. J. Waldau, Y. Hashimoto and K. Ito *Jpn. J. Appl. Phys.* **33** (1994) L 1775
- [4] S. Uenishi, K. Tohyama and K. Ito *Sol. Energy Mater. Sol. Cells* **35** (1994) 231
- [5] J. Klaer, J. Bruns, R. Henninger, K. Siemer, R. Klenk, K. Ellmer and D. Bräunig *Semicond. Sci. Technol.* **13** (1998) 1456
- [6] R. Scheer, T. Walter, H. W. Schock, M. L. Fearheiley and H. J. Lewerence ` *Appl. Phys. Lett.* **63** (24) (1993) 3294
- [7] D. Braunger, D. Hariskos, T. Walter and H. W. Schock *Sol. Energy Mater. Sol. Cells* **40** (1996) 97
- [8] Y. Onuma, K. Takeuchi, S. Ichikawa, M. Harada, H. Tanaka, A. Koizumi and Y. Miyajima *Sol. Energy Mater. Sol. Cells* **69** (2001) 261
- [9] G. C. Park, H. D. Chung, C. D. Kim, H. R. Park, W. J. Jeong, J. U. Kim, H. B. Gu and K. S. Lee *Sol. Energy Mater. Sol. Cells* **49** (1997) 365
- [10] Teny Theresa John, K. C. Wilson, P. M. Ratheesh Kumar, C. Sudha Kartha, K. P. Vijayakumar, Y. Kashiwaba, T. Abe and Y. Yasuhiro *Phys. Stat. Sol. (a)* **202** (1) (2005) 79
- [11] S. Bini, K. Bindu, M. Lakshmi, C. Sudha Kartha, K. P. Vijayakumar, Y. Kashiwaba and T. Abe *Renewable Energy* **20** (2000) 405
- [12] T. Watanabe, H. Nakazawa, M. Matsui, H. Ohbo and T. Nakada *Sol. Energy Mater. Sol. Cells* **49** (1997) 357
- [13] Teny Theresa John, C. Sudha Kartha , K. P. Vijayakumar, T. Abe and Y. Kashiwaba *Proc. MRSI Theme Symposium, Varanasi* (2004)
- [14] J. Kneisel, K. Siemer, I. Luck and D. Bräunig *J. Appl. Phys.* **88** (9) (2000) 5474
- [15] J. H. Schön and E. Bucher *Phys. Stat. Sol. (a)* **171** (1999) 511

- [16] P. Lange, H. Neff, M. L. Fearheiley and K. J. Bachmann *J. Electron. Mater.* **14**
(1985) 667
- [17] J. J. M. Binsma, L. J. Giling and J. Bloem, *J. Lumin.* **27**(1982) 35

Chapter 7

FABRICATION AND CHARACTERIZATION OF ALL-SPRAYED $\text{CuInS}_2/\text{In}_2\text{S}_3$ SOLAR CELL

7.1 Introduction

Photovoltaic device is probably the most suitable for the production of convenient and pollution free energy. But the major problem here is the development of easily available and eco friendly absorber that can give reasonably high efficiency cells which can produce electricity at the present cost. Recently, chalcopyrite semiconductors have been identified as absorber layers for polycrystalline thin film solar cells [1-3]. Among them, the ternary compound CuInS_2 (CIS) is a potential candidate due to its large absorption coefficient and optimum direct band gap of 1.5 eV, which matches well with the solar spectrum. Conversion efficiencies greater than 19% could be achieved for $\text{Cu}(\text{In,Ga})\text{Se}_2$ (CIGS) based solar cells, using CdS as buffer layer [4]. Most of the reported studies are on development of heterojunction between p-type CuInS_2 and n-CdS. However, it is equally important to explore the possibility of developing a heterojunction between CuInS_2 and another suitable n-type wide band gap compound semiconductor, without cadmium (Cd). Now serious efforts are going on for replacing this layer by other wide band gap materials such as ZnS, ZnSe, In_xSe_y , $\text{In}_x(\text{OH,S})_y$, In_2S_3 etc [5-9]. The motivation behind this is not only to eliminate toxic cadmium but also to improve light transmission in the blue wavelength region by using a material having band gap, wider than that of CdS.

Kazmerski et al first reported fabrication of photovoltaic device using CIS [10]. They fabricated CIS based homojunction solar cell with 3.62% efficiency. Recently CIS based solar cell, with an active area efficiency of 12.5%, was fabricated by Klaer et al [11]. The technology was based on sequential process using d.c. magnetron sputtering of the metals and sulfurization in elemental sulfur vapor. K. Siemer et al obtained efficiency of 11.4% by using rapid thermal process for the

preparation of CIS absorbers [12]. Cells having copper rich CIS phase, prepared using thermal evaporation method, could achieve efficiency of 10.2% [13]. All these cells were found to have CdS as buffer layer, deposited using Chemical Bath Deposition (CBD) technique.

Indium sulfide had already been studied as buffer layer for CIGS or CIS based solar cells [14-17]. Hariskos et al [8] achieved conversion efficiency of 15.7% using cadmium free $\text{In}_x(\text{OH}, \text{S})_y$ buffer layer for CIGS based solar cells. Here also the buffer layer was deposited using CBD technique. Fabrication of 11.4% efficient thin film solar cell based on CuInS_2 , with the same buffer layer, was reported by Braunger et al [18]. Efficiencies upto 14.9% for CIGS based laboratory cells, with indium sulfide buffer layer deposited using ALCVD, was reported by Spiering et al [9]. Rapid Thermal Process (RTP) for CuInS_2 absorber layer was found to be suitable to enhance efficiency of the cell [19]. Solar cells having superstrate configuration ZnO/CdS/CuInS_2 were prepared using Chemical Spray Pyrolysis (CSP) technique by Mere et al [20].

This chapter describes fabrication and characterization CuInS_2 based solar cell with Cd-free $\beta\text{-In}_2\text{S}_3$ buffer layer using CSP technique. This technique is quite suitable for solar cell production because of the possibility of large area deposition of thin films at low cost with controlled dopant profiles. It is easy to vary the stoichiometric composition as well as doping profile along the thickness of the sample and multi layer films with large area could be deposited. Moreover many of the thin film solar cells have one of the electrodes to be transparent conducting oxide. This layer could be conveniently deposited using CSP technique. Hence if we adopt CSP technique for cell fabrication, almost all the layers (except top metal electrode) could be deposited using this simple technique without a break. This is very convenient for large-scale production. Preliminary results of the $\text{CuInS}_2/\text{In}_2\text{S}_3$ solar cell fabrication and characterization are given here.

7.2 Device Fabrication

7.2.1 Back Contact (ITO)

Several types of transparent conducting oxides (TCOs) are commercially produced to be used as front/back contact of solar cells. The most common TCOs are tin oxide (SnO_2), doped tin oxide such as SnO_2 : F, indium tin oxide (ITO) and sometimes a combination of a tin oxide layer and indium tin oxide (ITO/ SnO_2) layer. Typically, these films should have low resistance, high optical transmission and should be thermally stable during the subsequent processing steps of cell fabrication. In the present work, we used commercially available ITO films as the bottom electrode for fabricating the cell. We also used spray pyrolysed SnO_2 : F, but the performance of the cells fabricated using this film as electrode was rather poor and hence the use of SnO_2 : F was discarded for the present work.

Fig.7.1 shows transmission spectrum of ITO films we used. The ITO layer was 1500 Å thick, having optical transmission around 82% and electrical resistivity $2.25 \times 10^{-4} \Omega\text{-cm}$. Structural analysis of the film was done using XRD and is given in Fig.7.2. The corresponding d values are listed in Table 7.1.

Table 7.1 XRD analysis of ITO film

2θ (degrees)	d [Å] (observed)	d [Å] (standard)	hkl
21.45	4.1400	4.1770	211
30.20	2.9570	2.9470	222
35.30	2.5406	2.5371	400
50.75	1.7975	1.7880	440
60.42	1.5310	1.5250	622

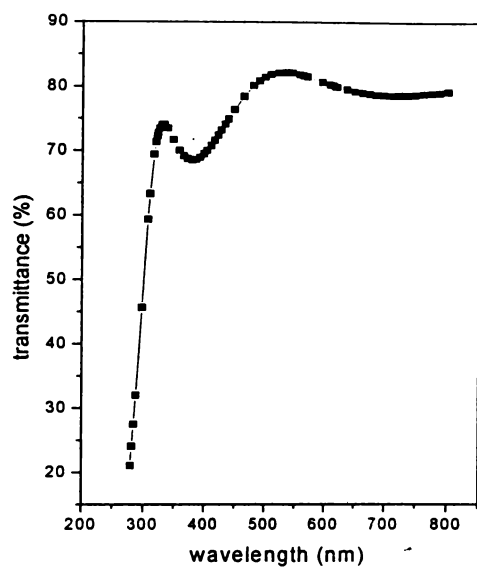


Fig. 7.1 Transmission spectrum of ITO

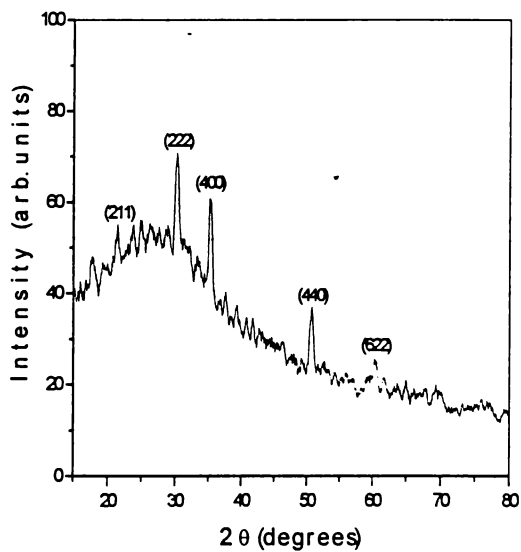


Fig. 7.2 XRD spectrum of ITO

7.2.2 CuInS_2 Absorber Layer

We deposited CIS layer first on the ITO surface using CSP technique. We had done extensive studies for the optimization of deposition condition of CIS using this technique and also for the characterization of the film using different techniques. Details of these studies are given in chapters 5 and 6. Hence the details of film deposition and characterization are not repeated here. We include, only a brief description of preparation conditions of junction alone. CuInS_2 thin films were deposited using aqueous solution containing copper chloride ($\text{CuCl}_2 \cdot 2\text{H}_2\text{O}$), indium chloride (InCl_3), and thiourea ($\text{CS}(\text{NH}_2)_2$). Total volume of the solution sprayed was 375 ml with the following composition $\text{CuCl}_2 \cdot 2\text{H}_2\text{O}$ - 0.0125 M (125 ml), InCl_3 - 0.0125 M (125 ml) and $\text{CS}(\text{NH}_2)_2$ - 0.0625 M (125 ml) for Cu/In ratio 1 and S/Cu ratio 5. The substrate was kept at $300 \pm 5^\circ\text{C}$ and the spray rate at 20 ml/min. Cu/In, S/Cu and In/S ratios of the films were controlled by varying molar concentrations of the respective compounds in the solutions. Absorber layer was found to have a tetragonal structure with preferential orientation along (112) plane. XRD spectrum of the absorber layer is given in Fig. 5.1. The band gap was found to be 1.4 eV [Fig.5.6].

7.2.3 In_2S_3 Buffer Layer

A detailed description on preparation and characterization of In_2S_3 films is given in an elaborate manner in chapter 3. Here we included only the essential aspects of preparation condition of the film deposited for junction fabrication only. In_2S_3 film was deposited over CuInS_2 film as buffer layer. Aqueous solution of indium chloride (InCl_3) and thiourea was used to deposit In_2S_3 films. For the fabrication of the solar cells we used In/S ratio 1.2/8 as it was giving maximum photosensitivity [Fig. 3.30]. For this the molarity of InCl_3 was kept at 0.015 M and that of thiourea at 0.1 M. XRD pattern of $\beta\text{-In}_2\text{S}_3$ buffer layer is given in Fig. 3.24. Band gap was found to be 2.65 eV, wider than that of CdS (2.4 eV) [Fig. 3.27]. Fig. 3.28 depicts the transmission spectrum of In_2S_3 film.

7.2.4 Electrode Deposition

We deposited Aluminium as the top electrode using Physical Vapour Deposition (PVD). The grain size of the samples being small (grain size of CuInS_2 is ~ 10 nm [Fig. 5.1] and grain size of In_2S_3 is ~ 14 nm [Fig.3.24], the grid or comb structure of the electrodes will result in the loss of photogenerated carriers collected at the electrode. Hence we have given the electrode as a square block having area 0.04 cm^2 and thickness 50 nm. Thus this structure of the electrode had to be selected due to the low grain size of the absorber and buffer layers and this was a limitation of CSP technique. But considering other advantages of this deposition technique, we accepted it for cell deposition, we decided to have the present electrode structure for the cells. Indium was also given as the top electrode, but it always resulted in the shorting of the bilayer structure. The structure of the cell fabricated is shown schematically in Fig.7.3.

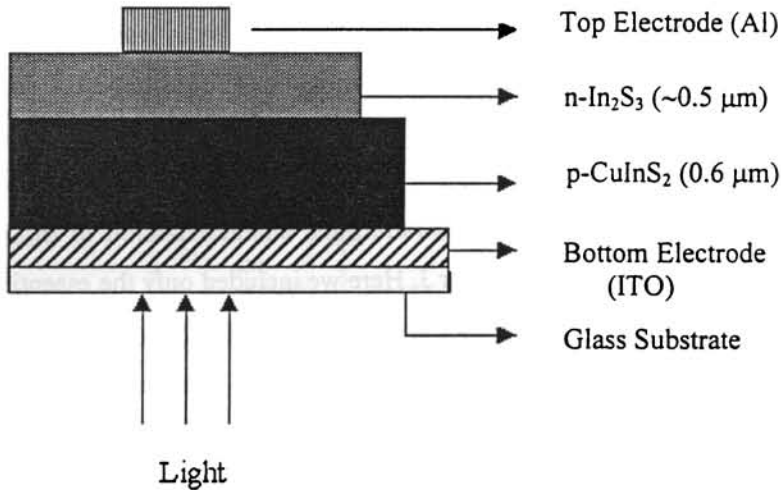


Fig. 7.3 Schematic diagram of the structure of the solar cell

7.3 J-V Characteristics of the Cell

Dark and illuminated J-V characteristics of the cell were measured using Keithley Source Measure Unit (SMU, K 236) and Metric's Interactive Characterization Software (ICS). The cell was illuminated using a tungsten halogen lamp having intensity 100 mW/cm^2 on the substrate surface. An infrared filter along with water jacket was used to remove heat content from the incident light to ensure that there was no heating of the cell during measurement. Input power was measured using a "suryamapi" (A-136 model of CEL). Distance between the cell and the source was 8 cm.

In the present work, we illuminated the junction through the substrate side. This was because of the structure of electrode. As stated earlier, electrode was deposited as a patch over In_2S_3 and hence illumination could not be given through the window layer. As the illumination was through absorber side, we wanted to make sure that enough intensity was reaching the junction region; we measured transmitted intensity on the In_2S_3 side. We found that transmitted intensity was $\sim 20 \text{ mW/cm}^2$ even when the thickness of absorber layer was increased to $0.6 \mu\text{m}$. This proved that enough intensity was reaching the junction region and hence there was no problem due to the illumination from absorber side. But transmission of about one fifth of the incident power unabsorbed was really undesirable and this could be a reason for low short circuit current.

Series resistance (R_s) of the cell could be calculated from the dark J-V characteristics of the cell. Inverse of the slope of far forward characteristics (in the first quadrant), where J-V becomes linear gives R_s [21]. Cell parameters V_{oc} , J_{sc} could be noted from the J-V curve and Fill Factor (FF) and efficiency (η) could be calculated using the corresponding equations. The slope of the $\ln J$ versus V graph gave diode quality factor (A) [22].

7.4 Results and Discussion

Effects of variation of atomic concentration as well as thickness of both absorber and buffer layers, on the electrical properties of the cell were studied. In all cases cells gave fairly good open circuit voltage, but low short circuit current and fill factor. Low value of fill factor might be due to the high series resistance of the sample. The presence of interface states causing trapping of photogenerated carriers might be the reason for lower value of short circuit current density. In the following sections we discuss effect of variation of important parameters like buffer/absorber layer thickness, atomic concentration etc on cell performance.

7.4.1 Effect of Having 'Superstrate' Structure

In the 'superstrate' structure the cell should have ITO/ In_2S_3 /CuInS₂/metal electrode and illumination should be given through ITO. Due to the limitation in the structure of the top electrode, we fabricated superstrate structure first. Here thickness and stoichiometry of both the layers were varied. Usually thickness of the buffer layer should be very low (~ 50 nm) in both substrate and superstrate configurations, in order to transmit maximum light to the absorber layer. We varied the thickness of In_2S_3 layer from 1 to 4 μm . At still lower thickness (<1 μm) spraying of CIS resulted in porous In_2S_3 . But thicker In_2S_3 layer resulted in inactive junction even on illumination. From the XPS analysis we found that the diffusion of Cu was much prominent in the superstrate structure [Fig. 7.4]. Also, much light will get absorbed in the thick In_2S_3 layer itself, without reaching the junction region. In another set of experiments we varied the Cu/In ratio of CIS keeping S/Cu ratio at 5. This also produced no effect on illuminating the cell. But on the other hand ITO/CuInS₂/ In_2S_3 /metal electrode clearly exhibited photovoltaic action on illumination. Moreover the dark J-V characteristic was also proving the action of *pn* junction. Hence here we had ITO/CuInS₂/ In_2S_3 /metal electrode structure and illumination was through CuInS₂ layer. This will be clear through the studies in the following sections.

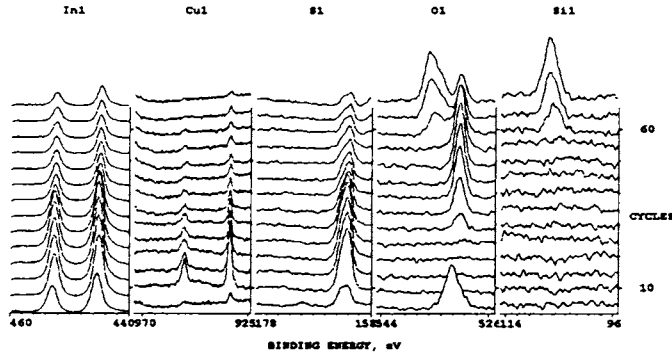
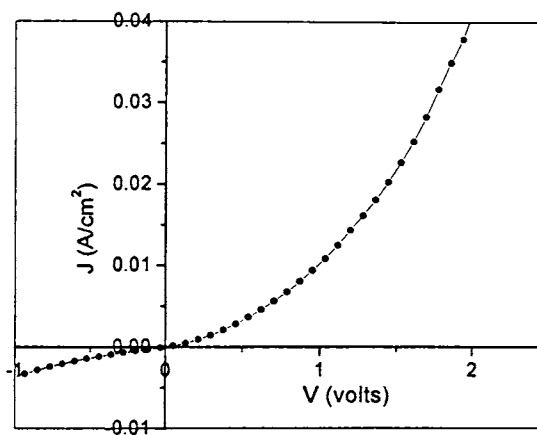


Fig. 7.4 Depth profile of the superstrate structure

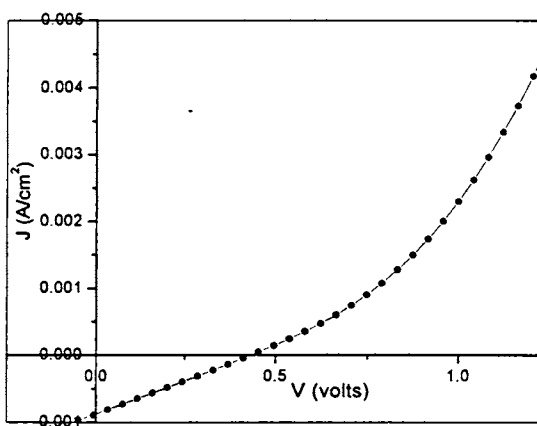
7.4.2 Effect of Layer Thickness Variation

375 ml of the solution was sprayed to get $\sim 0.6 \mu\text{m}$ thickness of the CIS absorber layer. In the case of In_2S_3 layer, we could get thickness of $\sim 0.5 \mu\text{m}$ by spraying 200 ml of the solution. Buffer layer thickness was varied between $0.5 \mu\text{m}$ and $0.25 \mu\text{m}$ by varying the volume of the solution sprayed. For CuInS_2 layer, Cu/In ratio was kept at 1 and S/Cu ratio at 5 and In/S ratio at 1.2/8 for In_2S_3 layer.

On decreasing buffer layer thickness, open circuit voltage was decreased while short circuit current density increased. Variation of the cell parameters with variation in the buffer layer thickness is listed in Table 7.1. This indicated that the buffer layer had strong influence on cell parameters even when illumination was from absorber side. As thickness decreased better carrier collection might be taking place at electrode. The dark and illuminated J-V characteristics of the cell with efficiency 0.104% is shown in Fig. 7.5 (a) and (b).



(a)



(b)

Fig. 7.5 J-V characteristics of the cell with buffer layer having $0.25 \mu\text{m}$ thickness (a) dark (b) illuminated

Table 7.1 Variation of cell parameters with thickness of the buffer layer

Thickness of CuInS₂ absorber layer ~ 0.6 μm (375 ml of solution)

Volume of the solution (ml)	Thickness (approx) (μm)	V _{oc} (mV)	J _{sc} (mA/cm ²)	FF (%)	η (%)
200	0.50	529.9	0.163	23.18	0.02
150	0.37	520.08	0.416	24.15	0.052
100	0.25	440.04	0.896	26.44	0.104

Keeping the thickness of the buffer layer at ~ 0.5 μm, absorber layer thickness was varied between 0.6 μm and 0.4 μm. Voltage and current density of the cell increased on decreasing the thickness of the absorber layer upto a particular value. Probably lower absorber layer thickness allowed good carrier collection at the electrode. Since light came from the absorber side in this case, lower thickness might have helped higher intensity of light to reach the junction region. But on further decreasing the absorber layer thickness both the values got reduced and this might probably be due to the reduction in absorption of light in the absorber layer. Variation of cell parameters with the variation in absorber layer thickness is given in Table 7.2. The dark and illuminated characteristics of the cell with absorber layer thickness 0.5 μm is shown in Fig.7.6.

Table 7.2 Variation of cell parameters with absorber layer thickness

Thickness of In₂S₃ layer ~ 0.5 μm (200 ml of solution)

Volume of the solution (ml)	Thickness (approx) (μm)	V _{oc} (mV)	J _{sc} (mA/cm ²)	FF (%)	η (%)
375	0.6	529.9	0.163	23.18	0.02
300	0.5	586.5	0.836	27.8	0.136
270	0.4	472.3	0.17	25.4	0.024

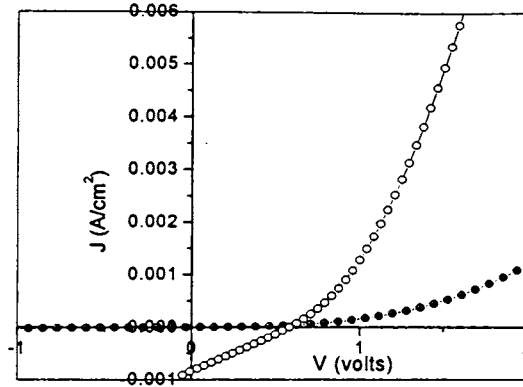


Fig.7.6 Dark and illuminated characteristics of the cell with absorber layer thickness $0.5 \mu\text{m}$

If the value of V_{oc} is reduced by thinning the cell, then poor interface passivation is suspected [23]. The effect was clear from the XPS measurements of the cell [Fig.7.7]. There was no sharp interface between the CuInS_2 and In_2S_3 layer, as copper diffused into In_2S_3 layer. Copper, detected at the In_2S_3 surface was due to diffusion. This might have happened due to the high temperature (300°C) in which CuInS_2 film was kept, during spraying of In_2S_3 layer. Copper diffusion resulted in the formation of intermediate phases between CuInS_2 and In_2S_3 as well as solid mixtures of these phases. Probably this might be one of the reasons for low value of short circuit current density. Copper diffusion is an easy process, as diffusion coefficient of Cu is rather high. Studies of copper diffusion in semiconductors, particularly in CuInSe_2 , indicated its high diffusivity [24]. Diffusion of other elements (eg. In) can also occur but the diffusion coefficient is low. Grain boundary diffusion coefficients are generally much higher than that of lattice diffusion, and hence copper may be diffusing mainly through grain boundaries [25]. In fact grain boundaries are very efficient diffusion paths. Depth profile and atomic concentration of the cell CIS/IS ($\text{Cu}/\text{In} = 1$, $\text{S}/\text{Cu} = 5$, $\sim 0.6 \mu\text{m}$ and $\text{In}/\text{S} = 1.2/8$, $\sim 0.5 \mu\text{m}$) are depicted in Fig.7.7 and 7.8. It was

evident from the XPS analysis that oxygen was present in CIS and In_2S_3 layers, probably a higher percentage of oxygen in In_2S_3 layer.

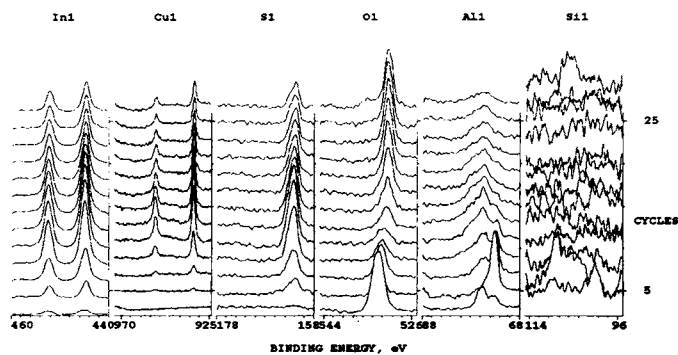


Fig.7.7 Depth analysis of the CIS/ In_2S_3 cell

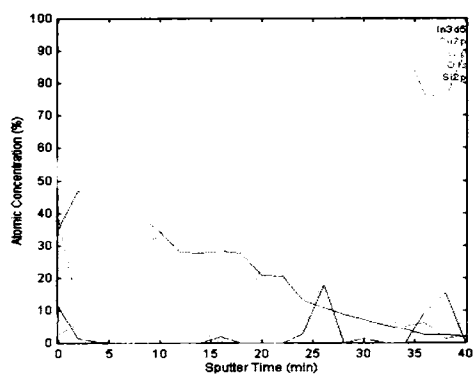


Fig. 7.8 Atomic concentration along the depth of the cell

Oxygen was present throughout the depth of the In_2S_3 layer when sprayed over CuInS_2 layer. Interestingly there was no oxygen in the bulk of the In_2S_3 sample when it was sprayed alone [Fig.3.25]. Since oxygen is more electronegative (3.5) than sulfur (2.4), presence of oxygen may be the reason for high resistance of In_2S_3 . This might have affected electrical resistivity of the two layers and hence the short circuit current.

For 0.5 μm thickness of the absorber layer (300 ml solution) and 0.37 μm thickness of the buffer layer (150 ml solution) (ie, decreasing the thickness of both layers), efficiency of the cell was found to be decreasing. Cell parameters obtained were $V_{oc} = 494.8$ mV, $J_{sc} = 0.063$ mA/cm², FF = 22.34% and $\eta = 0.007\%$.

7.4.3 Effect of Variation of Atomic Concentration

First we studied the effect of variation of atomic ratio of absorber layer. Keeping S/Cu ratio at 5, Cu/In ratio was varied as 0.8, 0.9, 1 and 1.2. In/S ratio was kept at 1.2/8 for In_2S_3 layer. Eventhough CuInS_2 film with Cu/In ratio 0.5 yielded maximum photosensitivity [Fig.5.8] it was showing n-type conductivity and thus could not be used while fabricating the cell. 375 ml of the solution was sprayed to get 0.6 μm thick absorber layer and 200 ml solution was sprayed for 0.5 μm thick In_2S_3 layer. The cell having Cu/In ratio 1.2 produced maximum current density (2.5 mA/cm²) but the voltage (405 mV) was slightly low. As the Cu/In ratio increased the dark resistivity decreased and thus more photogenerated carriers might be reaching the electrode contributing to increase in short circuit current. But increase in Cu/In ratio led to higher diffusion of Cu making junction more imperfect. This might be the reason for decrease in open circuit voltage. Efficiency decreased with decrease in Cu/In ratio. Indium rich CuInS_2 films had much lower hole concentration or the p-type nature of the film decreased. Enhancement of hole concentration is essential for higher efficiency of CuInS_2 based solar cells [26]. On increasing the sulfur concentration (S/Cu = 7) keeping the Cu/In ratio at 1, V_{oc} reduced while J_{sc} enhanced.

Increasing the sulfur concentration might be resulted in the reduction of sulfur vacancies and thus decrease recombination within the absorber layer [11]. Table 7.3 and 7.4 show variation of cell parameters with the Cu/In and S/Cu ratio of CuInS₂ layer. Among these, Cu/In ratio at 1.2 and S/Cu ratio at 5 gave the best result. The series resistance calculated from the dark forward characteristics, was found to be 30.08 Ω.

Table 7.3 Variation of cell parameters with Cu/In ratio (S/Cu = 5)

Cu/In ratio	V _{oc} (mV)	J _{sc} (mA/cm ²)	FF (%)	η (%)
0.8	516.1	0.022	22.40	0.003
0.9	495.0	0.153	23.83	0.018
1.0	529.9	0.163	23.18	0.02
1.2	405.3	2.5	25.90	0.26

The photosensitivity of CuInS₂ samples decreased drastically on increasing the Cu/In ratio [Fig.5.8]. As we increased the Cu/In ratio to 1.5, we did not get any voltage or current on illumination.

Table 7.4 Variation of cell parameters with S/Cu ratio (Cu/In = 1)

S/Cu ratio	V _{oc} (mV)	J _{sc} (mA/cm ²)	FF (%)	η (%)
3	559.40	0.052	17.80	0.005
5	529.90	0.163	23.83	0.02
6	444.08	1.070	25.40	0.12
7	472.30	1.920	24.20	0.22

On further increasing the sulfur concentration, there was no appreciable shift during illumination. This might be because of the reduction in photosensitivity of the

sample [27]. On increasing the Cu/In ratio to 1.2 keeping S/Cu ratio at 7, the short circuit current density dropped to 0.41 mA/cm^2 though the open circuit voltage remained almost the same ($V_{oc} = 476.9 \text{ mV}$).

For Cu/In ratio 1 and S/Cu ratio 7, which gave maximum efficiency among the samples for which sulfur concentration was varied, we tried variation of thicknesses of absorber and buffer layers. On reducing the buffer layer thickness to $0.37 \mu\text{m}$, efficiency reduced drastically to 0.09%. Keeping the buffer layer thickness at $0.5 \mu\text{m}$, when absorber layer thickness was reduced to $0.5 \mu\text{m}$, the efficiency got still reduced. The J-V characteristics of the cell having Cu/In ratio 1 and S/Cu ratio 7 is given in Fig.7.9.

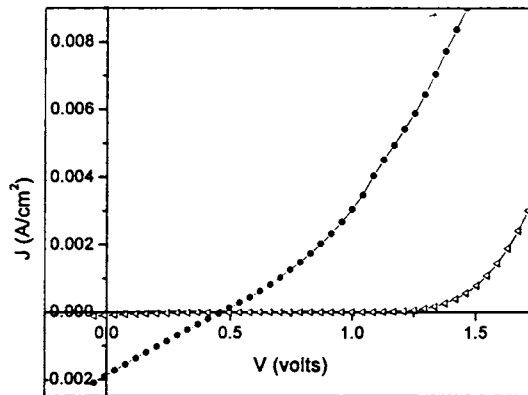


Fig. 7.9 The dark and illuminated J-V characteristics of the cell with Cu/In = 1 and S/Cu = 7

Photosensitivity of the buffer layer was found to be an important factor affecting the performance of the cell. In/S ratio was kept at 1.2/8 for the fabrication of the cells as it gave maximum photosensitivity even though bulk resistance of the sample was high [15]. On changing the ratio to 1.5/8 keeping the Cu/In and S/Cu ratios at 1 and 5 respectively, the current density increased while voltage decreased. This might be resulting from the reduction in resistivity of buffer layer due to increase

in indium concentration. But increasing the In/S ratio to 2/8 with the aim of reducing the series resistance of the cell produced no effect. As In/S ratio approached 2/8 resistivity might be very low affecting the survival of minority carriers. Values V_{oc} , J_{sc} , FF and efficiency are compared in Table 7.5.

Table 7.5 Variation of cell parameters with In/S ratio (Cu/In=1 and S/Cu=5)

In/S ratio	V_{oc} (mV)	J_{sc} (mA/cm ²)	FF (%)	η (%)
1.2/8	529.90	0.163	23.18	0.02
1.5/8	444.08	0.71	24	0.075
2/8	-	-	-	-

7.4.4 Effect of Post Deposition Annealing

The performance of the CIS/IS cell improved on annealing in air. Fig.7.10 shows J-V characteristics of the cell after annealing in air at 200°C for 30 minutes. Value of FF improved on annealing in air (31.1%). The cell parameters obtained were $V_{oc} = 528.5$ mV, $J_{sc} = 0.196$ mA/cm² and $\eta = 0.032\%$. Series resistance (from the dark characteristics of the cell) was found to be 19.45 Ω .

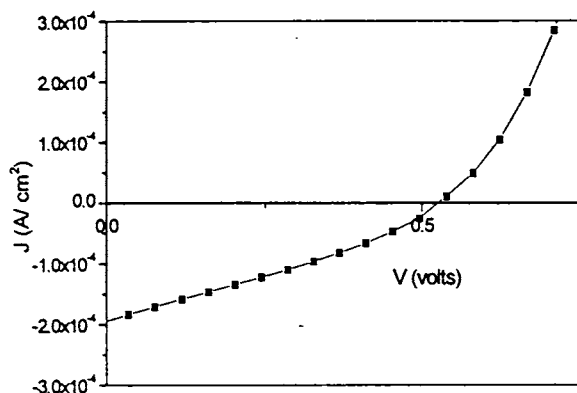


Fig. 7.10 J-V characteristics of the cell after annealing in air at 200°C for 30 minutes

This was not the case with all the samples as the effect depends on the atomic concentration and the thickness of the absorber and buffer layers.

The best results were obtained when the cell was kept at the preparation temperature (300°C) itself for 1 hour, after deposition [Fig.7.11]. Cell parameters of this cell were $V_{oc} = 529.7$ mV, $J_{sc} = 3.62$ mA/cm², FF = 29.88% and $\eta = 0.57\%$. Variation in the cell parameters after keeping the cell at the preparation temperature itself for 30 minutes, 45 minutes and 1 hour are listed in Table 7.6.

Also CuInS₂ layer was annealed for 1 hour after deposition before spraying In₂S₃ layer. Then the cell parameters obtained were $V_{oc} = 477$ mV, $J_{sc} = 0.94$ mA/cm², FF = 26.6% and $\eta = 0.12\%$. On increasing the Cu/In ratio to 1.2 with S/Cu ratio 5 and 7 and keeping the cell for 1 hour after deposition at the same temperature, efficiency was found to decrease. Larger Cu/In ratio might be resulting in greater diffusion of copper from CuInS₂ layer to In₂S₃ layer. When the CIS/IS cell was deposited at a higher temperature (350°C), the efficiency was found to be low. This may be due to increased diffusion of Cu from CIS to In₂S₃.

Table 7.6 Variation of cell parameters with variation in the time of annealing just after depositing the cell

Cu/In = 1 S/Cu = 5, In/S = 1.2/8

Time (min)	V_{oc} (mV)	J_{sc} (mA/cm ²)	FF (%)	η (%)
30	529.9	0.163	23.18	0.02
45	559.4	2.20	23.40	0.30
60	529.7	3.62	29.88	0.57

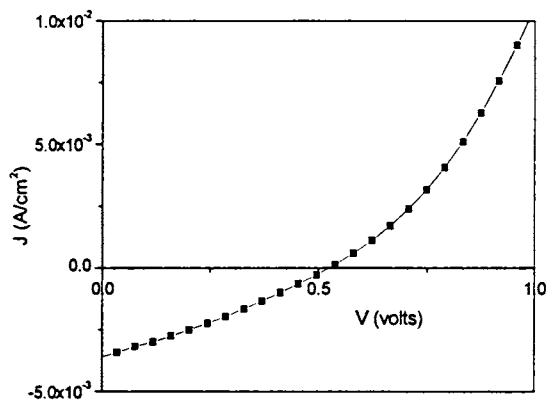


Fig. 7.11 J-V characteristics after keeping the cell at the preparation temperature (300°C) itself for 1 hour, after deposition

Absorption spectrum of the cell, which was kept at the preparation temperature itself for 1 hour, is given in Fig.7.12. It showed clear absorption edges for CuInS_2 layer (~ 1.5 eV) and indium sulfide layer (~ 2.67 eV).

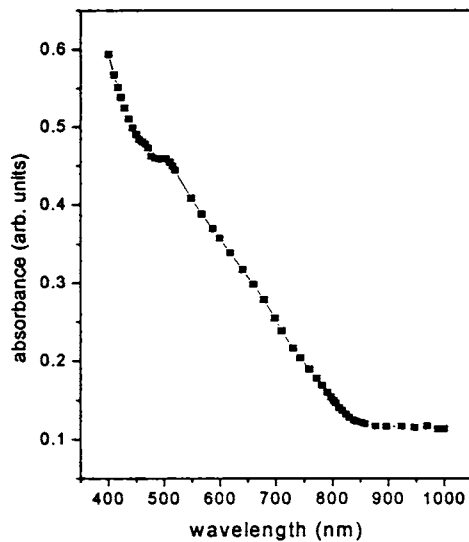


Fig. 7.12 Absorption spectrum of the best cell annealed for 1 hour

Series resistance (R_s) calculated from the inverse slope of the dark forward characteristics of the cell was 14.2 Ω . The value could also be calculated from the equation

$$R_s = \frac{1}{\lambda} \frac{1}{(I_2 - I_1)} \ln \left[\frac{I_{ph} - I_2}{I_{ph} - I_1} \right] - \left(\frac{V_2 - V_1}{I_2 - I_1} \right)$$

where, $\lambda = q/AkT$; A is diode quality factor, kT/q is thermal voltage, I_{ph} is the light generated current density, V_1, V_2, I_1 & I_2 are the voltage and current density values at any two points on the J-V characteristic curve [28].

Here $V_1 = 161.2$ mV, $I_1 = 2.75$ mA/cm²
 $V_2 = 331.3$ mV, $I_2 = 1.63$ mA/cm²
 $I_{ph} = 3.62$ mA/cm², $A = 3.3$, $T = 300$ K and $kT/q = 0.025$

Series resistance was found to be 15.18 Ω . This was in good agreement with the value obtained from the dark forward characteristics of the cell. Dark characteristics of the cell is given in Fig.7.13. Diode quality factor was calculated to be 3.3 from the slope of the dark characteristics of the cell, by plotting $\ln J$ vs V graph [Fig.7.14]. Diode quality factor >2 indicated domination of interface recombination [29], leading to reduced short circuit current density, J_{sc} . For the cells prepared using CSP technique, interface was not sharp as observed from XPS [Fig. 7.7] and this might be the reason for the low value of short circuit current density in the present work.

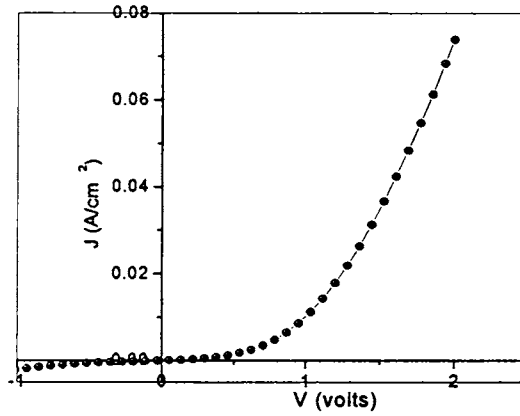
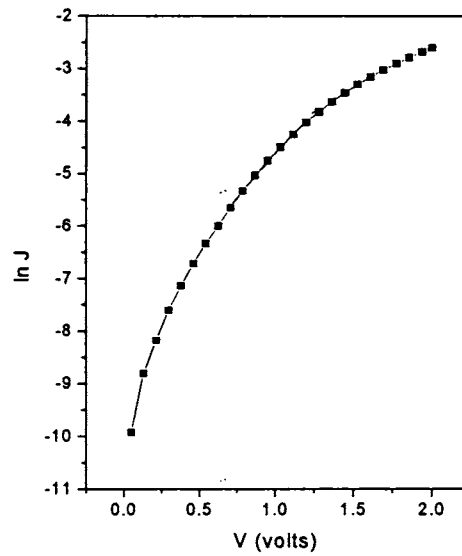


Fig. 7.13 Dark characteristics of the cell

Fig. 7.14 $\ln J$ vs V graph

7.5 Conclusion

It had been shown that In_2S_3 could be used as an alternative buffer layer material for CuInS_2 based solar cells. It was also proved that CSP technique could be

used for deposition of both absorber and buffer layers. Again the structure of the cell was ITO/CuInS₂/In₂S₃/metal electrode. This structure was adopted, as we could not prepare junction in the real superstrate structure. But we found that the superstrate structure was not having junction effect at all. From XPS analysis it was clear that Cu diffused into the In₂S₃ layer, which might be the reason for low value of short circuit current density. The best cell parameters obtained were $V_{oc} = 529.7$ mV, $J_{sc} = 3.62$ mA/cm², FF = 29.88% and $\eta = 0.57\%$. The most important step required for the improvement in the performance of the cell is the passivation of defects at the interface. However the possibility of establishment of this heterojunction using CSP technique is an encouraging result.

References

- [1] J. A. M. Abushama, S. Johnston, T. Moriarty, G. Teeter, K. Ramanathan and R. Noufi *Prog. Photovolt: Res. Appl.* **12** (2004) 39
- [2] M. Powalla and B. Dimmler *Thin Solid Films* **361-362** (2000) 540
- [3] T. Watanabe and M. Matsui *Jpn. J. Appl. Phys.* **38** (1999) L1379
- [4] K. Ramanathan, M. A. Contreras, C. L. Perkins, S. Asher, F. S. Hasoon, J. Keane, D. Young, M. Romero, W. Metzger, R. Noufi, J. Ward and A. Duda *Prog. Photovolt: Res. Appl.* **11** (2003) 225
- [5] T. Nakada, M. Mizutani, Y. Hagiwara and A. Kunioka *Sol. Energy Mater. Sol. Cells* **67** (2001) 255
- [6] Y. Ohtake, K. Kushiyal, M. Ichikawa, A. Yamada and M. Konagai *Jpn. J. Appl. Phys.* **37** (1998) 3220
- [7] G. Gordillo and C. Calderón *Sol. Energy Mater. Sol. Cells* **77** (2003) 163
- [8] D. Hariskos, M. Ruckh, U. Rühle, T. Walter, H. W. Schock, J. Hedström and L. Stolt *Sol. Energy Mater. Sol. Cells* **41/42** (1996) 345
- [9] S. Spiering, D. Hariskos, M. Powalla, N. Naghavi and D. Loncot *Thin Solid Films* **431- 432** (2003) 359
- [10] L. L. Kazmerski and G. A. Sanborn *J. Appl. Phys.* **48(7)** (1977) 3178
- [11] J. Klaer, J. Bruns, R. Henninger, K. Siemer, R. Klenk, K. Ellmer and D. Bräunig *Semicond. Sci. Technol.* **13** (1998) 1456
- [12] K. Siemer, J. Klaer, I. Luck, J. Bruns, R. Klenk and D. Bräunig *Sol. Energy Mater. Sol. Cells* **67** (2001) 159
- [13] R. Scheer, T. Walter, H. W. Schock, M. L. Fearheiley and H. J. Lewerenz *Appl. Phys. Lett.* **63(24)** (1993) 3294
- [14] T. Asikainen, M. Ritala and M. Leskelä *Appl. Surf. Sci.* **82/83** (1994) 122
- [15] Teny Theresa John, S. Bini, Y. Kashiwaba, T. Abe, Y. Yasuhiro, C. Sudha Kartha and K. P. Vijayakumar *Semicond. Sci. Technol.* **18** (2003) 491

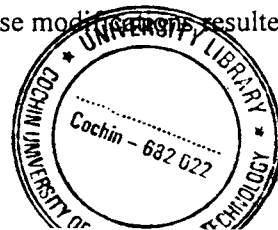
- [16] Rupa R Pai, Teny Theresa John, Y. Kashiwaba, T. Abe, K. P. Vijayakumar and C. Sudha Kartha *J. Mat. Sci.* **39** (2004) 1
- [17] Teny Theresa John, K. P. Vijayakumar, C. Sudha Kartha, T. Abe and Y. Kashiwaba *Proc. World Conference on Photovoltaic Energy Conversion (WCPEC- 3)* Osaka, Japan 1P-C3-24 (2003)
- [18] D. Braunger, D. Hariskos, T. Walter and H. W. Schock *Sol. Energy Mater. Sol. Cells* **40** (1996) 97
- [19] K. Siemer, J. Klaer, I. Luck, J. Bruns, R. Klenk and D. Bräunig *Sol. Energy Mater. Sol. Cells* **67** (2001) 159
- [20] A. Mere, O. Kijatkina, H. Rebane, J. Krustok and M. Krunks *J. Phys. Chem. Solids* **64** (2003) 2025
- [21] K. L. Chopra and S. R. Das *Thin Film Solar Cells*, Plenum Press, New York (1983)
- [22] Harold J. Hovel *Semiconductors and Semimetals; Vol. II, Solar Cells*, Academic Press, New York (1975)
- [23] S. R. Kurtz, J. M. Olson, D. J. Friedman, J. F. Geisz, K. A. Bertness and A. E. Kibbler *Proc. Mat. Res. Soc. Symp.* **573** (1999) 95
- [24] L. Chernyak, D. Cahen, S. Zhao and D. Maneman *Appl. Phys. Lett.* **65** (1994) 427
- [25] K. Djessas, S. Yapi, G. Massé, M. Ibannain and J. L. Gauffier *J. Appl. Phys.* **95(8)** (2004) 4111
- [26] T. Watanabe, H. Nakazawa, M. Matsui, H. Ohbo and T. Nakada *Sol. Energy Mater. Sol. Cells* **49** (1997) 357
- [27] S. Bini *Ph.D Thesis*, Department of Physics, Cochin University of Science and Technology, Kochi-682 022, India (2003)
- [28] M. K. El-Adawi and I. A. Al-Nuaim *Vacuum* **64** (2001) 33
- [29] M. Saad and A. Kassis *Sol. Energy Mater. Sol. Cells* **77** (2003) 415

Chapter 8**CuInS₂/In₂S₃ SOLAR CELL PREPARED USING CSP TECHNIQUE:
DESIGN MODIFICATIONS FOR IMPROVED PERFORMANCE****8.1 Introduction**

In the earlier chapter we described the details of preparation and characterization of CuInS₂/In₂S₃ solar cell. The speciality of our work was that we used CSP technique for the deposition of both absorber and buffer layers, as it is very convenient to dope or vary the stoichiometry of the semiconductor layer through this technique. Moreover, here the buffer layer was In₂S₃ which is a wide band gap material having no toxic element like cadmium.

The first difficulty, which we had to overcome in this work, was the sequence of deposition. We could not deposit CuInS₂ over In₂S₃ layer. Hence we could not prepare 'real' superstrate structure. Instead, we prepared the cell with structure ITO/CuInS₂/In₂S₃/electrode and illumination was given through CuInS₂ side. However measurements showed that there was enough intensity reaching the junction region for carrier generation. But much more difficulty was created by the diffusion of copper from CuInS₂ layer into In₂S₃ layer. This made the junction very much imperfect. Diffusion of copper from CuInS₂ led to the formation of Cu vacancies, making the layer highly resistive. It was quite clear that these changes affected junction barrier leading to considerable reduction in short circuit current and fill factor. Moreover the diode quality factor was rather high indicating high recombination loss.

In this chapter we describe in detail the modifications made in the design aspects of the cell, so as to minimize (if not avoid) the difficulties we have experienced in the functioning of the cell in the preliminary stages. Variations in the thickness and stoichiometry of absorber and buffer layers, and trying different materials for top electrode were the major changes and these modifications resulted in



large improvement of cell parameters. These modifications were selected based on our earlier studies done on these materials.

It is worth mentioning here that we did not try etching using KCN [1-3] to remove unwanted phases of copper or doping using Na [4]. We also did not give any antireflection coating to prevent loss due to reflection of light from cell surface.

8.2 Device Fabrication

As stated earlier, we tried variations in thickness of absorber and buffer layers of the cell. This was mainly to accommodate copper diffusion. When we increased thickness of In₂S₃ layer, we could get a layer of pure In₂S₃ layer over the Cu diffused region. Similarly when CIS layer thickness was increased we could get, in the lower region, a layer of CIS, having high Cu concentration. Usually the volume of solution sprayed for depositing CuInS₂ was 375 ml while for depositing In₂S₃ layer 200 ml solution was sprayed. Corresponding thickness of the absorber layer was 0.6 μm while that of buffer layer was 0.5 μm. In order to increase buffer layer thickness, considering the copper diffusion from the copper indium sulfide layer to indium sulfide layer, two layers of In₂S₃ were sprayed in two steps (by spraying first 200 ml and 150 ml later) so as to make the total buffer layer thickness ~ 0.85 μm. After spraying 200 ml, the cell was allowed to cool to room temperature. Then it was reheated to 300°C to spray the remaining 150 ml. This procedure was accepted to avoid formation of pinholes. After spraying 150 ml the cell was kept at the preparation temperature itself for half an hour. Similarly for increasing absorber layer thickness, two layers of CuInS₂ were deposited by spraying 375 ml first and 300 ml later, making absorber layer, 1.1 μm thick. Here, the cell was kept at the preparation temperature for 1 hour after deposition. If the whole solution were sprayed in a single stretch, it would have led to the formation of pinholes in the film. In the present work we prepared three sets of samples. The first one was having single layer absorber and buffer (named as Cell-A). The second one was having two layers of absorber (named

as Cell-B) and the third one was having two layers of buffer (named as Cell-C). These three cases will be discussed in the following sections.

Cu/In, S/Cu and In/S ratios of the films were controlled by varying the molar concentrations of respective solutions. In the case of CuInS₂ films, Cu/In ratio was kept at 1.2 and 1 while S/Cu ratio was kept at 5 in solution. While preparing In₂S₃ layer, In/S ratio was kept at 1.2/8 in the solution as it was showing maximum photosensitivity [5]. Top electrode was thin film of Al or Ag (~ 45 nm), which was deposited over the In₂S₃ layer using physical vapor deposition. In all the cases illumination was given through absorber side due to the nature of the electrode. Always incident intensity was 100 mW/cm² avoiding heating of the sample as described in section 7.3. We also measured transmitted intensity through In₂S₃ side for Cell A, B, and C and found that values are ~ 20 mW/cm² (Cell-A), ~10 mW/cm² (Cell- B and C) respectively. This proved that enough intensity was available at junction region for carrier generation.

8. 3 Results and Discussion

8.3.1 Cell-A

At first we deposited a single layer of CuInS₂ (by spraying 375 ml solution) and In₂S₃ (by spraying 200 ml solution). Here Cu/In ratio for CuInS₂ was kept at 1 in the solution. The films were slightly copper deficient (Cu/In=0.7) as observed from EDAX measurements. This avoided formation of Cu_xS, CuIn₅S₈ or introduction of Cu_{In} antisite defects [1]. Moreover, no such phases were identified from the structural (XRD) and stoichiometric (XPS) analysis. Again Cu rich films may give rise to leakage current through electron tunneling at the junction. Thus we could avoid the toxic KCN etching before fabricating the cell. We also observed that photosensitivity of CuInS₂ film increased on decreasing the Cu/In ratio.

A thin layer of indium (50 Å) was evaporated onto the top of the cell followed by annealing at 100°C for 30 minutes. Aluminium (Al) was deposited over this, using

physical vapor deposition, as the top electrode. Diffusion of indium might be reducing the sheet resistance of the cell near the top electrode, helping better collection of photogenerated carriers at the electrode. Also, even when there was diffusion of Cu, thermal diffusion of excess indium at the top may help in the formation of a layer of In₂S₃ free of Cu at the top. Cell parameters obtained were $V_{oc} = 533$ mV, $J_{sc} = 17.4$ mA/cm², FF = 28.6% and $\eta = 2.65\%$ [Fig. 8.1].

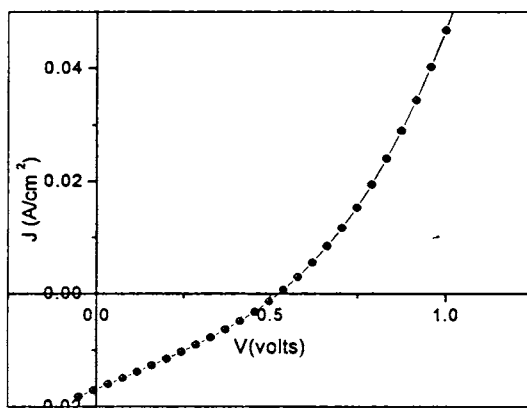


Fig. 8.1 J-V characteristics of Cell-A

XPS analysis of the cell [Fig.7.7] (before diffusing Indium) revealed diffusion of Cu from CuInS₂ layer to In₂S₃ layer. Copper diffusion is an easy process as the diffusion coefficient of Cu is high [6]. Moreover oxygen was present throughout the depth of the In₂S₃ layer when sprayed over CuInS₂, while there was no oxygen when In₂S₃ was sprayed alone [5]. This might have resulted in an increase of the resistance of the cell reducing FF.

8.3.2 Cell-B

The performance of the cell was improved by depositing two layers of CuInS₂ (as described earlier) and a single layer of In₂S₃. This time silver was deposited as the top electrode using vacuum evaporation. The area of electrode was 0.014 cm² and thickness ~ 45 nm. Fig. 8.2 shows the depth profile of the cell.

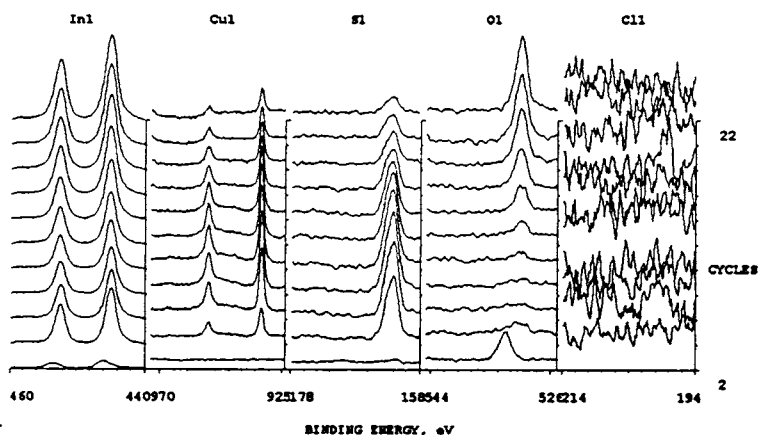


Fig. 8.2 XPS depth profile of Cell-B

Interestingly here it was clear from the XPS depth profile that there was no oxygen in the bulk of the sample when fabricated in three layers. This was not the case for the Cell-A having single layer of CuInS₂. This might be reducing resistance of the sample allowing better carrier collection at the electrode. However there was a peak at the surface of the cell, corresponding to binding energy 532.5 eV, representing presence of oxygen as surface contaminant. This was not doing any damage to the cell. Interestingly no peak corresponding to chlorine was present in the XPS results even though we used precursor solution containing chloride, for sample preparation. But when In₂S₃ layer was prepared, chlorine was present in it. Increase in the thickness of the absorber layer should increase the light absorption and hence the generation of photocarriers. Moreover concentration of Cu decreased towards the CIS/In₂S₃ interface as evident from peak height of binding energy of Cu in Fig.8.2. This probably made CIS layer near interface, more photosensitive. But still there was Cu diffusion as it was evident from the thin layer of In₂S₃ present over CuInS₂. Cell

parameters obtained in this case were $V_{oc} = 450$ mV, $J_{sc} = 44.03$ mA/cm², FF = 29.5 % and $\eta = 5.87$ %. The dark and illuminated J-V characteristics of the cell are given in Fig 8.3 and 8.4.

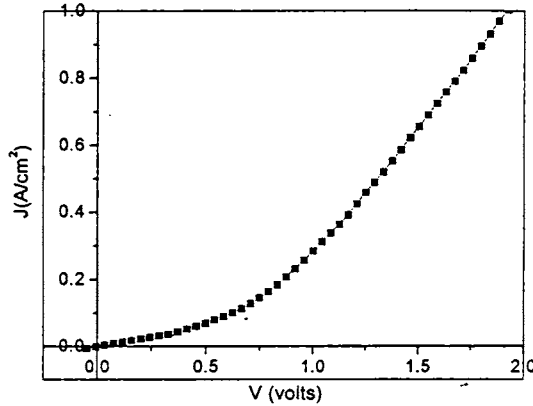


Fig. 8.3 Dark characteristics of Cell-B

Series resistance (R_s) calculated from the inverse slope of the dark forward characteristics of the cell was 1.23Ω . The value can also be calculated from the equation

$$R_s = \frac{1}{\lambda} \frac{1}{(I_2 - I_1)} \ln \left[\frac{I_{ph} - I_2}{I_{ph} - I_1} \right] - \left(\frac{V_2 - V_1}{I_2 - I_1} \right)$$

where, $\lambda = q/AkT$; A is diode quality factor, kT/q is thermal voltage, I_{ph} is the light generated current density, V_1, V_2, I_1 & I_2 are the voltage and current density values at any two points on the J-V characteristic curve [7]. Series resistance was found to be 1.16Ω . This was in good agreement with the value obtained from the dark forward characteristics of the cell.

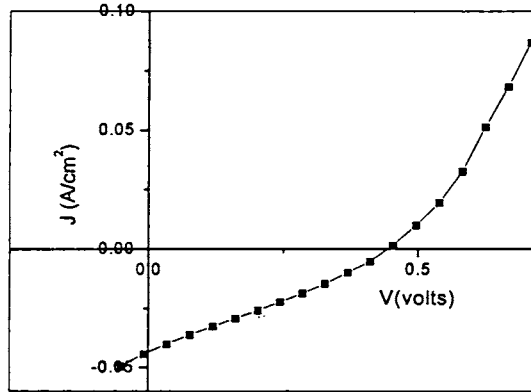


Fig.8.4 Illuminated J-V characteristics Cell-B

Diode quality factor calculated from the slope of the dark characteristics of the cell, by plotting $\ln(J)$ vs V graph was 2.5 [Fig. 8.5]. Therefore, forward dark J-V characteristics are dominated by the recombination-generation mechanism [8].

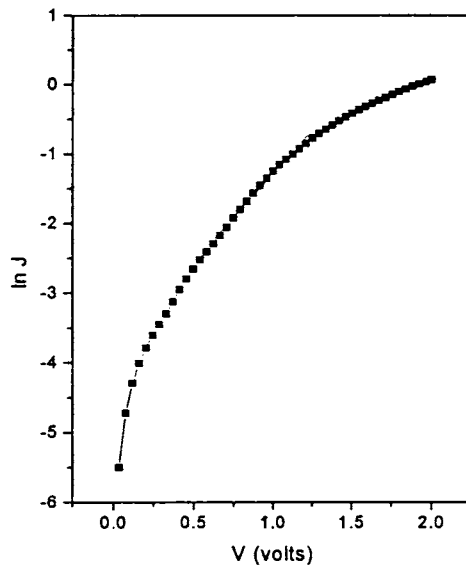
Fig. 8.5 $\ln J$ vs V graph (Cell-B)

Figure 8.6 shows results of XRD analysis of absorber and buffer layers of Cell-B. Both CuInS₂ and In₂S₃ phases are observed in the XRD results of the cell. In the absorption spectrum of the cell, the band edges corresponding to both the CuInS₂ and In₂S₃ layers were clearly observed [Fig.8.7].

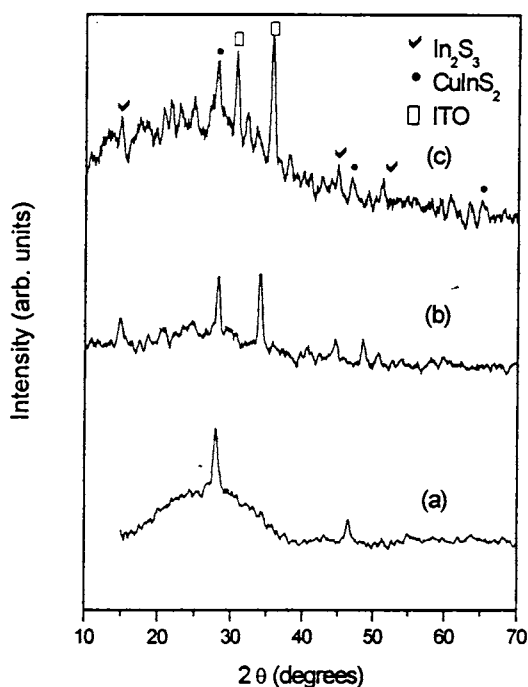


Fig. 8.6 XRD spectra of (a) CuInS₂ (b) In₂S₃ (c) ITO/CuInS₂/In₂S₃

Fig. 8.8 shows the spectral photoresponse of Cell-B. Cutoff at the short wavelength side was due to absorption in the In₂S₃ layer, while the long-wavelength cutoff corresponds to absorption edge of CuInS₂ film. Due to the higher band gap of Cd-free buffer layer, an enhanced response in the short wavelength region of the spectrum can be observed resulting in higher short circuit current. Collection property of this junction was sufficient as evident from the flatness of the spectral response.

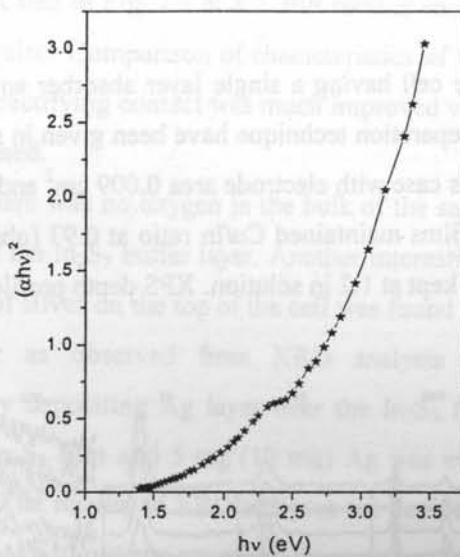


Fig. 8.7 (ahv)² vs hv plot for Cell-B

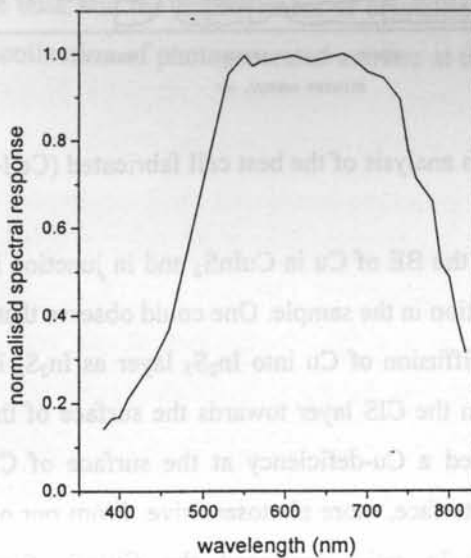


Fig. 8.8 Spectral response of Cell-B

8.3.3 Cell-C

Here we prepared the cell having a single layer absorber and a double layer of buffer layer. Details of preparation technique have been given in section 8.2. The top electrode was silver in this case with electrode area 0.009 cm² and thickness ~ 45 nm. In this case CuInS₂ thin films maintained Cu/In ratio at 0.93 (observed from EDAX analysis), as the ratio was kept at 1.2 in solution. XPS depth profile of the cell is given in Fig.8.9.

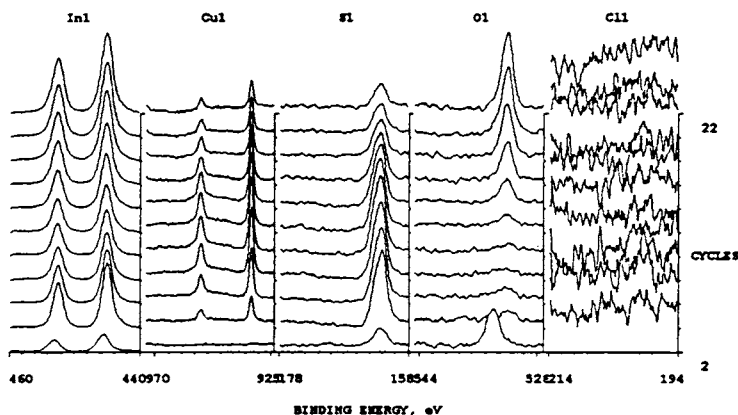


Fig. 8.9 Depth analysis of the best cell fabricated (Cell-C)

There was no shift in the BE of Cu in CuInS₂ and in junction indicating absence of any binary phase formation in the sample. One could observe that at the interface of CuInS₂/In₂S₃, there was diffusion of Cu into In₂S₃ layer as In₂S₃ is thin. Thus there was a gradient of Cu from the CIS layer towards the surface of the In₂S₃ film. This diffusion of copper created a Cu-deficiency at the surface of CIS layer probably making CIS layer, near interface, more photosensitive. From our own experience we had seen that when Cu/In ratio decreased the CuInS₂ films become more photosensitive [9]. However in the case of Cell-C one could see that there was a layer of In₂S₃ at the surface [Fig. 8.9] without any Cu. This layer of In₂S₃ was thicker than

such layers indicated in Fig. 7.7 & 8.2. But surface contamination due to oxygen was there in Cell-C also. Comparison of characteristics of this junction with earlier ones proved that the rectifying contact was much improved when the thickness of the In₂S₃ layer was increased.

Here also there was no oxygen in the bulk of the sample. This might be reducing the resistance of the In₂S₃ buffer layer. Another interesting point to be noted here was that deposition of silver on the top of the cell was found to improve the crystallinity of the In₂S₃ layer as observed from XRD analysis [Fig.8.10]. This was done independently by depositing Ag layer over the In₂S₃ film. 200 ml of solution was sprayed to get In₂S₃ film and 5 mg (10 mg) Ag was evaporated to deposit Ag film over In₂S₃ film. The results of XRD analyses are depicted in Fig. 8.10 (a) and (b). It was very clear that without any annealing there was good improvement in crystallinity of In₂S₃ sample (scale on Y-axis is the same for Fig. 8.10 (a), (b) and (c)). This might have resulted in considerable decrease in dark resistivity of In₂S₃. Hence the absence of oxygen in the bulk and the improvement of crystallinity of In₂S₃ might be helping to have a better collection of photogenerated carriers at the electrode.

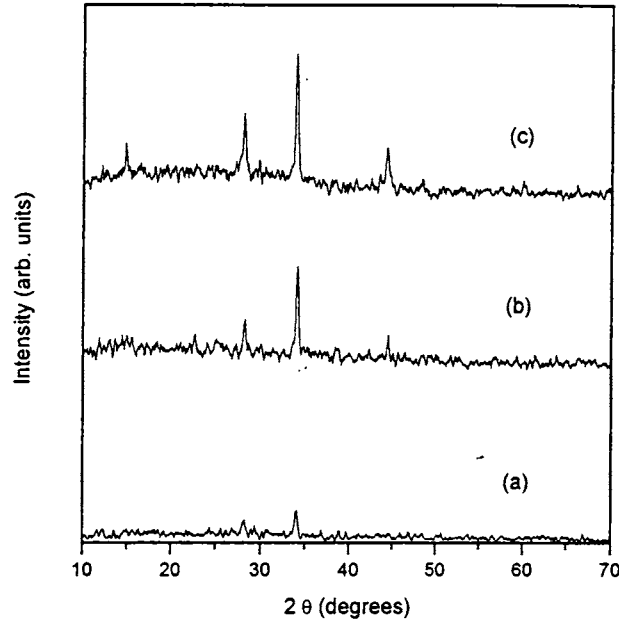


Fig. 8.10 XRD spectrum of In₂S₃ buffer layer (a) as prepared (b) coated with 5 mg Ag (c) coated with 10 mg Ag (without any annealing)

Dark and illuminated J-V characteristics of the cell fabricated in three layers is given in Fig.8.11. The cell parameters obtained were $V_{oc} = 588$ mV, $J_{sc} = 48.2$ mA/cm², FF = 33.5% and $\eta = 9.5\%$. To the best of our knowledge this is the maximum efficiency obtained so far for a CuInS₂/In₂S₃ cell fabricated using CSP technique. On increasing Cu/In ratio conductivity of the CuInS₂ film increased, compared to the previous cases. This enhancement of conductivity of CuInS₂ films might be another reason for the increase in the value of V_{oc} , J_{sc} and FF [10].

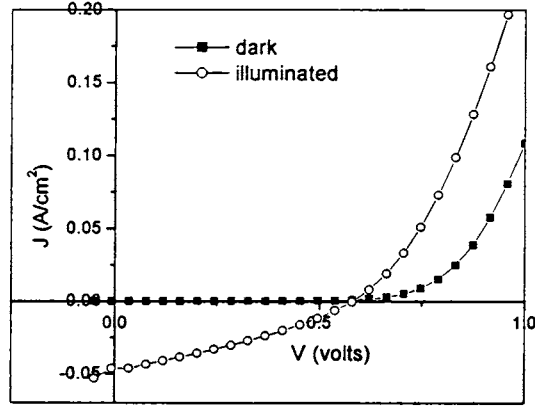


Fig. 8.11 Dark and illuminated J-V characteristics of the best cell fabricated (Cell-C)

We could find a violation of the superposition of light and dark characteristics, which is known as *cross over*; a phenomenon commonly encountered in CIS devices. Several publications [11-13] related this shift to the deep level acceptor states, which were present in the buffer layer or at the interface. In the present case also there could be deep level acceptors (like vacancy of In) in buffer layer as we kept In/S ratio equal to 1.2/8 to make indium low and sulfur excess as this resulted in high photosensitivity.

Series resistance (R_s) calculated from the inverse slope of the dark forward characteristics of the cell was 0.83 Ω . The value was found to be much less than that of Cell-A (14.2 Ω) and Cell-B (1.23 Ω). The J-V characteristics follow the general relationship $J \sim \exp(qV/nKT)$. Thus diode quality factor was calculated from the slope of the dark characteristics of the cell, by plotting $\ln(J)$ vs V graph. The value was found to be 2.2. Diode quality factor, greater than two, indicated the domination of generation - recombination process [14]. The interface recombination might be responsible for a moderate open circuit voltage and fill factor [15]. Absorption

spectrum of the cell was recorded in the wavelength range 350-950 nm. It showed clear absorption edges for both the absorber and buffer layers [Fig.8.12].

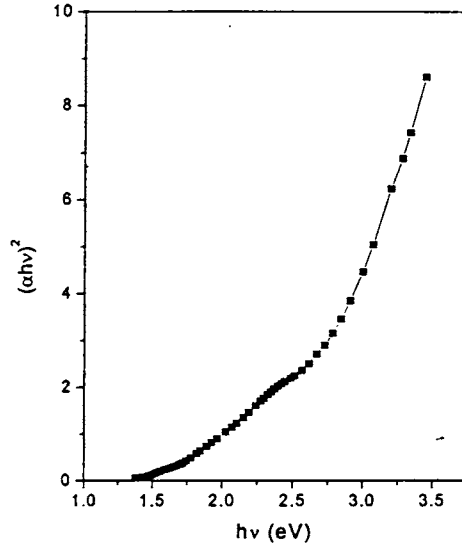


Fig. 8.12 Absorption edges for CuInS₂ and In₂S₃ (Cell-C)

Fig. 8.13 shows the normalized spectral response of the cell. The cutoff at short wavelength side was due to absorption in the In₂S₃ layer, while the long-wavelength cutoff corresponds to the absorption edge of CuInS₂ film. Due to the higher band gap of Cd-free buffer layer, an enhanced response in the short wavelength region of the spectrum can be observed resulting in a higher short circuit current. The overall response was flat indicating a sufficiently large collection width, ie, space charge region plus diffusion length [15].

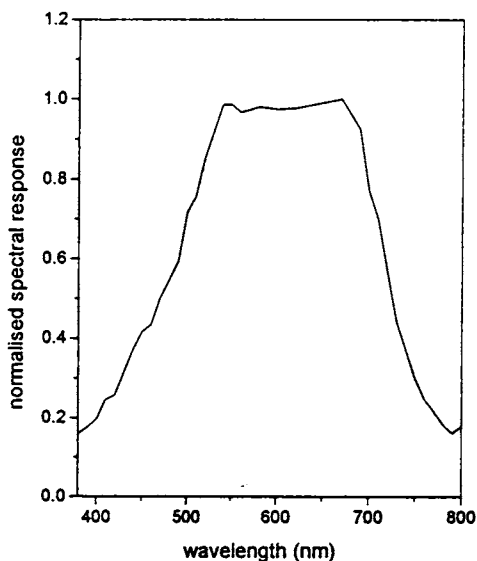


Fig. 8.13 Normalised spectral response of Cell-C

8.4 Conclusion

Cell fabricated with single layer of CuInS₂ and double layer of In₂S₃ (Cell-C) using CSP technique with Ag electrode (area 0.009 cm²) exhibited 9.5% efficiency. This is the highest efficiency ever reported for CuInS₂/In₂S₃ cell fabricated using CSP technique. We found that there was diffusion of copper from the CuInS₂ layer to the In₂S₃ layer from XPS analysis. Absence of oxygen in the bulk of the sample and the presence of a layer of In₂S₃ free of Cu at the top of the cell might be contributing to the improvement in the performance of the cell when fabricated in three layers. A layer of silver coated on the surface of the In₂S₃ buffer layer helped in improving the crystallinity of the In₂S₃ layer as observed from XRD analysis. This might be resulting in better collection of photogenerated carriers at the electrode. All these might have contributed to the high efficiency of the cell.

References

- [1] Y. Ogawa, A. Jäger-Waldau, Y. Hashimoto and K. Ito *Jpn. J. Appl. Phys.* **33** (1994) L1775
- [2] T. Negami, Y. Hashimoto, M. Nishitani and T. Wada *Sol. Energy Mater. Sol. Cells* **49** (1997) 343
- [3] J. Klaer, J. Bruns, R. Henninger, K. Siemer, R. Klenk, K. Ellmer and D. Bräunig *Semicond. Sci. Technol.* **13** (1998) 1456
- [4] T. Watanabe, H. Nakazawa, M. Matsui, H. Ohbo and T. Nakada *Sol. Energy Mater. Sol. Cells* **49** (1997) 357
- [5] Teny Theresa John, S. Bini, Y. Kashiwaba, T. Abe, Y. Yasuhiro, C. Sudha Kartha and K. P. Vijayakumar *Semicond. Sci. Technol.* **18** (2003) 491
- [6] K. Djessas, S. Yapi, G. Massé, M. Ibannain and J. L. Gauffier *J. Appl. Phys.* **95** (8) (2004) 4111
- [7] M. K. El-Adawi and I. A. Al-Nuaim *Vacuum* **64** (2001) 33
- [8] L. L. Kazmerski and G. A. Sanborn *J. Appl. Phys.* **48**(7) (1977) 3178
- [9] Teny Theresa John, K. C. Wilson, P. M. Ratheesh Kumar, C. Sudha Kartha, K. P. Vijayakumar, Y. Kashiwaba, T. Abe and Y. Yasuhiro *Phys. Stat. Sol. (a)* **202** (1) (2005) 79
- [10] R. Scheer, M. Alt, I. Luck and H. J. Lewerenz *Sol. Energy Mater. Sol. Cells* **49** (1997) 423
- [11] M. Igalson and C. Platzer-Björkman *Sol. Energy Mater. Sol. Cells* **84** (2004) 93
- [12] M. Gloeckler, C. R. Jenkins and J. R. Sites *Proc. Mat. Res. Soc. Symp.* **763** (2003) B5.20.1
- [13] I. L. Eisgruber, J. E. Granata, J. R. Sites, J. Hou and J. Kessler *Sol. Energy Mater. Sol. Cells* **53** (1998) 367
- [14] L. L. Kazmerski, F. R. White, M. S. Ayyagari, Y. J. Juang and R. P. Patterson *J. Vac. Sci. Technol.* **14**(1) (1977) 65

- [15] T. Walter, A. Content, K. O. Velthaus and H. W. Schock *Sol. Energy Mater. Sol. Cells* 26 (1992) 357.

Chapter 9

SUMMARY AND CONCLUSIONS

Semiconducting thin films of chalcopyrite group are currently under intensive investigation for highly efficient solar energy conversion. The chalcopyrite semiconductor CuInS_2 , is one of the most promising optical absorbers for efficient solar cells due to its optimum band gap (1.5 eV), which is matching well with solar spectrum. Moreover, constituents of this compound are abundant and have low toxicity. Lot of work is also going on for the effective replacement of CdS, using other buffer layers having wider band gap than that of CdS. This not only avoids toxic cadmium but also improves light transmission in the blue region. In_2S_3 is one such material.

We characterized both these materials (CuInS_2 and In_2S_3) prepared using CSP technique under different sample preparation temperatures and molar concentration ratios. CSP is a simple and low cost technique, which is well suited for deposition of large area films. Moreover, composition and doping profile of the thin film can be easily varied by varying molar concentration of the respective salt in the spray solutions used in this technique. This prompted us to select this technique for the deposition of these two films in the present work.

First, indium sulfide thin films were prepared using chloride based precursor solutions. The films showed $\beta\text{-In}_2\text{S}_3$ phase with preferential orientation along (220) plane. Band gap was found to be 2.67 eV for In/S ratio 2/3. XPS analysis of the samples revealed presence of oxygen as surface contamination on the surface, for all the samples. We could get good control over the stoichiometry of the films by varying the substrate temperature or In/S ratio in the film. The sample having In/S ratio 1.2/8 showed maximum photosensitivity ($\Delta I/I_D = 949.97$), but it was highly resistive. On increasing the indium concentration resistivity as well as photosensitivity of the samples decreased. These two parameters of a semiconductor are important

factors for the fabrication of efficient solar cells. High resistance of the films will increase the series resistance and reduce the fill factor of the cell. Thus we must have a compromise between these two parameters for solar cell applications. In the present work thick indium sulfide films ($4\ \mu\text{m}$) were prepared by spraying 1000 ml of the solution. Presence of chlorine also resulted in the increase of resistivity of the samples. In order to avoid this, we prepared indium sulfide films using nitrate based precursor solutions.

Interestingly for indium sulfide thin films, prepared using nitrate precursor solution, only the In/S ratio 2/3 showed good crystallinity with band gap 2.66 eV. But chloride samples showed better crystallinity on increasing sulfur concentration. We could get better control over stoichiometry while using nitrate solution. Moreover concentration of sulfur in the sample could be made even greater than 60% by increasing sulfur concentration in spray solution. Depth analysis of the sample using XPS indicated formation of In_2O_3 phase for sample having In/S ratio 2/4 which had maximum electrical resistivity and photosensitivity. But there was considerable decrease in the photosensitivity ($<10^2$) when compared to chloride-based samples. Another important point is that, unlike chloride-based samples, nitrate based one showed considerable increase in conductivity on increasing the sulfur concentration (2/6 to 2/8). In general, nitrate based samples were found to be more conducting, compared to chloride samples. As photosensitivity and crystallinity of the samples were not as good as chloride samples, chloride samples might be better as buffer layer for fabricating solar cells. But thickness of both samples could be increased upto $\sim 4\ \mu\text{m}$ in CSP technique.

We prepared and characterized CuInS_2 films also using two types of precursor solutions- nitrate and chloride. But in this case the major difficulty was that in a single spray, we could not increase the total volume of the solution sprayed beyond 375 ml as the samples got damaged. This corresponds to $0.6\ \mu\text{m}$ thickness of the sample.

Samples showed better crystallinity on increasing Cu/In ratio while band gap reduced. Electrical conductivity enhanced with Cu/In ratio in both cases. Cu-poor (In-rich) samples were found to be n-type. For nitrate-based samples Cu/In ratio followed faithfully the variation of molarity ratio of the solution better than that of chloride based ones. The atomic ratio was almost equal to that in the solution. Photosensitivity was slightly better for chloride samples. But the difference was small for Cu rich samples. Defect levels were identified using temperature dependent conductivity measurements and composition analysis. The shallow levels that were found in Cu rich samples, might be contributing to the high conductivity of these samples. Better crystallinity, stoichiometry, conductivity and photosensitivity of nitrate-based samples gave a feeling that these samples might be better for solar cells in the case of CuInS_2 samples.

We adopted 'multiple spray technique' to increase the thickness of CuInS_2 films because spraying large volume of the solution in a single stretch resulted in development of pin holes in the sample. Using this technique we prepared samples having thickness $>1 \mu\text{m}$. Greater Cu/In ratio resulted in better crystallite size and the band gap reduced from 1.49 eV to 1.3 eV. Depth analysis of the sample indicated absence of oxygen in the bulk of the sample even after multiple sprays. But Na was present throughout the depth of the sample, which might have diffused from the glass substrate. Cu/In ratio in the film was slightly less than that taken in the solution. Activation energies of defects of the sample were obtained using temperature dependent electrical conductivity measurements. Two distinct slopes corresponding to activation energies 390 meV (increases resistivity) and 196 meV (In_i or In_{Cu}) were obtained for sample having Cu/In ratio 0.5. Vacancy of copper, generated a level having activation energy 90 meV with the sample having Cu/In ratio 1. Here also we could find a shallow level for Cu/In ratio 1.5 contributing to its high conductivity.

In this work we fabricated solar cell having structure ITO/CuInS₂/In₂S₃/metal electrode and illumination was given from the substrate side. This structure was adopted, as we could not prepare junction in the real superstrate structure. Thin In₂S₃ layer was damaged while spraying CuInS₂ over it. But even when we prepared it in superstrate structure by using thick In₂S₃ layer, we found that the superstrate structure was not having any junction effect. Effect of atomic concentration as well as thicknesses of both absorber and buffer layers on the characteristics of the cell was studied. It was found that these two are very important factors affecting performance of the cell. Performance of the cell was improved when it was kept at the preparation temperature itself for 1 hour after deposition. The best cell parameters obtained were $V_{oc} = 529$ mV, $J_{sc} = 3.62$ mA/cm², FF = 29.88% and $\eta = 0.57\%$. XPS results indicated diffusion of copper from the CuInS₂ layer to the In₂S₃ layer, which might be one of the reasons for the low value of short circuit current. Also oxygen was detected throughout the depth of the cell leading to the increase of the series resistance. Efficiency of the cell increased to 2.65% when a thin layer (50 Å) of indium was deposited on the top of In₂S₃ layer followed by annealing at 100°C for 30 minutes. Thermal diffusion of indium at the top might have helped in the formation of a layer of In₂S₃ free of Cu at the top of the cell. Also it might be reducing the sheet resistance near the electrode. Aluminium deposited using vacuum evaporation was used as electrode in all these cases.

After the completion of works on single layer, CuInS₂ was sprayed in two steps (multiple spray) to increase thickness of the absorber layer without increasing thickness of In₂S₃ layer. The cell fabricated in this way had better efficiency of 5.87%. Concentration of Cu decreased towards CIS/In₂S₃ interface as evident from XPS analysis. Also there was no oxygen in the bulk of the cell, reducing the series resistance of the cell. Thick absorber layer should increase light absorption in the layer and hence the number of photogenerated carriers.

Maximum efficiency of 9.5% was obtained when the In_2S_3 layer was fabricated in two layers. This layer was thicker than the other cases. One could observe a layer of In_2S_3 free of Cu at the top of the cell. Diffusion of copper might have created Cu deficiency at the surface of the CIS layer probably making the CIS layer more photosensitive. Here also there was no oxygen in the bulk of the sample. Another interesting point was that deposition of silver at the top of In_2S_3 as top electrode could improve the crystallinity of In_2S_3 layer. Series resistance of the cell was reduced to 0.83Ω and this value was found to be much less than that of the other cases. Cell parameters obtained were $V_{oc} = 588 \text{ mV}$, $J_{sc} = 48.2 \text{ mA/cm}^2$, $FF = 33.5\%$ and $\eta = 9.5\%$. To the best of our knowledge this is the maximum efficiency obtained for a CIS/ In_2S_3 cell fabricated using CSP technique to deposit both the absorber and buffer layers. Moreover, we could effectively replace CdS using In_2S_3 as buffer layer.

Future Scopes

We could not prevent diffusion of copper from CIS layer to In_2S_3 layer because of the high temperature at which spraying has to be done. Hence we must adjust the thickness of CIS and In_2S_3 layers so as to compensate for diffusion. Fine adjustments in the atomic concentrations of both layers may also result in better efficiency of the cell. Reduction in the fill factor of the cell is another serious problem to be investigated. This could be achieved by reducing the series resistance of the cell. Doping the buffer layer (ie, In_2S_3) using Ag, In or Sn may reduce series resistance of the cell, increasing fill factor and thus efficiency. We characterized CuInS_2 and In_2S_3 films prepared using nitrate based precursor solutions, and effect of using these films for fabrication of the cell could also be investigated. Thickness and atomic concentrations of these layers also should be optimized by varying these two parameters in very fine steps for further improvement of cell properties. But this sort of fine-tuning of atomic concentration may not be possible through the adjustment of ratio of molar concentration of spray solution. Instead, we may have to use thermal

G8934

diffusion of very thin layer of the required material (Cu or In) deposited using vacuum evaporation. But after knowing the correct required concentration, this can be probably achieved through repeated adjustment of molar concentration in spray solution.

